SAPIENZA
UNIVERSITÀ DI ROMA

TOR VERGATA
UNIVERSITÀ
DEGLI STUDI
DI ROMA

INAF
ISTITUTO NAZIONALE
DI ASTROFISICA
NATIONAL INSTITUTE
FOR ASTROPHYSICS

PH.D. IN ASTRONOMY, ASTROPHYSICS
AND SPACE SCIENCE

CYCLE XXXII

Astrophysics with the Sunyaev–Zel'dovich effect in clusters of galaxies

Anna Silvia Baldi

A.Y. 2018/2019

Supervisor: Prof. Hervé Bourdin
Co-supervisor: Prof. Pasquale Mazzotta
Co-supervisor: Prof. Marco De Petris
Coordinator: Prof. Paolo De Bernardis
Deputy Coordinator: Prof. Nicola Vittorio

Abstract

Clusters of galaxies are unique systems in the universe. Being the largest gravitationally bound and virialized structures, they are "at the crossroads of astrophysics and cosmology". They host three main components: galaxies; hot, optically-thin plasma and non-baryonic dark matter. The Sunyaev–Zel'dovich effect, arising from the scattering of the photons of the cosmic microwave background off the free electrons in the ionized intra-cluster plasma, is one of the most valuable probes of cluster properties. Among these, cluster mass is the most important one, since it plays a central role in cluster-based cosmological studies. Direct measurements of the Sunyaev–Zel'dovich signal allow the investigation of the thermal pressure and of the projected velocity of the intra-cluster plasma along the observer's line of sight. This Thesis is devoted to the study of these quantities, which both play a relevant role in getting accurate estimates of cluster masses. More specifically, we focussed on: (*i*) the development and validation of an improved imaging algorithm to produce maps of the *thermal* component of the Sunyaev–Zel'dovich effect; (*ii*) an application of the *kinetic* Sunyaev–Zel'dovich effect to investigate cluster rotation. To this end, we used microwave data from real cluster observations with the *Planck* satellite, and mock data from a set of hydrodynamical simulations of galaxy clusters. Both these studies yielded interesting results, which can shed new light on largely addressed but yet unresolved issues in modern cluster science.

Contents

Introduction

The study of galaxy clusters plays a fundamental role in the vibrant field of modern cosmology. Clusters are the largest gravitationally bound and virialized objects in the universe, extending to virial radii of the order of a few Mpc[1]. The constituents of their total mass budget, which ranges from $10^{13}M_\odot$ to a few $10^{15}M_\odot$, are in the form of non-baryonic dark matter, hot intra-cluster gas, and hundreds of galaxies. Galaxy clusters provide an insight on the formation of cosmic structures and they allow constraining cosmological parameters which are sensitive to the content of non-relativistic matter in the universe. In these systems, gravity is the dominating force at play. At the smallest scales, however, the interactions governing the physics of collisional baryons enter the picture, thus impacting the observable properties of galaxy clusters and their evolution [see e.g. 454]. For this reason, astrophysics and cosmology are strictly connected in these systems.

At present, cluster science has to face some open issues, which are often related to our incomplete knowledge about the astrophysical processes at play, as well as about their modelling. For instance, the physics of the outermost cluster regions, where the accretion to the central halo is still ongoing is not fully understood, despite the enormous progress which has recently been made possible by observations and simulations [e.g. 459]. Even more important for its cosmological consequences [e.g. 355], is the problem of biases in the estimates of cluster masses, which are also sensitive to the effects lead by the physical processes characterising the outskirts. More specifically, the measurement of cluster masses based on the observable thermodynamic properties of the intra-cluster medium, usually rely on the assumptions of hydrostatic equilibrium and spherical symmetry. However, cosmological simulations highlighted a discrepancy between the mass values derived from observable-based methods and the true masses of clusters. A possible reason for this finding could be the non-fulfilment of the aforementioned conditions, which may originate a bias [e.g. 42].

The work presented in this Thesis tries to shed new light on this topic. To reach this goal, we exploited the Sunyaev–Zel'dovich effect [424–427] observable at millimetre wavelengths, with which it is possible to probe both the thermodynamic properties of the hot intra-cluster plasma and its dynamics. We used both the *thermal* and the *kinetic* Sunyaev–Zel'dovich effects for the study of cluster astrophysics in the context of two projects. The first one is dedicated to the imaging of the thermal Sunyaev–Zel'dovich effect for an efficient mapping of pressure structures at cluster

[1]By definition, 1 parsec (pc) corresponds to the distance at which the mean radius of the Earth subtends an angle of 1 arcsec. It is equivalent to 3.086×10^{16} m.

peripheries. The second one explores the possibility of using the kinetic Sunyaev–Zel'dovich effect to probe the dynamics of the intra-cluster gas, which may have to be taken into account to solve the issue of the observed mass bias.

The structure of the Thesis is as follows.
Chapter 1 gives a synthetic overview of modern cosmology, providing a general context for cluster studies, from the basic equations governing the evolution of the universe, to the theoretical foundations of structure formation.
In Chapter 2 we illustrate cluster formation through an overview on cosmological simulations. A discussion on the observable properties of clusters is then presented. Among these, the Sunyaev–Zel'dovich effect is treated in more detail, from both a theoretical and an observational point of view.
Chapter 3 concerns with the imaging of the thermal Sunyaev–Zel'dovich effect, tailored to the investigation of cluster outskirts. After a short summary on the existing methods to address the problem of component separation, we present an imaging algorithm based on wavelet and curvelet decompositions to optimally reconstruct anisotropies in the Sunyaev–Zel'dovich signal. We applied such a technique to a sample of nearby, well-resolved galaxy clusters observed by the *Planck* satellite [333], and which have been selected for the *XMM Cluster Outskirts Project* (X-COP hereafter) [144]. We conclude with the preliminary results on the ongoing study of the impact of overpressure detected in our maps on the radial pressure profiles of the intra-cluster gas.
Chapter 4 addresses an interesting, yet poorly explored topic: the presence of global rotational motions in clusters. Using data from the high-resolution *Marenostrum-mUltidark SImulations of galaxy Clusters* (MUSIC hereafter) [403], we first present a study on a possible rotation via the analysis of the angular momentum of gas and dark matter. Subsequently, we use the mock kinetic Sunyaev–Zel'dovich signal from the supposedly rotating clusters to reconstruct the rotational properties inferred from the angular momentum.

The methods and the results presented in Chapters 3 and 4 are the subjects of the following original papers:

- **A. S. Baldi**, H. Bourdin, P. Mazzotta, D. Eckert, S. Ettori, M. Gaspari, and M. Roncarelli. Spectral imaging of the thermal Sunyaev-Zel'dovich effect in X-COP galaxy clusters: method and validation. A&A, 630:A121, Oct. 2019;
- **A. S. Baldi**, M. De Petris, F. Sembolini, G. Yepes, W. Cui, and L. Lamagna. Kinetic Sunyaev-Zel'dovich effect in rotating galaxy clusters from MUSIC simulations. MNRAS, 479:4028, Sept. 2018;
- **A. S. Baldi**, M. De Petris, F. Sembolini, G. Yepes, L. Lamagna, and E. Rasia. On the coherent rotation of diffuse matter in numerical simulations of clusters of galaxies. MNRAS, 465:2584, Mar. 2017.

Furthermore, the authors contributed to the following works:

- W. Cui, A. Knebe, G. Yepes, et al. (including **A. S. Baldi**). The Three Hundred project: a large catalogue of theoretically modelled galaxy clusters for cosmological and astrophysical applications. MNRAS, 480:2898, Nov. 2018;

- G. Cialone, M. De Petris, F. Sembolini, G. Yepes, **A. S. Baldi**, and E. Rasia. Morphological estimators on Sunyaev–Zel'dovich maps of MUSIC clusters of galaxies. MNRAS, 477:139, June 2018.

Chapter 1

Cosmological context

The present Chapter provides an overview on the current cosmological picture. Specifically, we introduce the basics of the standard cosmological model describing the dynamics and the geometry of the universe, in the Friedmann–Lemaître–Robertson–Walker spacetime. Subsequently, we shortly review the cosmic microwave background radiation, which is the fossil residue of the Big Bang. The paradoxes raised by the standard model are then discussed, and a brief presentation of the inflationary solution is provided. It follows an overview of the theory of the formation of cosmic structures from the evolution of density perturbations in the linear and in the non-linear regimes. We conclude reporting the more recent constraints on the present-day values of the cosmological parameters, together with a short discussion on related open issues in the context of the cosmological model favoured by observations.

1.1 The standard model of cosmology

The study of galaxy clusters is deeply connected to cosmology. Cluster origin and evolution is based on the hierarchical scenario of structure formation, according to which large objects originate from the aggregation of smaller ones, as prescribed by the standard model of cosmology.
The latter represents our current understanding of the universe, which is built on fundamental physics and supported by observations. Its cornerstone is the principle of homogeneity and isotropy, or invariance under translations and rotations, which states there are no preferred positions or directions in the universe at large scales ($\gtrsim 100\,\mathrm{Mpc}$).
The universe is expanding since the Big Bang and its evolution is driven by its mass-energy content, according to Einstein's theory of general relativity [148].
During the first hundred thousand years after the Big Bang, the universe was dominated by relativistic matter (or *radiation*), and everything was in the form of a primeval photo-baryon fluid. As the temperature reached about ten thousand K, non-relativistic matter became the dominating component driving the evolution of the universe. The epoch at which matter and radiation densities were comparable is called *equivalence*. About four hundred thousand years after the Big Bang the universe was cool enough to allow baryons to decouple from photons, and to form the first neutral atoms. Several independent observations suggest that at the present

time, about ten billion years after the Big Bang, the expansion of the universe is mainly driven by two yet unknown physical components: *dark energy* in the form of a cosmological constant named Λ, and a form of non-relativistic, non-baryonic *cold dark matter*. For this reason, the current cosmological scenario supported by observations is called ΛCDM model [see e.g. 263].

1.1.1 Dynamics of the universe

By virtue of the cosmological principle of homogeneity and isotropy, the spacetime in an expanding universe can be represented by the Friedmann–Lemaître–Robertson–Walker (FLRW) metric [168, 258, 377, 458]:

$$ds^2 = -c^2dt^2 + a^2\left[\frac{dr^2}{1-\kappa r^2} + r^2(d\theta^2 + \sin^2\theta d\phi^2)\right] \ , \tag{1.1}$$

in spherical spatial coordinates, where c is the speed of light. The radial coordinate, r is che *comoving distance* and $a = a(t)$, which depends on the time coordinate, is the *scale factor* encoding the expansion. The *proper distance* between two objects is obtained by multiplying the comoving distance by the scale factor:

$$d = ar \ . \tag{1.2}$$

At the present time, t_0, the scale factor is $a_0 = a(t_0) = 1$, therefore proper and comoving distances coincide. The κ constant in equation (1.1) is the spatial curvature, which is positive, negative or null for close, open and flat universes, respectively.
The dynamics of the universe is given by Einstein's field equations:

$$G_{\mu\nu} = \frac{8\pi G}{c^4}T_{\mu\nu} \ , \tag{1.3}$$

being $G_{\mu\nu} = R_{\mu\nu} - \frac{1}{2}g_{\mu\nu}$ the Einstein tensor, $R_{\mu\nu}$ the Riemann tensor and G the gravitational constant; $g_{\mu\nu}$ is the metric tensor that allows one to compute the infinitesimal distance element ds^2 through the relation:

$$ds^2 = g_{\mu\nu}dx^\mu dx^\nu \ , \tag{1.4}$$

being $\vec{x}$ the four-dimensional coordinate vector.
Supposing that the universe is filled with a homogeneous and isotropic perfect fluid having pressure p and density ρ, the stress-energy tensor is:

$$T_{\mu\nu} = (c^2\rho + p)u_\mu u_\nu + pg_{\mu\nu} \tag{1.5}$$

where $\vec{u}$ is the four-velocity vector.
Pressure and density are connected via an equation of state of the form:

$$p = wc^2\rho \ , \tag{1.6}$$

where the constant w takes the values 0, 1/3 and -1 for non-relativistic matter, relativistic matter and the cosmological constant, respectively.
Plugging the FLRW metric of equation (1.1) and the stress-energy tensor as in

equation (1.5), explicitly accounting for a dark energy pressure $p_\Lambda = -\Lambda c^4/(8\pi G)$ into the equations (1.3), one obtains the two *Friedmann equations* [e.g. 263]:

$$\left(\frac{\dot{a}}{a}\right)^2 = \frac{8\pi G}{3}\rho - \frac{\kappa c^2}{a^2} + \frac{\Lambda c^2}{3} \tag{1.7}$$

from the time component of Einstein's equations, and

$$\frac{\ddot{a}}{a} = -\frac{4\pi G}{3}\left(\rho + \frac{3p}{c^2}\right) + \frac{\Lambda c^2}{3} \tag{1.8}$$

when considering the spatial components. Equation (1.7) describes the expansion rate of the universe as a function of time, depending on the dominating components of the cosmic fluid, while equation (1.8) concerns with the acceleration of the expansion. In particular, it can be seen that a non-zero cosmological constant leads to a positive acceleration, while the other components of the cosmic fluid slow down the expansion. The left-hand side of equation (1.7) is the *Hubble parameter*, whose integration describes how the universe expands with time:

$$H = \frac{\dot{a}}{a} \ , \tag{1.9}$$

being dimensioned as an inverse time.
By introducing the *critical density* at the time t as

$$\rho_{\rm cr}(t) = \frac{3H^2}{8\pi G} \ , \tag{1.10}$$

it is possible to write the first Friedmann equation (1.7) in the following form:

$$\rho_{\rm cr}\left(1 + \frac{\kappa c^2}{a^2 H^2}\right) = \rho_{\rm tot} \ , \tag{1.11}$$

where $\rho_{\rm tot}$ takes into account all mass-energy species. Normalizing both sides of equation (1.11) to the critical density, the following compact form is obtained:

$$\Omega_{\rm tot} = 1 - \Omega_\kappa \ , \tag{1.12}$$

being $\Omega_\kappa = -\kappa c^2 (aH)^{-2}$, and having introduced the *cosmological density parameters*, defined as the ratio between the density of the cosmic fluid (or any of its single components) and the critical density at a given time: $\Omega = \rho/\rho_{\rm cr}$. Such a way of recasting the first Friedmann equation links directly the mass-energy content of the universe to its spatial curvature. If the measured values of the cosmological density parameters is such that their sum equals unity, then the curvature component must necessarily vanish, by virtue of equation (1.12).
The value of the critical density at the present time is:

$$\rho_{\rm cr0} = \frac{3H_0^2}{8\pi G} = 2.78 \times 10^{11} h^2 \ {\rm M}_\odot \ {\rm Mpc}^{-3} \ ,$$

where $\rm M_\odot$ is the Solar mass.
The Hubble parameter evaluated at the present time, H_0, is called *Hubble constant*,

which is frequently written as $H_0 = 100\ h\ \mathrm{km\,s^{-1}\,Mpc^{-1}}$, being h a constant factor [115]. Its inverse gives the *Hubble time*:

$$t_H = 9.78\ h^{-1}\ \mathrm{Gyr}\ ,$$

which multiplied by the speed of light defines the *Hubble distance*, $d_H = cH_0^{-1}$:

$$d_H = 3.00\ h^{-1}\ \mathrm{Gpc}\ .$$

A further way of writing the first Friedmann equation (1.7), referring to the present-time values of the cosmological parameters, is the following:

$$\begin{aligned} \frac{H^2}{H_0^2} &= E^2(z) \\ &= \Omega_{r0}(1+z)^4 + \Omega_{m0}(1+z)^3 + \Omega_{\kappa 0}(1+z)^2 + \Omega_\Lambda\ , \end{aligned} \tag{1.13}$$

which descends from the explicit substitution of all the density terms properly scaled with redshift in equation (1.11). In particular, the density terms in equation (1.13) pertain to a universe which has a non-vanishing spatial curvature ($\Omega_{\kappa 0}$), and which contains relativistic matter (Ω_{r0}), non-relativistic matter (Ω_{m0}), plus a cosmological constant (Ω_Λ; see also section 1.5).

A proper combination of the two Friedmann equations leads to the continuity equation giving the conservation of mass and energy, that is [e.g. 138]

$$\dot{\rho} = -3\rho(1+w)\frac{\dot{a}}{a}\ , \tag{1.14}$$

where we made use of the equation of state (1.6). By integrating the continuity equation it is possible to find the evolution of density with time through the scale factor:

$$\rho = \rho_0 a^{-3(1+w)}\ , \tag{1.15}$$

being $\rho_0 = \rho(a = a_0)$, which can be solved for each single component.

The scale factor is related to a fundamental cosmological observable: the *redshift*, i.e. the relative difference between the observed wavelength of the electromagnetic radiation from a source and the emitted one:

$$z = \frac{\lambda_{\mathrm{obs}}}{\lambda_{\mathrm{em}}} - 1\ , \tag{1.16}$$

which, in a non-relativistic regime, arises from the relative motion between the observer and the source (i.e. the Doppler effect). The cosmological redshift is given by both the relative motion and the expansion of the universe, which adds a further velocity component to the peculiar one, called the *Hubble flow*. The redshift is connected to the scale factor by:

$$a = \frac{a_0}{1+z}\ , \tag{1.17}$$

which implies that the scale factor at any epoch can be determined from a measurement of the redshift. The above relation descends from the geodesic motion of massless particles in a FLRW universe, according to which the wavelengths of the electromagnetic radiation emitted by a source keep increasing as the space dilates, as well as proper distances between objects.

1.1.2 Distances in cosmology

In general relativity, distances are not measured in space, but rather along radial null trajectories in spacetime, since they are necessarily based on observations [203]. Astronomical distances are usually determined via a *distance ladder*: at each step one applies a suitable method whose calibration is derived from the previous step in the ladder, to get distances over increasing scales [461].
There are three main definitions of distance which are useful in cosmology: the *comoving distance*, the *luminosity distance* and the *angular diameter distance*. They are briefly described in the following.

Comoving distance

The comoving distance gives the separation between two objects both moving with the Hubble flow. In a FLRW spacetime, a photon travelling along a radial geodesic from an emitting source at redshift z to an observer at redshift $z = 0$, is at a comoving distance [203]:

$$r = \begin{cases} \kappa^{-1/2} \sin(\kappa^{-1/2}\, \mathcal{I}(z)) & \text{if } \kappa > 0 \\ \mathcal{I}(z) & \text{if } \kappa = 0 \\ |\kappa|^{-1/2} \sinh(|\kappa|^{-1/2}\, \mathcal{I}(z)) & \text{if } \kappa < 0 \end{cases} . \tag{1.18}$$

The integral $\mathcal{I}(z)$ encodes the dependence on the cosmological parameters through the first Friedmann equation, being defined as

$$\mathcal{I}(z) = c \int_0^z H^{-1}\, dz \;\; = c \int_{\frac{1}{1+z}}^1 H^{-1}\, \frac{da}{a^2} \;, \tag{1.19}$$

corresponding to the distance travelled by light from the time t to the present time t_0. By integrating equation (1.19) from the time of the beginning of the universe, $t = 0$ (corresponding to $a = 0$), one gets the *comoving horizon* (also called *particle horizon*), which sets the maximum distance within which two objects in the universe can be in causal contact.

Luminosity distance

In a static universe, the flux received by an observer from an isotropically emitting source is given by:

$$F = \frac{L}{4\pi r^2} \;, \tag{1.20}$$

that is the luminosity of the source, L, over the surface of a sphere having radius equal to its comoving distance to the observer, r, here coinciding with the proper distance. If the universe expands, the luminosity is reduced by a factor of $(1 + z)^2$, being z the redshift of the emitting source. One factor comes from the fact that energy is greater as the radiation leaves the source. The other one is due to the radiation being redshifted because of the expansion. The flux received by the observer in an expanding universe is then:

$$F = \frac{L}{4\pi r^2 (1 + z)^2} \;, \tag{1.21}$$

so that the luminosity distance is *defined* as

$$d_L = r(1+z) \ . \tag{1.22}$$

Angular diameter distance

If the universe does not expand, the distance to an object having proper size R and subtending an angle θ is given by the approximate relation (for small θ):

$$r = \frac{R}{\theta} \ . \tag{1.23}$$

In a FLRW universe, the comoving distance R travelled by photons along a radial direction is given by:

$$R = \frac{r\theta}{(1+z)} \ , \tag{1.24}$$

which compared to equation (1.23) gives the definition of the angular diameter distance:

$$d_A = \frac{r}{1+z} \ . \tag{1.25}$$

Depending on the cosmological model, the latter can decrease with increasing redshift (e.g. in the case of null spatial curvature), making very distant objects to appear larger.

As can be seen from their definitions, the above two distances are linked by the so-called *duality relation* [153]:

$$d_L = d_A(1+z)^2 \ . \tag{1.26}$$

It is useful to give here the scaling with redshift of the brightness from an extended source (e.g. a galaxy cluster). Indeed, brightness – also called *surface* brightness – is defined as a flux per unit solid angle; the flux scales with redshift as $(1+z)^{-2}$, while the solid angle is proportional to the inverse square of the angular diameter distance. Thus, from the duality relation of equation (1.26), it descends that the brightness from a source at redshift z scales as

$$S \ \propto \ \frac{d_A^2}{d_L^2} \ \propto (1+z)^{-4} \ . \tag{1.27}$$

Both the luminosity and the angular diameter distance are sensitive to the cosmological parameters describing the composition and the dynamics of the universe, being proportional to the comoving distance. Figure 1.1 shows the three distances as a function of the redshift for two cosmological models. It can be seen that for low redshift values the three definitions are equivalent. Indeed, it is possible to show that by plugging a series expansion of the scale factor around the present-day time in equation (1.18), the comoving distance at low redshifts coincides with the Hubble distance, as well as with the proper distance [263].
It is clear that accurate measurements of these distances are crucial to constrain the cosmological parameters describing the geometry and the dynamics of the universe.

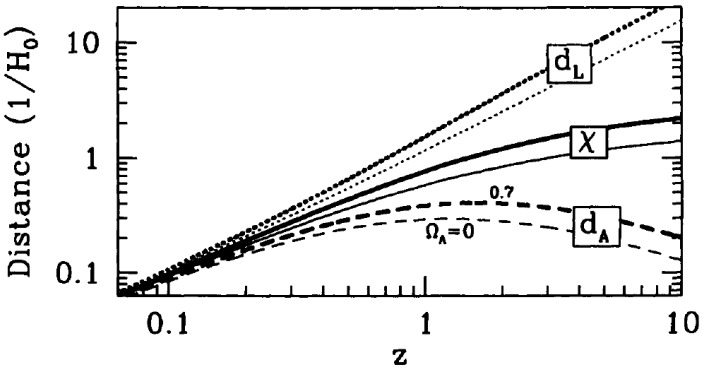

Figure 1.1. Comoving distance (χ), luminosity distance (d_L) and angular diameter distance (d_A) as functions of redshift for two spatially flat cosmologies. Thick curves represent the case of a universe with a cosmological constant with density parameter $\Omega_\Lambda = 0.7$; thin curves refer to the case in which non-relativistic matter is the only component [taken from 138].

However, to determine such distances to an object, either its intrinsic luminosity or its angular size must be known. For this reason, one refers to *standard candles* and to *standard rulers*, respectively, whose properties are known on a theoretical basis. Historically, the first observational hint of the expansion of the universe came from measurements of the spectroscopic velocities of distant galaxies, made by Hubble in 1929. Relating these velocities to the proper distances, estimated through the periodicity of the absolute magnitude of Cepheid stars [e.g. 174], he found the well-known *Hubble's law* [210]:

$$d = vH_0^{-1} \ . \tag{1.28}$$

Putting $v = cz$, the above linear relation gives the lowest-order of the relation between proper distance and redshift (see also Figure 1.1), whose full expression comes from the integration of the line-of-sight comoving distance of equation (1.19).

1.2 The cosmic microwave background radiation

The photons of the cosmic microwave background (CMB hereafter) represent the most ancient observable radiation in the universe. Its serendipitous discovery in 1964 [325] represents the second observational milestone of cosmic expansion. They originated from the annihilation of elementary particles and antiparticles in the early universe [170, 9, 133]. Before recombination, i.e. the formation of the first neutral atoms that occurred at redshift $z \approx 1100$, photons were strongly interacting, mainly via Thomson scattering [see e.g. 387], with the free charged particles constituting the primeval plasma, or photo-baryon fluid [324]. The universe was opaque prior to recombination, thus the CMB photons are considered to come from the so-called *last scattering surface*, which is the spherical surface, conventionally centred in our Galaxy, where the last Thomson scattering happened. Since recombination, photons could freely propagate. As a consequence of the expansion of the universe, their wavelength increased, so that at recent epochs they can be detected as a diffuse,

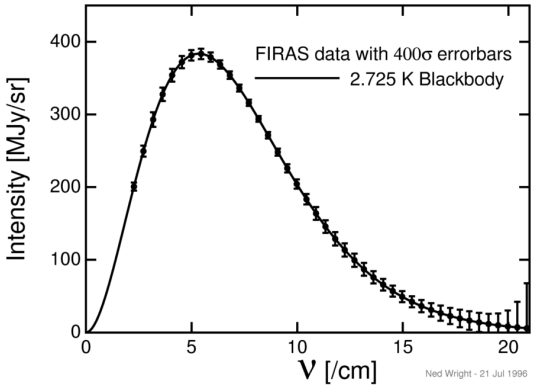

Figure 1.2. Brightness of the CMB radiation measured by COBE/FIRAS [166]. The error bars on the experimental data have been enlarged by a factor of 400 to make them visible. The solid line represents the best-fit curve [taken from http://www.astro.ucla.edu/~wright/cosmo_01.htm].

isotropic background with a black body spectrum peaked at microwave frequencies.

The discovery of CMB radiation definitively marked the beginning of observational cosmology. Since microwave radiation is absorbed by molecular gases in the Earth's troposphere, the optimal way to measure the CMB is from space. The very first space mission dedicated to CMB observations was the *COsmic Background Explorer* satellite (*COBE*) [278]. The *Far InfraRed Absolute Spectrophotometer* (FIRAS) onboard *COBE*, equipped with a Martin-Puplett interferometer [274], produced a measurement of the spectral energy density of the CMB radiation as a function of the photon frequency, revealing a perfect agreement with a black body spectrum (shown in Figure 1.2):

$$B(\nu; T_{\rm CMB}) = \frac{2h_P\nu^3}{c^2}\frac{1}{\exp\left(\frac{h_P\nu}{k_B T_{\rm CMB}}\right) - 1} \ , \tag{1.29}$$

where h_P is Planck constant, and k_B is Boltzmann constant. The temperature of the CMB is, from the combination of several subsequent experiments [165]:

$$T_{\rm CMB} = (2.72548 \pm 0.00057)\ {\rm K} \ .$$

Measurements from the *Differential Microwave Radiometer* (*COBE*/DMR), revealed for the first time that the temperature of the CMB is not exactly the same at every position in the sky. More generally, CMB temperature anisotropies are of two kinds. One has *primary* anisotropies, which are produced by physical processes taking place in the early universe, prior to recombination. On the other hand, *secondary* anisotropies plus polarization anisotropies occur as the CMB photons propagate, as a result of gravitational interactions or Thomson scattering off free electrons [209].

CMB temperature anisotropies are described as functions of the angular scale through a decomposition in spherical harmonics. Under the assumption of Gaussianity of the perturbations (see also section 1.3), their statistics is all encoded in the angular

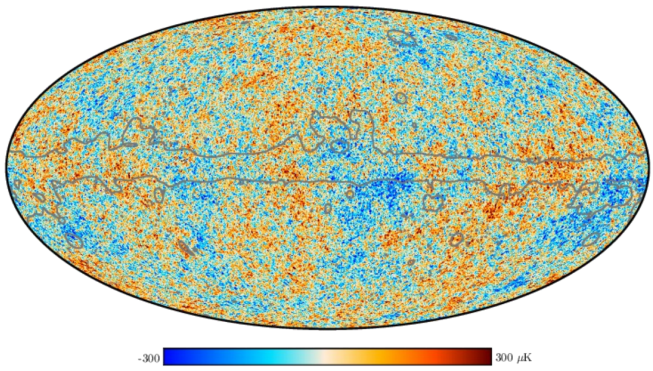

(a)

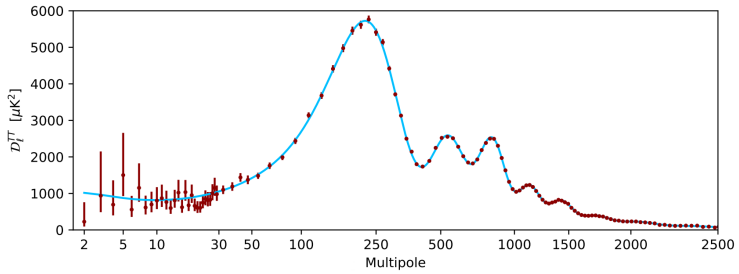

(b)

Figure 1.3. Temperature anisotropies of the CMB from the latest *Planck* data. **(a)** All-sky map in Mollweide projection. Light grey lines highlights the boundaries of the mask applied to the Galactic region, which is strongly contaminated by foregrounds (see also section 3.1). **(b)** Angular power spectrum. Data are shown as red points, while the best-fit is represented by the cyan curve, favouring a ΛCDM cosmology [taken from 349].

power spectrum. Figure 1.3 shows the map of the CMB anisotropies and their angular power spectrum from the most recent data by the *Planck* satellite [333]. The physical explanation of the observed power spectrum relies on gravitational effects, and on the dynamics of the photo-baryon fluid. Indeed, it is possible to distinguish three main regions: the Sachs–Wolfe plateau on large scales [388], baryon acoustic oscillations on scales smaller than the comoving sound horizon at recombination, and the Silk damping on scales below a few arc-minutes [412]. The exact shape of the power spectrum is sensitive to the cosmological parameters. In particular, the multipole of the first acoustic peak corresponds to the angular scale of the comoving sound horizon at recombination, and it constrains the spatial geometry of the universe, since it depends on the sum of the cosmological parameters [28].
The Sachs–Wolfe effect and its second-order term on smaller scales, known as Rees–Sciama effect [366], is a *gravitational* secondary anisotropy. The Sunyaev–Zel'dovich effect [425] is, instead, a source of *scattering* secondary anisotropies, which will be addressed in detail in section 2.2.

1.3 Paradoxes of the standard model and inflation

The FLRW model of the universe raises some critical aspects, known such as the *horizon paradox*, the *flatness paradox* and the *magnetic monopole paradox*.
The horizon paradox arises from the observed homogeneity of the CMB: temperature fluctuations due to primary anisotropies are indeed of the order of $\Delta T_{\rm CMB}/T_{\rm CMB} \approx 10^{-5}$ across the sky. Such small variations could be justified only assuming thermal equilibrium, made possible by causal contact, of regions within the horizon scale at recombination. Nevertheless, the angle subtended by the horizon at recombination today is of the order of 1 degree, meaning that patches in the sky separated by greater angles were *not* in causal contact at recombination, raising the question on how they reached thermal equilibrium to explain the amplitude of the temperature fluctuations observed today. Moreover, given the homogeneity of the universe, the standard model does not provide a mechanism capable of originating the density fluctuations causing the occurrence of anisotropies in the CMB temperature, which are the seeds for the formation and growth of cosmic structures.
The flatness paradox deals with the spatial curvature of the universe. The value of the density parameter of curvature measured today, $\Omega_{\kappa 0}$, is found to be consistent with zero (see section 1.5), implying the spatial flatness of the universe, by means of equation (1.12). However, the values of the density parameters in the early universe had to be extraordinarily tuned to provide $\Omega_{\rm tot} \simeq 1$, given that the curvature parameter Ω_κ increases with increasing time, in a standard scenario [see e.g. 324]. Clearly, a fine tuning is an unsatisfactory and unlikely explanation of spatial flatness.
The last controversial aspect of the FLRW universe is the lack of observational evidences for the existence of relic particles such as magnetic monopoles. In grand unified theories such massive particles are expected to be produced in the early universe as topological defects generated by phase transitions, at temperatures $T_{\rm GUT} \approx 10^{28}\,{\rm K}$ [e.g. 263].

The inflationary solution

The physical mechanism which could solve all the above paradoxes of the standard cosmological model, and being responsible for the generation of primeval perturbations is called *inflation*, proposed in the early 1980s [186, 264, 188].
Inflation is a phase in which the expansion of the universe is exponentially accelerated. It is believed to have taken place in the very early stages of the evolution of the universe, during the radiation-dominated epoch. As it can be seen from the second Friedmann equation (1.8), the expansion accelerates if the dynamics of the universe is dominated by some fluid with negative pressure, similar to the modern cosmological constant. The scale factor during inflation evolves as

$$a = a_i e^{H_i (t - t_i)} \,, \tag{1.30}$$

being t_i the time at which inflation starts, with corresponding scale factor a_i. During this epoch the comoving Hubble distance, $(aH)^{-1} = \dot{a}^{-1}$, *decreases* with increasing time, contrarily to the standard behaviour, while the Hubble parameter stays constant, $H = H_i$. This fact is the key to solve both the horizon and the flatness problems.

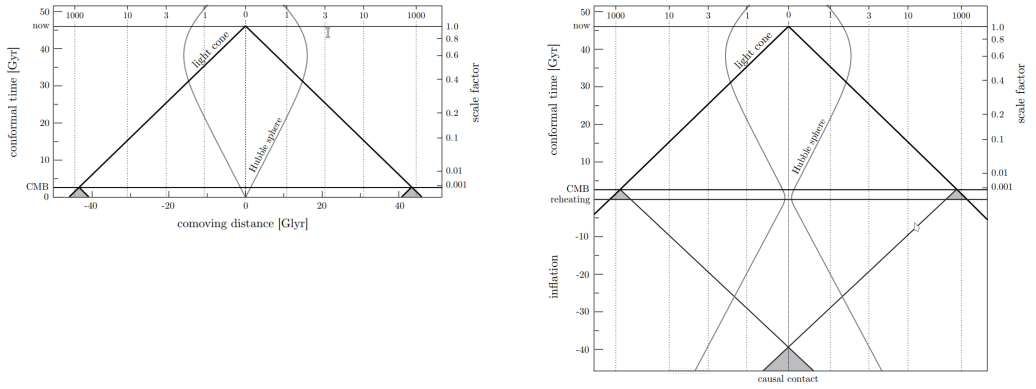

(a) Horizon paradox **(b)** Inflationary solution

Figure 1.4. Illustration of the horizon paradox and its inflationary solution. **(a)** In the standard scenario, the comoving Hubble distance grows with time, so it does the horizon (in the absence of accelerating components as dark energy). Thus, all the CMB regions which are separated today by angular distances greater than $\approx 1°$ in the sky could not reach causal contact in the past. This is because their light cones (marked in grey) did not overlap before the spacetime was terminated by the initial singularity at $\tau = 0$. **(b)** During inflation, the comoving Hubble distance shrinks with increasing time and then expands during the conventional evolution. Inflation corresponds to an additional span of (negative) conformal time, during which all the regions in the CMB have overlapping light cones, and therefore originated from a causally connected region of space [taken from 33].

Indeed, the comoving horizon distance is proportional to the comoving Hubble distance; therefore, if it was larger in the past than at recombination, the CMB would come from regions that were causally connected during inflation, provided this phase lasts for a sufficient time. If inflation ends at a time t_e, its duration is quantified by the number of e-foldings, N_f, defined as

$$N_f = H_i(t_e - t_i) \ , \tag{1.31}$$

where H_i is the Hubble parameter during inflation. In order to solve all the FLRW paradoxes consistently with observations, the number of e-foldings in any theory of inflation must be $N_f > 65$ [e.g. 187]. Figure 1.4 gives a visual explanation of the solution to the horizon paradox. The role of inflation is that of providing an additional span of conformal time between the origin of the universe and recombination, during which causal connection happened. Conformal time is a convenient rescaling of the coordinate time by the scale factor, so it is defined as: $d\tau = a^{-1}\, dt$; this quantity is negative if the scale factor grows exponentially as in equation (1.30).
On the other hand, the curvature cosmological parameter Ω_κ is proportional to $(aH)^{-2}$, therefore a decreasing comoving Hubble distance would *naturally* lead to smaller values of the spatial curvature in the past, thus solving the flatness paradox. Finally, the accelerated expansion during inflation caused the number density of magnetic monopoles to be diluted over a huge volume, thus reducing drastically the probability of observing them.

The simplest form of mass-energy having negative pressure is a scalar field, φ

(or *inflaton*), which has an associated potential energy density, $V(\varphi)$. Inflation corresponds to the phase transition of the inflaton field arising from a spontaneous symmetry breaking, as prescribed by quantum field theory. At the beginning of inflation, the inflaton is in a false vacuum state (i.e. a local minimum of the potential), which is metastable. During the inflationary phase, the field evolves towards the true vacuum state (global minimum of the potential). To have $V(\varphi) \gg \dot{\varphi}$, and to ensure this phase lasts enough to drive the total density parameter towards unity, the field has to "roll" slowly along an almost flat region of its potential. This translates into the following so-called *slow-roll conditions*:

$$\epsilon = \frac{1}{24\pi G}\left(\frac{V'}{V}\right)^2 \ll 1 \tag{1.32}$$

$$\eta = \frac{1}{8\pi G}\frac{V''}{V} \ll 1 \ , \tag{1.33}$$

where $' = \frac{d}{d\varphi}$. Inflation ends when the true vacuum state is reached and the slow-roll conditions are no longer valid. In this regime the kinetic term dominates over the potential, and the field starts oscillating around the minimum, to eventually decay into the ordinary matter of the standard model of particles. The latter stage is called *reheating*, as the universe gets repopulated after the inflaton domain [28].
Nevertheless, as any other quantum scalar field, the inflaton undergoes spatially-varying fluctuations, besides its homogeneous evolution. This means that inflation does not end simultaneously in every position in the universe, so the time at which inflation effectively ends at the position $\boldsymbol{x}$, is:

$$t_e(\boldsymbol{x}) = \langle t_e \rangle_{\boldsymbol{x}} + \delta t_e(\boldsymbol{x}) \ , \tag{1.34}$$

that is an average time plus some fluctuations. The latter can be ultimately translated into density perturbations which are encoded in the primary anisotropies of the CMB, and whose evolution over cosmic times depicts the standard scenario of the formation of cosmic structures, which will be addressed in section 1.4.
Linear density fluctuations from inflation arise from the superposition of many independent, incoherent modes whose amplitudes and wave numbers are drawn from the same distribution. Therefore, they are predicted to be Gaussian and adiabatic. Moreover, under the slow-roll conditions, they are characterized by a scale-invariant power spectrum, as will be briefly discussed in the next section.

1.4 Formation of cosmic structures

In the standard cosmological scenario, all the gravitationally bound structures constituting the observable universe today formed from the growth of density perturbations under the action of gravity [e.g. 109]. To describe the growth of perturbations whose scales are smaller than the horizon in the domain of non-relativistic matter, a classical Newtonian treatment is adequate. To study super-horizon perturbations, as well as the evolution of perturbations in the domain of relativistic matter within the horizon, general relativity is necessary, instead [we refer the reader to 301, for a complete review].
In the following, a synthetic overview of the evolution of perturbations on sub-horizon scales is provided.

1.4.1 Linear regime

Supposing the universe has a mean density $\bar{\rho}$, perturbed by a density fluctuation $\delta\rho$, the linear regime holds if $\delta\rho \ll \bar{\rho}$. According to Jeans theory, all perturbations of size larger than the *Jeans' length* grow exponentially, until gravitational collapse occurs [220].
The starting point is to consider a perfect isotropic and homogeneous fluid obeying the three fundamental equations of fluid dynamics:

$$\frac{\partial \rho}{\partial t} + \boldsymbol{\nabla}_{\boldsymbol{x}} \cdot (\rho \boldsymbol{u}) = 0 \tag{1.35}$$

$$\rho \frac{\partial \boldsymbol{u}}{\partial t} + \rho(\boldsymbol{u} \cdot \boldsymbol{\nabla}_{\boldsymbol{x}})\boldsymbol{u} = -\boldsymbol{\nabla}_{\boldsymbol{x}} p - \rho \boldsymbol{\nabla}_{\boldsymbol{x}} \Phi \ , \tag{1.36}$$

$$\nabla^2_{\boldsymbol{x}} \Phi = 4\pi G \rho \tag{1.37}$$

which are the continuity equation giving conservation of mass, Euler's equation expressing the conservation of momentum, and Poisson's equation relating the density of the fluid, $\rho = \rho(t, \boldsymbol{x})$, to the Newtonian gravitational potential Φ, being $\boldsymbol{x}$ the proper position. The pressure of the fluid, $p = p(t, \boldsymbol{x})$, is related to its density by means of a suitable equation of state, and $\boldsymbol{u} = \boldsymbol{u}(t, \boldsymbol{x})$ is the velocity of the fluid. By perturbing density, pressure, velocity and the gravitational potential in the above equations (1.35), (1.36) and (1.37), and retaining only the first-order terms in the perturbations, one has:

$$\frac{\partial \delta\rho}{\partial t} = -\boldsymbol{\nabla}_{\boldsymbol{x}} \cdot (\bar{\rho} \delta \boldsymbol{u}) \tag{1.38}$$

$$\bar{\rho} \frac{\partial \delta \boldsymbol{u}}{\partial t} = -c_s^2 \boldsymbol{\nabla}_{\boldsymbol{x}} \delta\rho - \bar{\rho} \boldsymbol{\nabla}_{\boldsymbol{x}} \delta\Phi \ , \tag{1.39}$$

$$\nabla^2_{\boldsymbol{x}} \delta\Phi = 4\pi G \delta\rho \tag{1.40}$$

where, by virtue of the equation of state, the pressure perturbation is written as

$$\delta p = \left.\frac{\partial p}{\partial \rho}\right|_s \delta\rho = c_s^2 \delta\rho \ , \tag{1.41}$$

under the adiabatic condition $\delta s = 0$, being s the entropy of the fluid and c_s the adiabatic speed of sound.
A suitable combination of equations (1.38), (1.39) and (1.40) yields the sound wave equation for the density perturbations:

$$\nabla^2_{\boldsymbol{x}} \delta\rho - \frac{1}{c_s^2} \frac{\partial^2 \delta\rho}{\partial t^2} = -\frac{4\pi G \bar{\rho}}{c_s^2} \delta\rho \ . \tag{1.42}$$

It is convenient to express the above wave equation in Fourier space, where in the linear regime all modes evolve independently from each other. Recurring to the formal substitutions:

$$\frac{\partial}{\partial t} \ \rightarrow \ i\omega \tag{1.43}$$

$$\boldsymbol{\nabla}_{\boldsymbol{x}} \ \rightarrow \ i\boldsymbol{k} \ , \tag{1.44}$$

being i is the imaginary unit, ω the time pulsation and $\boldsymbol{k}$ the (proper) wave vector equation (1.42) in the adiabatic regime can be rewritten as

$$(\omega^2 - k^2 c_s^2)\delta\rho_{\boldsymbol{k}} = -4\pi G\bar{\rho}\delta\rho_{\boldsymbol{k}} \ , \tag{1.45}$$

which has solutions in the form of plane waves:

$$\delta\rho(t, \boldsymbol{x}) = \frac{1}{(2\pi)^3}\int \delta\rho_{\boldsymbol{k}}\ e^{i(\boldsymbol{k}\cdot\boldsymbol{x}\ \pm\ \omega_{\boldsymbol{k}}t)}\ d\boldsymbol{k} \ . \tag{1.46}$$

Setting $\omega^2 = 0$ in equation (1.45) defines the Jeans' wave number, k_J, and the corresponding Jeans' length, $l_J = \frac{2\pi}{k_J}$, giving the critical scale for the growth of perturbations:

$$l_J = c_s\sqrt{\frac{\pi}{G\bar{\rho}}} \ . \tag{1.47}$$

It can be seen that for perturbation sizes $l > l_J$ the dispersion relation yields $\omega^2 < 0$, therefore the solution (1.46) oscillates with amplitude which exponentially grows or decreases over time. Vice-versa, for perturbation sizes $l < l_J$ one has $\omega^2 > 0$, thus the perturbation evolves as a sound wave of constant amplitude.

Perturbations in an expanding universe

When the expansion of the universe is taken into account, all the above equations must be rewritten in comoving coordinates. The proper position becomes:

$$\boldsymbol{x} = a\boldsymbol{r} \ , \tag{1.48}$$

while the velocity is:

$$\boldsymbol{u} = H\boldsymbol{x} + \boldsymbol{v} \ , \tag{1.49}$$

being $H\boldsymbol{x}$ the Hubble flow and $\boldsymbol{v} = a\dot{\boldsymbol{r}}$ the peculiar velocity. Taking into account the relation between time and spatial derivatives in proper vs comoving coordinates, the above steps can be repeated by calculating the linear perturbation of equations (1.35)–(1.37). One eventually gets the instability equation in a universe dominated by non-relativistic matter (so that $\bar{\rho} \propto a^{-3}$), describing the evolution with time of each comoving Fourier mode (hereafter $k = 2\pi/r$):

$$\ddot{\delta}_{\boldsymbol{k}} + 2H\dot{\delta}_{\boldsymbol{k}} + (k^2 c_s^2 - 4\pi G\bar{\rho})\delta_{\boldsymbol{k}} = 0 \ , \tag{1.50}$$

having introduced the *density contrast*:

$$\delta_{\boldsymbol{k}} = \frac{\delta\rho_{\boldsymbol{k}}}{\bar{\rho}} \ . \tag{1.51}$$

The solution of equation (1.50) is different for the different energy components. From the first Friedmann equation, which sets the evolution of the mean density $\bar{\rho}$ with time, it is possible to describe the evolution of linear density perturbations for each component of the cosmic fluid, depending on the dominating species at a given epoch.
As a general result, the only component whose Jeans length is always small enough

to allow gravity to overcome pressure gradient forces is dark matter. Perturbations of the density of baryonic matter can grow only after the decoupling from radiation. Indeed, during radiation domain, the photo-baryon plasma oscillates until the equivalence, after which baryon perturbations catch up with dark matter ones and start growing [109]. At the same time, the growth of dark matter perturbations during radiation domain is suppressed by the Hubble friction term $2H\dot{\delta}_{\boldsymbol{k}}$ also in this case until the equivalence, as they undergo the Meszaros effect [288]. Lastly, perturbations of relativistic matter density can never grow at any epoch, remaining in a permanent oscillation state, since the Jeans length for radiation is always greater than the horizon size.
Typically, the growing mode $\delta_{\boldsymbol{k},+}$ of a perturbation is a linear function of the scale factor:

$$\delta_{\boldsymbol{k},+} \propto a \ , \tag{1.52}$$

therefore, if $t_{\rm eq}$ is the time at which the matter-radiation equivalence occurs, one has:

$$\delta_{\boldsymbol{k},+} \propto \begin{cases} t^{1/2} & \text{at } t < t_{\rm eq} \\ t^{2/3} & \text{at } t \geq t_{\rm eq} \ , \end{cases} \tag{1.53}$$

where the behaviour of a can be derived from the integration of the first Friedmann equation. Outside the horizon, where general-relativistic effects dominate, perturbations always grow as $\delta_{\boldsymbol{k},+} \propto a^2$.

Power spectrum of density fluctuations

Density fluctuations in the universe originate from quantum fluctuations of the inflaton field, as discussed in section 1.3. Therefore, defining the field of the density contrast at a given comoving position $\boldsymbol{r}$ in the sky as

$$\delta(\boldsymbol{r}) = \frac{\rho(\boldsymbol{r}) - \bar{\rho}}{\bar{\rho}} \ , \tag{1.54}$$

its statistics will be completely described by its power spectrum, under the hypothesis of Gaussianity. The field of the density contrast in Fourier space is:

$$\hat{\delta}(\boldsymbol{k}) = \frac{1}{(2\pi)^3} \int \delta(\boldsymbol{r}) e^{-i\boldsymbol{k}\cdot\boldsymbol{r}} \, d\boldsymbol{r} \ , \tag{1.55}$$

and the average of the product of fluctuations at different wave vectors $\boldsymbol{k}$ and $\boldsymbol{k}'$ is:

$$\langle \hat{\delta}(\boldsymbol{k}) \hat{\delta}(\boldsymbol{k}') \rangle = (2\pi)^3 P(k) \ \delta_D(\boldsymbol{k} - \boldsymbol{k}') \ , \tag{1.56}$$

where δ_D is Dirac delta function, which ensures the independence of different modes. The quantity $P(k)$ is the *power spectrum* of fluctuations, having dimensions of a power density, which depends only on the modulus of the comoving wave vector, by virtue of isotropy. The integral of the power spectrum across all wave numbers gives the variance of the field of the density contrast:

$$\sigma^2 = \langle \delta^2(\boldsymbol{r}) \rangle = \frac{1}{(2\pi)^3} \int P(k) \ d\boldsymbol{k} \ . \tag{1.57}$$

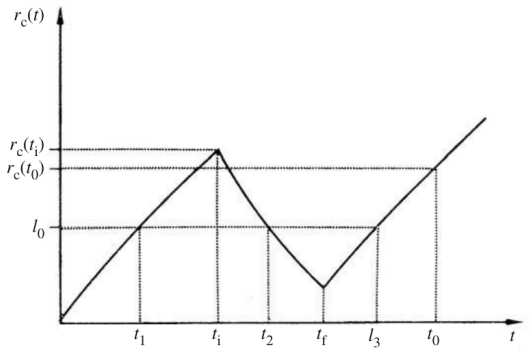

Figure 1.5. Variation of the comoving Hubble distance $(aH)^{-1}$ with time and its effect on a perturbation of comoving size l_0. At times $0 < t < t_i$ and $t_f < t < t_{\rm eq}$ the universe is radiation-dominated, therefore the comoving horizon grows with time as $\propto t^{1/2}$. Inflation occurs at times $t_i < t < t_f$, and the comoving horizon shrinks. The perturbation enters the horizon for the first time during the domain of radiation, at the time t_1, getting causal connection. It then leaves at the time t_2 (first Hubble crossing) during inflation and re-enters the horizon at the time t_3 (second Hubble crossing), when inflation has ended [taken from 109].

having used that the average of the field (1.54) is zero, by definition.
To ensure the homogeneity prescribed by the cosmological principle, the power spectrum should have the form of a power law, at least at large scales (low k), so that $P(k) \to 0$ as $k \to 0$. Furthermore, it cannot lead to a diverging variance, which implies that its spectral index must necessarily be smaller than -3, from equation (1.57).
The shape of the power spectrum of primordial perturbations is derived from the statistics of vacuum fluctuations in the inflaton field. In particular, since inflation shrinks the comoving Hubble length, perturbations are rapidly thrown out of the horizon (at the first *Hubble crossing*), then they re-enter the horizon at the second Hubble crossing, when the comoving Hubble size increased sufficiently with time. When they exit the horizon, such perturbations get causally disconnected, so they "freeze" to the state they had before, until they re-enter the horizon. Figure 1.5 shows this phenomenon for a perturbation of comoving size l_0, as the comoving Hubble distance varies with time. The calculation of the variance of quantum fluctuations of the inflaton field at the second Hubble crossing yields a power spectrum:

$$P(k) \propto k^{n_s-4} , \tag{1.58}$$

where n_s is the *primordial* spectral index at the first Hubble crossing, where the power spectrum was again in the form of a power law, $P(k) \propto k^{n_s}$. The primordial spectral index n_s is derived from the slow-roll parameters of equations (1.32) and (1.33) [187]:

$$n_s = 1 + 2\eta - 6\epsilon , \tag{1.59}$$

which is $n_s \approx 1$ if the slow-roll conditions hold. This particular kind of primordial power spectrum, $P(k) \propto k$, also called *Harrison–Zel'dovich power spectrum*, features the property of *scale invariance* at horizon crossing, i.e. the power does not vary

with the scale. Power is indeed defined as [e.g. 109]:

$$\mathfrak{P}_k = \frac{1}{2\pi^2} P(k)\ k^3\ , \tag{1.60}$$

therefore one has $\mathfrak{P}_k \approx const.$ if $P(k)$ is of the form given in equation (1.58) with n_s close to unity. The property of scale-invariance is inherited also by the fluctuations of the gravitational potential [191, 324, 472]. Indeed, they behave as

$$\delta\Phi\ \propto\ k^{(n_s-1)/2}\ , \tag{1.61}$$

which is clearly independent on the scale, $r = 2\pi/k$, for $n_s \approx 1$.
For observational purposes, it is more convenient to refer to the *mass variance*, rather than to the variance of the field of the density contrast. Therefore, the variance (1.57) gets filtered through a Gaussian window function in Fourier space, with a cut-off wave number corresponding to a characteristic radius, $R = 1/k_R$, defining a sphere of density $\bar{\rho}$ enclosing the mass $M = 4/3\pi\bar{\rho}R^3$. Denoting as $\hat{W}(k_R)$ such a smoothing function (which is the Fourier transform of the $W(R)$ window function), the mass variance is given by:

$$\sigma_M^2 = \frac{1}{2\pi^2} \int P(k)\ \hat{W}^2(k_R)\ k^2\ dk \tag{1.62}$$

by virtue of Parseval's theorem on convolution. For a Harrison–Zel'dovich primordial power spectrum, the mass variance scales as

$$\sigma_M^2\ \propto\ k^{n_s+3}\ \propto\ M^{-(n_s+3)/3} \approx M^{-4/3}\ , \tag{1.63}$$

while at the Hubble crossing, substituting $P(k)\ \propto\ k^{-3}$, one gets scale-invariance with respect to the mass.
Inflationary models constrain the shape of the primordial power spectrum via the spectral index, but they do not provide any information on its amplitude. Thus, the normalization of $P(k)$ must be determined observationally. Early galaxy surveys showed that the square root of the mass variance of galaxy counts, $\sigma_M = \delta_M/M$, was of the order of unity on the comoving length scale of $8h^{-1}$ Mpc [119]. For this reason, the amplitude of the power spectrum is usually defined through the σ_8 parameter, which is simply the square root of the mass variance (1.62) with $k_R = 1/(8h^{-1}\ \mathrm{Mpc})$.
The shape of the primordial power spectrum $P(k)$ is not the same at all the inverse comoving scales k. Indeed, it is sensitive to the epoch at which perturbations re-enter the horizon, and it gets affected by possible microphysics processes, which manifest especially at the smallest scales. A natural crossing scale is given by the size of the comoving horizon at the equivalence, which sets the wave number k_{eq}. Indeed, if a matter perturbation is big enough to re-enter the horizon after the equivalence, it will always grow with time as it did outside the horizon. A perturbation having smaller size, on the contrary, may enter the horizon during the radiation domain, undergoing either oscillations (in the case of baryonic matter perturbations) or the Meszaros stagnation (in the case of cold dark matter perturbations), and its growth is suppressed.

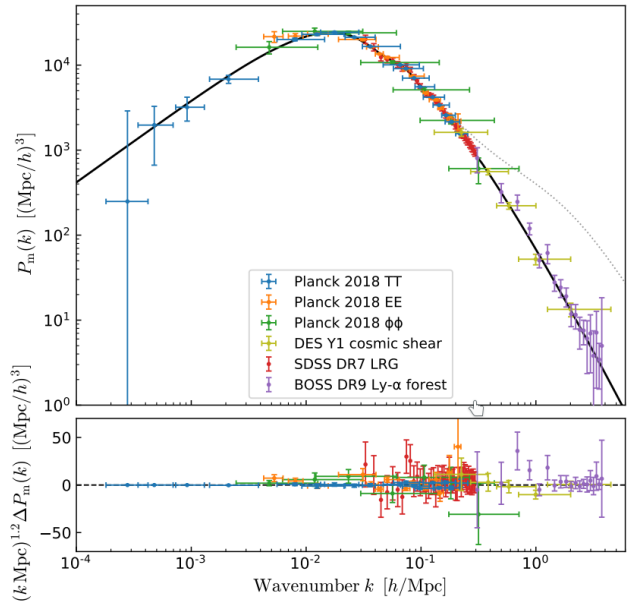

Figure 1.6. Linear power spectrum of the density fluctuations of cold dark matter inferred by a compilation of independent data sets on different scales. The black solid curve is the best-fit, which is consistent with the prediction from the ΛCDM with the parameters from *Planck* 2018 results, given in section 1.5. The dotted line represents the theoretical expectation from the add of non-linear effects, while the residuals are shown in the bottom panel. The peak is at $k_{\mathrm{eq}} = 0.01$ Mpc^{-1} [taken from 99].

Recalling that $P(k) \propto \delta^2$ with $\delta \propto a^2$ before entering the horizon, and that the scale factor at the equivalence horizon crossing goes as $a_{\mathrm{eq}} \propto k^{-2}$, one has:

$$P(k) \propto \begin{cases} k^{n_s} & \text{for } k < k_{\mathrm{eq}} \\ k^{n_s-4} & \text{for } k \geq k_{\mathrm{eq}} \end{cases}, \tag{1.64}$$

which is illustrated in Figure 1.6 for cold dark matter. It can be seen that for a primordial Harrison–Zel'dovich spectrum, the suppression during the radiation domain scales as k^{-3}.

1.4.2 Non-linear regime

As density perturbations grow with time, they get to become comparable or larger with respect to the mean density. Therefore, the linear regime breaks and the evolution of perturbations must be studied using a different theoretical approach.

Spherical collapse

The simplest analytical solution in this context is provided by the *spherical collapse model* [184]. This model describes the evolution of a single spherical perturbation in a matter-dominated universe with no spatial curvature (or Einstein–de Sitter universe). The perturbation can be treated as a universe on its own which evolves separately with respect to the background, still preserving its spherical shape by

virtue of Buchdahl's theorem [76]. Supposing non-linearity occurs at a time t_i, the density of the perturbation at this time is given by:

$$\rho_i = (1 + \delta_i)\rho_b \ , \tag{1.65}$$

being ρ_b the background density of the universe, and $\delta_i \geq 1$ is the *total* matter perturbation, such that the spatial curvature of the perturbation-universe is positive. During matter domination, the total solution to the instability equation (1.50) according to linear theory is composed by a growing mode, δ_+ and by a decaying mode, δ_-, so that:

$$\delta(t) = \delta_+ \left(\frac{t}{t_i}\right)^{2/3} + \delta_- \left(\frac{t}{t_i}\right)^{-1} \ . \tag{1.66}$$

When non-linearity occurs, the spherical perturbation stops expanding with the Hubble flow. Then, at $t = t_i$ the velocity $\dot{\delta}(t) = 0$, which yields the following relation between the growing mode and the total perturbation:

$$\delta_+ = \frac{3}{5}\delta_i \ . \tag{1.67}$$

For the collapse to occur as a consequence of the positive curvature of the perturbation, the latter must have a density parameter, Ω_p greater than one. Being $\Omega_p = (1 + \delta)\Omega_b$ at any time, it must be:

$$\delta_+ > \frac{3}{5}\frac{(1 - \Omega_{b,i})}{\Omega_{b,i}} \equiv \delta_{c,i} \ , \tag{1.68}$$

where the quantity on the right hand side of the above inequality gives the *critical value* for the collapse at the time t_i. As a general prescription, all perturbations exceeding the critical value will collapse.
The latter happens in three stages, that are: the turn-around phase, the collapse phase and the virialization phase. The physical size and density of the perturbation in all these stages are fully determined by the initial conditions.
At the turn-around time $t_{\rm ta}$, the background density still evolves according to the first Friedmann equation for flat universes dominated by matter (see equation (1.11)), so that:

$$\rho_{b,\rm ta} = \frac{1}{6\pi G t_{\rm ta}^2} \ . \tag{1.69}$$

On the other hand, the evolution of the perturbation can be solved from the first Friedmann equation from a matter-dominated and positively-curved universe. For the sake of simplicity, it is also possible to describe the "crunch" of the perturbation in a more straightforward way. Indeed, the time interval between turn-around and collapse corresponds to the free-fall time of a uniform sphere:

$$t_{\rm coll} - t_{\rm ta} = t_{\rm ff} = \sqrt{\frac{3\pi}{32 G \rho_{\rm ta}}} \ , \tag{1.70}$$

Therefore, being $t_{\rm coll} = 2t_{\rm ta}$, its density at the turn-around time is given by:

$$\rho_{\rm ta} = \frac{3\pi}{32 G t_{\rm ta}^2} = \left(\frac{3\pi}{4}\right)^2 \rho_{b,\rm ta} \ , \tag{1.71}$$

and the corresponding critical value set by the linear theory according to equation (1.68) is:

$$\delta_{c,\mathrm{ta}} \simeq \frac{3}{5}\left(\frac{3\pi}{4}\right)^{2/3} \approx 1.06 \ . \tag{1.72}$$

After the perturbation contracts, it does not end up as an actual crunch, since at times $t > 2t_{\mathrm{ta}}$ a violent relaxation takes place, and the structure rapidly *virializes*. The conservation of energy between the turn-around and the virialization implies that:

$$T_{\mathrm{ta}} + U_{\mathrm{ta}} = \mathcal{K}_{\mathrm{vir}} + U_{\mathrm{vir}} \ , \tag{1.73}$$

where the kinetic term at the turn-around, $\mathcal{K}_{\mathrm{ta}}$, vanishes since the energy is only in form of potential energy (and the perturbation is at its maximum size). Using the virialization condition, the conservation of energy becomes therefore:

$$U_{\mathrm{ta}} = \frac{U_{\mathrm{vir}}}{2} \ , \tag{1.74}$$

that is

$$R_{\mathrm{ta}} = 2R_{\mathrm{vir}} \ , \tag{1.75}$$

which is equivalent to state that between the start of the turn-around and the virialization the size of the perturbation decreases by a factor of 2. Correspondingly, its density grows by a factor of 2^3:

$$\rho_{\mathrm{vir}} = 8\rho_{\mathrm{ta}} = \rho_{\mathrm{coll}} \ , \tag{1.76}$$

and $t_{\mathrm{vir}} \gtrsim 2t_{\mathrm{ta}}$.
The density contrast, also called *spherical overdensity*, at virialization is given by:

$$\Delta_{\mathrm{vir}} \equiv \frac{\rho_{\mathrm{vir}}}{\rho_{b,\mathrm{vir}}} = \delta_{\mathrm{vir}} + 1 \ , \tag{1.77}$$

and plugging equations (1.69), (1.71) and (1.76) into equation (1.77), one finds:

$$\Delta_{\mathrm{vir}} = 18\pi^2 = 178 \approx 200 \ , \tag{1.78}$$

which is the reason why the virial overdensity is denoted also as $\Delta = 200$. The important aspect is that all collapsed objects feature the same final density, whatever their initial mass. Therefore, for an object which is collapsed at a time t, it must hold $\rho_t = const. = \Delta\rho_{b,t}$, that is:

$$\frac{M_\Delta}{R_\Delta^3} = \frac{4}{3}\pi\Delta\rho_{b,t} \ . \tag{1.79}$$

This result can be interpreted as a consequence of the initial power spectrum being scale-invariant, which translates in the *self-similarity* of cosmic structures with respect to time [225]. In this case, if the initial overdensity δ would grow only at a linear rate, the critical value for the perturbation to collapse would be:

$$\delta_{c,\mathrm{coll}} = \delta_{c,i}\left(\frac{t_{\mathrm{coll}}}{t_i}\right)^{2/3} \approx 1.06 \cdot 2^{2/3} \approx 1.68 \ . \tag{1.80}$$

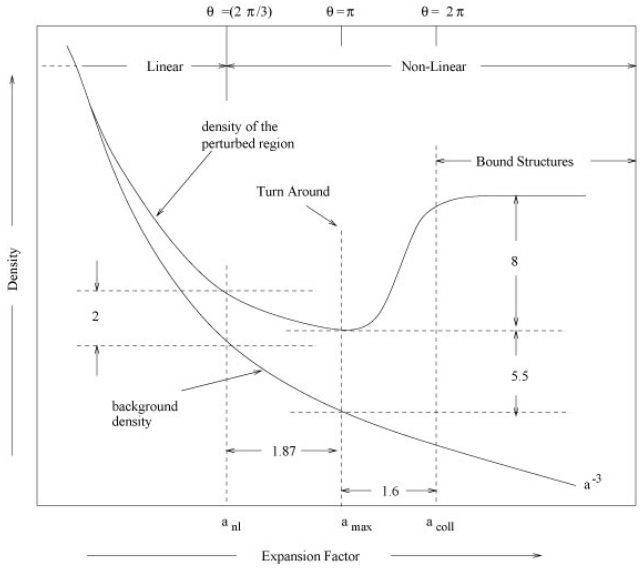

Figure 1.7. Evolution of the density of a perturbation in the simple spherical collapse model (upper curve), compared to the evolution of the background universe (lower curve) in the domain of non-relativistic matter [taken from 319].

This means that whenever perturbations are larger than the critical value of 1.68 in the linear regime, they actually correspond to collapsed spheres with a density ≈ 200 times the critical density, whatever their mass.
The critical density at a given time, which is 8 times the density at the beginning of the collapse, depends only on the underlying cosmology governing the evolution of the background density. Indeed, here one must keep in mind that the above results hold true for a flat universe with only matter and no cosmological constant. In a flat universe with non-zero cosmological constant the virial overdensity is determined numerically as [73]:

$$\Delta_{\rm vir} = 18\pi^2 + 82(\Omega_m - 1) - 39(\Omega_m - 1)^2 \ , \tag{1.81}$$

where the contribution from radiation has been neglected. More generally, the critical overdensity is found to depend weakly on the matter and dark energy cosmological density parameters [251, 149].
Figure 1.7 shows the overall evolution of the density of a spherical perturbation as a function of the scale factor, as derived from the spherical collapse model.

Halo mass function

The critical value of the overdensity at a given time t (or redshift), δ_c, allows one to predict whether a given density perturbation smaller than unity at the initial time t_i will collapse into a gravitationally bound object at t. Indeed, the growing mode of the perturbation must satisfy the simple condition $\delta_+ = \delta_i(t/t_i)^{2/3} > \delta_c$, defined in equation (1.68). The characterization of the overdensity field, namely the determination of its variance, is made possible only through observational quantities, e.g the mass of collapsed structures. Gravitationally bound structures are usually

referred to as *haloes*, which are distinct "units of mass" whose spatial extension is smaller than the typical distance between them. The mass distribution in the universe can therefore be investigated on larger scales through the spatial distribution of such haloes, and on smaller scales by considering the matter distribution within each single halo. The abundance, the spatial distribution and the inner structure of haloes all depend primarily on their mass [113]. In this context, it is useful to overview the theoretical halo mass function according to the formalism by Press & Schechter [356].

As discussed in section 1.4.1, the overdensity field is a null-averaged Gaussian field. The associated field of mass fluctuations inherits this property, since it is given by the smoothing of the overdensity field with a window function of characteristic spatial scale $R = 3M/(4\pi\bar{\rho})$. Therefore, the probability density function of mass fluctuations is given by:

$$\mathcal{P}(\delta_M)d\delta_M = \frac{1}{(2\pi\sigma_M^2)^{1/2}} \exp\left(-\frac{\delta_M^2}{2\sigma_M^2}\right) d\delta_M \tag{1.82}$$

being σ_M^2 the mass variance defined in equation (1.62). To connect the observation of massive objects with the properties of the perturbation field, the approach is based on "predicting" which density contrast will actually produce collapsed objects at late times, starting from a Gaussian perturbation field in the linear regime. To have a collapsed object, any density perturbation should be larger than the critical value δ_c at a given redshift, which is "calibrated" between the linear and the non-linear theory with the spherical collapse model. Given a critical density, the probability to have a mass perturbation corresponding to a density perturbation larger than the critical value, δ_c, is simply given by the integral of equation (1.82):

$$\mathcal{P}(\delta > \delta_c) = \mathcal{P}_{>\delta_c}(M) = \int_{\delta_c}^{\infty} \mathcal{P}(\delta_M)d\delta_M \ . \tag{1.83}$$

However, this quantity is proportional to the number of cosmic structures which can be either isolated or clustered within larger objects (problem of the cloud-in-cloud counting). To take into account only the largest possible structures, one must compute the differential probability distribution function:

$$\frac{dN}{dM} = [\mathcal{P}_{(>\delta_c)}(M) - \mathcal{P}_{(>\delta_c)}(M + dM)] \tag{1.84}$$

where the term $\mathcal{P}_{(>\delta_c)}(M + dM)$ is subtracted to avoid to count twice the collapsed objects which are contained into larger ones. Since it does account only for the *over*-dense half of the Gaussian probability distribution function, a factor of 2 is also missing, which is simply "put by hand" to get the correct result.

The number of collapsed objects per unit mass and comoving volume defines the *halo mass function*:

$$n_M(M) = \frac{dN}{dMdV} \ , \tag{1.85}$$

which from (1.84) reads:

$$n_M(M) = 2\ \frac{\rho_m}{M}\frac{d\mathcal{P}_{(>\delta_c)}(M)}{dM} = 2\ \frac{\rho_m}{M}\frac{d\mathcal{P}_{(>\delta_c)}(M)}{d\sigma_M}\left|\frac{d\sigma_M}{dM}\right| , \tag{1.86}$$

where the mass M at the denominator is needed to correctly take into account the total number of objects *of mass* M, and $\rho_m = dM/dV = \Omega_m \rho_{\rm cr}$.
The quantity:

$$-2\sigma_M \frac{d\mathcal{P}_{(>\delta_c)}(M)}{d\sigma_M} \equiv f(\sigma_M) \tag{1.87}$$

is called *multiplicity function*, and it takes a different form for different models describing the halo mass function, which is therefore compactly written as

$$n_M(M) = -\frac{1}{2} f(\sigma_M) \frac{\Omega_m \rho_{\rm cr}}{M^2} \left| \frac{d\log\sigma_M^2}{d\log M} \right| . \tag{1.88}$$

The multiplicity function in the Press–Schechter case is:

$$f(\sigma_M) = -\sqrt{\frac{2}{\pi}} \frac{\delta_c}{\sigma_M} \exp\left(-\frac{\delta_c^2}{2\sigma_M^2}\right) , \tag{1.89}$$

yielding the Press–Schechter mass function [356]:

$$n_M(M) = \sqrt{\frac{2}{\pi}} \frac{\delta_c}{\sigma_M} \exp\left(-\frac{\delta_c^2}{2\sigma_M^2}\right) \frac{\Omega_m \rho_{\rm cr}}{M^2} \left| \frac{d\log\sigma_M^2}{d\log M} \right| . \tag{1.90}$$

According to this model, the number of massive objects decreases quadratically with mass in the low-mass end. On the other hand, the suppression given by the exponential term implies that at larger critical overdensities (with the critical value growing when "looking back" at the linear regime), less collapsed objects are expected. Since gravity has no preferred scales, the non-linear scale is set as the one corresponding to the mass collapsing at a given redshift, for which the *peak height* at that redshift, $\mu = \delta_c/\sigma_M$, equals unity.
The Press–Schechter mass function of equation (1.90) can be derived in a rigorous way, i.e. with no need to add the ad hoc factor of 2, through the method of excursion sets [56]. The basic idea consists in taking the primordial Gaussian field of density perturbations and trying to predict the number of virialized objects that one will likely count at later times. To do this, one can suppose to take the field and start evaluating the matter density by filtering the field over spheres of decreasing radius R. Starting from large radii ensures the largest possible collapsed objects are considered, and the cloud-in-cloud problem is naturally solved. If linear density fluctuations are larger than the critical value for the collapse (see equation (1.80)) when smoothed over a scale R, the latter defines a patch that will likely collapse to form a virialized halo at later times, which will enclose a density about 200 times the critical density, as prescribed by the spherical collapse model. It can be shown analitically that each linear Fourier mode in the field of density perturbations, $\delta(\boldsymbol{k})$, follows Brownian-like trajectories across redshift, called excursion sets. Any value of the critical overdensity at a given redshift acts as a fixed "barrier" for these trajectories. Therefore, starting from large filtering scales (large masses), each time a trajectory crosses the critical barrier, one has the collapse of an object at the corresponding filtering mass. Subsequent crossings correspond to smaller collapsed objects, which formed earlier.

More generally, the halo mass function is a crucial quantity for cosmological studies with clusters of galaxies. Indeed, varying cosmology implies varying the

critical overdensity, as well as the whole process of structure formation, resulting in different scaling of the halo mass function [see e.g. 7, for a review]. This quantity is also needed to evaluate the angular power spectrum of the Sunyaev–Zel'dovich effect, which is another fundamental tool to probe the matter density parameter and σ_8 [244]. For this reason, an accurate modelling of the halo mass function is fundamental to get reliable cosmological constraints. The spherical collapse model upon which all the above results are based, represents a useful but oversimplified framework for the study of non-linear growth of perturbations and the formation of collapsed objects. A more realistic treatment of non-linear growth of density perturbations is represented by the semi-analytical approach of *Zel'dovich approximation* [471]. This simple approach gives acceptable results only in weakly non-linear regimes, and it can be used to describe the evolution of structures only up to the first collapse. The most complete picture of the formation of cosmic structures can be achieved through cosmological N-body simulations, which ultimately allow one to validate the predictions from both fully analytical and semi-analytical models. For instance, in the context of estimating the halo mass function, numerical simulations helped in testing more refined models, with respect to the Press–Schechter result based on the spherical collapse [409, 222, 408, 435, 436, 50].
In section 2.1.1 a short overview of cosmological simulations is provided; in particular, in section 4.2 the simulations used in the present Thesis work are introduced.

Self-similarity

The evolution of the observational properties of cosmic structures can be predicted theoretically – and eventually compared with the result from numerical simulations – by virtue of their self-similarity with respect to time [225]. Self-similarity implies that two collapsed haloes at two different redshifts are just scaled versions of each other. The only underlying assumption is the scale-free shape of the initial power spectrum of matter perturbations, as predicted by inflation and confirmed experimentally (see Fig. 1.6). Indeed, as already pointed out earlier in this section, under this condition, the only physically-relevant scale for the collapse is set by the non-linear mass. The latter is defined as the mass at which the matter fluctuations $\delta M/M$, and thus the mass variance σ_M^2, are equal to 1. The mass variance scales with the expansion factor as a power law. Indeed, from equation (1.62), and recalling that the power spectrum scales as $P(k) \propto \delta^2 \propto a^2$ for growing modes, one has:

$$\sigma_M^2 = a\ M^{-(n_s+3)/3} \tag{1.91}$$

and being $a \propto t^{1/2}$ and $a \propto t^{2/3}$ during radiation and matter domination, respectively, it follows that the non-linear mass, $M_{\rm NL}$, scales as a power law of time as well. This is exactly the formulation of the hierarchical scenario: smaller masses collapse at earlier times; more massive objects form at later times from the aggregation of the smaller ones.
Any dimensionless statistics depending on the ratio $M/M_{\rm NL}$ of a collapsed object will inherit the self-similarity with respect to time. Such statistical properties are generally expressed as functions of the overdensity Δ (defined in section 1.4.2). In particular, consistently with the spherical collapse prediction, if two objects collapse at the same time t, then self-similarity implies their densities are the same, equal to

$\Delta\rho_{b,t}$, being $\rho_{b,t}$ the background density at the time t. The latter usually coincides with the *critical* density, but it may be replaced by the *mean matter* density in some cases. This allows one to define the mass within a sphere enclosing a density equal to Δ times the background density as

$$M_\Delta = \frac{4}{3}\pi R_\Delta^3 \Delta\ \rho_b\ . \tag{1.92}$$

In the following, we will always assume $\rho_b = \rho_{\rm cr}$, unless differently specified. Equation (1.92) implies that any observational quantity related to the radius R_Δ can be directly related to the mass at the same overdensity (at a given time or redshift). Such relations between observables and masses are in form of power laws called *scaling relations* [see e.g. 176, for a review], which are derived under the assumption of (*i*) spherical symmetry of the system; (*ii*) hydrostatic equilibrium, and (*iii*) no dependence of the power law slopes on the mass of the object.

1.5 Cosmological parameters

The current cosmological scenario can be described though two sets of parameters. The first set describes the dynamics and the geometry of the universe by means of the expansion rate, the density parameters of all the mass-energy components, the equation of state of dark energy and spatial curvature. The second set is constituted by the spectral index and normalization of the power spectrum of primordial density fluctuations which originated all the gravitationally bound structures we see today.

1.5.1 Dynamics and geometry of the universe

This section is dedicated to the parameters describing the mass-energy content of the universe, from which its global dynamics and geometry are determined. Specifically, they are: the Hubble constant; the cosmological density parameters of relativistic matter, non-relativistic matter, spatial curvature and dark energy, and finally the equation of state parameter of dark energy.

Hubble constant

As discussed in section 1.1.1, the Hubble constant is the expansion rate of the universe evaluated at the present time. To date, the most precise estimates of the Hubble constant are provided by the angular power spectrum of CMB primary anisotropies, and by direct distance measurements of the absolute magnitude of type Ia supernovae (which are standard candles upon a proper calibration of their light curve). There are several other probes of this parameter, based both on high-redshift and local observables. For instance, recent estimates of H_0 include the use of: galaxy clustering combined with weak lensing [128]; measurements of the angular diameter distance from joint X-ray and Sunyaev–Zel'dovich measurements from galaxy clusters [e.g. 53, 247]; gravitational waves from standard sirens [129]; lensed quasars [467]. All these methods, however, rely on a number of assumptions which limit their competitiveness in terms of precision, compared to the estimates based

on type Ia supernovae and on the CMB.
The most recent work using supernovae quotes [376]:

$$H_0 = (74.03 \pm 1.42)\,\mathrm{km\,s^{-1}\,Mpc^{-1}} \ ;$$

on the other hand, the indirect, model-dependent best-fit estimate based on the latest *Planck* CMB data reports [348]:

$$H_0 = (67.36 \pm 0.54)\,\mathrm{km\,s^{-1}\,Mpc^{-1}} \ .$$

The 4.4σ tension between the above measurements represents one of the major open issues in modern cosmology, which lead to a plethora of proposed possible solutions. Nevertheless, at the time of writing none of them has convincingly solved the above tension.

Relativistic matter

Relativistic matter (or radiation) is constituted by all those particles satisfying the condition:

$$mc^2 \ll k_B T \ , \tag{1.93}$$

being m the particle mass and T the temperature of the cosmic fluid. At the present time, the only particles which can satisfy this property are photons, being always non-relativistic at any temperature, and neutrinos.
The photon content of the universe is mainly in the form of the CMB radiation (see section 1.2), which is characterized by the spectral energy density of a black body at the present-day temperature $T_{\mathrm{CMB}} \approx 3$ K. The corresponding energy density can be obtained from Bose-Einstein statistics [62], whose only relevant physical parameter is given by the thermodynamic temperature. The density of photons relative to the critical density at the present time is thus estimated to be:

$$\Omega_{r0} h^2 = 2.47 \times 10^{-5} \ ,$$

meaning that they do not affect significantly the dynamics of the universe.
Another candidate species of relativistic particle is represented by neutrinos. They are electrically neutral fermions accompanying their corresponding electrically-charged leptons (electrons, muons and tau) in electro-weak decay processes, by virtue of the conservation of energy and momentum. These particles have very small masses, whose values have not been measured directly yet [see e.g. 19, for a recent review]. From the combination of acoustic oscillation data in the late and in the early universe, plus gravitational lensing measurements, the sum of the three mass eigenvalues of neutrinos is found to be [349]:

$$\sum_{\nu} m_\nu < 0.12\,\mathrm{eV} \ ,$$

at 95% confidence level. The neutrinos that would contribute to the radiation component today, are supposed to constitute a relic background, similarly to the CMB, called cosmic neutrino background [399, 1]. From basic considerations descending on the different quantum statistics obeyed by bosons and fermions, it is possible to

derive a theoretical estimate of the temperature of the relic neutrino background, that is:

$$T_{\nu,0} = \left(\frac{4}{11}\right)^{1/3} T_{\rm CMB} = 1.945\,{\rm K}\ , \tag{1.94}$$

corresponding to an energy of 0.168 meV, which is still very challenging to observe.

Non-relativistic matter

Non-relativistic matter is constituted by all particles for which it holds:

$$mc^2 \gg k_B T\ , \tag{1.95}$$

which at the present time include baryons after the decoupling from radiation, and non-baryonic cold dark matter [see e.g. 470, for a review].
The baryonic component is in form of either galaxies or diffuse gaseous medium, whose emission can be detected in different bands. Its density may therefore be constrained from the radiative properties of each observable. The most sensitive cosmological probes of the baryon density are baryon acoustic oscillations in the power spectrum of primary CMB anisotropies and the abundance of elements produced in the Big Bang nucleosynthesis. Also, the ratio between this parameter and the density parameter of the total of baryonic plus non-baryonic matter can be constrained from the gas fraction in galaxy clusters [272]. The most recent value from the analyses of *Planck* data gives [348]:

$$\Omega_{b0}h^2 = 0.02237 \pm 0.00015$$

for baryons, and

$$\Omega_{\rm cdm0}h^2 = 0.1200 \pm 0.0012\ ,$$

for cold dark matter, so that the inferred total density parameter for non-relativistic matter is:

$$\Omega_{m0} = 0.3153 \pm 0.0073\ .$$

Despite it is the dominant contributor to the budget of non-relativistic matter, to date there is no indication on the nature of dark matter, which is a major issue of the ΛCDM model. Candidate dark matter particles must be stable on cosmological time-scales; they must interact very weakly with electromagnetic radiation, and they must have a relic density consistent with observations. In this respect, proposals for candidates include primordial black holes, axions, sterile neutrinos and weakly interacting massive particles [see e.g. 320, and references therein].

Spatial curvature

As discussed in section 1.2, the angular power spectrum of primary CMB anisotropies is a probe of the geometry of the universe, which can be inferred from the localization of the first peak of baryon acoustic oscillations. Indeed, the latter is sensitive to the sum of the cosmological density parameters. Measurements of the CMB at sufficiently high angular resolutions allow a precise localization of the peak, which is found to be consistent with a total density parameter close to unity [e.g. 122]. The

most recent value of the curvature parameter from the combination of *Planck* data with baryon acoustic oscillations is [348]:

$$\Omega_{\kappa 0} = 0.0007 \pm 0.0019 \ ,$$

which is well consistent with a flat universe, in agreement with inflationary predictions.

Dark energy

The Hubble diagram relating the luminosity distance to the redshift of type Ia supernovae showed for the first time two decades ago that the expansion of the universe is currently accelerating [375, 326]. As discussed in section 1.3, an accelerated expansion requires the cosmic fluid to be dominated by some physical component with negative pressure, dubbed dark energy because of its yet unknown nature. The simplest scenario assumes dark energy to be in the form of the Λ cosmological constant, whose density parameter can be inferred with high precision from CMB data, relying on the direct estimate of the matter density parameter. Assuming the universe is spatially flat – as prescribed by inflation and according to the measured value of the curvature parameter – the most recent constraint on the density of the cosmological constant from *Planck* results is [348]:

$$\Omega_\Lambda = 0.6847 \pm 0.0073 \ .$$

For a non-evolving dark energy component, the equation of state parameter is found to be:

$$w = -1.028 \pm 0.032 \ ,$$

yielded by the combination of CMB data with lensing, supernovae and baryon acoustic oscillation data. Such a consistency with the value of -1 is also supported by the combination of independent constraints from galaxy clusters and supernovae [e.g. 401]. Although the hypothesis of a cosmological constant is supported by many observational data, such an explanation for the acceleration of the expansion is unsatisfactory, as it raises the so-called *fine-tuning problem* and the *coincidence problem* [see e.g. 462, 94]. This fact motivated many works aiming at tackling the origin and the nature of dark energy in a physically-consistent way. For instance, a number of theories known as *quintessence models* [e.g. 13] interpret dark energy as a scalar field evolving with time (similarly to the inflaton). Another possibility is to consider modifications of general relativity at cosmological scales in extended theories of gravity [see e.g. 86, for a recent review]. However, none of the theories proposed so far has been capable of solving the dark energy problem.

1.5.2 Primordial power spectrum of density fluctuations

The primordial power spectrum of the inhomogeneities originated from inflation is in the form of a power law, as discussed in section 1.4.2. The only two parameters needed to describe this quantity are therefore its spectral index and its normalization.

Spectral index The primordial power spectrum is expected to be linear with respect to the inverse comoving scale, corresponding to a scale-invariant power. Its shape can be primarily probed by primary anisotropies of the CMB, as well as by the clustering of large-scale structures [e.g. 72, 261]. The latest value from a combination of *Planck*, baryon acoustic oscillations and lensing data provides [348]:

$$n_s = 0.9665 \pm 0.0038 \ ,$$

which is well consistent with the deviation from unity predicted from inflation.

Normalization The amplitude of the power spectrum of fluctuations can only be constrained from direct observations. The most sensitive probes of this parameter are the CMB primordial power spectrum, the clustering of large-scale structures, particularly the halo mass function [329, 464] and related quantities such as the angular power spectrum of the thermal Sunyaev–Zel'dovich effect [244]. The most recent value obtained from the primary anisotropies of the CMB measured by *Planck* is:

$$\sigma_8 = 0.8111 \pm 0.0060 \ ,$$

which lies in the range expected from other probes, which is $0.7 < \sigma_8 < 1.0$ [e.g. 454]. An important quantity derived from a suitable combination of σ_8 and the Ω_{m0} parameter is the normalization of the angular power spectrum of the thermal Sunyaev–Zel'dovich effect. It is worth mentioning that the estimate of such a normalization represents another major issue in the context of ΛCDM cosmology. Indeed, while being estimated from the very same *Planck* data, the joint constraints on σ_8 and Ω_{m0} from the angular power spectra of the CMB (which allows a direct estimate) and of the thermal Sunyaev–Zel'dovich effect from cluster counts, show a significant tension. This problem has been investigated in recent works proposing different solutions, such as: relying on higher-order statistics; assuming a variation with redshift and mass of the bias in the estimate of the masses of galaxy clusters; considering different parametrizations of cluster pressure profiles [389, 390, 386, 52]. Nevertheless, none of the above proposed studies has solved the tension yet.

Chapter 2

Clusters of galaxies and Sunyaev–Zel'dovich effect

This Chapter presents an overview of clusters of galaxies and of the Sunyaev–Zel'dovich effect. The first section starts with an introduction on cosmological simulations, which are the ultimate tool to theoretically describe the formation of structures in the universe. Subsequently, a general overview of cluster observables is provided. Among them, the Sunyaev–Zel'dovich effect, which allows the detection of clusters in the microwave band, is treated separately in the second section. Specifically, after a theoretical review of the effect, a short discussion on the existing dedicated observational techniques is presented.

2.1 Clusters of galaxies

According to the standard model of cosmology, all the gravitationally bound structures form in a hierarchical way, from the smallest to the largest ones, via aggregation and merging. Clusters of galaxies represent the latest stage of structure formation, therefore they are the most recent, largest and gravitationally bound objects [454]. They form at the peaks of the field of density fluctuations [24], and they can aggregate into larger structures, from superclusters to the *cosmic web*, which are not virialized yet.

Since a galaxy cluster has not a well-defined boundary which separates it from the surrounding space, its size is usually quantified by the *virial radius*, $R_{\rm vir}$. The latter can be defined in terms of the overdensity at which, according to the simple spherical collapse model, the structure reaches the equilibrium configuration after a violent relaxation. In a flat, matter-dominated universe with no cosmological constant, such an overdensity is $\Delta \approx 200$ (see also section 1.4.2). Virial radii of galaxy clusters are of the order of a few Mpc. The mass enclosed within a virial radius, called *virial mass* ($M_{\rm vir}$), ranges between a few $10^{13}\mathrm{M}_\odot$ in the case of *galaxy groups*, and a few $10^{15}\mathrm{M}_\odot$ for the most massive clusters.

The most abundant constituent of the mass of a galaxy cluster is non-baryonic cold dark matter, which indeed represents roughly 80 per cent of the total. As for baryons, they are mostly in the form of a diffuse, ionized gas called intra-cluster medium (ICM hereafter). The latter constitutes about 17 per cent of the total cluster mass,

while the remaining 3 per cent consists of galaxies.

2.1.1 Cosmological simulations

Numerical simulations of structure formation in the universe provide a more realistic theoretical description of the origin of galaxy clusters, and they may help in understanding cluster properties. The initial conditions of a cosmological simulation are set according to the favoured cosmological model. In particular, the statistics of the initial density field is determined by the primordial power spectrum. The evolution of the field is treated using semi-analytical methods such as the Zel'dovich approximation in mildly non-linear regimes [e.g. 358]. They eventually set the initial conditions for the N-body simulation, which is run in a box of a suitable size to represent a portion of the universe.
The cosmological box gets filled with fluid elements (or *particles*) of two species: (*i*) dark matter, obeying the collisionless Boltzmann equation; (*ii*) gas (or baryons), for which a more complex set of hydrodynamical equations is needed, possibly accounting also for dissipation due to radiative processes. All the dark matter and gas particles interact by means of gravity, and their evolution in time is traced through the numerical integration of their equations of motion. Then, for the i-th particle one has to solve:

$$\frac{d^2\boldsymbol{r}_i}{dt^2} + 2\,\frac{\dot{a}}{a}\frac{d\boldsymbol{r}_i}{dt} = -\frac{1}{a^2}\boldsymbol{\nabla}_{\boldsymbol{r}_i}\Phi(\boldsymbol{r}_i) \tag{2.1}$$

$$\nabla^2_{\boldsymbol{r}_i}\Phi(\boldsymbol{r}_i) = \frac{3H_0^2\Omega_{\mathrm{tot}0}}{2a}\;\delta(t,\boldsymbol{r}_i)\;, \tag{2.2}$$

in comoving coordinates (see also section 1.4). At each *snapshot* in time, the three-dimensional positions and velocities of all the particles are known. Therefore, it is clear that suitable computational resources are needed to run such simulations. An example showing the evolution of the initial density field in a N-body simulation is illustrated in Figure 2.1. It can be seen how the two different cosmological models adopted in this example have a significant impact on the distribution of dark matter at earlier epochs, while the clustering and the large-scale structure have been matched at redshift $z = 0$.

Historically, the first simulation runs were performed in the 1970s and 1980s following the evolution of only dark matter particles [323, 465]. Between the late 1980s and the early 1990s baryon particles entered the picture, in the so-called *adiabatic* or *non-radiative* (NR hereafter) runs [e.g. 155, 434, 230, 74, 305], which broadly confirmed the gravity-driven predictions of the self-similar model.
Subsequent observations with X-ray telescopes at high angular resolution revealed significant differences in the core regions of cluster profiles, compared to the expectations from the self-similar model. This fact suggested that non-gravitational processes do have an impact in shaping the observed properties of galaxy clusters. Therefore, more realistic simulations featuring radiative feedback have been proposed. In particular, a pre-heating phase at high redshifts ($z > 3$), possibly due to the combined action of supernovae and active galactic nuclei (AGN hereafter), has been postulated [156, 226, 438]. Heating from arbitrary pre-heating mechanisms [e.g. 38, 60, 300], showed that an agreement with observations from the breaking of

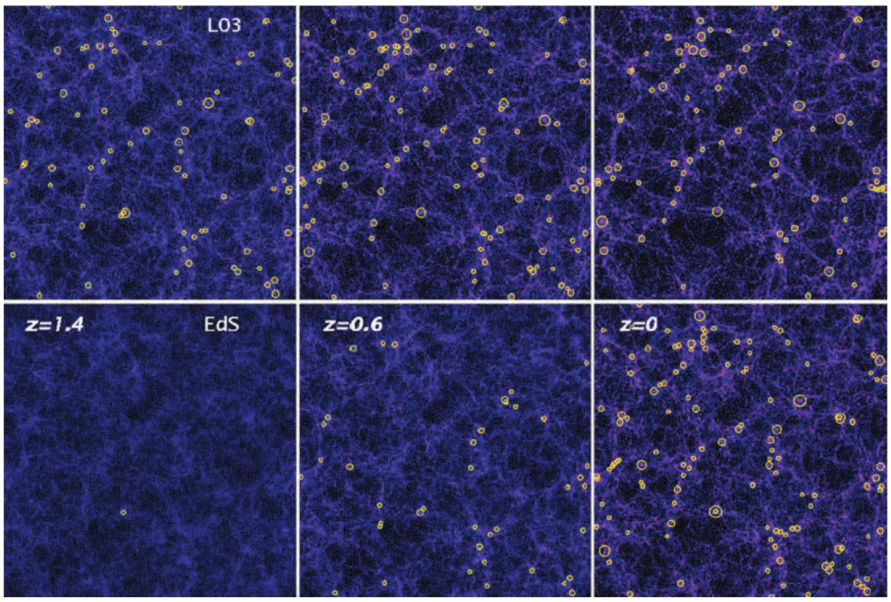

Figure 2.1. Evolution of dark matter distribution on large scales according to a cosmological N-body simulation run with two different cosmologies [58]. The top and bottom rows refer to the ΛCDM and to the Einstein–de Sitter cosmological models, respectively, assuming a null spatial curvature. Left, middle and right columns correspond to three different snapshots at the redshift indicated on top of each figure. The yellow circles mark the positions of galaxy clusters that would emit in X-rays at temperatures $T > 3\,\mathrm{keV}$. The size of each circle is proportional to temperature [taken from 59].

self-similarity requires an injection of energy between 0.5 and 1 keV per gas particle. Since such an amount of energy cannot be provided by supernovae, AGN have been proposed as the most likely responsible for pre-heating [e.g. 69].
Further comparison with data suggested that these processes must be complemented by radiative mechanisms during the formation of the cluster itself, since they introduce additional physically-relevant scales responsible for breaking self-similarity [455]. Specifically, the feedback from supernovae in cluster galaxies [289, 61, 118] and radiative cooling plus star formation (CSF hereafter) have been prescribed [321, 117, 444, 231, 303, 403].
While providing a promising enhancement with respect to numerical schemes based only on gravity, cooling and star formation mechanisms are not sufficient to solve the discrepancies between the properties of simulated versus observed clusters. For instance, the stellar mass of the brightest central galaxies (BCGs) in clusters from CSF simulations turn out to be a factor of two to three larger than the observed stellar masses. This motivated the need of a further feedback mechanism associated to AGN, which turned out to be able to prevent the excess of cooling. AGN feedback is appreciable on scales that are too small to be followed by the simulation. Therefore, it is necessary to include this effect via phenomenological prescriptions, based either on Bondi gas accretion [57, 416] or winds capable to heat the surrounding gas through shocks [171].
Despite the success of the most recent, state-of-the-art AGN prescriptions [see e.g.

365], there is not a definitive, concordance recipe of small-scale baryonic processes. Specifically, the modelling of AGN is an effective theory, whose outcomes strongly depend on the specific sub-grid scheme which is implemented.
From a computational point of view, the use of modern data-driven techniques based on machine learning are getting more and more diffused in the context of cosmological simulations, yielding very promising results [see e.g. 228, and subsequent works]. On the other hand, a great effort is put in the optimization of codes, to exploit at best the available computational resources in view of the upcoming exascale era of high-performance computing [e.g. 181].

The two main descriptors which characterize a cosmological simulation are its resolution in mass and space, and the numerical scheme used to compute the gravitational and hydrodynamical forces between particles [59].
Focussing on the latter aspect, the gravitational interaction between all the fluid elements in the simulation box can be ideally computed from the direct summation of the force between couples of particles. Such an approach defines the *particle methods*, which are clearly not suitable to treat large simulation volumes. Another strategy which can considerably reduce the computational time, is represented by the class of *Particle-Mesh* (PM) and *Particle-Particle/Particle-Mesh* (P^3M) methods [114], which are Eulerian schemes based on the partition of the simulation box by means of a grid. Clearly, the latter limits the resolution of the simulation to the mesh size; to possibly overcome this issue, variants of mesh-based methods with non-uniform grid sizes have been proposed [2]. The general idea behind PM techniques consists in discretising Poisson's equation over the grid, and then to solve it by means of the calculation of a *Fast Fourier Transform* (FFT) [110] or via a multi-grid relaxation solver. The corresponding gravitational force is computed by differentiating the potential produced by the Poisson solver and it allows one to update the dynamical variables of all the particles in each grid shell. The P^3M variant is based on splitting the interaction into a long-range plus a short-range term, so that the first one can be treated with the classical PM scheme, while the second one is solved using the more accurate particle-particle direct summation.
Another solution is provided by the Lagrangian (or particle-based) *Tree* method [27]. With this technique, one computes the gravitational interaction between neighbouring particles by means of a multipole expansion, which is performed after dividing the particles into different groups. At higher particle density one has increasing resolution, and each level corresponds to a branch of the tree. On the other hand, the hybrid *Tree-PM* method [18] employs the fast PM algorithm on the largest scales, jointly with the Tree algorithm on the smallest scales.
As for the treatment of hydrodynamical forces, the most used scheme is the Lagrangian *Smoothed Particle Hydrodynamics* (SPH hereafter) [175]. Differently from grid-based techniques, this method does not introduce any characteristic spatial scale in the problem, thus it does not impose any maximum spatial resolution. Furthermore, it does not constrain the global geometry of the system, thus the mass resolution can vary, according to the evolution of the local density. The fluid is divided in mass particles, for which every interaction is smoothed by a kernel function if the distance between the particles is smaller than the *smoothing length*, which sets the range of the kernel. All the relevant physical quantities of each fluid element (e.g. its temperature, density and so on) are determined by summing over

the nearby particles located within the smoothing length. Although they are very sensitive to local conditions, SPH codes allow one to reach a very high resolution, which is necessary in the implementation of models of radiative processes acting on the smallest scales.

2.1.2 Short overview of cluster formation

N-body simulations of the evolution of collisionless dark matter particles highlighted important differences with respect to the predictions of the spherical collapse. In the following, we briefly report the three most important aspects [248].

i. Real peaks in the field of primordial density fluctuations do not have a sharp top hat-like edge, nor a constant density (that is a constant *barrier* setting the occurrence of the collapse). On the contrary, each peak is characterized by a radial profile [24]. As a consequence, the collapse of a peak does not happen all at once, but it occurs at different times in different regions of the peak itself [136]. Therefore, it is non-trivial to define the mass and the radius of a cluster, since there is no sharp boundary. A possibility consists in determining the mass via the *friends-of-friends* (FoF) algorithm [146], according to which all the particles located at mutual distances smaller than a given value belong to the same halo. Despite the FoF-derived mass can take into account the triaxial distribution of matter, it is not straightforward to relate it to observations. The latter problem can be easily overcome by adopting a definition of the mass which refers instead to some overdensity value, under the simplifying assumption of spherical symmetry.

ii. The peaks filtered on a given scale are not isolated, but they are surrounded by other peaks. Tidal forces between these inhomogeneities originate subsequent growth occurring along massive filaments connecting them, and which constitute the cosmic web [55].

iii. The density distribution within the peaks contains fluctuations on all scales, despite the main scale of a peak is defined by the radius of the window function $W(R)$ (see e.g. equation (1.62)). This implies the presence of smaller collapsed substructures within haloes, as a consequence of the collapse to happen simultaneously on different scales at the earlier epochs. Thus, haloes at higher redshifts feature a number of substructures which eventually merge towards the centre, to form a more massive and relaxed system at later epochs.

Once the dark matter halo has formed, matter sets into an equilibrium configuration. Collisional gas particles get heated by adiabatic compression and shocks produced by the gravitational collapse, and they set into the potential well of the dark matter halo. Thus, the kinetic energy they acquired in the collapse gets converted into thermal energy. The gas temperature reaches values of the order of millions of K, at which X-ray emission occurs. The gas cools by means of radiative mechanisms (mainly ionization of hydrogen and helium and bremsstrahlung), as soon as the cooling time becomes smaller than the Hubble time. The gas then loses the support of hydrostatic pressure and starts collapsing towards the centre of the halo on dynamical time-scales

of the order of the free-fall time, and the subsequent violent relaxation involving the collisionless component settles the structure in a virialized configuration.
On galactic scales, the gas can leave the hot phase to form the stellar component, as soon as its density has increased sufficiently. Stars may eventually originate supernovae or black holes [32]. The latter, as well as the central supermassive black hole in the BCG of the cluster (i.e. the cluster AGN), inject substantial heat into the ICM via radiative feedback, and they chemically enrich the cluster [398].

Density profiles

The inner structure of collapsed haloes is determined by the density profile tracing the distribution of the dark and the baryonic matter, which are usually derived approximating cluster shapes as spherical.
Cosmological simulations indicate that the radial profile of the dark matter density of collapsed structures after relaxation is well approximated by the *universal* Navarro–Frenk–White (NFW hereafter). Its analytical form is [306]

$$\rho_{\rm NFW}(r) = \frac{\rho_{\rm cr} A_{c_\Delta}}{(r/r_s)(1+r/r_s)^2} \ , \tag{2.3}$$

where $\rho_{\rm cr}$ is the critical density at a given redshift, and r_s is a characteristic scale radius which localizes the steepening of the profiles (where the logarithmic slope is equal to -2). Both the normalization value $\rho_{\rm cr} A_{c_\Delta}$ and the above radius are particularly sensitive to the cosmological parameters and to the initial conditions set in the simulation [307]. Indeed, the factor $A_{c_\Delta} = 4\rho_{\rm NFW}(r_s)/\rho_{\rm cr}$ referred to a given overdensity Δ, is defined as

$$A_{c_\Delta} \equiv \frac{\Delta \ c_\Delta^3}{3\left[\ln(1+c_\Delta) - c_\Delta/(1+c_\Delta)\right]} \ , \tag{2.4}$$

so that the mass within the radius R_Δ can be expressed as

$$M_{\rm NFW}(< R_\Delta) = \frac{4}{3}\pi R_\Delta^3 \ \Delta \ \rho_{\rm cr} \ . \tag{2.5}$$

The quantity c_Δ is the *concentration* of the mass distribution, and it is defined as

$$c_\Delta \equiv \frac{R_\Delta}{r_s} \ , \tag{2.6}$$

that is the ratio between the reference radius R_Δ and the scaling radius of the NFW profile, r_s.
Subsequent numerical works suggested that, more generally, dark matter density profiles can be written in the form: $\rho_{\rm cdm}(r) \ \propto (r/r_s)^{-A}(1+r/r_s)^{A-B}$ [454]. The NFW case, which still remains the most used, corresponds to the asymptotic inner slope $A = 1$ and to $B = 3$. Other parametrizations have $A = 1.5$ and $B = 3$ [295], or $A = 1$ and $B = 2.5$ [362], as determined from the fit to the profiles obtained from different sets of numerical simulations.

The density profile of the baryonic component is expected to trace the density distribution of dark matter. Nevertheless, as testified by simulations and measurements of the X-ray surface brightness (see section 2.1.3), the radial profiles of the

gas density flatten at scales below the Jeans length. Such a smoothing comes from the support from thermal pressure, since the gas is collisional [59].
Historically, one of the most popular parametrizations for the gas density profile inferred from observations is the so-called *isothermal β-model* proposed by Cavaliere and Fusco-Femiano [98]. Such a model is based on two assumptions. The first one is that the matter is in thermodynamic equilibrium, with a constant temperature T, independent on the cluster radius. The second assumption is that the gas density is equal to the density of the galaxy members to some power β. Under the hypothesis that the velocities of the galaxies also follow an isothermal distribution, the density profile of the galaxies derived from optical measurements of the one-dimensional velocity dispersion, σ_v^2, is well represented by a *King profile* [236]:

$$\rho_{\rm gal}(r) = \frac{\rho_{\rm gal0}}{[1+(r/r_c)^2]^{3/2}} \ . \tag{2.7}$$

The parameter r_c defines the *core radius*, with values of the order of hundreds of kpc, while $\rho_{\rm gal0}$ is a normalization density. The dependence on the core radius prevents the density to diverge at the cluster centre, as it would happen considering a singular isothermal sphere.
Then, the β-model for the gas density reads:

$$\rho_{\rm ICM}(r) = \frac{\rho_{\rm ICM0}}{[1+(r/r_c)^2]^{3\beta/2}} \ , \tag{2.8}$$

being β the ratio between the kinetic energy of the galaxies and that of the gas at temperature T:

$$\beta = \frac{\mu m_H \sigma_v^2}{k_B T} \ , \tag{2.9}$$

where μ is the mean molecular weight of the gas particles in units of the hydrogen mass, m_H (which is approximatively equal to the proton mass).
Numerical simulations show that the distribution of galaxies – which are approximatively non-collisional within clusters – can be modelled with the NFW distribution as well [e.g. 89]. Furthermore, the β-model cannot jointly fit the density profiles probed by multi-wavelength observations of clusters aiming at a complete analysis of the thermodynamic properties across the largest possible radial range. Therefore, a number of alternative analytical fitting profiles have been proposed from both the theoretical and the observational sides.
A modification of the β-model based on X-ray observations has been introduced by Vikhlinin and collaborators [453], aiming at a better description of the features in the core and at the NFW scale radius r_s. Rewriting the density of equation (2.8) in terms of the electron number density, n_e times the ion number density, n_i, the generalized *Vikhlinin model* reads:

$$n_e n_i(r) = n_0^2 \ \frac{(r/r_c)^{-\alpha}}{[1+(r/r_c)^2]^{3\beta-\alpha/2}} \ \frac{1}{[1+(r/r_s)^\gamma]^{\varepsilon/\gamma}} + \frac{n_{02}^2}{[1+(r/r_{c2})^2]^{3\beta_2}} \ , \tag{2.10}$$

where n_0^2 and n_{02}^2 are two normalization densities. The r_c and r_s scaling radii have the same physical meaning as in the β-model and in the NFW model, respectively. The additional slope α sets the cuspiness of the profile near the centre, preventing an

excessive flattening. On the other hand, the ε parameter sets a change of the slope of the profile near the r_s radius, while γ controls the width of the transition region. It is worth to note that one has to impose the condition $\varepsilon < 5$, to avoid unphysical divergences in the core. The third term added in equation (2.10) represents a second β-model parametrized by $r_{c2} < r_c$ and β_2, which further constrains the profile in the centre. Under the hypothesis that the gas traces the dark matter in the outer cluster regions, the universal profiles of gas temperature and density descending from the NFW density profile have been derived theoretically in [243]. A widely-adopted parametrization of the gas pressure profile, which can be related to the density via a suitable equation of state (with a non-constant temperature), is given by the so-called *generalized NFW* (gNFW). This analytical model has been introduced by Nagai and collaborators to fit the profiles from a set of hydrodynamical simulations of clusters [303]. The pressure profile prescribed by the gNFW model for the electron gas is given by:

$$p(r) = P_\Delta \frac{p_0}{(r/r_s)^\gamma [1 + (r/r_s)^\alpha]^{(\beta-\gamma)/\alpha}} , \tag{2.11}$$

where in this case the slopes γ, α and β refer to the radial regions $r/r_s \ll 1$, $r/r_s \simeq 1$ and $r/r_s \gg 1$, respectively, while P_Δ gives the pressure within a sphere of radius R_Δ.

A fundamental thermodynamic quantity which is strictly connected with the density and temperature of the gas is the *entropy*, defined as [454]

$$K \equiv \frac{k_B T}{\mu m_H \rho^{2/3}} = k_B T n_e^{-2/3} , \tag{2.12}$$

where the ICM subscript of the density has been dropped for brevity.
The entropy of the ICM can be interpreted in terms of classical thermodynamics, since it is related to the standard entropy per particle as $s_p \sim k_B \ln K^{3/2}$. Furthermore, it represents the constant of proportionality between pressure and density in the equation of state of an adiabatic mono-atomic gas, i.e. $p = K\rho^{5/3}$. Neglecting galaxy formation processes, the only mechanism that can heat up the intra-cluster gas and generate entropy, is gravitational heating via shocks driven by hierarchical structure formation.
The radial profile $K(r)$ is useful to describe the structure of the ICM, and it encloses its thermodynamic history. Indeed, high-entropy gas tends to float, while low-entropy gas tends to sink. Therefore, entropy can trace the gravitational potential, since the gas convects until its isentropic surfaces coincide with the equipotential surfaces of the dark matter potential. Numerical simulations and observations indicate that entropy scales with the cluster radius as $K(r) \propto r^{1.1}$ outside the cluster core. In the innermost regions, instead, a large scatter from cluster to cluster is found, because of the non-negligible impact of radiative mechanisms related to galaxy formation [456].

2.1.3 Observational properties

The diverse matter components in galaxy clusters allow us to probe them through several observables. Indeed, the baryonic components are involved in different emission and scattering processes, yielding detectable signals from the X-ray to the radio bands. On the other hand, the dark matter component can be traced

via its gravitational effects, namely through gravitational lensing. In the following, we provide an overview of the observable properties of galaxy clusters, namely the emission in the X-ray, optical and radio bands, plus gravitational lensing. An extended treatment of the observations of clusters in the microwave band via the Sunyaev–Zel'dovich effect is provided in the dedicated section 2.2.

X-ray emission

The ICM in galaxy clusters is in the form of a hot, optically-thin plasma, the optical depth being $\lesssim 10^{-2}$, with temperatures ranging roughly between $\approx 6 \times 10^6$ and 10^8 K (i.e. at energies between 0.5 and 10 keV). Such values are consistent with the virial temperature, estimated from the virial theorem to be:

$$T_{\rm vir} = \frac{\mu m_H G}{2 k_B} \frac{M_{\rm vir}}{R_{\rm vir}} \ . \tag{2.13}$$

The most abundant element in the ICM is hydrogen, which is totally ionized at these temperatures; heavier, partially-ionized elements are also present, and their abundances are consistent with solar metallicity [12, 286]. Specifically, the most abundant heavy elements are iron, oxygen, nickel and silicon. They originated from nuclear reactions or radioactive decay in stars which ended their lives exploding as either core-collapse or type Ia supernovae [e.g. 285], depending on their mass and dynamical configuration [see e.g. 237].
The main emission from such a plasma is in the form of bremsstrahlung radiation caused by the deceleration of free electrons by nucleons, which is observed in the X-ray band [387]. Assuming that the electrons belong to an isothermal population with the velocities following a Maxwell-Boltzmann distribution, the emitted energy per unit volume and frequency via bremsstrahlung is given by:

$$\varepsilon_V(\nu; T) = C \exp\left(-\frac{h_P \nu}{k_B T}\right) n_e \ T^{-\frac{1}{2}} \sum_i^{N_n} Z_i^2 \ n_i \ g_f(\nu, T, Z_i) \ , \tag{2.14}$$

where the sum extends to all the ionized nucleon species, having atomic number Z_i; n_e and n_i are the number densities of electrons and ions, respectively; C is a numerical constant depending on the electron mass and electric charge, and $g(\nu, T, Z)$ is the Gaunt factor, which takes into account quantum effects. Since the major contribution to bremsstrahlung comes from fully ionized hydrogen, one considers $n_i = n_e$, therefore the volume emissivity is proportional to the square of the electron number density.
The integral of the volume emissivity per unit solid angle along the line of sight (los) gives the X-ray brightness (often called *surface* brightness). In the case of a galaxy cluster at redshift z, the brightness is:

$$S_X(\nu; T) = \frac{1}{4\pi(1+z)^4} \int_{\rm los} \varepsilon_V(\nu; T) \ dl \ , \tag{2.15}$$

where the $(4\pi)^{-1}$ factor arises from the assumption of isotropic emission, while the factor $(1+z)^{-4}$ takes into account the dimming of the flux and the relation between the comoving and the angular diameter distance, descending from the expansion of

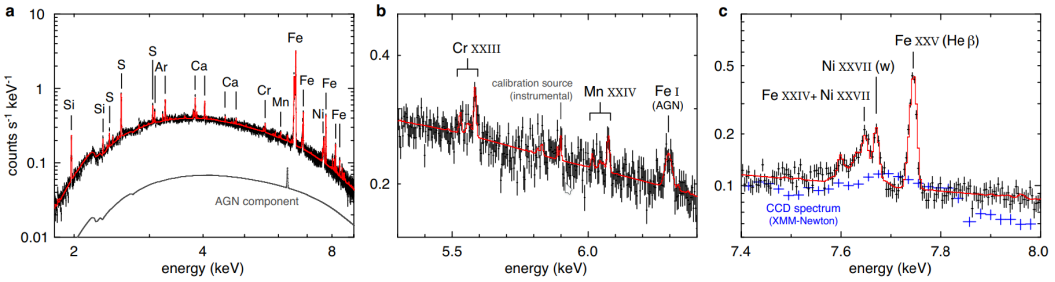

Figure 2.2. Spectrum of the X-ray emission from Perseus cluster as measured with the SXS spectrometer onboard the *Hitomi* satellite, formerly known as *ASTRO-H* [429]. The left panel shows the full spectrum (black line) with the superimposition of the best-fit curve (in red). The middle and right panels show a zoom in the 5.3-6.4 keV band and in the 7.4-8.0 keV band, respectiely [taken from 200].

the universe (see section 1.1.2).

At sufficiently high temperatures, the continuum spectrum of bremsstrahlung emission is characterized by peaks at the energies corresponding to the emission lines from ionized heavy elements, which range between about 2 and 10 keV, as shown in Figure 2.2. The most prominent emission is due to the complex of iron He_α-like lines marking the transitions from the K shell to the L shell, at energies between 7.5 and 8.5 keV. The emission from lines also scales proportionally to the product of the number density of ions and electrons, by virtue of the hypothesis of collisional ionization equilibrium. Indeed, the ionization fraction of an element depends only on the electron temperature, so its density – which sets the intensity of the corresponding spectral lines – is proportional to the proton density times the abundance of that element relative to hydrogen.

Given that the emissivity of all X-ray radiative processes in the ICM scales as $n_i n_e \approx n_e^2$, the X-ray luminosity of galaxy clusters is expressed in terms of a *cooling rate*, $\Lambda_{cX}(T)$, depending on the electron temperature T. Specifically, the cooling rate is defined in such a way that the quantity $n_i n_e\ \Lambda_{cX}(T)$ has the dimensions of a luminosity per unit volume [454]. Therefore,

$$L_X = \int n_i n_e\ \Lambda_{cX}(T)\ dV\ , \tag{2.16}$$

where the cooling function usually scales as $T^{1/2}$. Considering only hydrogen yields $L_X \propto n_e^2 T^{1/2}$.

From joint measurements of the X-ray luminosity and spectral lines, it is possible to derive the electron number density and temperature, respectively. Therefore, the thermodynamic properties of the ICM can be fully determined by suitable combinations of these two quantities. In particular, from the profile of the electron number density measured at different (projected) distances from the cluster centre, it is possible to derive the density profile. The latter, in turn, can be used to get the thermal pressure profile by means of the equation of state. Under the reasonable hypothesis that the ICM behaves as a perfect fluid and it has a spherical symmetry, the equation of state reads:

$$p(r) = n_e(r) k_B T(r) = \frac{\rho(r)}{\mu m_H} k_B T(r)\ . \tag{2.17}$$

Most notably, measurements of density and temperature allow the estimate of the total mass of a galaxy cluster, assuming that the gas is in hydrostatic equilibrium. Indeed, by equating the gravitational force to the pressure gradient force and making use of the equation of state, one has:

$$M_{\rm he}(<r) = -\frac{k_B r T(r)}{G\mu m_H}\left[\frac{d\ln\rho(r)}{d\ln r} + \frac{d\ln T(r)}{d\ln r}\right] , \tag{2.18}$$

which can be recast in terms of pressure and density as

$$M_{\rm he}(<r) = -\frac{rp(r)}{G\rho(r)}\frac{d\ln p(r)}{d\ln r} , \tag{2.19}$$

known as the *hydrostatic mass*.
Besides bremsstrahlung (free-free) and line emission, the ICM is characterised by additional, less prominent emission mechanisms, such as the free-bound and the stimulated two-photon emissions [see e.g. 51].

As a consequence of the proportionality to the squared number density of the gas, X-ray observations of galaxy clusters are naturally biased towards the brightest objects. In particular, clusters exhibiting a significantly peaked emission in the core (named *cool core* clusters) are more frequently detected, contrarily to the *non-cool core* ones. A prominent X-ray emission is expected to efficiently lower the ICM temperature by means of cooling flows [158, 211], thus lowering the central entropy (see equation (2.12)) and increasing the support from thermal pressure. Nevertheless, X-ray spectroscopic measurements do not provide a hint for such a decrease of the temperature of cluster cores [see e.g. 327, for a review]. Consistently with that, the observed low star formation rates in the BCGs suggest the presence of a heating mechanism capable of injecting sufficient energy to balance the cooling due to the X-ray emission. Recent improvements in hydrodynamical simulations allow the identification of such a mechanism with the activity of a central AGN (see also section 2.1.1).

Optical and infrared emission

Optical and infrared emission from clusters is due to the emission from the stars belonging to the galaxy members. The largest and brightest galaxies are located at the centre of the cluster, and the predominant morphology is that of early-type galaxies. The most important observables in this context are the optical richness, i.e. the number of galaxies inside a given radius, the luminosity and the colour. The luminosity from galaxies can be related to the galactic mass of the cluster by means of the luminosity function, n_L, via $n_L dL = n_{M_{\rm gal}} dM_{\rm gal}$, being $n_{M_{\rm gal}}$ the halo mass function evaluated at galactic scales.
Spectroscopic measurements yielding the velocity of clusters member galaxies along the line of sight, hence their velocity dispersion, provide another way of probing the total mass of a galaxy cluster. Indeed, galaxies in clusters can be regarded as collisionless particles, since mutual interactions between them are relatively rare. For a fluid made of collisionless particles in dynamical equilibrium, the mass can be estimated by virtue of *Jeans' equation*. Under the assumption of spherical symmetry

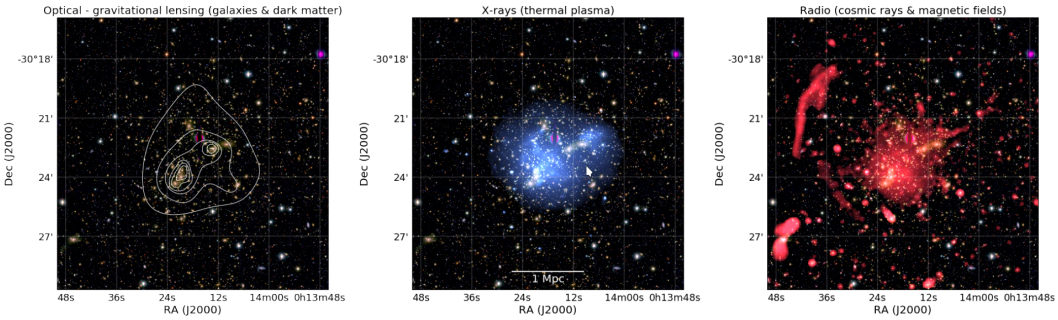

Figure 2.3. Multi-wavelength views of cluster A2744, superimposed on the optical image. from Subaru BRz [279]. **Left panel.** White contours giving the mass distribution inferred from gravitational lensing as in [287]. **Middle panel.** X-ray image from *Chandra* [463] in the 0.5-2.0 keV band. **Right panel.** Radio emission traced by the Very Large Array [193] in the frequency range 1-4 GHz [taken from 448].

in a non-rotating system, the mass is given by [43]:

$$M_J(<r) = -\frac{\sigma_r^2(r)\ r}{G}\left[\frac{d\ln n_{\rm gal}(r)}{d\ln r} + \frac{d\ln \sigma_r^2(r)}{d\ln r} + 2\beta_v(r)\right]\ , \qquad (2.20)$$

where $\sigma_r^2(r)$ is the velocity dispersion in the radial direction, $n_{\rm gal}(r)$ is the number density of galaxies normalized to the total number of galaxies themselves, and $\beta_v(r)$ is the anisotropy parameter. The latter is defined from the ratio between the velocity dispersion along the tangential direction over the dispersion along the radial direction, $\beta_v(r) = 1 - \sigma_t^2/(2\sigma_r^2)$.

Radio emission

Interferometric observations of galaxy clusters at radio frequencies reveal that the ICM hosts magnetic fields and cosmic rays [see e.g. 448, for a recent review]. The diffuse radio emission from a cluster can be classified into radio haloes and radio relics (or shocks). The main difference between the two is their spatial localization, since haloes are found at the cluster centre, while the emission from relics occurs at the peripheries. The emission mechanism leading to this kind of radiation is synchrotron, which is non-thermal. It is produced by the acceleration of free relativistic charged particles in the presence of a magnetic field [see e.g. 387]. Free charged particles in the ICM can be accelerated to relativistic velocities by shock waves or turbulence; therefore, emission in the radio band is more prominent in merging or disturbed systems, mostly in the form of radio haloes.
Large-scale magnetic fields in galaxy clusters, which are responsible for such an emission, have strengths between 0.1 and 10 µGauss [223] which also inhibit mechanisms of radiative transfer, like heat conduction and spatial mixing of gas.

Gravitational lensing

According to general relativity, light gets deflected in the presence of a gravitational field, as a consequence of the curvature of the spacetime. Therefore, when the light

from distant sources encounters a cluster of galaxies, it may produce luminous arcs or rings, in optical images of the cluster.
The amount of light deflection, which is strictly connected with the gravitational potential, can be used to infer the distribution of matter within clusters. Indeed, the integration of the gravitational potential over the so-called *lensing plane* gives the *lensing potential*, whose spatial first derivative coincides with the observed deflection angle. Proper combinations of the second derivatives of the lensing potential define instead the components of the *lensing matrix*. The latter features two important quantities, named *shear* and *convergence*, which quantify the stretching and the magnification (or de-magnification) of the source image, respectively [see e.g. 29].
The estimates of cluster masses based on gravitational lensing are affected by biases, though they are less prone to uncertainties in the modelling of astrophysical properties, For this reason, lensing-derived masses can be more robustly characterized by means of numerical simulations with respect to e.g. estimates based on ICM observations. Therefore, the calibration of cluster masses usually relies on lensing measurements [see e.g. the large project 457]. It is worth to note that, however, lensing-based mass estimates for single clusters are still characterized by large errors, mainly due to projection effects connected to cluster asphericity [443, 196]. In this respect, an improvement in the modelling, especially in the case of the strong lensing effect, consists in taking into account suitable priors, e.g. galaxy kinematics [79, 37].

2.2 The Sunyaev–Zel'dovich effect

The Sunyaev–Zel'dovich (SZ hereafter) effect is a distortion of the black body spectrum of the CMB. It occurs when the CMB photons propagate through the ICM, interacting via inverse Compton scattering with the free electrons [424–426]. If the electrons are at rest with respect to the CMB, there is no net effect when integrating over all possible scattering directions. On the contrary, if the electrons have a non-zero velocity in the CMB rest frame, they transfer some kinetic energy to the photons. The final frequency ν_f of a photon undergoing a single inverse Compton scattering with an electron is given by [e.g. 299]:

$$\nu_f = \nu_i \, \frac{1 - \beta_e \mu_i}{1 - \beta_e \mu_f + \frac{h_P \nu_i}{\gamma m_e c^2}(1 - \mu_{\rm sc})} \, , \tag{2.21}$$

where m_e is the electron mass, ν_i is the initial frequency of the photon, μ_i and μ_f are the direction cosines of the incoming and scattered photon with respect to the electron, and $\mu_{\rm sc}$ is the direction cosine between the incoming and scattered photon. The factor $\beta_e = V_e/c$ is the ratio between the electron velocity and the speed of light, while γ is the Lorentz factor, $\gamma = (1 - \beta_e^2)^{-1/2}$. In the case of CMB photons, the condition $h_P \nu_i / (\gamma m_e c^2) \ll 1$ holds, therefore the final frequency of the photons can be written as

$$\nu_f = \nu_i \, \frac{1 - \beta_e \mu_i}{1 - \beta_e \mu_f} \, , \tag{2.22}$$

so that the scattering can be treated in the Thomson limit. The net effect of the scattering is the redistribution of the photons from the Rayleigh–Jeans to the Wien region of the spectrum, which produces a change of the specific brightness of the

CMB signal [see e.g. 45]. The spectral shape of the distortion depends on the velocity distribution of the electrons. In this respect, it is possible to decompose the SZ effect into a *thermal* and a *kinetic* component. Furthermore, non-thermal distributions of relativistic electron velocities, which may occur for instance in the presence of magnetic fields, are responsible for additional non-thermal terms in the SZ effect [46, 150].

2.2.1 Thermal component

The thermal SZ (tSZ hereafter) effect is derived assuming that the velocities of the electrons involved in the scattering follow a Maxwell–Boltzmann distribution. Since the majority of the observed values of the electron temperature T in clusters of galaxies satisfy the condition $T \ll m_e c^2/k_B$, the relations describing the SZ effect are generally derived in the non-relativistic limit, using the Kompaneets approximation [246]. Introducing the dimensionless frequency:

$$x = \frac{h_P \nu}{k_B T_{\rm CMB}} \ , \tag{2.23}$$

The Kompaneets equation gives the change of the photon occupation number, $\bar{n} = (e^x - 1)^{-1}$, with time:

$$\frac{d\bar{n}}{dt} = \frac{k_B T_{\rm CMB}}{m_e c} \frac{\sigma_T n_e}{x^2} \frac{\partial}{\partial x} \left[x^4 \left(\frac{T}{T_{\rm CMB}} \frac{\partial \bar{n}}{\partial x} + \bar{n} + \bar{n}^2 \right) \right] \ , \tag{2.24}$$

where σ_T is Thomson cross section. Such a quantity can be translated directly into a change of the specific brightness of the CMB black body, $B(\nu; T_{\rm CMB})$, in the limit $T/T_{\rm CMB} \gg 1$. Figure 2.4 shows the comparison between the unperturbed CMB spectrum and the same spectrum distorted by the tSZ effect from a fictional massive having a mass 1000 times larger than the usual values. It can be seen that the distorted spectrum is not exactly that of a black body, and that the specific brightness decreases or increases with respect to the unperturbed spectrum, depending on the frequency.

From the integration of the CMB Comptonization along the path of the radiation to the observer along the line of sight, the tSZ spectral distortion can be expressed in terms of the specific brightness as [see e.g. 91]:

$$\Delta I_{\rm tSZ} = I_{\rm CMB} \ y \ g_{\rm tSZ}(x) \tag{2.25}$$

where $I_{\rm CMB} = 2(k_B T_{\rm CMB})^3/(h_P c)^2$, being $T_{\rm CMB}$ the CMB temperature given in section 1.2.

The y factor of equation (2.25) – also called *Comptonization parameter* or *Compton y-parameter* – encloses the dependence on the physics of the electron gas. It is defined as

$$y = \frac{\sigma_T}{m_e c^2} \int_{\rm los} n_e k_B T \ dl \ , \tag{2.26}$$

where the integration is carried along the line of sight (los). If the ICM follows a perfect gas law, the integrand in equation (2.26) corresponds to $p = n_e k_B T$, which is the thermal pressure of the electron gas. Alternatively, it is possible to express

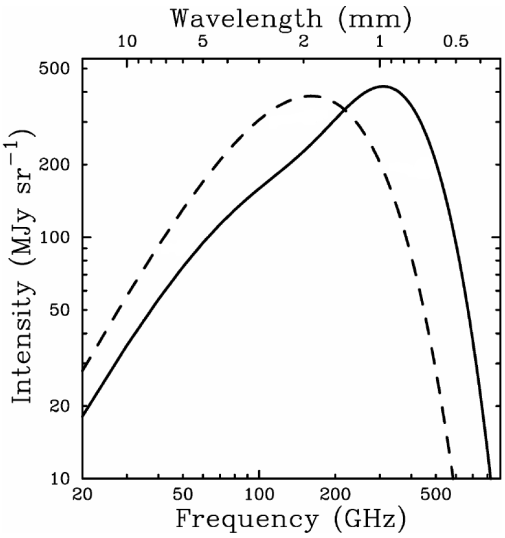

Figure 2.4. Spectrum of the CMB radiation as distorted by the tSZ effect (solid line). The dashed line represents the unperturbed spectrum [adapted from 91].

the Comptonization parameter in terms of the optical depth, $d\tau = n_e \sigma_T \, dl$.
The $g_{\rm tSZ}$ function of equation (2.25) defines the spectral behaviour of the tSZ effect with respect to the frequency of the incoming radiation:

$$g_{\rm tSZ}(x) = \frac{x^4 e^x}{(e^x - 1)^2} \left[\frac{x(e^x + 1)}{e^x - 1} - 4 \right] \ . \tag{2.27}$$

It can be seen that this function has a minimum at at 130 GHz, a maximum at 370 GHz, and it vanishes at 217 GHz. Therefore, the tSZ effect manifests as a decrement (increment) of the specific brightness of the CMB at frequencies lower (higher) than 217 GHz, as illustrated by the yellow curve in Figure 2.5, when relativistic corrections are not taken into account. In the Rayleigh–Jeans limit, the brightness shift of equation (2.25) can be also expressed in terms of brightness temperature $T_{\rm RJ}$ [see e.g. 71, for its definition], so that:

$$\Delta T_{\rm RJ,tSZ} = \Delta I_{\rm tSZ} \, \frac{c^2}{2 k_B \nu^2} \ , \tag{2.28}$$

which is illustrated in Figure 2.6, compared to the variation of the specific brightness. In terms of fluctuations of the CMB temperature, the change produced by the tSZ effect can be derived from the intensity shift through the derivative of the black body function with respect to the temperature. Its final expression is:

$$\Delta T_{\rm tSZ} = T_{\rm CMB} \ y \ f_{\rm tSZ}(x) \tag{2.29}$$

where the $f_{\rm tSZ}(x)$ function is defined as

$$f_{\rm tSZ}(x) = \frac{x(e^x + 1)}{e^x - 1} - 4 \ . \tag{2.30}$$

Also in this case, the shift vanishes at 217 GHz and it has the same sign of the variation in brightness.

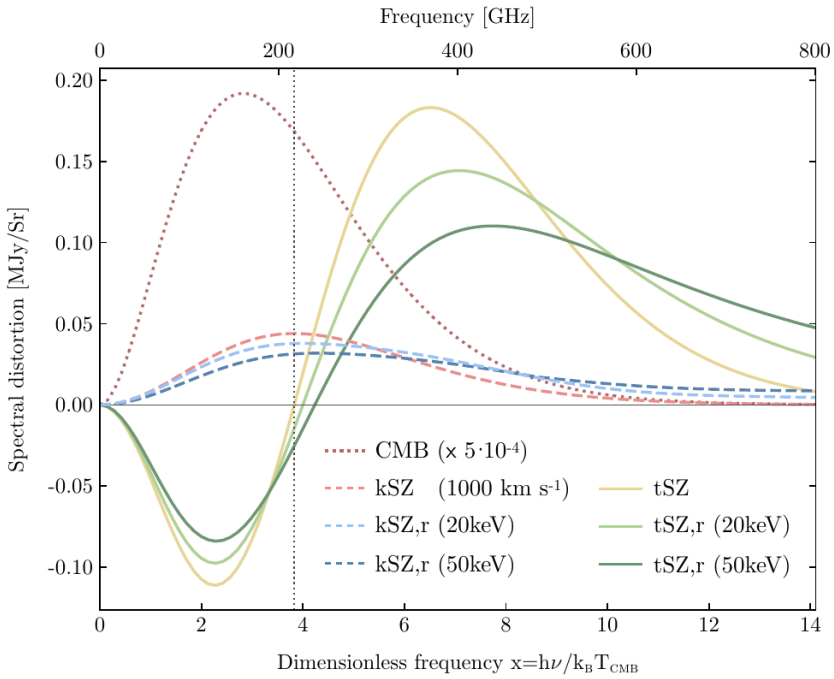

Figure 2.5. Spectral distortions produced by the tSZ (solid lines) and by the kSZ effects for a cluster approaching the observer (dashed lines). The different colours refer to different temperatures of the electrons in the ICM, and relativistic corrections are also included (see also sections 2.2.2 and 2.2.3). All the distortions are derived assuming an optical depth $\tau = 10^{-2}$ and a Comptonization parameter $y = 10^{-4}$. The dotted dark red curve is the un-scattered CMB spectrum multiplied by a factor 5×10^{-4} [taken from 299].

Figure 2.7 shows an example of the presence of the SZ effect (mainly the thermal component) in the temperature maps from the High Frequency Instrument onboard *Planck* satellite [333, 341], centred on a cluster detected with a high signal-to-noise ratio. At the two lowest frequencies ($\nu < 217\,\mathrm{GHz}$) the cluster can be seen at the centre of the maps as an excess of negative signal in the temperature fluctuations; it disappears at the zero frequency of 217 GHz, and it can be seen again at higher frequencies, as an excess of positive signal. Generally speaking, clusters cannot be easily seen in raw frequency maps because of the stronger contribution from contaminant sources, which motivates the need of efficient techniques for the extraction of the SZ signal. We will address this topic in detail in Chapter 3.

2.2.2 Kinetic component

If the electrons in the ICM move as a whole relatively to the Hubble flow, an additional non-vanishing Doppler term of the first order in β_e must be taken into account in the treatment of Compton scattering. This is known as the kinetic SZ (kSZ hereafter) effect. If the bulk velocity of the cluster projected along the line of sight is v_p (so that here $\beta_e = v_p/c$), the change of the specific brightness of the CMB radiation produced by the kSZ effect in the non-relativistic limit is [see e.g. 370]:

$$\Delta I_{\mathrm{kSZ}} = -I_{\mathrm{CMB}} \, \frac{v_p}{c} \, \tau \, g_{\mathrm{kSZ}}(x) \ , \tag{2.31}$$

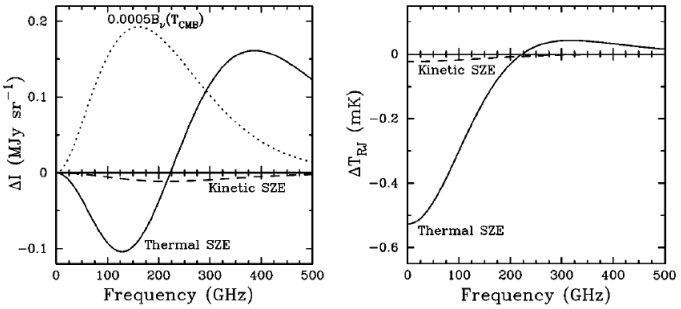

Figure 2.6. Comparison between the shift of the specific brightness (left panel) and of the brightness temperature (right panel) as produced by the SZ effect (see section 2.2.2 for a description of the kinematic component). Both functions are evaluated in the Kompaneets approximation for a cluster having a Comptonization parameter $y = 10^{-4}$, an electron temperature of 10 keV and a peculiar velocity of 500 km s^{-1}. The dotted line in the left panel represents the CMB blackbody spectrum times a factor 5×10^{-4} [taken from 91].

which is negative if the cluster approaches to the observer, which corresponds to $v_p > 0$. The optical depth τ is given by:

$$\tau = \int_{\text{los}} n_e \sigma_T \, dl \ , \tag{2.32}$$

while the $g_{\text{kSZ}}(x)$ function is defined as

$$g_{\text{kSZ}}(x) = \frac{x^4 e^x}{(e^x - 1)^2} \ . \tag{2.33}$$

As can be seen also from Figure 2.5, the latter has the same spectral behaviour of a Planck black body function, meaning that the kSZ effect does not alter the frequency dependence of the CMB spectrum. On the other hand, the former appears to have a slightly different temperature, shifted by:

$$\Delta T_{\text{kSZ}} = -T_{\text{CMB}} \, \frac{v_p}{c} \, \tau \tag{2.34}$$

whatever the frequency of the radiation.
This fact is one of the reasons why the kSZ effect is more difficult to be detected with respect to the thermal one: indeed, since it does not have a characteristic spectral signature, it cannot be easily disentangled from other sources at millimetre wavelengths using multi-frequency data. In Kompaneets approximation, the shift in specific brightness produced by the kSZ effect takes its maximum where the tSZ is null. Thus, the best frequency for measuring the kSZ effect is around 217 GHz, where the dominating astrophysical contaminant is the CMB itself.
Another reason why the measurement of the kSZ effect is challenging, is the intrinsically lower amplitude of the distortion. If v_e is the rms thermal velocity of the electrons, equations (2.25) and (2.31) yield:

$$\frac{\Delta I_{\text{kSZ}}}{\Delta I_{\text{tSZ}}} = \frac{1}{2} \frac{v_p}{c} \left(\frac{m_e c^2}{k_B T} \right) \approx c \, \frac{v_p}{v_e^2} \ , \tag{2.35}$$

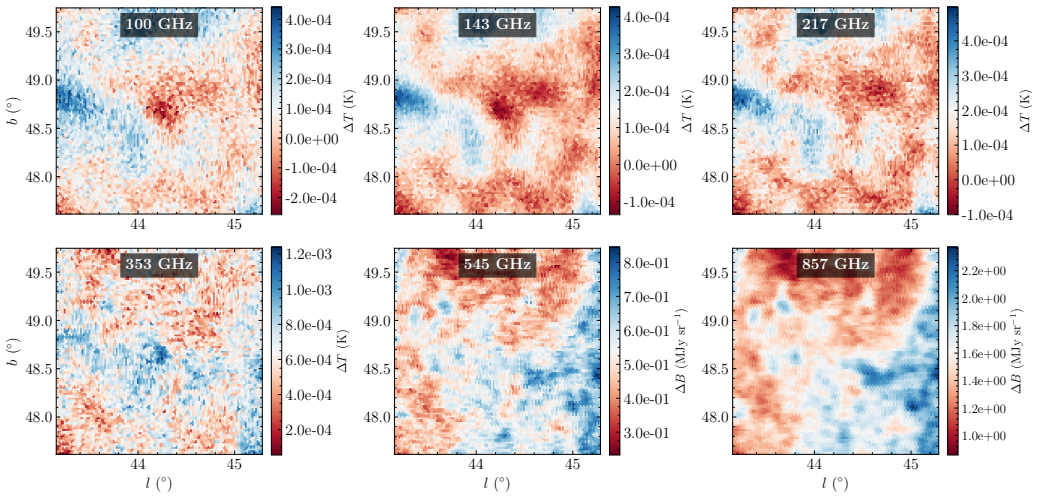

Figure 2.7. Raw maps of the region around cluster A2142 from the 2015 data release of the *Planck* satellite at its six highest frequencies (reproduced with permission). The cluster can be clearly seen at the centre of the maps through the tSZ effect as a decrement (increment) of the signal at frequencies lower (higher) than 217 GHz. At the zero frequency the signal in the map is dominated by the CMB, while at the two highest frequencies it practically coincides with the emission from dust.

which is equal to 0.085 for projected bulk velocities of $10^3\,\mathrm{km\,s^{-1}}$ and electron temperatures of 10 keV, supposing that the cluster is observed at a frequency at which $g_{\mathrm{tSZ}}(x) \approx g_{\mathrm{kSZ}}(x)$.
In principle, any coherent, non-thermal motion of the electrons in the ICM contributes to the kSZ effect. A very interesting case, which can shed some light on the problem of mass bias (see section 2.1.3), and which can provide useful insights on the process of cluster formation is represented by the occurrence of rotational motions. A detailed study on this component of the kSZ effect is treated in Chapter 4.

A remarkable aspect of the SZ effect which can be immediately seen from all the expressions shown so far, is that it does not depend on the redshift of the cluster. In other words, the SZ signal is not affected by the dimming of the specific brightness which plagues X-ray observations (see section 2.1.3), since both the perturbed and the unperturbed photons evolve with redshift as a black body. This property makes the SZ effect a unique probe of the high-redshift universe, as testified by a number of new discoveries of clusters [see e.g. 192, 47] that would be hard to detect through emission-based mechanisms with current instruments.

2.2.3 Relativistic corrections

At electron temperatures $T \gtrsim 10\,\mathrm{keV}$ Kompaneets approximation does not hold, thus the spectral distortions from the tSZ and the kSZ effect must include relativistic corrections [e.g. 371]. Specifically, one has to take into account both higher-order derivatives of the occupation number, and higher-order terms in $k_B T/(m_e c^2)$ and β_e which occur in the scattering kernel.
Figure 2.5 shows the effect of such relativistic corrections on the spectral distortions

$\Delta I_{\rm tSZ}$ and $\Delta I_{\rm kSZ}$ of equations (2.25) and (2.31), for different values of the electron temperature. It can be seen that the distortions produced by both the thermal and kinetic components of the SZ effect are broadened, with a systematic shift towards higher frequencies. This is due to the fact that the energy shift and broadening per single scattering are larger at higher electron temperatures, with respect to the non-relativistic limit.
The terms giving the relativistic corrections to the SZ effect have been derived by evaluating the Compton collision term with a variety of numerical methods [e.g. 315, 219, 316, 314, 102]. In practice, the spectral functions $f_{\rm tSZ}(x)$, $g_{\rm tSZ}(x)$ and $g_{\rm kSZ}(x)$ get modified according to the electron temperature. Taking relativistic effects into account allows the use of the SZ effect as a probe of several quantities which are important for cluster astrophysics and cosmology. They are, for instance: the electron temperature of both individual [e.g. 357, 103] and stacked targets [e.g. 212, 152]; the relation between the temperature of the CMB and the redshift (when the cluster temperature is known) [e.g. 31, 267]; two out of the three projected components of the bulk velocity, the third one being accessible by means of the polarized SZ effect [e.g. 100].

2.2.4 Observational considerations

Observationally speaking, the SZ effect has been detected roughly twenty years after it was predicted [224]. Later on, the continuous development of observational techniques in millimetre astronomy, with the improvement of the detector sensitivity and of the control of systematic errors [91], has led to a considerable growth of SZ-based cluster catalogues. At present, the largest available repository of all-sky maps of this effect is the archive built from the observations with the *Planck* satellite [333]. It is constituted by the PSZ1 and PSZ2 catalogues, which contain a total of 1245 confirmed detections over 1944 [340, 346]. From the largest ground-based surveys produced with the data from the 6-m Atacama Cosmology Telescope (ACT) [428] and the 10-m South Pole Telescope (SPT) [93], instead, there have been detections of hundreds of clusters, including new discoveries [192, 47].

For electron temperatures between ~ 0.5 and $\sim 10\,\mathrm{keV}$, and optical depths $\tau < 0.01$, the change in specific brightness produced by the tSZ effect is relatively small, ranging from $\sim 10^{-5}$ to $\sim 10^{-4}$. As to obtain high-precision measurements of any weak cosmological signal, the detection of the SZ effect requires a suitable instrumental sensitivity. Furthermore, to efficiently reject ground noise and instrumental emissions, a differential technique i.e. the alternation of the signal from the sky with some known reference source is also necessary. Lastly, the instrument should provide a sufficiently high angular resolution on cluster scales, which translates in large telescope areas, or in the use of the interferometric techniques. Indeed, in the ideal condition of diffraction-limited observations, the angular resolution of a telescope is proportional to the ratio between the wavelength of the radiation of interest and the diameter of the entrance pupil of the optical system [see e.g. 400]. Considering cluster angular sizes, that span from tens of arcseconds to a few degrees in the case of the farthest and closest objects, respectively, the diameter of the primary mirror of the telescope for observations at millimetre wavelengths has to be $\gtrsim 1.5\,\mathrm{m}$. This is particularly important to resolve the farthest clusters. Indeed, since

SZ measurements are *flux* measurements, they are proportional to the integral of the Comptonization parameter over the solid angle subtended by the cluster. If the solid angle is significantly smaller than the beam size of the instrument – as it is likely to happen in the case of high-redshift clusters – the signal gets dimmed because it is diluted over a larger area. For this reason, SZ observations would be effectively independent on redshift only in the ideal case of infinite angular resolution.

There are two main classes of instruments that are used for the observation of the SZ effect. They are (*i*) single-dish telescopes at radio and microwave frequencies and (*ii*) interferometers, i.e. multiple single-dish radio-telescopes [91]. We will give here a brief description of them, and we will provide some examples of current and future relevant experiments.

Single-dish observations

Being mostly suitable for large-scale measurements and cluster surveys, observations carried out with a single telescope coupled to radio receivers have been made since the very first attempts to measure the SZ effect. For instance, measurements of the temperature decrement produced by the tSZ effect at low frequencies towards nearby clusters, observed at the Owens Valley Radio Observatory (OVRO) at 20.3 and 32 GHz, have been reported in [44] and in [195], respectively.

The number of SZ observations with single-dish telescopes in the microwave band has then increased significantly since the development of high-sensitivity bolometers. They are easy-to-build thermal detectors which allow the spanning of a wide range of frequencies, and that can be easily assembled into arrays to cover large focal planes and to reduce the observational time [see e.g. 372, for a review]. Some historical examples are the SCUBA camera at the 15-m James Clerk Maxwell Telescope [205] operating at 353 GHz, the SuZIE and BOLOCAM cameras at the 10.4-m Caltech Submillimeter Observatory (CSO) [208, 178], and DIABOLO at the IRAM 30-m telescope [131]. With a frequency coverage between 100 and 300 GHz, the above instruments allowed the first spectral measurements of the SZ effect, from the combination of data from different observatories [see e.g. 253]. Through the years, the performance of bolometers improved drastically, for instance by means of the use of superconducting materials instead of semiconductors, together with the development of more efficient techniques to keep the detectors operating in vacuum at cryogenic temperatures, with better control of systematic errors. For this reason they have been employed in a variety of recent CMB and SZ-dedicated experiments. Some examples include the *Planck* satellite [333], which uses photon noise-limited germanium bolometers, and ground-based instruments as: MITO [123] (also employing germanium bolometers), SCUBA-2 [206], APEX-SZ [137], ACT [428], SPT [93] and MUSTANG [134], all equipped with transition edge sensor (TES) bolometers. Other projects for SZ observations using new generation TES bolometers, are normally upgrades of existing ground-based experiments, like ACTpol [312], SPT-3G [36] and MUSTANG-2 [469], that will produce new cluster catalogues with improved sensitivity.

Even better performances with respect to bolometers can be reached with kinetic inductance detectors (KIDs). The operation principle of a KID is based on the production of abundant non-equilibrium quasi-particles arising from the break of

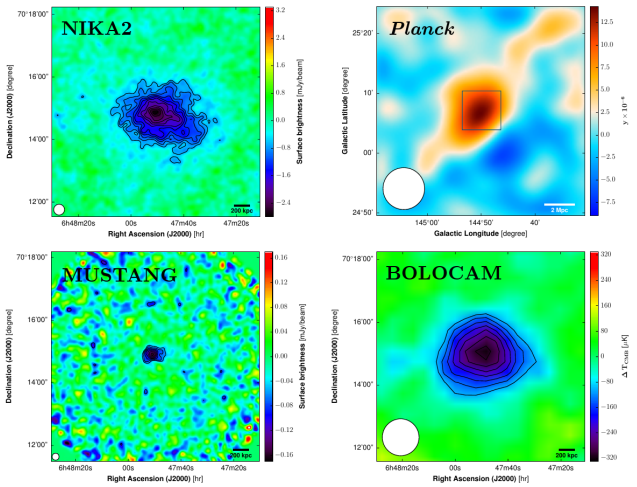

Figure 2.8. TSZ signal of cluster PSZ2 G144.83+25.11 from single-dish observations with four instruments having different angular resolutions (see the beams represented as white circles in the bottom left corner of each map). **Top left.** Surface brightness mapped by NIKA2 at 150 GHz. **Top right.** Compton y-parameter reconstructed from *Planck* HFI data. The blue square gives the size of the region covered by the maps shown in the other panels. **Bottom left.** Surface brightness mapped by MUSTANG at 90 GHz. **Bottom right.** Temperature signal measured by BOLOCAM at 140 GHz [adapted from 385, see the references for the single maps therein].

Cooper pairs [111] in a superconducting material. This phenomenon happens when a superconductor maintained at temperatures below the critical temperature at which the superconducting transition occurs, gets illuminated with radiation of suitable energy. The quasi-particles have a long lifetime, and a variation of their number density induces a variation of the kinetic inductance of the superconducting element. Since the kinetic inductance can be treated as an impedance, it can be combined with a capacitor to build a microwave resonator whose resonant frequency changes with the absorption of photons [120]. KIDs are currently the best candidates for large arrays of microwave detectors, also because they are less prone to suffer from temperature fluctuations and microphone noise, compared to TES bolometers [294]. Some examples of new-generation cameras where bolometers have been replaced by KIDs are BOLOCAM, superseded by the MUSIC camera [391] at the CSO, and DIABOLO, replaced by NIKA [294] and NIKA2 [78] at the IRAM observatory. An example of a recent comparison between the mapping capabilities of different single-dish observatories coupled to microwave detectors is provided in Figure 2.8. An alternative observational strategy conceived for the balloon-borne experiment OLIMPO [276], consists in performing flux observations at a limited number of frequency bands, together with spectroscopic measurements within each band, through the use of a differential Fourier transform spectrometer [397]. Other examples of future SZ-dedicated experiments that will use such a joint photometric and spectroscopic configuration are KISS [384], CONCERTO [252] and the space-based *MILLIMETRON* observatory [414].

Interferometric observations

The very first imaging of a cluster of galaxies with the SZ effect was obtained through an interferometric detection at 15 GHz, using five out of the eight 13-m radio-telescopes constituting the Ryle Telescope [224]. Interferometric arrays are constituted by a number of single-dish telescopes (array elements), and they are usually optimized for high resolution observations at radio frequencies of single point-source targets at small spatial scales in the sky. The output signal is the time-averaged correlated signal coming from the same source, as observed simultaneously by all the array elements. It is proportional to the Fourier transform of the signal from the sky convolved with the beam of each element of the telescope array, at well-defined spatial frequencies. Specifically, given the *baseline* $\mathfrak{b}$, which is the component of the vector connecting two array elements oriented perpendicularly to the source, interferometers are sensitive only to spatial frequencies larger than $\mathfrak{b}/\lambda$ (small angular scales), being λ the wavelength of the radiation. Thus, in the case of radio wavelengths, large baselines allow high-resolution measurements of point-like sources. Interferometers can be used to measure the decrement of the tSZ effect towards nearby clusters, taking advantage of the larger stability relatively to systematics and large-scale gradients, in comparison with single-dish measurements. An example is provided by the case of the OVRO-BIMA array [92], where a low baseline and a coupling with low-noise cm-wave receivers are used. Some SZ-dedicated interferometers built over the years are e.g. SZA [204], AMI [11], AMiBA [201] and ALMA [8]. The latter recently allowed the mapping of the tSZ effect at 92 GHz with an angular resolution of 5 arcsec, which is the highest resolution to date achieved in SZ measurements [238].

The interesting recent review by [299] provides an exhaustive perspective on future high-resolution observatories, in view of the CMB-Stage 4 (CMB-S4) [90].

Observations of the kSZ effect from single clusters

The intrinsic weakness of the kSZ effect makes its detection particularly challenging. As discussed in section 2.2.2, the temperature anisotropy produced by the kSZ effect in the hottest clusters can be as smaller as about one order of magnitude with respect to the one induced by the tSZ effect, thus requiring high-sensitivity detectors. Furthermore, multi-frequency data are useful to disentangle this signal from synchrotron and dust, but not from the CMB, which has the same spectrum. The only feature which allows the distinction between the kSZ effect and the CMB is their different spatial distribution. Indeed, cluster angular scales are generally much smaller than the degree-scale of CMB primary anisotropies. Also, both components of the SZ effect are expected to show strong spatial correlations [167]. This implies the requirement of another important instrumental feature, that is a sufficiently high angular resolution.

In any case, the major issue plaguing the measurement of cluster velocities, which represent the most interesting physical quantity that can be derived from the kSZ signal, are the large relative errors, mostly due to contaminants of astrophysical or instrumental origin. Moreover, it should be noticed that the kSZ signal alone is not sufficient to derive the projected bulk velocity of a cluster, since it is degener-

ate with the optical depth of the electron gas (see equation (2.34)). The latter is usually constrained using bolometric or spectroscopic X-ray measurements, whose uncertainties can significantly contribute to the overall error on the estimate of the peculiar velocity.
Historically, one of the first attempts to put an upper limit to the kSZ effect and to cluster peculiar velocities has been made with SuZIE [207]. More recent detections with higher angular resolutions and new-generation cameras point to very promising results, despite the aforementioned difficulties [298, 392, 395]. For instance, the NIKA camera allowed the first high-significance detection of the kSZ effect to date. Specifically, the kSZ signal towards the complex system MACS J0717.5+3745 has been detected with a significance of 3.4 and 5.1σ in two substructures belonging to the cluster, respectively [4]. However, the constraints on the bulk velocity derived from the combination with ancillary X-ray data are still affected by large errors. Another recent study focussed on a sample of ten clusters [396] reported the detection of the kSZ effect at significances between 2 and 4σ, with an angular resolution of 70 arcsec. However, no significant evidence for bulk motions in the single objects has been found.

For the sake of completeness, we mention here an observational strategy applied to large samples of clusters, with which the kSZ effect has been detected for the first time [190]. The goal of such a technique is to integrate statistical errors by measuring cumulative quantities which are dominated by the overall bulk flow. Several works reported the detection of cluster motions at high significance using this method, namely by measuring the pairwise momentum between couples of galaxies through its imprint on CMB data [see 347, 130, 121, 262].

Chapter 3

Spectral imaging of the thermal Sunyaev–Zel'dovich effect

This Chapter is dedicated to the tests and the enhancements of a new spectral imaging algorithm tailored to mapping the tSZ effect from galaxy clusters. It starts with an introduction on the general problem of component separation at millimetre wavelengths, and with an overview on existing techniques. Subsequently, we provide an introductory summary on wavelet and curvelet decompositions, which constitute a core feature of our novel algorithm. The latter is then described in all its technical details, focussing on the improvements that have been implemented to enhance its stability and the quality of the reconstructed maps. We then illustrate the application of the algorithm to the target clusters of the X-COP project, which is a study devoted to the characterization of cluster outskirts. We conclude with a preliminary scientific application of our new maps, which is the derivation of unbiased cluster pressure profiles from the masking of overpressure structures detected in the outskirts.

3.1 The sky at millimetre wavelengths

Between a few tens and a few thousands of GHz, namely from the microwave to the far infrared region of the electromagnetic spectrum, the sky is very bright. Indeed, the signal collected at these frequencies is a mixture of contributions from emission or scattering from either diffuse or point-like astrophysical sources.
At low Galactic latitudes, the most prominent contribution comes from the interstellar medium in the Galaxy. It consists in both cold and fully ionized gas, mostly in the form of neutral (HI) or molecular hydrogen, and ionized hydrogen (HII), respectively. Also, a dust component made of silicate and carbonate grains is present, both in the cold molecular clouds concentrated in the Galactic plane and in the thin, diffuse halo of the Galaxy. Figure 3.1 shows the emission observed at the frequencies scanned by the Low Frequency Instrument (LFI) and the High Frequency Instrument (HFI hereafter) onboard the *Planck* satellite. It can be seen that, apart from that of the CMB, the sky signal comes from: synchrotron, thermal bremsstrahlung, thermal dust, spinning dust, and carbon monoxide. The first two emission processes dominate at frequencies below $\approx 50\,\mathrm{GHz}$. Thermal dust emission dominates at frequencies

$\gtrsim 100\,\mathrm{GHz}$, while spinning dust steeply decreases above $\approx 40\,\mathrm{GHz}$. The rotational transition in CO molecules between the levels $J = 1 - 0$, which traces molecular hydrogen, is relevant only at frequencies around 115 GHz (see Figure 3.1a).
Besides Galactic emission, also extragalactic sources must be considered. A diffuse source emitting at high frequencies is given by the infrared radiation from unresolved and dusty high-redshift objects, which originates the so-called cosmic infrared background (or CIB) [see 359, and references therein]. The CIB and the Galactic thermal dust are characterised by a similar spectral energy density, but they can be disentangled by means of the statistical properties of their spatial fluctuations [see e.g. 259, and references therein]. In any case, the contribution from the CIB is subdominant with respect to the Galactic one when focussing on the observations of low-redshift objects, especially at low Galactic latitudes. On the other hand, among extragalactic point sources, clusters of galaxies are the most important ones for the purposes of the present work. They are detectable via the SZ effect at frequencies up to $\approx 800\,\mathrm{GHz}$ (see the plot of the tSZ Rayleigh–Jeans temperature in Figure 2.6). In addition, point-like synchrotron sources at radio frequencies, or dusty galaxies emitting at infrared wavelengths are also present.
Lastly, all the components of the Solar system emit at high frequencies in the microwave region. In particular, the so-called *zodiacal light* is the diffuse signal emitted by grains and dust particles located in the ecliptic plane [275].

3.1.1 Overview of the dominant signals

In the following, we will shortly describe the most important diffuse sources – namely synchrotron, free-free and thermal dust – and their spectral characteristics. We refer the reader to sections 1.2 and 2.2 for the description of the CMB and of the SZ effect, respectively. For a discussion on the emission from spinning dust (also referred as to the *anomalous microwave emission*) and on the complete set of CO emission lines, see e.g. [343] and references therein.

Synchrotron radiation

Synchrotron radiation is emitted by free charged particles accelerated by a magnetic field (see also section 2.1.3). Indeed, synchrotron emitters are relativistic electrons boosted by cosmic rays or by supernovae explosions, which spiral in the Galactic magnetic field. Besides the H_α line of the Balmer series, this is the main emission mechanism which allows the observation of the HII regions. The spectrum of this radiation features a flattening at frequencies lower than ≈ 1 GHz, while it is well represented by a single power law with a constant spectral index in the range $[-3.1, -2.5]$ at higher frequencies. Also, this radiation may be polarized up to a 40% level.

Free-free (or thermal bremsstrahlung) radiation

Free-free radiation is emitted by free electrons decelerated by nuclei (see also section 2.1.3). Therefore, like synchrotron radiation, thermal bremsstrahlung is mostly produced by the ionized interstellar medium. The spectrum scales as a power law as a function of the frequency, with a spectral index around -2.1 which varies very

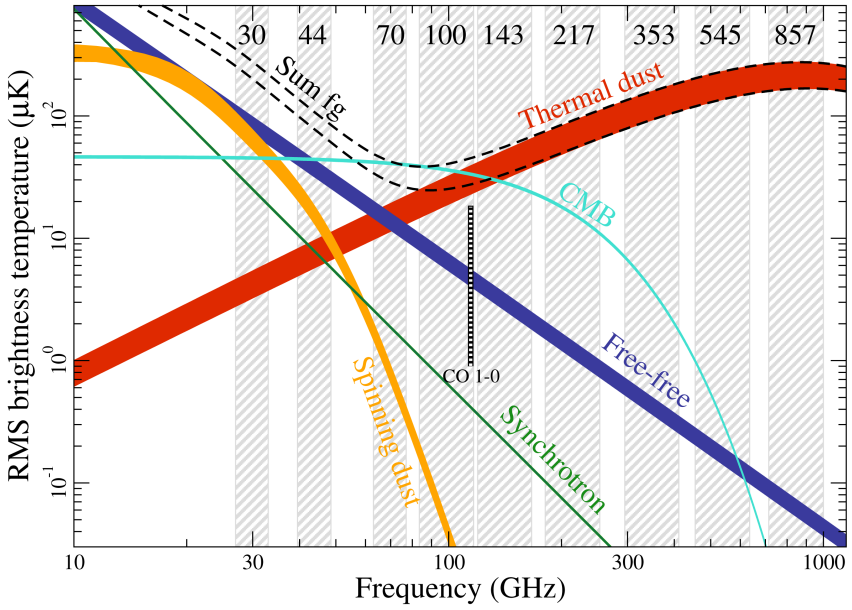

(a) Spectra

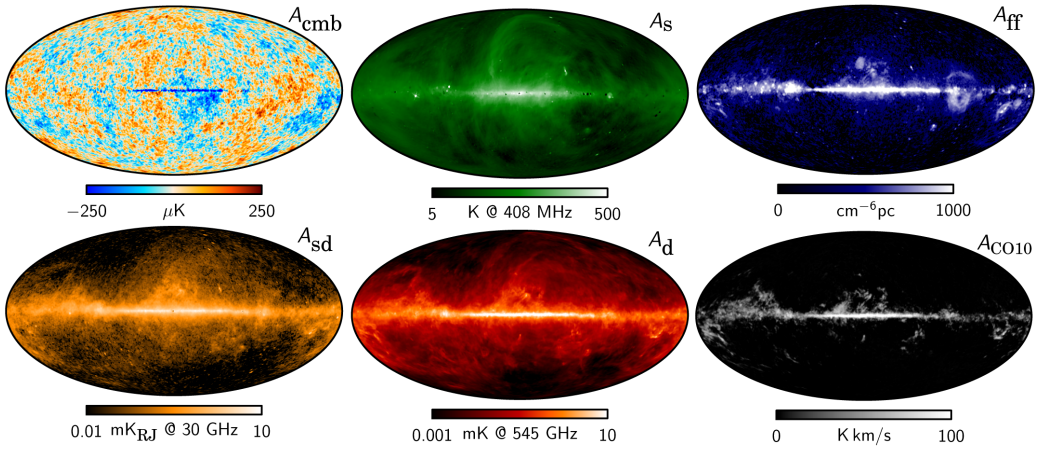

(b) Maps

Figure 3.1. Dominating emitting sources in the microwave sky as seen by *Planck*. **(a)** Root mean square of the Rayleigh–Jeans temperature at frequencies between 10 GHz and 1 THz. Upper and lower edges of the lines are defined accounting for 93% and 81% of the sky, respectively. Shaded bands in light grey are centred on the frequencies scanned by *Planck* bolometers. **(b)** Mollweide projection in Galactic coordinates of the all-sky maps showing the intensity of the signal from the CMB and from microwave foregrounds, colour-coded as in panel **(a)** [adapted from 343].

slightly with the frequency and with the electron temperature, which in this case can range from a few hundreds to tens of thousands of K.

Emission from thermal dust

Dust consists of small particles of silicate and carbonaceous grains, which originated from the aggregation of material injected in space during stellar evolution. Dust populates the various phases of the interstellar medium, and it is a good tracer of star-forming HI regions. Dust grains efficiently absorb optical and ultraviolet radiation from e.g. newborn stars, and they are heated up to temperatures of a few tens of K. Therefore, they emit radiation at infrared wavelengths, and their contribution is dominant at frequencies of hundreds of GHz [71].
In the Galaxy, different species of dust characterised by specific chemical compositions and average temperatures, tend to trace both atomic and molecular hydrogen. In particular, the emissivity of Galactic thermal dust at high Galactic latitudes shows spatial variations that correlate with the column density of HI, which can be mapped via the spin-flip emission at 21 cm in the radio band [64]. Moreover, this dust component has been known from *COBE*/FIRAS measurements to exhibit the spectral energy density of a grey body. The latter is defined as a modified black body, by means of the product with a power law function of the frequency that accounts for opacity effects:

$$B_{\mathrm{gb}}(\nu; T_{\mathrm{td}}) = \tau_{\mathrm{td}}(\nu_0) \left(\frac{\nu}{\nu_0}\right)^{\beta_{\mathrm{td}}} B(\nu; T_{\mathrm{td}}) \ , \tag{3.1}$$

where $B(\nu; T_{\mathrm{td}})$ is the specific brightness of a black body (or Planck function, see also section 1.2) at the temperature of the dust grains, T_{td}; ν_0 is a reference frequency; β_{td} is the spectral index; $\tau_{\mathrm{td}}(\nu_0)$ gives the amplitude of the signal. It represents the value of the optical depth at the reference frequency, defined as

$$\tau_{\mathrm{td}}(\nu_0) = \int_{\mathrm{los}} n_{\mathrm{td}} \sigma_{\mathrm{td}}(\nu_0) \, dl \ , \tag{3.2}$$

being n_{td} and $\sigma_{\mathrm{td}}(\nu)$ the number density and the cross section of thermal dust grains, respectively.
The grey body model of equation (3.1) has been adopted by the *Planck* Collaboration to model the emission from dust across the sky (thus, also at high Galactic latitudes) [337]. They fit equation (3.1) with $\nu_0 = 353\,\mathrm{GHz}$ to *Planck* HFI data at 353, 545 and 857 GHz, plus data at 3000 GHz obtained from a combination of *IRAS* [311] and *COBE*/DIRBE [278] measurements. The best-fit values for the temperature and the spectral index of the dust grains are found to be:

$$\begin{aligned} T_{\mathrm{td}} &= (19.7 \pm 1.4)\,\mathrm{K} \\ \beta_{\mathrm{td}} &= 1.62 \pm 0.10 \ , \end{aligned}$$

which are the average values on the full sky. Nevertheless, in [164] it has been argued that the flattening of the spectrum in the low frequency range as observed by the *COBE*/FIRAS and *COBE*/DIRBE experiments cannot be modelled from the

Table 3.1. Best-fit parameters to the double and single grey body models of equations (3.1) and (3.3), as derived by MF15.

Model	f_1	q_1/q_2	β_1	β_2	T_2	T_1	$\mathfrak{N}$	$\chi^2_{\rm red}$
double grey body	0.0485	8.22	1.63	2.82	15.70	9.75	0.980	1.33
single grey body	0	–	–	1.59	19.63	–	0.999	5.65

extrapolation of a single grey body spectrum. Therefore, a more sophisticated model featuring two populations of dust grains having different temperatures and spectral indexes has been hypothesized, to solve such a discrepancy. This motivated the work by Meisner & Finkbeiner (2015) [280] (MF15 hereafter). Specifically, with the aim of providing a consistent description of thermal dust emission from 100 to 3000 GHz, they revisit the dust model proposed in [337] using: *Planck* data at all the six HFI bands; *COBE*/DIRBE data at 1250, 2141 and 3000 GHz, and *IRAS* data at 3000 GHz. The modified specific brightness of the two grey body is therefore:

$$B_{\rm 2gb}(\nu;T_1,T_2) = \mathfrak{N}\, f_1 \frac{q_1}{q_2}\left(\frac{\nu}{\nu_0}\right)^{\beta_1} B(\nu;T_1) + (1-f_1)\left(\frac{\nu}{\nu_0}\right)^{\beta_2} B(\nu;T_2)\ , \qquad (3.3)$$

where the dimensionless constant factors f_1 and q_1/q_2 refer to the relative contribution from the coldest component at temperature T_1 and the hottest component at temperature T_2. The β_1 and β_2 parameters give the slopes of the two different power laws, while $B(\nu;T_1)$ and $B(\nu;T_2)$ are the corresponding Planck functions describing the black body spectrum; $\mathfrak{N}$ is a normalization factor. In MF15 they constrain the free parameters of the model in equation (3.3) via a correlation slope analysis, setting $\nu_0 = 3000\,$GHz. In principle, the set of parameters to be determined by the fit would be $(\mathfrak{N}, f_1, q_1/q_2, \beta_1, T_1, \beta_2, T_2)$, as observed along all lines of sight. Nevertheless, assuming that both dust populations are within the same interstellar radiation field, it is possible to link their two temperatures, T_1 and T_2, via a power law whose normalization and slope depend on a proper combination of β_1, β_2 and q_1/q_2 [164]. Despite T_1 can be derived from the rest of the parameters, it is still difficult to *spatially* constrain the entire set, on a basis of five broad-band high-resolution measurements. Therefore, the parameters β_1, β_2, f_1 and q_1/q_2 are treated in the fit as spatially constant across the sky, allowing only for spatial variations of the temperature T_2 and of the normalization factor. Table 3.1 reports the values of the best-fit parameters set as described above, plus the values of the corresponding parameters in a possible single grey body scenario (which can be recovered from equation (3.3) by setting $f_1 = 0$). Figure 3.2 shows the corresponding best-fit curves on top of the available data. It is possible to see that the contribution from the cold component (represented by the magenta line) is important at low frequencies. Both the ratio of the average intensities and the value of the reduced chi-square in Table 3.1 indicate that the two grey body model produces a better description of the observed data than the single component model. The results from the *Planck* Collaboration are also shown, to better highlight that the double grey body model is more suitable to fit the data at the lowest frequencies.

For our purposes of mapping the tSZ effect from the HFI multi-frequency maps,

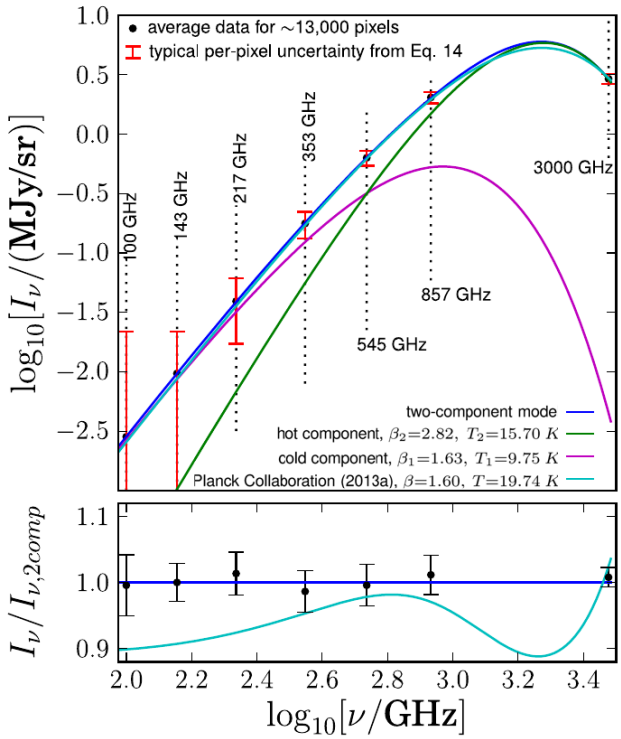

Figure 3.2. Comparison between double and single grey body models, from the fit to the averaged HFI and DIRBE data between 100 and 3000 GHz (black dots). Red error bars give the uncertainty per pixel. The bottom panel shows the average intensity from the data (black dots) and from the grey body model by the *Planck* Collaboration, both normalized to the average intensity from the double grey body model of MF15, from which this figure is taken.

we will rely on the modified model by MF15, given its better performances in the range [100, 217] GHz (see section 3.3).

3.1.2 Techniques for component separation

Component separation is a necessary operation that must be performed to extract the signal from a particular source of interest, as the tSZ effect, from the signature of a mixture of sources registered at multiple frequencies. In millimetre astronomy, data are usually in form of temperature maps in units of $\mathrm{K_{CMB}}$, i.e. the measured quantity is the temperature fluctuation ΔT relative to the CMB temperature in K, detected across the sky. Such maps can be expressed at each frequency ν as the superimposition of the signals from N_s different astrophysical sources (see section 3.1).
In matrix notation, the problem is usually formulated as

$$\boldsymbol{D} = A\boldsymbol{s} + \boldsymbol{\eta} \ , \tag{3.4}$$

where $\boldsymbol{D}$, and $\boldsymbol{\eta}$ are vectors representing the observed data and the instrumental noise, respectively, both having a number of elements equal to the number of observed frequency channels, N_ν. The vector $\boldsymbol{s}$ represents the amplitude of the physical signal

to separate at a given reference frequency (e.g. the specific brightness, or the optical depth), while A is a *mixing matrix* having size $N_\nu \times N_s$, which contains the spectral energy density of each source at the different frequencies, convolved with the transmission of the instrument at each band. Its entries are therefore $A_{\nu i} = f_i(\nu)$, being $f_i(\nu)$ a function describing the spectral energy density of the i-th component. Therefore, the component separation problem at each frequency is stated as

$$D_\nu = \sum_i^{N_s} A_{\nu i}\ s_i + \eta_\nu\ , \tag{3.5}$$

where, in the context of the estimate of a single component, η_ν may also contain the uninteresting signal from the remaining $N_s - 1$ components, plus all kind of contaminants.

The goal is to recover each s_i from the available data, D_ν, while minimizing the contamination from the remaining sources, treated as nuisances.
The angular resolution and frequency coverage of the instrument collecting the data under study are important aspects that have to be taken into account, besides the characterization of its noise. Indeed, ground-based experiments are equipped with large telescopes, which provide high angular resolutions, but their frequency coverage is usually limited to a few channels. Indeed, measurements from the ground are difficult because of the absorption and the emission of radiation at microwave frequencies by the Earth's atmosphere. On the other hand, satellites allow observations at a large number of frequencies, but their telescopes have smaller apertures (thus moderate angular resolutions), mainly because of the limited housing in space vectors.
All the algorithms conceived to address the problem of component separation are designed to exploit at best the advantages provided by the observational configuration in each case. For instance, in deep observations targeting high-redshift objects it is convenient to isolate clusters by means of methods which are typically employed in point source detections. On the contrary, to map the tSZ emission from well-resolved or relatively close objects, techniques used for the extraction of diffuse signals are more suitable.
The methods to perform component separation can be divided in three main categories: (*i*) semi-blind methods (internal linear combinations and matching filters); (*ii*) blind methods (independent component analysis) and (*iii*) parametric methods. In the following, we will synthetically overview all the three typologies, focusing on their application to the extraction of the signal from the tSZ effect. Subsequently, we will focus on a new method combining the sparse and the parametric approach – i.e. a spectral imaging algorithm – which constitutes the core of this work.

Semi-blind methods: internal linear combination and matching filters

The *Internal Linear Combination* (ILC) is a semi-blind technique originally proposed to extract the CMB primary temperature anisotropies using data from the *WMAP* satellite over six frequency bands [35, 151]. This method consists in getting an estimate (denoted with a tilde hereafter) of the map of a specific source component

by writing it as a linear combination of the maps at all available frequencies:

$$\tilde{s}_i = \sum_{\nu}^{N_\nu} w_{i,\nu} D_\nu \ . \tag{3.6}$$

The coefficients $w_{i,\nu}$ used to weight each frequency map are chosen so that they provide unit response with respect to s_i, that is

$$\sum_{\nu}^{N_\nu} w_{i,\nu} A_{\nu i} = 1 \ , \tag{3.7}$$

while, at the same time, they allow the variance $\mathrm{var}(\tilde{s}_i)$ to be minimum. The set of weights which satisfy both these properties can be found via the method of Lagrange multipliers, by solving the system:

$$\begin{cases} \boldsymbol{\nabla} \mathrm{var}(\tilde{s}_i) - \lambda \boldsymbol{\nabla} \mathfrak{g} = 0 \\ \mathfrak{g} = \sum_{\nu}^{N_\nu} w_{i,\nu} A_{\nu i} = 1 \end{cases} \tag{3.8}$$

which has solution:

$$\boldsymbol{w}_i = \frac{\boldsymbol{A}_i^T \mathcal{C}^{-1}}{\boldsymbol{A}_i^T \mathcal{C}^{-1} \boldsymbol{A}_i} \ , \tag{3.9}$$

where $\mathcal{C}^{-1} = \mathrm{cov}^{-1}(D_\nu, D_\mu)$ is the inverse covariance matrix of the data:

$$\mathrm{cov}(D_\nu, D_\mu) = \frac{1}{N_{\mathrm{pix}}} \sum_{k}^{N_{\mathrm{pix}}} (D_\nu - \langle D_\nu \rangle_k)(D_\mu - \langle D_\mu \rangle_k) \ , \tag{3.10}$$

for each couple of frequencies (ν, μ), and being N_{pix} the number of pixels. The $\boldsymbol{A}_i$ vector of equation (3.9) is the column of the mixing matrix encoding the spectral energy density of the i-th source across all frequencies. In the case of CMB, one has $A_{\nu i=\mathrm{CMB}} = 1$ at all frequencies, and the result from [151] is found.
The only two assumptions on which this technique is based, are the absence of correlation between the different source components, and a prior knowledge of their spectral energy density. If the first hypothesis is not fulfilled, though, the final result can be affected by possible biases, especially when considering sources that are strongly concentrated in a given region of the sky (e.g. the Galactic plane) [275]. A further drawback of this method is represented by the fact that it cannot properly account for the different angular resolutions of the frequency channels. Indeed, to compute the linear combination of equation (3.6), all data maps D_ν must have the same angular resolution, which is the lowest one provided by the instrument. This implies the loss of information at the smallest angular scales in the reconstructed map, as usually happens with all pixel-based component separation methods [49].
Since its original proposal, the ILC method has been refined to improve its efficiency in extracting both the CMB [see e.g. 126], and the tSZ signals. In particular, the advent of the *Planck* satellite motivated a series of works aiming at optimizing the ILC technique to map the tSZ effect, like the constrained ILC [369], the *Modified ILC Algorithm*, MILCA [215] (which has been adopted by the *Planck* Collaboration to map the tSZ across the full sky), and the most recent MILCANN, which features

the use of neural networks [214]. The main difference with respect to the original implementation is the addition of further constraints when calculating the weights, aimed at removing contamination from other existing components as much as possible, while maximising the response towards the Comptonization parameter. Further variants of the ILC for the estimate of the tSZ have been proposed to combine both satellite-based and ground-based data, to exploit both a large number of frequency channels and high angular resolutions. A relevant example in this respect is the implementation of the *Needlet ILC* (NILC), which features sparse decomposition [368]. In this method, the localization of the signal in both pixel and multipole space is achieved thanks to the use of particular wavelet bases defined over spherical domains, i.e. needlets [183]. They allow one both to select patches centred on galaxy clusters, and to account for the instrumental beam at different frequencies via a simple multiplication with the signal in the multipole space, instead of a convolution in the pixel space. More recently, a combination of data from *Planck* and ACT for optimal mapping of the tSZ effect has been proposed with both the MILCA method, and a matching-filter approach [6].

Filtering techniques allow the separation of a single component based on a prior knowledge of its spatial distribution, and of the power spectrum of the nuisance signals. *Matched multi-filters* (MMF) represent a generalization of existing filtering techniques for CMB extraction, tailored to separate the tSZ signal from multi-frequency data [197, 198, 281]. Similarly to the result obtained with ILC techniques, the map of the component of interest is estimated from a weighted average of all the available data maps, with the constraint of minimum variance. The weights are here represented by a spatially-variable filter, which accounts for both the spectral dependence of the signal of interest and its spatial distribution. The estimated tSZ signal is therefore given by the convolution:

$$\tilde{s}_{\rm tSZ}(k_0) = \sum_{k}^{N_{\rm pix}} \boldsymbol{\Psi}^T_{r_c}(k - k_0) \cdot \boldsymbol{D}(k), \tag{3.11}$$

where k is an index to identify a generic pixel, k_0 is the pixel corresponding to the cluster centre, and $\boldsymbol{\Psi}_{r_c}$ is the filter vector having N_ν components. It accounts for the cluster scale radius r_c that is a parameter of the spatial distribution of the signal, which is usually assumed to be spherically symmetric. With a suitable tuning of these priors, the filter is *matched* to the the tSZ effect. The frequency dependence is well-defined when assuming a non-relativistic spectrum (see section 2.2.1), and the only feature that has to be set is the spatial modelling, which may be e.g. the projection of a three-dimensional electron density profile following the β-model (see section 2.1.2). The condition of minimum variance of the filter can be conveniently expressed in the Fourier space, via the information on the noise power spectrum:

$$\sigma^2_{r_c} = \sum_{\iota}^{N_{\rm pix}} \hat{s}_i(\iota) \boldsymbol{A}^T_i P^{-1}(\iota) \boldsymbol{A}_i \hat{s}_i(\iota) \tag{3.12}$$

where the index ι labels pixels in the Fourier space, $\hat{s}_i$ is the Fourier transform of s_i, and P is the noise power spectrum matrix, which is defined from:

$$\langle \hat{\eta}_\nu(\iota) \hat{\eta}^*_\mu(\iota') \rangle = P_{\nu\mu} \delta(\iota - \iota') \ , \tag{3.13}$$

where $\hat{\eta}_\nu$ is the Fourier transform of instrumental noise plus nuisance foregrounds at the frequency ν, and δ_D is Dirac delta function. An interesting variant of this kind of methods is based on the use of a Daubechies wavelet filter (see section 3.2.1), under the assumption that clusters are localized, non-Gaussian and non-spherical objects in the sky, which may be easily extracted via sparse filtering [328]. Furthermore, the joint application of matching filters to microwave and X-ray data has been proven to enhance the signal-to-noise ratio of the detection of clusters from all-sky surveys [432, 253, 431]. Generally speaking, algorithms based on MMF are suitable to *detect* clusters of galaxies by means of their tSZ signal, since they give the detection probability from the prior knowledge of the source shape. In fact, filtering methods have been applied to deep surveys delivered by large ground-based telescopes, as SPT and ACT [445, 192, 47]. Clearly, MMFs cannot be used to map the source morphology as probed by the Compton y-parameter from single, well-resolved objects.

Blind methods: independent component analysis

Methods performing a blind source separation do not set any prior modelling of the components contributing to the total signal. In this case, both the mixing matrix A and the source vector $\boldsymbol{s}$ are unknown, and they are determined by only assuming that all the source components are identically distributed, statistically independent and spatially localized. For this reason, these method are often addressed as to *Independent Component Analysis* (ICA). The idea is to solve equation (3.4) by means of a "separation matrix" W, so that $\tilde{\boldsymbol{s}} \propto W\boldsymbol{D}$, while providing the independence of the entries of the $\tilde{\boldsymbol{s}}$ vector. A possible way of imposing such an independence is to set to zero all correlation terms:

$$\frac{1}{N_{\rm pix}} \sum_{k}^{N_{\rm pix}} \tilde{s}_i(k)\ \tilde{s}_j(k) = 0 \quad \text{where } 1 < i \neq j < N_s\ , \tag{3.14}$$

although the symmetry of this condition over pairs of sources (i, j) does not provide a sufficient number of equations to solve the system. To break the symmetry, non-linear correlation can be nullified, imposing e.g.:

$$\frac{1}{N_{\rm pix}} \sum_{k}^{N_{\rm pix}} F(\tilde{s}_i(k))\ \tilde{s}_j(k) = 0\ , \tag{3.15}$$

where F is some non-linear function. Alternatively, it is possible to assume local absence of correlations via a piecewise constant variance, setting:

$$\frac{1}{N_{\rm pix}} \sum_{k}^{N_{\rm pix}} \frac{\tilde{s}_i(k)}{\sigma^2_{ik}}\ \tilde{s}_j(k) = 0\ . \tag{3.16}$$

Relevant examples of this kind of algorithms are the *Joint Approximate Diagonalization of Eigenmatrices* (JADE) [87], and the *Spectral Matching ICA* (SMICA) [125, 88]. The latter assumes mixed stationary Gaussian components, and it has been developed mainly to provide an optimal separation of the CMB, using second-order statistics. JADE, instead, is based on fourth-order statistics and assumes non-Gaussian sources.

Thanks to this feature, this algorithm has been used in a promising procedure to detect galaxy clusters via the tSZ effect. Specifically, the JADE method is applied to the sparse coefficients obtained via a wavelet transform of multi-frequency synthetic data maps. The use of wavelets ensures the localization of the sources of interest, while preserving the characteristics of the mixing matrix [331]. Another improvement in the separation efficiency for CMB and tSZ has been achieved with the *Generalized Morphological Component Analysis* (GMCA) [48]. In this method, all the data are represented through sparse decompositions via non-orthogonal wavelet bases (see section 3.2.1), chosen so that each single component is sparsely represented in one of the bases. The separation is realized by imposing that the number of significant coefficients required to reconstruct the data is minimum.
As in the case of methods based on matched filtering, the major limitation of ICA is the applicability to very localized sources. Moreover, it does not rely on the *known* properties of the components to be separated, which may play a significant role in enhancing reliability and efficiency in reconstructing the signals of interest.

Parametric methods

As opposed to the class of blind and semi-blind detections, parametric methods require the modelling of *all* the source components. With this approach, the latter are treated as *parameters* to be estimated via the maximisation of either the spatial entropy or the likelihood.

In the context of information theory, entropy measures how much information is contained in a probability distribution [406]. Given a set of N values of a continuous random variable X, the best guess for its probability distribution $\mathcal{P}(X)$, is the least informative one which maximises the entropy of the variable, defined as

$$S(X) = -\int_{-\infty}^{\infty} \mathcal{P}(X') \ln \mathcal{P}(X') \, dX' \, . \tag{3.17}$$

In the opposite case, i.e. when the outcome of the distribution is certain, the optimal choice is the one which minimizes entropy. If only some prior information is known, it is possible to maximise entropy with the constraints given by the additional knowledge about the probability distribution. For instance, if the mean and the variance are known, then the Gaussian distribution is naturally picked by the principle of maximum entropy. It is worth noting that Gaussianity is a valid assumption for the CMB component, and in this limit the condition of maximum entropy corresponds to the technique of Wiener filtering [see 466] to solve the linear system of equation (3.4) [275].
In a Bayesian approach [439], the X variable represents a parameter of the model, so that the probability distribution $\mathcal{P}(X)$ may be taken as the prior for that parameter. The *Maximum Entropy Method* (MEM) proposed to solve the component separation problem is indeed based on this choice [202]. Ideally, to access the prior distribution of the sources, one should measure the empirical distribution of temperature fluctuations they induce over a set of different realizations. Since this is not feasible, it is possible to pick an entropic prior with the only requirement of subset independence, coordinate invariance and system independence. In [421] the above approach has

been extended to map the all-sky signal in harmonic space. Despite they provide a better reconstruction of non-Gaussian signals with respect to e.g. Wiener filters, MEM-based procedures may not be completely physically motivated, and they do not properly take into account the effects arising from the components being non-stationary.

In a similar way, one may estimate the source component $\tilde{s}_i$ as

$$\tilde{s}_i = \underset{s_i}{\mathrm{argmax}}(\mathcal{L}) \ , \tag{3.18}$$

where $\mathcal{L}$ is the likelihood function, which is related to a chi-square statistics for a Gaussian process via:

$$\mathcal{L} = \exp\left(-\frac{\chi^2}{2}\right) \ , \tag{3.19}$$

being χ^2 is the usual sum of the squared residuals weighted by the covariance of the data. This kind of approach has been demonstrated to be particularly robust for the separation of diffuse components [see e.g. 337, 280]. Examples of applications to the detection of the tSZ towards clusters include parameter estimates in a Bayesian fashion through a sampling from the posterior distribution [273, 163, 132], or via least-squares minimization [234].

In the above paragraphs, we provided a short review of the existing methods for disentangling the signal from multiple sources contributing to a set of frequency maps. It is clear that the choice of a given technique is driven by each specific application. In this context, it is worth mentioning a couple of comparison projects focusing on several component separation algorithms. For instance, [257] details a component separation challenge to extract the CMB, Galactic, tSZ and point source signals from *Planck* data. An interesting similar work focusing on the production of an all-sky cluster catalogue based on the extraction of the tSZ effect only is reported in [282]. Here a series of non-parametric methods are tested, i.e.: several variants of the ILC; a number of different MMF; a semi-blind, Bayesian technique [135]; the PowellSnakes filtering algorithm for Bayesian point source detection [95, 96] and GMCA. The main outcome of this project from a comparison of the relative yields of all methods, is that they all give consistent results, and they offer promising optimization perspectives, in the context of observations at moderate angular resolutions as in the case of *Planck*.

3.2 Sparse representations

A common operation to extract information from a signal (which may be a sequence of data over time, or a two-dimensional image), is to decompose it to extract e.g. its frequency content. In this respect, the most known and used method is undoubtedly the Fourier transform [see e.g. 70]. It consists in projecting a given signal characterized by some level of periodicity onto orthonormal bases of sines and cosines. Referring to a signal $f(x)$ defined over a spatial domain:

$$\hat{f}(\xi) = \int_{-\infty}^{\infty} f(x) \ e^{-i\xi x} dx \ , \tag{3.20}$$

where $\xi = 2\pi/x$ is the spatial frequency. The major limitation of the Fourier transform is that it cannot provide spatial localization, since the basis sines and cosines extend in space up to infinity. Therefore, all information about *where* a certain frequency component is dominating the signal is necessarily lost when the transform is computed.

To provide localization in both space and spatial frequency, Gábor first introduced the concept of *windowed* Fourier transforms, which are obtained by multiplying the Fourier basis functions with a filter centred at a given position b, $G(b-x)$ [169]. In this way, one obtains a Gábor transform:

$$\hat{f}_G(\xi, b) = \int_{-\infty}^{\infty} f(x)\ G^*(b-x)\ e^{-i\xi x} dx\ , \tag{3.21}$$

where * denotes the complex conjugation. It can be clearly seen that the effect of the filter, G, is that of localizing the transform by translating the Fourier kernel, to pick up a only certain window among the overall spatial extension of the signal. Despite it provides a basic way of localizing the signal both in space and in spatial frequency, the Gábor transform (also known as "short-time Fourier transform") suffers from the consequences of using a fixed spatial windowing. Indeed, all information encoded in scales larger than the characteristic size of the filter G is completely lost, whereas setting a large filter size corresponds to losing spatial resolution. On the other hand, it is not possible to simultaneously localize information with high-resolution in terms of both space and spatial frequency, consistently with Heisenberg's uncertainty principle [194]. A way of solving this issue, is to generalize Gábor transform allowing the size of the spatial window to vary, while shifting the kernel over different positions.

3.2.1 Wavelets

The introduction of wavelets might be attributed a posteriori to Haar, who defined the orthogonal bases of multi-scale step-like functions which carry his name in 1909. The first rigorous mathematical treatment has been then proposed by Grossmann and Morlet in the early 1980s [352]. Since then the use of wavelets in signal processing increased significantly in a broad range of disciplines, including astronomy. Indeed, they provide localization in both space and frequency domain in a natural way, since this feature is encoded in their own mathematical definition.
A wavelet (from the French word *ondelette*, which means "small wave"), is a continuous function whose dilations and translations constitute an orthonormal basis in the $L^2(\mathbb{R})$ space [182]. A generic wavelet can be written as follows:

$$\psi_{u,b}(x) = \frac{1}{\sqrt{u}}\ \psi\left(\frac{x-b}{u}\right) \tag{3.22}$$

where x represents the spatial coordinate, while u and b are two characteristic parameters. Specifically, u is the *scale* parameter, which is a positive factor giving the compression or expansion of the wavelet, while b is the *position* parameter which quantifies its translation. It is common to refer to $\psi_{1,0}(x)$ as to the *mother wavelet*, that is not rescaled nor translated. An example of wavelet function with some sets of u and b parameters is illustrated in Figure 3.3.
Unlike Fourier basis functions, wavelets are not unique and several families of such

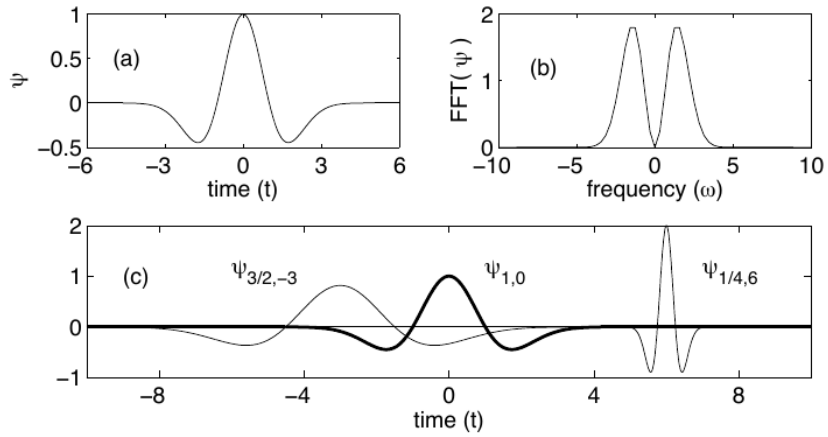

Figure 3.3. Example of wavelet function in the time-frequency domain. **(a)** Mexican hat wavelet. **(b)** Fourier transform of the Mexican hat wavelet. **(c)** A couple of examples showing scaling and translation [taken from 250].

functions exist and can be built in many ways. For instance, Morlet's wavalets are obtained similarly to the kernels of the Gábor transform, i.e. by multiplying Fourier basis functions by suitable filters. Another possibility is to compute subsequent convolutions of step functions with themselves, as in the case of spline wavelets [420]. A gallery of different wavelet families with their definition is shown in Figure 3.4.

However defined, wavelets have to satisfy three main properties:

i. normalization: $\int_{-\infty}^{\infty} \psi_{u,b}(x)\psi^*_{u,b}(x)\ dx = 1$;

ii. zero average: $\int_{-\infty}^{\infty} \psi_{u,b}(x)\ dx = 0$;

iii. compact support: this is equivalent to require localization in both space and spatial frequency domains, according to Heisenberg's uncertainty principle.

A common choice of the wavelet parameters which ensures the properties listed above, is the *dyadic* scheme, in which the scale and position parameters are respectively set to:

$$u = 2^j \ ; \tag{3.23}$$

$$b = 2^j n \ , \tag{3.24}$$

with $j, n \in \mathbb{Z}$. In this scheme the wavelet function can be rewritten as

$$\psi_{j,n}(x) = 2^{-j/2}\ \psi(2^{-j}x - n) \ , \tag{3.25}$$

where 2^{-j} is called *resolution* (that is the inverse of the scale), and the index j is referred as to the resolution level.

The localization of a wavelet in space and frequency can be quantified by computing the second-order moments of the wavelet $\psi_{u,b}(x)$, and of its Fourier transform,

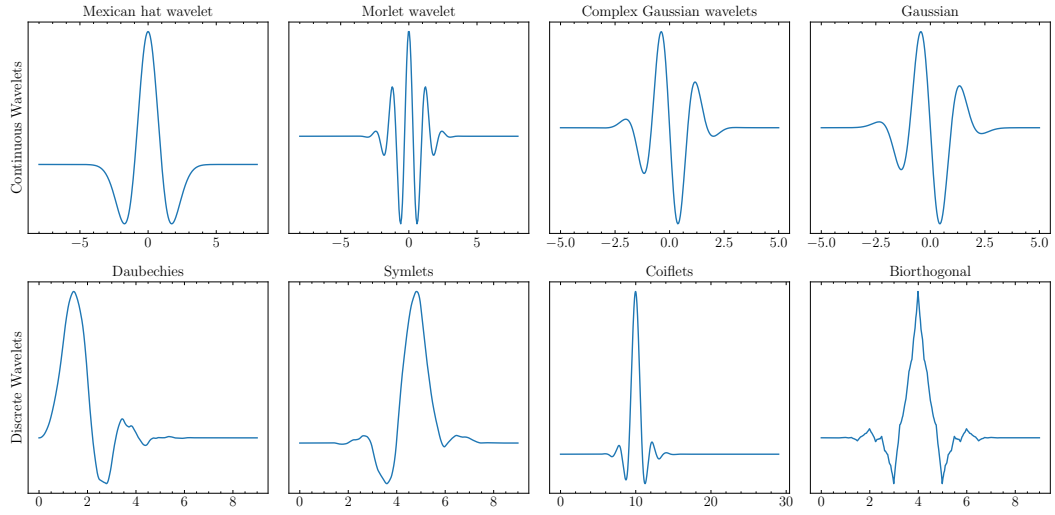

Figure 3.4. Examples of different families of continuous (top panels) and discrete wavelets (bottom panels) obtained using the `pywavelets` python package, available at https://pypi.org/project/PyWavelets/.

$\hat{\psi}_{u,b}(\xi)$, respectively [250]:

$$\sigma_x = \int_{-\infty}^{\infty} (x - \langle x \rangle)^2 \ |\psi_{u,b}(x)|^2 dx \ ; \tag{3.26}$$

$$\sigma_\xi = \int_{-\infty}^{\infty} (\xi - \langle \xi \rangle)^2 \ |\hat{\psi}_{u,b}(\xi)|^2 d\xi \ , \tag{3.27}$$

being:

$$\hat{\psi}_{u,b}(\xi) = \frac{1}{\sqrt{u}} \int_{-\infty}^{\infty} \psi \left(\frac{x-b}{u} \right) \ e^{-i\xi x} \ dx \ . \tag{3.28}$$

Equation (3.28) can be rewritten as

$$\hat{\psi}_{u,b}(\xi) = \sqrt{u} \ \hat{\psi}(u\xi) \ e^{-i\xi b} \ , \tag{3.29}$$

which implies that any rescaling of ψ by a factor of u^{-1} in the spatial domain corresponds to a scaling by a factor of u in the frequency domain. In dyadic terms, if the wavelet gets spatially dilated by 2^j, then the frequency will be shrank by 2^{-j}. From equation (3.27) it is clear that, to ensure frequency localization, the Fourier transform of the wavelet function must remain finite. This is encoded in the fulfilment of the following admissibility condition:

$$\int_{-\infty}^{\infty} \frac{|\hat{\psi}_{u,b}(\xi)|^2}{|\xi|} \ d\xi < \infty \ . \tag{3.30}$$

The localization properties of wavelet bases can be visually represented by means of Heisenberg's diagrams, as shown in Figure 3.5. Each series of rectangles represents a resolution level. The analysis of the signal is performed starting from low spatial resolution, i.e. accounting for all the spatial domain. This corresponds to computing a Fourier transform, therefore the frequency resolution is high. Subsequently, the

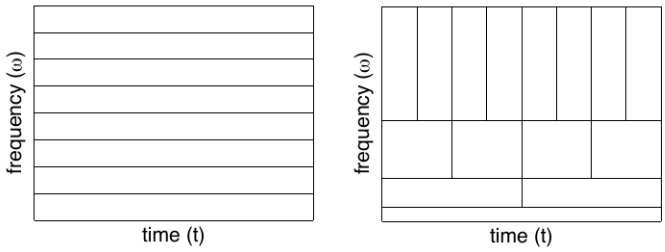

Figure 3.5. Localization properties of Fourier (left panel) and wavelet bases (right panel) in terms of time and frequency resolutions (the same reasoning holds for the spatial coordinate x and the spatial frequency ξ). The area of all boxes is constant, to ensure the validity of Heisenbergs' uncertainty principle [adapted from 250].

spatial domain is divided into two sub-domains, which is equivalent to increasing the spatial resolution by a factor of two. The corresponding frequency resolution, which is the height of the box one has just constructed, gets reduced by the same factor, to fulfil he uncertainty principle. The same reasoning applies to all subsequent detail levels, with increasing powers of 2. Here the substantial difference between wavelet and Fourier transforms becomes evident: indeed, in Fourier transforms one always picks up all the spatial domain, as only the frequency domain gets binned with fixed resolution, and all resolution boxes are equal.

3.2.2 The wavelet transform and multi-resolution analysis

Similarly to performing a Fourier decomposition, any signal $f(x)$ can be represented by means of its wavelet transform, provided the orthogonality of the basis functions. The projection of $f(x)$ onto a wavelet basis $\psi_{u,b}(x)$ defines its wavelet coefficients:

$$a_{u,b} = \langle f(x), \psi_{u,b}(x) \rangle = \int_{-\infty}^{\infty} f(x)\ \psi^*_{u,b}(x)\ dx\ , \tag{3.31}$$

where brackets represent the inner product. The wavelet coefficients recombined together provide, for discretized values of u and b:

$$\hat{f}_w(x) = \sum_{u=0}^{\infty} \sum_{b=-\infty}^{\infty} a_{u,b}\ \psi_{u,b}(x) \tag{3.32}$$

that is the discrete *wavelet transform* of $f(x)$.
The inverse wavelet transform allows the reconstruction of the function $f(x)$ knowing its wavelet coefficients, as [182]:

$$f(x) = \frac{1}{C_\psi} \int_0^{\infty} \int_{-\infty}^{\infty} a_{u,b}\ \psi_{u,b}(x)\ \frac{db\ du}{u^2}\ , \tag{3.33}$$

being:

$$C_\psi = \int_0^{\infty} \frac{\hat{\psi}^*(\xi)\hat{\psi}(\xi)}{\xi}\ d\xi\ . \tag{3.34}$$

By adopting a dyadic sampling, and plugging equation (3.25) into equations (3.31) and (3.32), one has, respectively:

$$a_{j,n} = 2^{-j/2} \int_{-\infty}^{\infty} f(x)\ \psi^*(2^{-j}x - n)\ dx\ , \tag{3.35}$$

for the wavelet coefficients, and:

$$\hat{f}_w(x) = 2^{-j/2} \sum_{j=-\infty}^{\infty} \sum_{n=-\infty}^{\infty} a_{j,n}\ \psi(2^{-j}x - n) \tag{3.36}$$

for the wavelet transform of $f(x)$.

The decomposition in equation (3.36) is equivalent to perform a multi-resolution analysis of the signal. Indeed, starting from an arbitrary low resolution, 2^{-j_0}, corresponding to the largest scale accessible from the data, the wavelet transform can be separated into an approximation term, encoding the information of the signal at the scale 2^{j_0}, plus a term giving the decomposition over the remaining smaller scales. The latter term is provided by the dyadic sampling of spatial scales, and it contains all the information on the details of the signal.
In mathematical terms, multi-resolution analysis involves a set of embedded sub-spaces $\{V_j\}$ in $L^2(\mathbb{R})$ such that the following properties are satisfied [270, 290]:

- sub-spaces at each level of resolution are included in the successive higher-resolution levels:

$$V_{j+N} \subset \cdots \subset V_{j+1} \subset V_j \subset V_{j-1} \subset \cdots \subset V_{j-N} \qquad \forall j \in \mathbb{Z}\ , \tag{3.37}$$

  going from low to high resolution;

- the union of all sub-spaces is the whole $L^2(\mathbb{R})$:

$$\bigcup_{j=-\infty}^{\infty} V_j = L^2(\mathbb{R}) \tag{3.38}$$

- the intersection of all sub-spaces is the null set:

$$\bigcap_{j=-\infty}^{\infty} V_j = \{0\}\ ; \tag{3.39}$$

- functions defined in each subspace pick a specific spatial resolution according to the following rule:

$$f(x) \in V_j \Leftrightarrow f(2^{-1}x) \in V_{j+1}\ , \tag{3.40}$$

  i.e. the spatial frequency is higher by a factor of 2 when increasing the resolution (or lowering the scale) between two subsequent levels;

- all sub-spaces are invariant by any translation proportional to the scale 2^j:

$$f(x) \in V_j \Leftrightarrow f(x - 2^j n) \in V_j\ ; \tag{3.41}$$

- existence of the scaling function ϕ which is an orthonormal basis of the subset V_{j_0} at the approximation scale 2^{j_0}.

Given the dual (orthogonal) sub-space W_j for V_j, the wavelet function ψ_j is a basis function for W_j. In particular, since the subspace V_{j+1} is contained in V_j by means of the causality property of equation (3.37), it is possible to write:

$$V_j = V_{j+1} \oplus W_{j+1} \ . \tag{3.42}$$

This yields a scaling equation connecting the basis functions of V (i.e. the scaling functions, ϕ), with the basis functions of W (i.e. the wavelet functions, ψ).
Referring to the cases of $j = 0$ and $j = 1$ as the highest and lowest resolutions, respectively, one has $V_1 \subset V_0$, therefore $V_0 = V_1 + W_1$. Thus, it is possible to write the scaling function $2^{-1/2}\phi(2^{-1}x)$ in V_1 (with $n = 0$) as a linear combination of the bases for V_0, $\phi(x - n)$, across all translations, as

$$2^{-1/2}\phi(2^{-1}x) = \sum_{n=-\infty}^{\infty} h[n]\ \phi(x - n) \ , \tag{3.43}$$

where the coefficients, $h[n]$, are given by:

$$h[n] = \langle 2^{-1/2}\phi(2^{-1}x), \phi(x - n)\rangle \ , \tag{3.44}$$

which are basically orthogonal projectors corresponding to a low-pass filtering.
By virtue of equation (3.42), a similar decomposition holds for the wavelet basis function $2^{-1/2}\psi(2^{-1}x)$ of W_1, in terms of the basis functions of V_0, so that:

$$2^{-1/2}\psi(2^{-1}x) = \sum_{n=-\infty}^{\infty} g[n]\ \phi(x - n) \ , \tag{3.45}$$

where now:

$$g[n] = \langle 2^{-1/2}\psi(2^{-1}x), \phi(x - n)\rangle \ , \tag{3.46}$$

which is interpreted as a high-pass filter.
Equations (3.43) and (3.45) relate bases across different resolutions. The corresponding Fourier transforms are:

$$\hat{\phi}(2\xi) = 2^{-1/2}\ \hat{h}(\xi)\hat{\phi}(\xi) \tag{3.47}$$

for the scaling function, and:

$$\hat{\psi}(2\xi) = 2^{-1/2}\ \hat{g}(\xi)\hat{\phi}(\xi) \ , \tag{3.48}$$

for the wavelet function, respectively.

By virtue of the above scaling relations, the decomposition of any function $f(x)$ at the given resolution level $j - 1$ can be expressed as the sum of its approximation and detail coefficients at the successive lower-resolution level j. Specifically, the approximation coefficients are given by the projection of $f(x)$ onto the bases of V_j, while detail coefficients are given by its projection onto the bases of W_j. Therefore, the wavelet transform of equation (3.36) in terms of multi-resolution analysis reads:

$$\hat{f}_w(x) = \hat{f}_{w,\mathrm{approx}}(x) + \hat{f}_{w,\mathrm{detail}}(x) \ . \tag{3.49}$$

Since the number of scales that can be accessed in the decomposition is limited by the largest (smallest) spatial scale (resolution) imposed by the signal itself, one has:

$$\hat{f}_{w,\text{approx}}(x) = \sum_{n=-\infty}^{\infty} \bar{a}_{j_0,n}\ \phi_{j_0,n}(x)\ ; \tag{3.50}$$

$$\hat{f}_{w,\text{detail}}(x) = \sum_{j=j_0}^{N_{\text{scales}}} \sum_{n=-\infty}^{\infty} a_{j,n}\ \psi_{j,n}(x)\ , \tag{3.51}$$

where the approximation and detail coefficients are respectively given by:

$$\bar{a}_{j_0,n} = \int_{-\infty}^{\infty} f(x)\ \phi^*_{j_0,n}(x)\ dx\ ; \tag{3.52}$$

$$a_{j,n} = \int_{-\infty}^{\infty} f(x)\ \psi^*_{j,n}(x)\ dx\ . \tag{3.53}$$

All the above considerations are valid also when applied to multi-dimensional signals, e.g. images. In this case the decomposition is performed via a projection of the signal onto the four-dimensional space $L^2(\mathbb{R}^2)$ [65]. This corresponds to computing the approximation and detail coefficients along rows first, then on columns. The formalism of multi-resolution analysis can be extended by defining two-dimensional and separable sub-spaces V_j^2 in two dimensions, at each resolution level, j. Such sub-spaces are constructed from the tensor product of one-dimensional sub-spaces, as

$$V_j^2 = V_j \otimes V_j\ . \tag{3.54}$$

Therefore, the detail subs-spaces W_j^2 are the orthogonal complements of V_j^2 so that one has:

$$V_{j-1}^2 = V_j^2 \oplus W_j^2\ . \tag{3.55}$$

Recalling the complementarity between one-dimensional sub-spaces given in equation (3.42), it is possible to rewrite equation (3.55) as

$$\begin{aligned} V_j^2 \oplus W_j^2 &= V_{j-1} \otimes V_{j-1} \\ &= (V_j \oplus W_j) \otimes (V_j \oplus W_j) \\ &= V_j^2 \oplus (V_j \otimes W_j) \oplus (W_j \otimes V_j) \oplus (W_j \otimes W_j) \end{aligned} \tag{3.56}$$

which yields:

$$W_j^2 = (V_j \otimes W_j) \oplus (W_j \otimes V_j) \oplus (W_j \otimes W_j)\ . \tag{3.57}$$

Therefore, the two-dimensional wavelet sub-space W_j^2 is defined by the direct summation of three sub-spaces, whose bases are generated by the three wavelet functions $\psi^H_{j,k,l}$, $\psi^V_{j,k,l}$ and $\psi^D_{j,k,l}$ with translation indices $k, l \in \mathbb{Z}^2$, constructed from the corresponding one-dimensional bases $\phi_{j,n}$ and $\psi_{j,n}$ with $n \in \mathbb{Z}$ of V_j and W_j, respectively. Specifically, one has:

$$\psi^H_{j,k,l}(k,l) = \phi_{j,k}(k)\ \psi_{j,l}(l) \tag{3.58}$$

$$\psi^V_{j,k,l}(k,l) = \psi_{j,k}(k)\ \phi_{j,l}(l) \tag{3.59}$$

$$\psi^D_{j,k,l}(k,l) = \psi_{j,k}(k)\ \psi_{j,l}(l)\ . \tag{3.60}$$

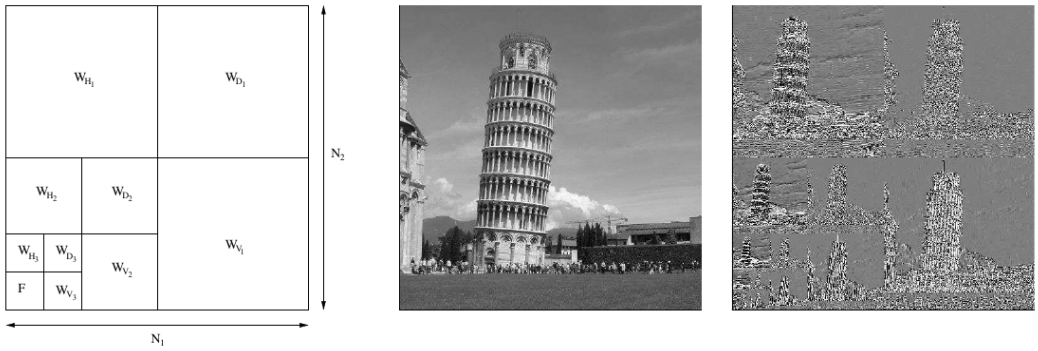

Figure 3.6. Example of wavelet transform computed over three scales on an image of size $N_1 \times N_2$ using an orthonormal basis. **Left panel.** Schematic decomposition of the image into its detail levels at all the three scales along the horizontal, vertical and diagonal directions, W_H, W_V and W_A, respectively. The approximation level is denoted as F, and it is obtained from the low-pass filtering. **Middle panel.** Original image. **Right panel.** Maps of the wavelet coefficients according to the same scheme as in the left panel [taken from 65].

The wavelets $\psi^H_{j,k,l}$ and $\psi^V_{j,k,l}$ associated with the sub-spaces $(V_j \otimes W_j)$ and $(W_j \otimes V_j)$, behave as high-pass filters oriented along the horizontal and vertical axes of the image, respectively (hence the superscripts). The wavelet $\psi^D_{j,k,l}$ associated with the $(W_j \otimes W_j)$ sub-space, instead, encodes the details of the image from a high-pass filtering along the diagonal direction, according to the behaviour of the corresponding one-dimensional wavelet $\psi_{j,n}$ under parity. By adding the fourth basis of the V_j^2 sub-space, given by $\phi^A_{j,k,l}(k,l) = \phi_{j,k}(k)\ \phi_{j,l}(l)$, which corresponds to the approximation details, one can define a complete wavelet transform of an image in two dimensions. The scaling function $\phi^A_{j,k,l}(k,l)$ corresponds to a low-pass filtering of the image, which is a smoothing at the lowest resolution 2^{j_0}. An example of successive decompositions at all resolution levels obtained from a wavelet transform in two dimensions applied to an image is shown in Figure 3.6. As a consequence of the orthogonality of wavelet bases, the coefficients computed at different scales are complementary, that is to say that the loss of information encoded in the detail coefficients at lower resolutions, is compensated by a reduction of the size of the image by a factor of 2 at each level of increasing resolution. Therefore, if the processed image has size $N_1 \times N_2$, the detail coefficients at the scale 2^{-j} are contained in an image having size $N_1/2^j \times N_2/2^j$.

If non-orthogonal bases are used, the coefficients are no longer complementary, so they can be represented on maps having the same size of the original image. In this case, the wavelet basis is classified as *redundant*. An example of such a decomposition is shown in Figure 3.7, where the three detail spaces of the multi-resolution algorithm are expanded into bi-orthogonal bases, following the procedure by Coifman & Donoho [108]. On the other hand, the use of isotropic wavelets such as the cubic spline (see Figure 3.16a), allow the construction of redundant bases with only one detail space. In other words, only one detail component is computed at each scale, instead of the three sets of details along the horizontal, vertical and diagonal directions. Such bases are employed in the so-called *à trous* (i.e. "with holes") algorithms [see e.g. 420]. By applying these algorithms, one has a $N_1 \times N_2$-sized

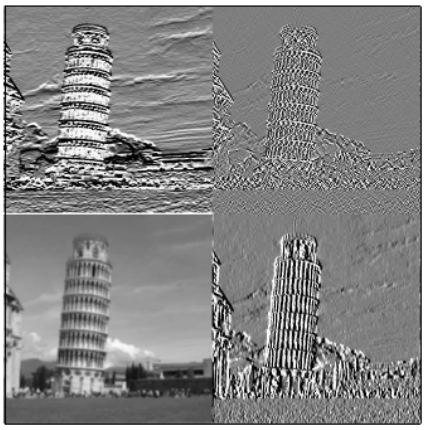

Figure 3.7. Example of wavelet transform computed over three scales on an image of size $N_1 \times N_2$ using a redundant, non-orthogonal basis. The input image is the same as in the middle panel of Figure 3.6. In this case, the top left, top right and bottom right panels represent the isotropic detail coefficients at the three resolution scales, while the bottom left panel shows the approximation coefficients. All the maps have the same size of the transformed image, $N_1 \times N_2$ [adapted from 65].

map of detail coefficients at each decomposition scale, plus a so-called *last smooth* image given by the approximation level, which consists in a low-pass filtering of the original input image.
Contrarily to classical wavelet bases, redundant wavelets are shift-invariant. This feature is very important for the application of wavelet transforms to astronomical images; thus it motivates us to use a B_3 spline à trous algorithm for the imaging purposes of this work. In this respect, Figures 3.22a and 3.22b show the last smooth image and the wavelet coefficients, respectively, for the tSZ map of a cluster of galaxies that we obtained with the aforementioned algorithm.

3.2.3 Signal denoising via wavelet transforms

The most important purposes of wavelet transforms in signal processing are compression and denoising. Indeed, given the localization properties of such a transform, the relevant information from the signal is contained in a few, large coefficients which occur where the signal shows significant spatial variations. In this sense, wavelet coefficients are sparse, i.e. they are mostly zeros, except where the correlation with the given wavelet is significant. This property can be used to compress the signal, or to clean it from noise, upon the choice of a suitable wavelet basis for the decomposition. In particular, wavelet denoising is a technique which is widely used in astronomy.
Noise is expected to provide contribution only at the highest frequencies, and to be characterized by slower variations compared to the signal across different spatial scales. Consequently, it is poorly correlated with the wavelet basis, so that its wavelet coefficients are not localized and they have a small amplitude. Hence, by discarding the coefficient values below a chosen significance threshold, it is possible

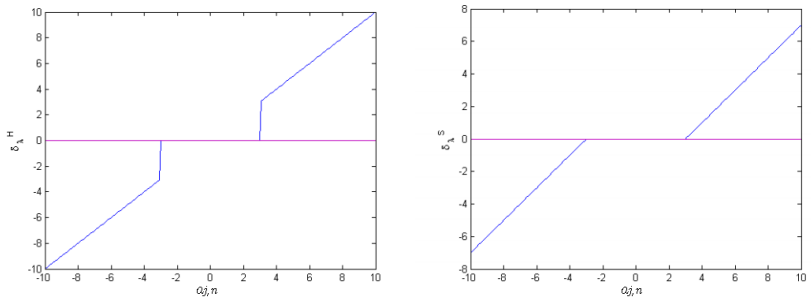

Figure 3.8. Schematic representation of hard (left panel) and soft (right panel) thresholding of detail wavelet coefficients. The quantity $\delta_\lambda^{H,S}$ on the y axis represents the thresholded coefficient. The threshold value is set to $\lambda = 3$ in this example [adapted from 107].

to remove the contribution from noise at each resolution level. The denoised signal can then be reconstructed via its wavelet transform, by keeping only the thresholded (i.e. significant) coefficients in the reconstruction. The level of the threshold is typically determined from the statistics of the coefficients themselves, and it may be e.g. a multiple of their variance. In the case of signals characterized by spatially correlated noise, thresholds are tabulated at each specific position accounting for the data covariance matrix. More generally, the threshold value λ depends on the resolution level j.

The thresholding of wavelet coefficients can be made according to two criteria, named *soft* and *hard* thresholding. In the case of hard thresholding, the coefficients are set to zero if their absolute value is lower than the threshold, λ_j, i.e.:

$$a_{j,n}^H = \begin{cases} 0 & \text{if} \quad |a_{j,n}| \leq \lambda_j \\ a_{j,n} & \text{if} \quad |a_{j,n}| > \lambda_j \ . \end{cases} \tag{3.61}$$

If a soft thresholding is applied, instead, the condition for discarding the coefficients becomes:

$$a_{j,n}^S = \begin{cases} 0 & \text{if} \quad |a_{j,n}| \leq \lambda_j \\ a_{j,n} - \lambda_j & \text{if} \quad a_{j,n} > \lambda_j \\ a_{j,n} + \lambda_j & \text{if} \quad a_{j,n} < -\lambda_j \ . \end{cases} \tag{3.62}$$

A representation of the two different thresholding schemes is illustrated in Figure 3.8. The choice of the most suitable scheme depends on the specific application. Hard thresholding has the advantage of preserving the flux, but it is more prone to introduce discontinuties and abrupt changes in the final reconstruction. On the contrary, soft thresholding allows the removal of artefacts and discontinuities in a smoother way, provided they are consistent with zero.

3.2.4 Ridgelet and curvelet transforms

Candès & Donoho argued in the early 2000s that elongated and anisotropic structures in two-dimensional images are not efficiently detected by wavelets, since they are not sensitive to any particular direction. Indeed, wavelet transforms are computed from nearly isotropic means of neighbouring pixel values, therefore they do not

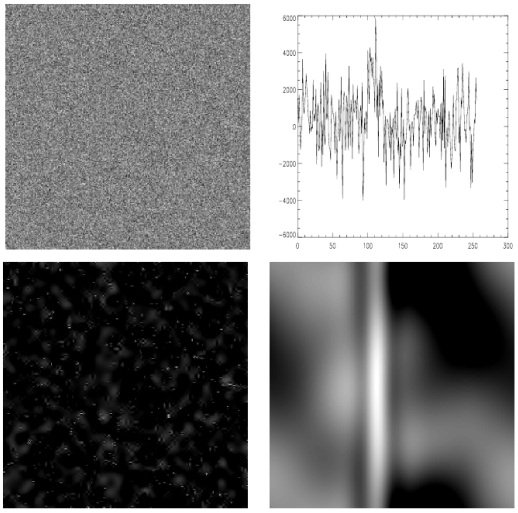

Figure 3.9. Example illustrating the comparison between wavelet and curvelet reconstruction of an image featuring a stripe embedded in noise. **Top left panel.** Input image, where the stripe is completely hidden by the noise. **Top right panel.** Average of the same image computed along columns. **Bottom left panel.** Reconstruction from the thresholding of wavelet coefficients. **Bottom right panel.** Reconstruction of the signal from the thresholding of ridgelet coefficients [taken from 419].

correlate well with e.g. linearly-shaped patterns. On the other hand, if directional generalization of wavelet bases are used, like *ridgelets* and *curvelets*, signals with anisotropic features are characterized by a higher number of sparse coefficients with respect to wavelet decomposition [83].

Figure 3.9 shows an example which testifies the inadequacy of wavelets in detecting linear structures. Although it cannot be seen by eye, the signal in the input image in the upper left panel contains a vertical stripe, here completely dominated by noise. The images in bottom panels highlight that the reconstruction from wavelet transform (left panel) is not able to detect the stripe in the signal which, on the contrary, is efficiently recovered with ridgelets (right panel). On the other hand, the one-dimensional profile of the signal in the image taken from averages along columns, provides a hint for the presence of such a structure (upper right panel). In fact, the underlying idea in ridgelet transforms is to compute the average of the signal along lines, by exploring all possible directions and positions.

Ridgelets are bivariate functions defined in $L(\mathbb{R}^2)$ which represent a higher-dimensional generalization of wavelets. Indeed, they are described by a third parameter, which is the angle giving the *direction* of the function. Taking a sufficiently decaying, normalized, zero-averaged wavelet, ψ, which satisfies the admissibility condition of equation (3.30), then for each set of parameters $u > 0$ (scale), $b \in \mathbb{R}$ (translation) and $\theta \in [0, 2\pi)$ (direction), one can define a ridgelet as [80, 81]:

$$\psi_{u,b,\theta}(x) = \frac{1}{\sqrt{u}}\, \psi\left(\frac{x_1 \cos\theta + x_2 \sin\theta - b}{u}\right) , \tag{3.63}$$

where x is the modulus of the two-dimensional vector $\boldsymbol{x} = (x_1, x_2)$. Equation (3.63)

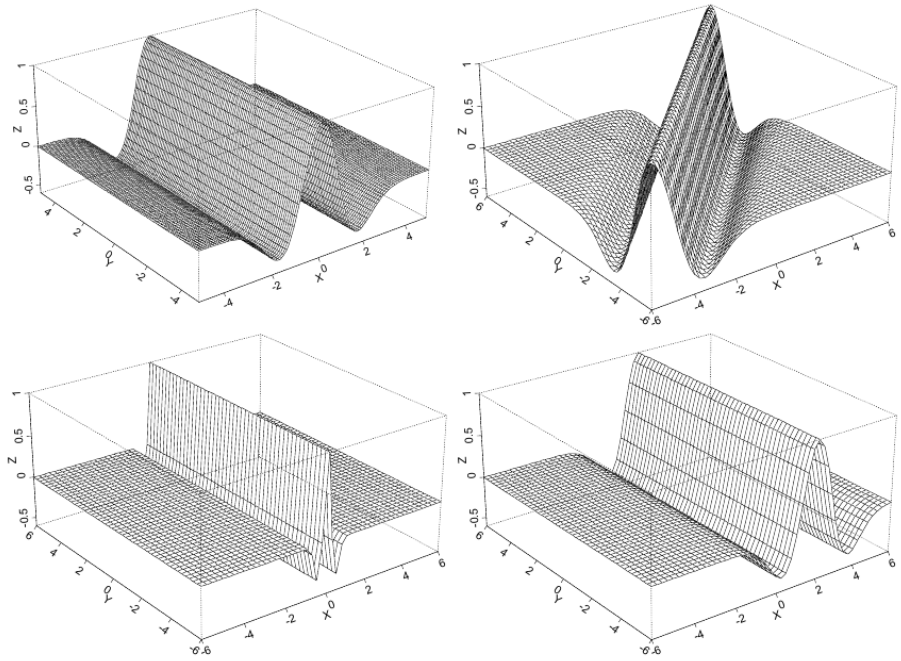

Figure 3.10. Examples of ridgelets. Functions represented in the top right, bottom left and bottom right panels are obtained from rotation, rescaling and shifting of the top left ridgelet, respectively [taken from 419].

in the dyadic scheme (see equations (3.23) and (3.24)) becomes:

$$\psi_{j,n,\theta}(x) = 2^{-j/2}\ \psi\left(2^{-j}(x_1\cos\theta + x_2\sin\theta) - n\right)\ . \tag{3.64}$$

Such a function is constant along ridge lines, $x_1\cos\theta + x_2\sin\theta$, while it is a wavelet transversely to the ridges, hence the name. This property can be seen in Figure 3.10, showing a few examples of ridgelets.

The ridgelet coefficients of a function $f(x)$ are given by:

$$\varrho_{u,b,\theta} = \int_{-\infty}^{\infty} f(x)\ \psi^*_{u,b,\theta}(x)\ d^2x\ , \tag{3.65}$$

and the continuous ridgelet transform is given by the exact reconstruction formula:

$$f(x) = \int_0^{2\pi}\int_0^{\infty}\int_{-\infty}^{\infty} \varrho_{u,b,\theta}\ \psi_{u,b,\theta}(x)\ \frac{du}{u^3}\ db\ \frac{d\theta}{4\pi}\ . \tag{3.66}$$

Ridgelet transforms are the equivalent of wavelet transforms in the Radon domain [see e.g. 124, for a discussion on Radon transforms]. Indeed, the Radon transform, $\hat{f}_R$, of a function f is a collection of line integrals labelled via the angle and translation parameters, $(\theta, t) \in [0, 2\pi) \times \mathbb{R}$, such that:

$$\hat{f}_R(x) = \int_{-\infty}^{\infty}\int_{-\infty}^{\infty} f(x_1, x_2)\ \delta(x_1\cos\theta + x_2\sin\theta - t)\ dx_1 dx_2 \tag{3.67}$$

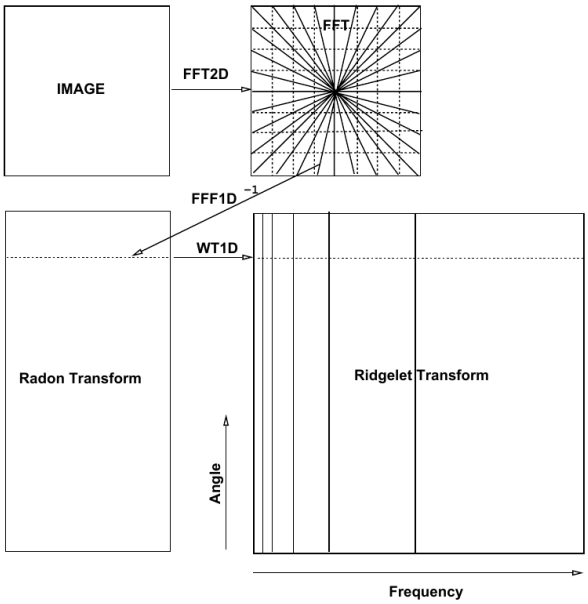

Figure 3.11. Flowgraph of a ridgelet transform [taken from 418].

where δ_D is the Dirac delta function. From equations (3.63), (3.65) and (3.67), the ridgelet coefficients can be thus written as

$$\varrho_{u,b,\theta} = \int_{-\infty}^{\infty} \hat{f}_R(x)\ u^{-1/2}\psi^*\left(\frac{t-b}{u}\right)\ dt\ . \tag{3.68}$$

In other words, the ridgelet transform is equivalent to a one-dimensional wavelet transform applied to the slices of a Radon transform at a fixed angle θ and varying translation. This property allows one to exploit the fact that the Radon transform is equivalent to computing the inverse one-dimensional Fourier transform to the coefficients of a two-dimensional Fourier transform restricted along radial lines passing through the origin of the frequency plane. Mathematically this can be expressed as the projection-slice formula:

$$\hat{f}(\alpha\cos\theta, \alpha\sin\theta) = \int_{-\infty}^{\infty} \hat{f}_R(x)\ e^{-i\alpha t}\ dt\ ; \tag{3.69}$$

for any projection angle α. Therefore, discrete ridgelet transforms can be implemented via Radon transforms in the Fourier domain. The steps are illustrated by the scheme in Figure 3.11, and they are synthetically described in the following [418].

i. The image is first processed via a two-dimensional Fourier transform, whose coefficients are interpolated along radial straight lines passing through the centre of the frequency plane, in number equal to the selected projections. The slope of each line equals the projection angle α;

ii. by virtue of the aforementioned projection-slice property, the Radon transform can then be computed as the inverse one-dimensional Fourier transform along each radial line;

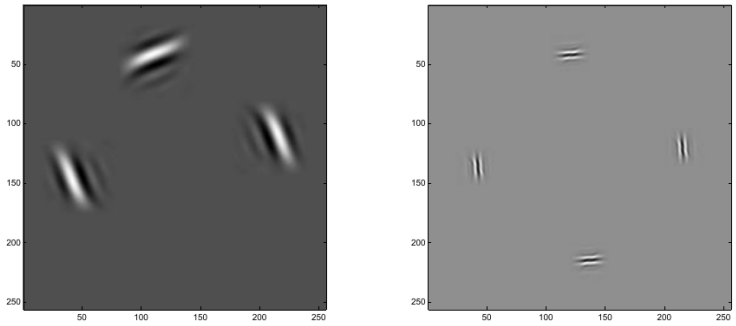

Figure 3.12. Images showing a few curvelets having different orientations at scales $u = 2$ (left panel) and $u = 3$ (right panel) [taken from 83].

iii. finally, the ridgelet transform is obtained as the one-dimensional wavelet transform computed at fixed angle θ towards the ridgelet bands.

Curvelets

Ridgelets constitute an anisotropic class of basis functions which, by definition, are particularly efficient in detecting straight lines. Nevertheless, such features do not frequently occur in images, especially in astronomy. Therefore, to describe localized curved patterns, Candès and Donoho introduced curvelets as a generalized version of ridgelets [82]. Similarly to ridgelets, curvelets are described by a scale quantifying dilation, a position to quantify translation and an orientation given by the angle of rotation. Some examples of curvelets are provided in Figure 3.12. The main difference with respect to wavelets is that the dilation obeys a parabolic law of the kind [269]:

$$\varphi_u(x) \approx u^{-3/4}\ \varphi(u^{-1/2}x_1 + u^{-1}x_2)\ , \tag{3.70}$$

being φ the main basis curvelet function. A more compact way of writing equation (3.70) is by means of the parabolic scaling matrix:

$$D_u = \begin{pmatrix} u^{-1/2} & 0 \\ 0 & u^{-1} \end{pmatrix}\ , \tag{3.71}$$

so that:

$$\varphi_u(x) \approx u^{-3/4}\ \varphi(D_u x)\ . \tag{3.72}$$

Such a scaling is a peculiar characteristic of curvelets, and it is fundamental to allow their use in sparse representations [see 85, for a discussion]. As a consequence, the length of a curvelet, ℓ is related to a fourth parameter called *width*, $\mathcal{W}$, according to the power law:

$$\ell = \mathcal{W}^{\vartheta} \qquad \text{with} \qquad \vartheta = 2\ ; \tag{3.73}$$

note that in the limit $\vartheta \to \infty$ one gets a ridgelet. Rotation is defined – similarly to the case of ridgelets – via the rotation matrix:

$$R_\theta = \begin{pmatrix} \cos\theta & \sin\theta \\ -\sin\theta & \cos\theta \end{pmatrix}\ , \tag{3.74}$$

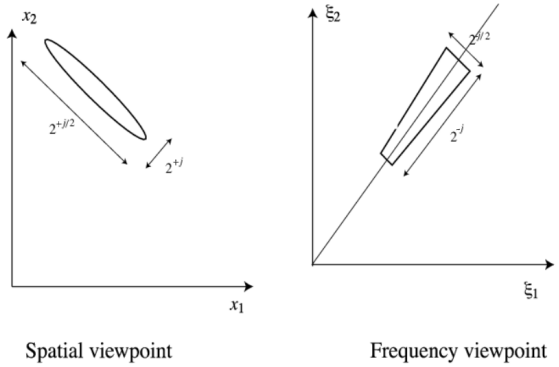

Figure 3.13. Schematic illustration of the support of curvelets and their Fourier transforms, in the spatial domain and in the frequency domain, respectively (see text for details) [adapted from 85].

so that the rotated, translated and dilated curvelet takes the form [84]:

$$\varphi_{u,b,\theta}(x) = u^{-3/4}\ \varphi(D_u R_\theta x - b)\ . \tag{3.75}$$

When imposing a dyadic sampling, the spatial curvelet support is represented by oriented ellipses with axes approximately equal to $2^{j/2}$ and 2^j, as illustrated in Figure 3.13. Another relevant difference between curvelets and wavelets is their frequency support upon Fourier transform. Indeed, as discussed in section 3.2.1, the support of wavelets is represented by rectangular Heisenberg boxes of constant area and varying linear sizes across different scales, according to the dyadic sampling. Curvelet support, instead, is represented by wedges, as a consequence of their parabolic scaling. Indeed, defining the two-dimensional spatial frequency vector in polar coordinates, $\xi = |\xi|(\cos\alpha, \sin\alpha)$, the Fourier transform of a curvelet at the scale 2^j can be written as

$$\hat{\varphi}_j(\xi) = 2^{\frac{3j}{4}}\ \hat{\psi}(2^j|\xi|)\ \hat{V}\left(\frac{2\alpha}{2^{\lfloor j/2 \rfloor}\pi}\right)\ , \tag{3.76}$$

that is the product of two smooth window functions, $\hat{\psi}$ and $\hat{V}$. The first one, $\hat{\psi}$, is the Fourier transform of a one-dimensional wavelet chosen to have compact support in the range $[-1/2, 2]$ and satisfying the dyadic frequency covering, so that $\sum_{j=-\infty}^{\infty} |\hat{\psi}(2^j|\xi|)|^2 = 1$ for all values of $|\xi|$. This function plays the role of a radial window which selects a radial segment having length equal to 2^{-j}. The second one, $\hat{V}$, is a one-dimensional angular window function that selects an arc having length $2^{-j/2}$. The joint effect of such functions is that of localizing the compact support of the Fourier transform of the curvelet, $\hat{\varphi}_j(\xi)$, in a polar parabolic wedge, as illustrated in Figures 3.13 and 3.14.

Curvelets possess the important property of satisfying the principle of harmonic analysis, i.e. any arbitrary function $f(x)$ can be represented as a series of curvelets as one does with orthonormal bases. Indexing with μ the set of discretized parameters (u, b, θ), the curvelet transform of a function $f(x)$ can therefore be written as

$$f(x) = \sum_{\mu} \langle f(x), \varphi_\mu(x) \rangle\ \varphi_\mu(x)\ , \tag{3.77}$$

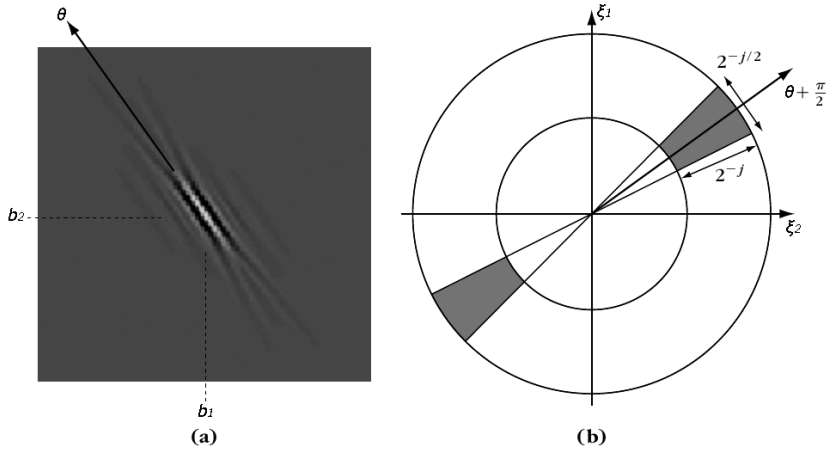

Figure 3.14. A curvelet and its frequency support. **(a)** Example of curvelet in spatial coordinates translated by b_1 and b_2 along the x_1 and x_2 axes, respectively. **(b)** Wedge-shaped frequency support of the Fourier transform, $\hat{\varphi}_j(\xi)$, as obtained from the product of the angular window function $\hat{V}$ with the radial window function $\hat{\psi}$, as in equation (3.76) [adapted from 269].

where $\langle f(x), \varphi_\mu(x) \rangle$ are the curvelet coefficients. The above mathematical formalism defines the so-called "second-generation curvelet transform", introduced in [84, 85] for the first time.

Originally, curvelet bases were constructed from ridgelets, multi-scale ridgelet transforms and bandpass filtering [see 82, 83, for details]. With this approach, the curvelet transform is computed according to the so-called "first-generation" scheme described also in e.g. [418, 419] with a stress on the application to astronomical images. The underlying idea is that of approximating curved patterns with linear patterns over sufficiently localized portions (or blocks) of the image, and to apply a ridgelet transform to each block. A schematic representation of this technique is given in Figure 3.15; the corresponding steps are synthetically described in the following.

i. The input image is processed via a two-dimensional wavelet transform over all scales;

ii. each wavelet band (i.e. each set of wavelet coefficients) undergoes a discrete ridgelet transform, according to the procedure described in page 79. Such a transform over each block, gives a localized curvelet transform. Indeed, the cells defined by the radial grid in the two-dimensional Fourier space, represent an approximation of the wedges over which curvelets are localized in the frequency domain.

While second-generation curvelets provide us with compact bases in the spatial frequency domain, the simpler, first-generation curvelets are highly redundant. Therefore, they allow a straightforward link with kernel smoothing in the direct space, which we exploited, in particular, to implement a spectral imaging algorithm from a wavelet-weighted likelihood. Hereafter, we will refer to the first-generation scheme whenever a curvelet transform is invoked.

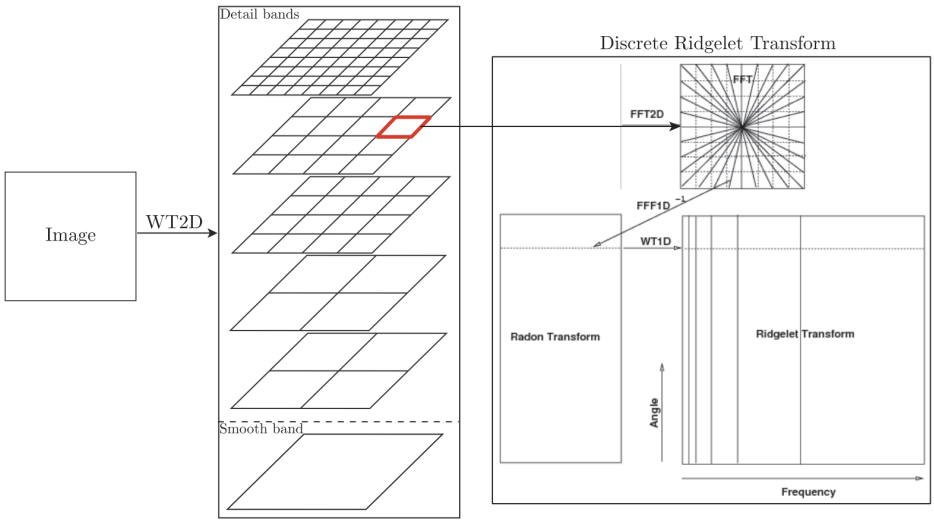

Figure 3.15. Flowgraph of the first-generation curvelet transform (see text for details) [taken from 160].

In the following sections, we apply sparse representations based on both wavelet and curvelet to a specific astrophysical case: mapping the signal from the gas in galaxy clusters at millimetre wavelengths, observed via the thermal SZ effect.

3.3 The spectral imaging algorithm

In Bourdin et al. (2015) [67] (B15 hereafter) the authors propose for the first time to combine sparse representations with the maximum likelihood approach of parametric component separation, into a *spectral imaging algorithm*. Their method has been validated using synthetic galaxy clusters from the hydrodynamical simulations presented in [350, 364], featuring cooling, star formation and AGN feedback mechanisms. Specifically, they extract three example cases of interacting galaxy clusters from the simulations and they produce mock frequency maps accounting for *Planck*'s response and noise properties. The three dynamical configurations are those of an accreting cluster at redshift $z = 0.25$, a connected cluster pair at $z = 0$ (that is the evolution of the same Lagrangian region hosting the aforementioned accreting cluster), and a colliding system at $z = 0$.

3.3.1 Basic features

The algorithm solves the component separation problem of equation (3.5) adopting a parametric scheme. Therefore, the model map at the k-th pixel and at the frequency ν is defined as

$$\mathcal{M}(\nu, k; \boldsymbol{s}) = \sum_{i}^{N_s} f_i(\nu)\ s_i + \eta(\nu)\ , \tag{3.78}$$

where $\boldsymbol{s}$ is the usual vector of the source components, having size N_s, and $\eta(\nu)$ gives the instrumental noise.

For the purpose of mapping the Compton y-parameter, the application of the algorithm is limited to the bands covered by *Planck*/HFI, for a total of $N_\nu = 6$ frequency maps, namely at 100, 143, 217, 353, 545 and 857 GHz. Indeed, the data at these frequencies provide the highest signal-to-noise ratio (SNR hereafter) for the SZ-based detection of galaxy clusters, as discussed extensively by the *Planck* Collaboration in [338]. The three dominating physical components in this frequency range are: (*i*) the CMB, (*ii*) the emission from Galactic thermal dust and (*iii*) the tSZ effect (see also Figures 3.1a and 2.6). Therefore, equation (3.78) can be explicitly written in terms of the source components as

$$\begin{aligned} \mathcal{M}(\nu, k; \boldsymbol{s}) &= f_{\rm CMB}(\nu)\ s_{\rm CMB} + f_{\rm td}(\nu)\ s_{\rm td} + f_{\rm tSZ}(\nu)\ s_{\rm tSZ} + \eta(\nu) \\ &= \Delta T_{\rm CMB} + \Delta T_{\rm td} + \Delta T_{\rm tSZ} + \eta(\nu)\ , \end{aligned} \tag{3.79}$$

and such a model map will be compared to the data map from HFI at the corresponding frequency, $D_{\rm HFI}(\nu)$.
At frequencies in the range $[100, 353]$ GHz, $D_{\rm HFI}(\nu)$ gives the temperature fluctuation ΔT measured by the bolometers in units of $\mathrm{K_{CMB}}$, i.e. in K - $T_{\rm CMB}$(K). At 545 and 857 GHz, instead, where the dominating emission comes from thermal dust, data are given in MJy sr^{-1} so that they measure the change in specific brightness, ΔB, assuming a constant $B_{\rm gb} = \nu B(\nu; T)$. The conversion factors used to homogenize unities across frequencies are 58.0623 and 2.27053, at 545 and 857 GHz, respectively [336]. Apart from the case of the CMB, the amplitude of the component signals are given by dimensionless quantities; therefore the spectral functions of equation (3.79) must have the proper physical units. Each of the three terms – $\Delta T_{\rm CMB}$, $\Delta T_{\rm td}$, $\Delta T_{\rm tSZ}$ – is described in detail in the following.

i. CMB term. The spectrum of CMB radiation is that of a black body (see section 1.2). Thus, the spectral dependence of the fluctuations of its thermodynamic temperature, in units of $\mathrm{K_{CMB}}$, is equal to unity at all frequencies:

$$f_{\rm CMB}(\nu) = 1\ , \tag{3.80}$$

and the component $s_{\rm CMB}$ of the source vector gives the amplitude of temperature anisotropies $\Delta T_{\rm CMB}$ in physical units.

ii. Thermal dust term. The original version of the algorithm by B15 takes the spectral model of thermal dust of [337]. Therefore, it is represented by a single grey body with the emission law of equation (3.1). To homogenize units in the maps, any fluctuation in the specific brightness has to be converted into a temperature fluctuation. This is easily achieved in the Rayleigh–Jeans limit using the definition of the brightness temperature, that is [71]:

$$T_{\rm RJ}(\nu) = \frac{c^2}{2k_B\nu^2}\ B_{\rm gb}(\nu; T)\ , \tag{3.81}$$

with the usual meaning of the involved quantities.
Rigorously, the conversion is carried out by taking the derivative of the brightness function with respect to the temperature. Nevertheless, for a population

of dust grains at $T_{\rm td} \approx 20\,{\rm K}$, the thermodynamic temperature can be approximated with the antenna temperature up to $\approx 400\,{\rm GHz}$. Then, the spectral variation of the temperature of thermal dust is given by the function:

$$f_{\rm td}(\nu) = \frac{1}{k_B}\left(\frac{\nu}{\nu_0}\right)^{\beta_{\rm td}} \frac{h_P\nu}{\exp\left(\frac{h_P\nu}{k_B T_{\rm td}}\right)-1} \ . \tag{3.82}$$

The spectral index is set to be spatially constant and equal to $\beta_{\rm td} = 1.8$, and the scaling frequency ν_0 is set to 353 GHz. As pointed out in section 3.1.1, the physical signal $s_{\rm td}$ carried by dust is the optical depth at the scaling frequency (see equation (3.2)). It follows that the thermal dust term is:

$$\Delta T_{\rm td} = \frac{1}{k_B}\left(\frac{\nu}{\nu_0}\right)^{\beta_{\rm td}} \frac{h_P\nu}{\exp\left(\frac{h_P\nu}{k_B T_{\rm td}}\right)-1}\ \tau_{\rm td}(\nu_0) \ . \tag{3.83}$$

iii. TSZ term. As pointed out in section 2.2.1, the temperature change induced by the tSZ has the spectral dependence given by the function $f_{\rm tSZ}$ of equation (2.30) in the non-relativistic limit, which we rewrite here for convenience in the following form:

$$f_{\rm tSZ}(\nu) = \left(\frac{h_P\nu}{k_B T_{\rm CMB}}\right)\coth\left(\frac{h_P\nu}{k_B T_{\rm CMB}}\right) - 4 \ . \tag{3.84}$$

Consistently with equation (2.29), the physical signal $s_{\rm tSZ}$ in this case is given by the Compton y-parameter:

$$y = \frac{\sigma_T}{m_e c^2}\int_{\rm los} p(l)\ dl \ , \tag{3.85}$$

which is given here in terms of the electron thermal pressure of the ICM along the line of sight, $p(l)$ (see also equation (2.26)). Thus, the tSZ term is:

$$\Delta T_{\rm tSZ} = T_{\rm CMB}\ \left[\left(\frac{h_P\nu}{k_B T_{\rm CMB}}\right)\coth\left(\frac{h_P\nu}{k_B T_{\rm CMB}}\right) - 4\right]\ y \ . \tag{3.86}$$

The terms described above can be plugged into equation (3.79) to construct the model map. The squared residuals between the model map and the data map normalized to the variance of the data, are given at each frequency by:

$${\rm res}^2(\nu, k; \boldsymbol{s}) = \frac{[D_{\rm HFI}(\nu,k) - \mathcal{M}(\nu,k;\boldsymbol{s})]^2}{\sigma^2_{\rm HFI}(\nu,k)} \ , \tag{3.87}$$

being $\sigma^2_{\rm HFI}(\nu,k)$ the HFI variance map, so that the estimate of the parameters, $\boldsymbol{s} = (s_{\rm CMB}, s_{\rm td}, s_{\rm tSZ})$ is obtained from the minimization of the chi-square constructed by summing those residuals.

It is important to note that HFI data are pre-processed by means of the subtraction of an offset value encoding astrophysical contamination on large scale, which accounts for the CIB and the tSZ background. The values of the offsets at each frequency are listed in Table 3.2. We derived them following the same procedure described

Table 3.2. Frequencies, full width at half maximum of the beams [adapted from 341], and astrophysical offset corrections of *Planck* HFI data (see text for the origin of these numerical values).

Frequency (GHz)	$F_{\mathcal{B},\nu}$ (arcmin)	Offset
100	9.69	1.47×10^{-5} K_{CMB}
143	7.30	2.32×10^{-5} K_{CMB}
217	5.02	7.02×10^{-5} K_{CMB}
353	4.94	4.12×10^{-4} K_{CMB}
545	4.83	3.41×10^{-1} MJy sr^{-1}
857	4.64	5.84×10^{-1} MJy sr^{-1}

in [337]. In particular, we exploit the spatial correlation between dust and neutral hydrogen [64], which are traced by HFI data at 857 GHz, and by the data delivered by the Leiden/Argentine/Bonn (LAB) radio survey of Galactic HI [227], respectively. The pixels in the sky that are used to compute this correlation are selected according to the values of both the column density and the velocity of HI clouds. To remove the contamination from galaxy clusters, and to account for the calibration at high frequencies, we also added two more selection criteria. One of them is based on masking pixels where the Comptonization parameter, estimated from the maps obtained with the MILCA algorithm [215], exceeds the threshold value of 10^{-5}. The second one accounts for a correction of the CMB using SMICA maps [88] at frequencies between 100 GHz and 353 GHz as templates.

In B15's algorithm, the calculation of the chi-square is where sparsity enters the picture. Indeed, instead of computing the "usual" chi-square:

$$\chi^2 = \sum_{\nu}^{N_\nu} \sum_{k}^{N_{\rm pix}} \mathrm{res}^2(\nu, k; \boldsymbol{s}) \ , \tag{3.88}$$

one computes a *weighted* chi-square, which follows from taking a wavelet transform of the squared residuals normalized to the variance.

Local likelihood (or chi-square) estimates of a spatially-variant parameter may be connected to a kernel smoothing [as shown e.g. in 127]. The work by B15 proposes a generalisation of this fact to multivariate distributions (e.g. the presence of multiple parameters). In the latter case, the multivariate nature of the distribution introduces a source separation problem that gets solved through the explicit minimization of the chi-square. In this context, wavelet bases represent a natural choice for performing a kernel-weighting.

Following this approach, the squared residuals of equation (3.87) are written in terms of a multi-resolution decomposition as the sum of an approximation term, plus a term giving the information on the details of the signal [270]. The new, weighted residuals are thus (see also equation (3.49)):

$$\mathrm{res}^2_\psi(\nu, k; \boldsymbol{s}) = \sum_{n}^{N_{\rm pix}} \bar{a}_{j_0,n}(\nu; \boldsymbol{s}) \ \phi_{j_0,n}(k) \ + \sum_{j=j_0}^{N_{\rm scales}} \sum_{n}^{N_{\rm pix}} a_{j,n}(\nu; \boldsymbol{s}) \ \psi_{j,n}(k) \ , \tag{3.89}$$

where j and n give the dilation and the translation of the wavelet basis function ψ,

respectively, being 2^j the wavelet scale. The wavelet basis function is a cubic (B_3) spline, and ϕ is the dual scaling function of ψ at the scale j_0. This scale corresponds to the approximation level – also called *last smooth* – which encodes signal information at the lowest resolution. Both functions are represented in Figure 3.16a.
The wavelet coefficients in equation (3.89) are given by:

$$\bar{a}_{j_0,n}(\nu;\boldsymbol{s}) = \sum_{k}^{N_{\rm pix}} \mathrm{res}^2(\nu,k;\boldsymbol{s})\ \phi^*_{j_0,n}(k)\ ; \tag{3.90}$$

$$a_{j,n}(\nu;\boldsymbol{s}) = \sum_{k}^{N_{\rm pix}} \mathrm{res}^2(\nu,k;\boldsymbol{s})\ \psi^*_{j,n}(k)\ , \tag{3.91}$$

for the approximation and the detail levels, respectively.
To ensure normalization and positivity when weighting the residuals, the wavelet kernel ψ is split in its positive and negative parts, ψ_+ and ψ_-, as illustrated in Figure 3.16b. This yields the minimization of two separate chi-squares, which can be expressed as the sum across all the frequencies and pixels (N_ν and $N_{\rm pix}$, respectively) of such weighted squared residuals:

$$\chi^2_{\psi_\pm} = \sum_{\nu}^{N_\nu}\sum_{k}^{N_{\rm pix}}\ \mathrm{res}^2_{\psi_\pm}(\nu,k;\boldsymbol{s})\ . \tag{3.92}$$

The allowed number of scales for the calculation of the wavelet transform of equation (3.89) is linked to the number of pixels on each side of the image through the following relation:

$$N_{\rm scales} = \mathrm{floor}[\log(N_{\rm pix})/\log 2] - 4\ . \tag{3.93}$$

The maps in B15 have $N_{\rm pix} = 256$, implying that the maximum number of wavelet scales that can be analysed is four. The resolution per pixel is equal to 1 arcmin, so they span 4.3° on each side. Generally speaking, images decomposed at the maximum number of scales are smoother with respect to the results from the decomposition over less scales (e.g. when comparing four vs three scales in 256-pixel maps). This is because when less scales are used, the information encoded in the "missing" detail level is contained in the last smooth, and it does not get thresholded, so it can retain more contributions to the signal from noisy small scales. The choice of the number of wavelet scales in the analysis is particularly crucial when dealing with clusters detected with low SNR. Clearly, the optimal value should be determined as a trade-off between discarding the noise and keeping the relevant signal.
The minimisation of the weighted chi-square yields the final estimate of the component source maps:

$$\tilde{\boldsymbol{s}} = \frac{1}{2}\left[\underset{\boldsymbol{s}}{\mathrm{argmin}}(\chi^2_{\psi_+}) - \underset{\boldsymbol{s}}{\mathrm{argmin}}(\chi^2_{\psi_-})\right]\ , \tag{3.94}$$

as prescribed by the parametric approach.
A noticeable feature of B15's algorithm which makes it particularly suitable for mapping the ICM structure in the outskirts (see section 3.4), is the tuning of the sparse bases to perform the multi-resolution decomposition. As discussed in section 3.2.4, wavelets are suitable to represent isotropic signals, such as the CMB. On the contrary, they do not correlate well with sources like thermal dust or the

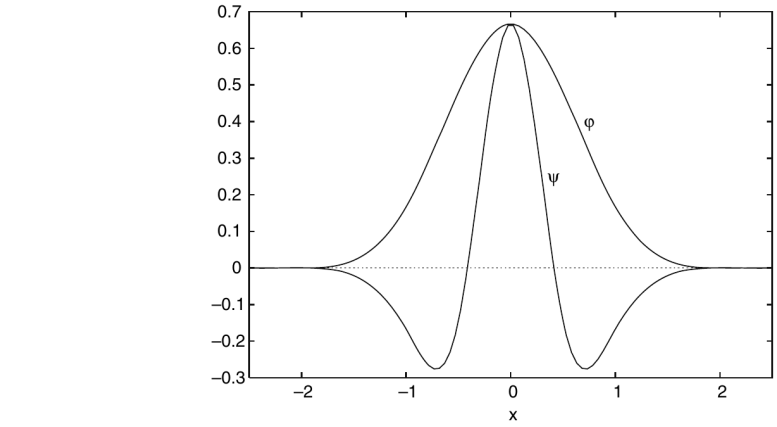

(a)

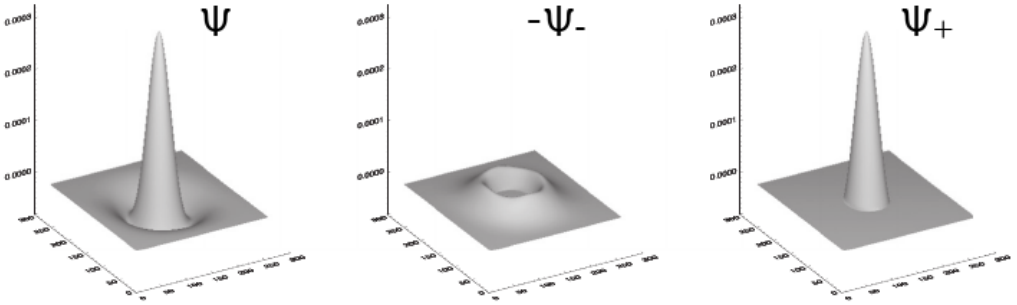

(b)

Figure 3.16. Wavelet basis used in the spectral imaging algorithm. **(a)** Cubic spline wavelet, $\psi_{1,0}(x)$, and its associated scaling function, $\phi_{1,0}(x)$, in one dimension [taken from 275]. **(b)** Decomposition of a two-dimensional cubic spline wavelet into its positive and negative parts [adapted from B15].

tSZ effect, which are localized and anisotropic across the sky. For instance, a possible shock occurring at the periphery of a cluster should be seen as an abrupt pressure discontinuity in the tSZ signal. Also, inhomogeneities due to clumps or accreting substructures would affect the projected pressure in a similar manner, and an optimal basis for the detection of such features is provided by curvelets. Therefore, the signals from dust and tSZ are processed via a curvelet transform, which is implemented according to the "first-generation" scheme, both in B15 and in the rest of this work. For convenience, we recall here that it requires the two following steps: (*i*) calculation of the wavelet coefficients of each component at all scales; (*ii*) calculation of a discrete ridgelet transform for the all wavelet bands. The ridgelet transform is practically computed as a one-dimensional wavelet transform applied to the coefficients of a two-dimensional Fourier transform along radial lines passing through the centre of the frequency plane.
To denoise the signal, both wavelet and curvelet coefficients get denoised via a soft thresholding at 1σ level (see section 3.2.3). In other words, all coefficients whose

values do not exceed the square root of their variance are discarded. The residuals that effectively enter the chi-square are therefore:

$$\mathrm{res}^2_{\psi_\pm}(\nu, k; \boldsymbol{s}) = \mathcal{R}(\bar{a}_{j_0,n}, a^S_{j,n}) \ , \tag{3.95}$$

being $a^S_{j,n}$ the soft-thresholded detail coefficients; $\mathcal{R}$ is the restoration operator which allows the reconstruction of the signal from its wavelet and curvelet coefficients.

Each calculation of the chi-square mixes all the angular resolutions available from the input frequency maps (see equation (3.92)). Therefore, it is necessary to introduce the effect of the instrumental beam into the reconstructed residuals by means of a deconvolution. The procedure adopted in B15 is based on the sparse regularization of the Van Cittert deconvolution [446]. Specifically, the thresholded curvelet coefficients of thermal dust and tSZ are iteratively corrected, to match the angular resolution between the model map, $\mathcal{M}(\nu; \boldsymbol{s})$, and the data map, $D_{\mathrm{HFI}}(\nu; \boldsymbol{s})$, involved in the residuals [302]. At the $(t+1)$-th iteration, the thresholded coefficients are therefore given by:

$$a^S_{j,n,t+1}(\nu; \boldsymbol{s}) = a^S_{j,n,t}(\nu; \boldsymbol{s}) + \alpha \ \varrho_t(\nu; \boldsymbol{s}) \ , \tag{3.96}$$

where α is a constant parameter which tunes the regularization, while the correction calculated at the previous iteration, with index t, is given by:

$$\varrho_t(\nu; \boldsymbol{s}) = a^S_{j,n}(\nu; \boldsymbol{s}) - \mathcal{B}(\nu) \otimes a^S_{j,n,t}(\nu; \boldsymbol{s}) \ , \tag{3.97}$$

where $a^S_{j,n}(\nu; \boldsymbol{s})$ is the initial values of the thresholded coefficients, and $\mathcal{B}(\nu)$ is the instrumental beam. In B15, the α parameter is set to 0.25, and the number of iterations is equal to three. The final results for the tSZ maps of the mock systems considered in this work are illustrated in Figure 3.17.

3.3.2 Procedure for error assessment

To associate a statistical error to the estimate of the component maps, we used a bootstrap procedure that allowed us to simulate N_{tot} sets of HFI maps. More specifically, we followed the three steps below [22].

i. We generated $N_{\mathrm{tot}} = 100$ Monte Carlo realisations of the noise at each HFI frequency, $\eta_u(\nu)$, with $u = 1, \ldots, N_{\mathrm{tot}}$ referring to the u-th extraction. We chose the value of N_{tot} as a trade-off between the computational time needed to perform wavelet and curvelet transforms and the statistical significance. We assumed the instrumental noise to be Gaussian and spatially correlated with no correlation among the different frequencies, and we imposed the noise maps to have the same power spectrum as the jackknife maps (which deviates significantly from the spectrum of white noise). The extracted noise maps are therefore constrained to have the same power spectrum as the jackknife maps themselves. The latter are produced as the half-difference of the so-called *half-ring* HFI maps. A "ring" identifies a stable pointing period, during which the pixels of the focal plane have been visited. The half-difference of such maps eliminates almost completely the signal from the sky, as well as the majority of HFI systematics [see 342, for details].

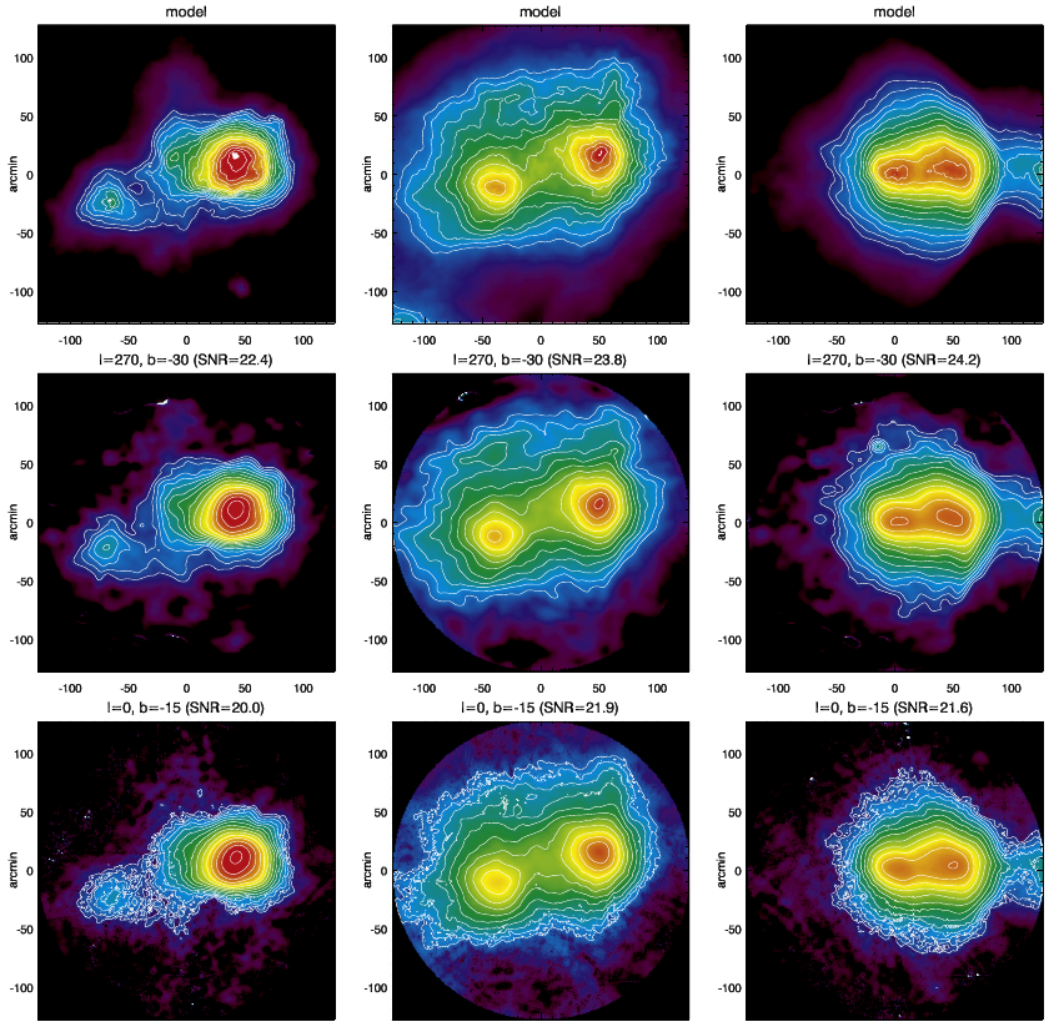

Figure 3.17. Maps of the tSZ effect showing the accreting, connected and colliding systems considered in B15, extracted from hydrodynamical simulations [350]. Contours are logarithmically spaced by a factor of $\sqrt[4]{2}$. **Top panels.** True maps of the Compton y-parameter from the simulation. **Middle panels.** Reconstructed maps obtained with the spectral imaging algorithm when positioning the clusters in a sky region characterized by a low variance of the instrumental noise (and a higher SNR). **Bottom panels.** The same as the middle panels, but positioning the clusters in a sky region with lower SNR [taken from B15].

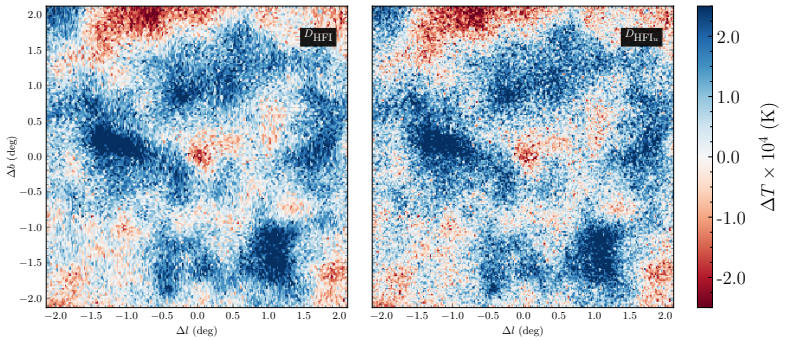

Figure 3.18. Comparison between the raw map at 100 GHz (left panel) and a synthetic HFI map constructed as prescribed in equation (3.98) (right panel), centred on cluster A2142.

ii. The HFI raw data at each frequency, $D_{\rm HFI}(\nu)$, have been denoised through a simple wavelet-based procedure, by calculating the wavelet transform on three scales, and soft-thresholding the coefficients at 1.5σ. This procedure relies on spatially-variant thresholds for each wavelet band, which have been preliminarily inferred by computing the variance of the coefficients across wavelet transforms of the noise maps, $\eta_u(\nu)$. The amplitude of the noise residuals in the $D_{\rm HFI,den}(\nu)$ maps is, in any case, negligible with respect to the amplitude of the noise in the maps extracted as in step *i.*, which confirms the efficiency of the denoising.

iii. The mock data have been obtained as the summation of the denoised maps as derived from step (*ii*), $D_{\rm HFI,den}(\nu)$, and the u-th noise realization, i.e.:

$$D_{{\rm HFI}u}(\nu) = D_{\rm HFI,den}(\nu) + \eta_u(\nu) \ . \tag{3.98}$$

An example of mock HFI map obtained with this procedure is shown in Figure 3.18 for cluster A2142 at 100 GHz. We used this set of $N_{\rm tot}$ synthetic data as input to the imaging algorithm to obtain vectors of maps of each source component of the kind: $\boldsymbol{s}_{\rm tSZ} = (s^1_{\rm tSZ}, \dots, s^{N_{\rm tot}}_{\rm tSZ})$, $\boldsymbol{s}_{\rm td} = (s^1_{\rm td}, \dots, s^{N_{\rm tot}}_{\rm td})$, $\boldsymbol{s}_{\rm CMB} = (s^1_{\rm CMB}, \dots, s^{N_{\rm tot}}_{\rm CMB})$.

The standard deviation of all the bootstrap-based sets – i.e. std($\boldsymbol{s}_{\rm tSZ}$), std($\boldsymbol{s}_{\rm td}$) and std($\boldsymbol{s}_{\rm CMB}$) – represents our error estimate for each component. In the following, we label as $\sigma_y = {\rm std}(\boldsymbol{s}_{\rm tSZ})$ the error for the tSZ signal only. The level of significance of the signal, particularly of blobs and filaments occurring in the tSZ images of a cluster, can be assessed through the ratio y/σ_y, for a given maximum value of σ_y. We adopt a conventional threshold of $y/\sigma_y = 3$ to identify a detection as significant.

3.3.3 Improvements and new features

The spectral imaging technique described above has been applied on real cluster data collected by HFI and publicly released by the *Planck* Collaboration in 2015[1].

[1] Available in the *Planck* Legacy Archive (PLA) at: https://pla.esac.esa.int.

The test targets we used to assess the performances of the algorithm are the twelve highest-SNR SZ detections of clusters whose angular sizes exceed 10 arcmin, constituting the X-COP sample (see section 3.4.1). These systems highlighted some critical aspects due to:

- the application of the algorithm to *real* astrophysical data;
- the use of Van Cittert algorithm to perform the deconvolution.

It is worth highlighting that the single grey body model of the original implementation presented in B15 has been replaced with the double grey body model, as prescribed in section 3.1.1, before the start of this thesis work. Therefore, all the tests that are explicitly reported here already account for such a modelling, even if the adoption of a double grey body is sometimes referred as to a *new* feature, to be consistent with what is reported in B15.

Astrophysical contaminants Despite the double grey body model is more suitable to describe the signal from Galactic thermal dust, the tSZ maps of a few clusters revealed that the algorithm still suffered from residual contaminations on large scales. This can be seen for instance in the left panels of Figure 3.19, showing the Compton-y parameter reconstructed for clusters A2319, A644 and A1644, which are affected by large-scale gradients due to diffuse dust.
To solve this problem, we excluded the 857 GHz channel from the reconstruction of the last smooth image, i.e. at the approximation level. Practically, we do not account for the term $\bar{a}_{j_0,n}(\nu = 857\,\mathrm{GHz}; \boldsymbol{s})$ of equation (3.90) in the reconstruction of $\mathrm{res}_{\psi_\pm}$. Indeed, such a signal contains only the features at the lowest resolution, therefore it is poorly sensitive to the contribution from data at the highest frequency, which are the most resolved, yet also more prone to be contaminated from dust. The middle panels in Figure 3.19 show indeed that this procedure helps in removing such an unwanted signal, which can influence the detection of interesting features in cluster outskirts (see also sections 3.4 and 3.4.1).

The diffuse residual dust signal, is not the only residual contamination we found in the maps after removing the highest frequency from the approximation level. The most relevant example in this case is cluster A3266, for which we detected a significant contribution to the signal due to un-modelled infrared point sources, "mistaken" as tSZ sources by the algorithm. At frequencies smaller than 353 GHz they are mostly radio sources, while emission at higher frequencies is likely due to infrared galaxies. Figure 3.20 shows the mask of these point sources at 857 GHz and their impact on the tSZ map of cluster A3266.
To prevent this kind of contamination, we produced gnomonic projections of the sky region centred in the clusters of interest from the all-sky masks based on the objects identified by the *Planck* Collaboration and listed in the second *Planck Catalogue of Compact Sources*[2] (PCCS) [339, 345]. The masks have been extracted at the single HFI bands (see the example case of cluster A3266 in Figure 3.21a), and they have been subsequently merged into a single map, which we used to mask the residuals.

[2] Also available in the PLA.

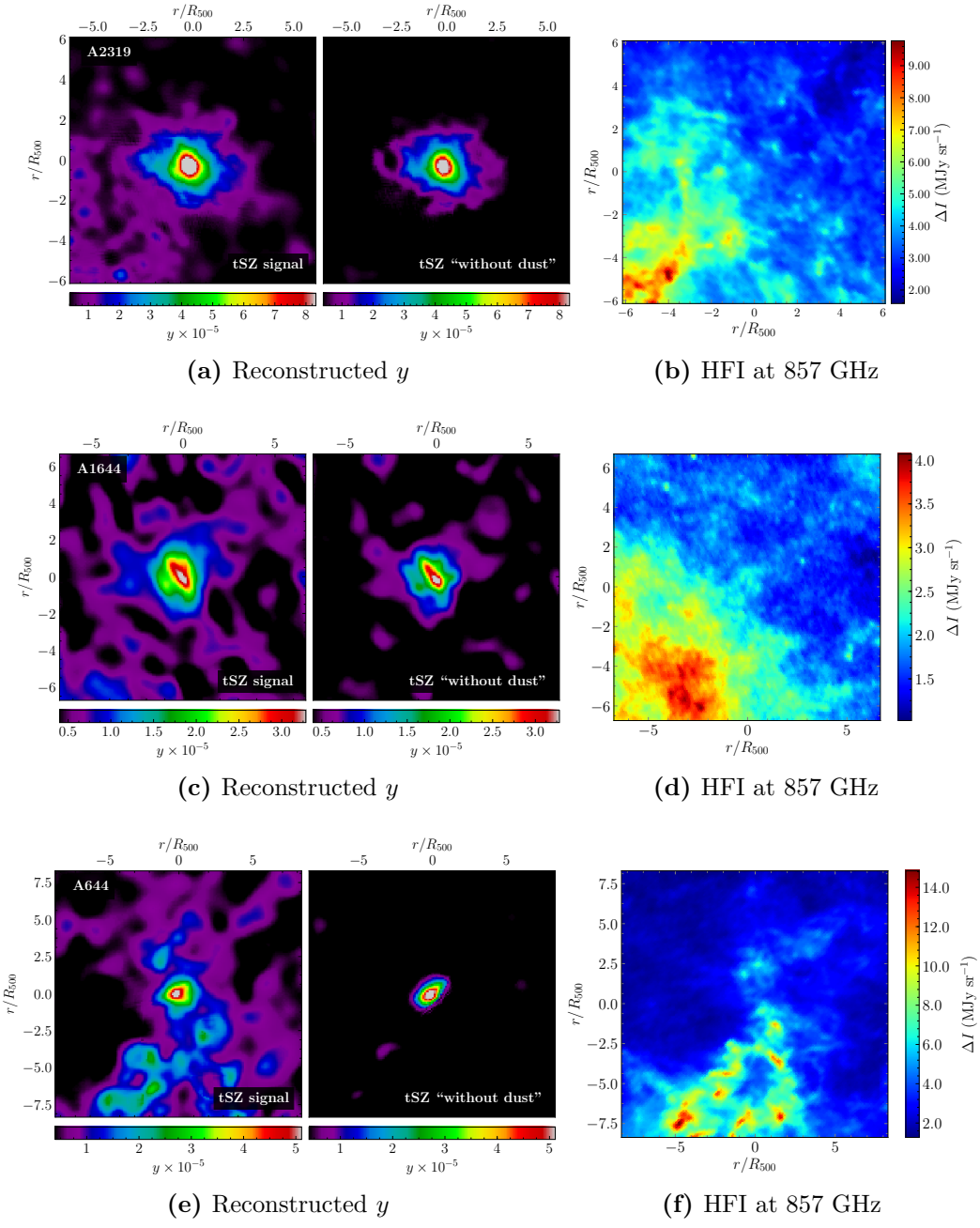

(a) Reconstructed y **(b)** HFI at 857 GHz

(c) Reconstructed y **(d)** HFI at 857 GHz

(e) Reconstructed y **(f)** HFI at 857 GHz

Figure 3.19. Comptonization parameter from the spectral imaging algorithm using three wavelet scales, and maps at 857 GHz of the regions centred on clusters A2319, A644 and A1644. Left and middle panels show the signal obtained with and without accounting for the 857 GHz channel in the approximation level of wavelet decomposition, respectively. Right panels show the raw data at 857 GHz from *Planck* 2015 release.

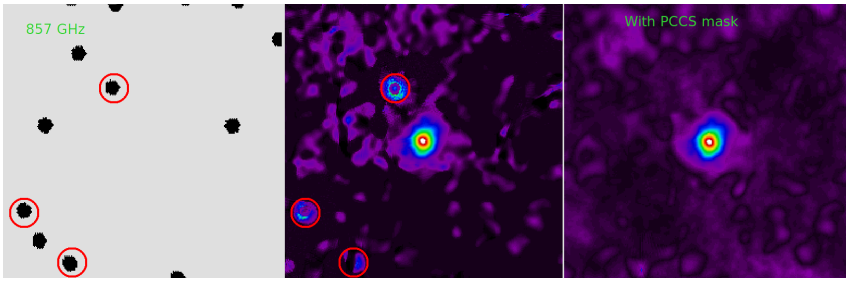

Figure 3.20. Identification and removal of contaminating point sources in the field of cluster A3266. **Left panel.** Mask of the point sources identified in the second PCCS (see text) at 857 GHz. **Middle panel.** Map of the Comptonization parameter of A3266 from the spectral imaging algorithm, as obtained without accounting for the 857 GHz channel in the last smooth. It is possible to recognize three point sources, marked with red circles in both images. **Right panel.** Reconstructed tSZ map from cluster A3266 after applying the mask of point sources constructed as prescribed in the text, and shown in Figure 3.21c.

Specifically, we first smoothed each mask with a top hat kernel having radius:

$$r_{\rm mask}(\nu) = \frac{1}{2}\sqrt{F_{\rm ref}^2 - F_{\mathcal{B},\nu}^2}\ , \tag{3.99}$$

being $F_{\rm ref}$ a reference full width at half maximum, here set to 18 arcmin; $F_{\mathcal{B},\nu}$ is the full width at half maximum of each beam, with the values listed in Table 3.2. The value of $F_{\rm ref}$ has been chosen to be larger than the maximum beam width, to avoid ring-shaped patterns that could introduce spurious artefacts which might correlate with the curvelet coefficients; the smoothed maps are shown in Figure 3.21b. The final mask has been then constructed as the product of the single smoothed ones, as shown in Figure 3.21c. The resulting tSZ map of cluster A3266 we obtained after masking the point sources is illustrated in the right panel of Figure 3.20. From the comparison with the map in the middle panel of the same Figure, it is evident that the masking performed well in removing the residual contamination from the identified point sources. To avoid possible divergences that could originate because of the sharp edges of the masked regions, we masked only a few particularly contaminated clusters. In the case of the X-COP sample, they are clusters A3266, A85 and ZW1215.

Besides the aforementioned explicit masking of astrophysical sources, we also added constraints on the values of the thresholded wavelet coefficients of the tSZ component, prior to the computation of the curvelet transform. To be specific, we discarded pixels where the value of the chi-square exceeded the following empirical threshold:

$$\chi^2_{\rm max}(j) = 4000 \times 2^{-j}\ , \tag{3.100}$$

which increases (decreases) with the wavelet resolution (scale). At the same time, we imposed a condition of regularity on the amplitude of the error (i.e. the square root of the variance) of the wavelet coefficients, to select regions characterized by a high SNR of the tSZ component. The threshold value in this case has been set to:

$$\sigma_{a,\rm max}(j) = 0.25 \times 2^{j}\ , \tag{3.101}$$

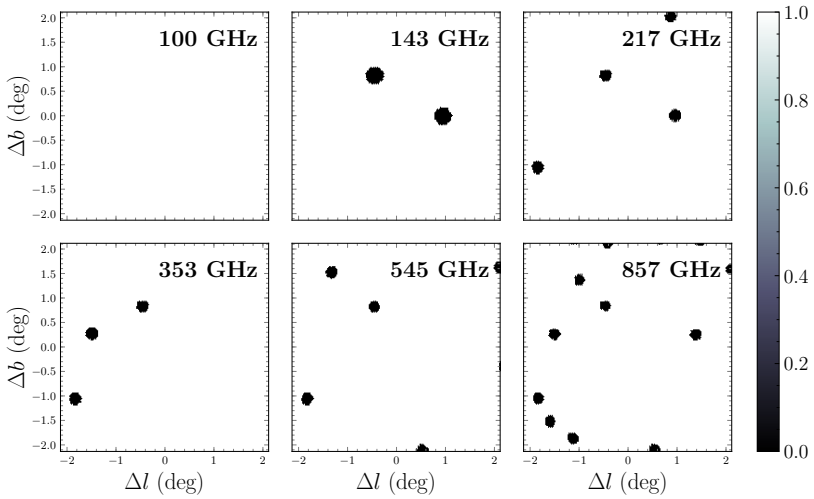

(a) Original masks at the single frequencies

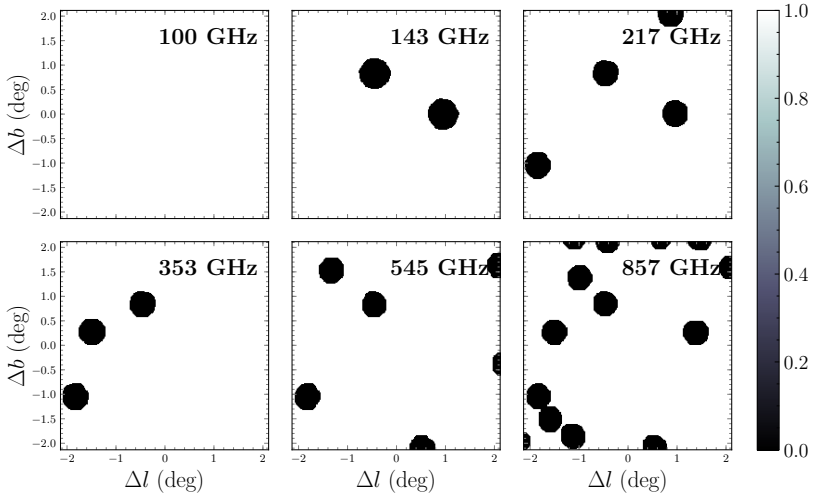

(b) Smoothed masks at the single frequencies

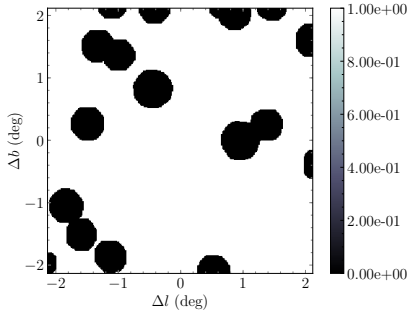

(c) Final unique mask

Figure 3.21. Masks of compact point sources in the region centred in cluster A3266 (see text for details).

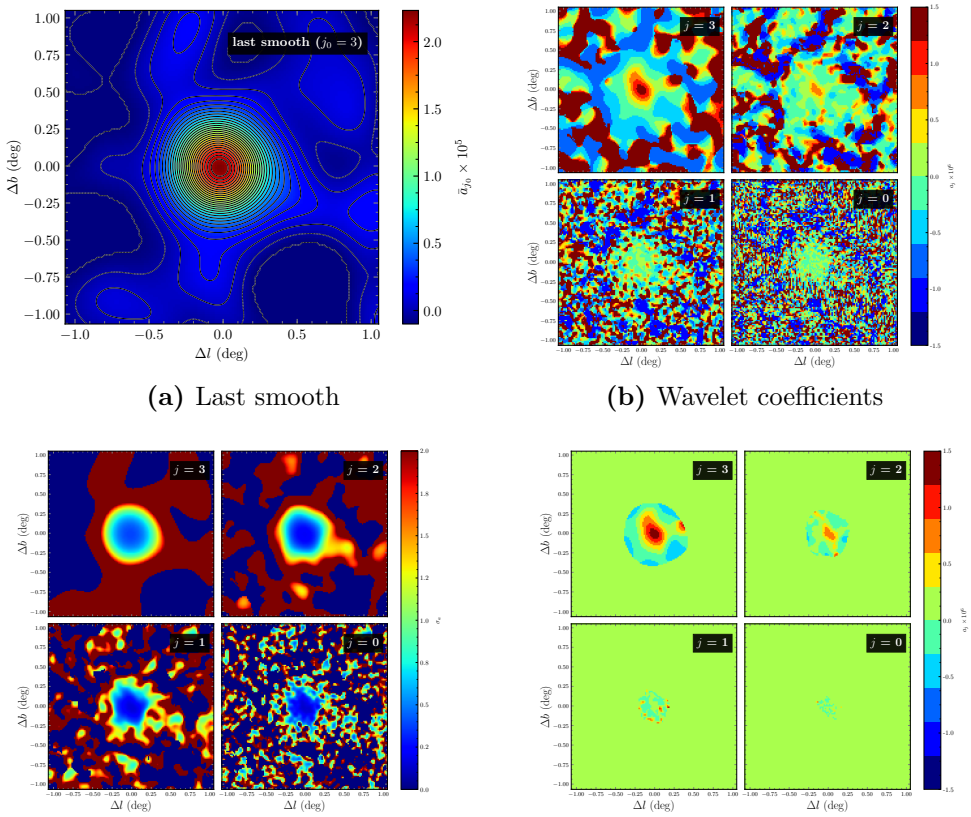

(a) Last smooth **(b)** Wavelet coefficients

(c) Error on wavelet coefficients **(d)** Masked wavelet coefficients

Figure 3.22. Zoomed maps showing the multi-resolution decomposition of the tSZ signal from cluster A2142 from the wavelet transform over four scales. **(a)** Last smooth image. **(b)** Thresholded coefficients at the four scales. **(c)** Error on the coefficients at the four scales. **(d)** Thresholded coefficients at the four scales after applying the masks retaining only the pixels where both the chi-square and the coefficient error are smaller than the corresponding thresholds given in equations (3.100) and (3.101), respectively.

increasing with the wavelet scale. The example case of cluster A2142 is shown in Figure 3.22, where we report the coefficient maps at four scales before and after the masking from the two joint conditions. It can be seen that the masks are mostly dominated by the constraint of regularity of the error of wavelet coefficients, given the decreasing size of the unmasked region with increasing resolution. The application of the restoration operator to the masked coefficients leads to the final estimate of the best-fit Compton y-parameter, according to the procedure described in section 3.3.1.

New deconvolution procedure In B15, a regularized Van Cittert deconvolution is applied to the significant curvelet coefficients to correct the residuals, to match the angular resolution of the model and the data maps. This method is iterative, and there is not a theoretical prescription to fix the optimal number of iterations to use. For the purposes of validating the algorithm using mock galaxy clusters, a

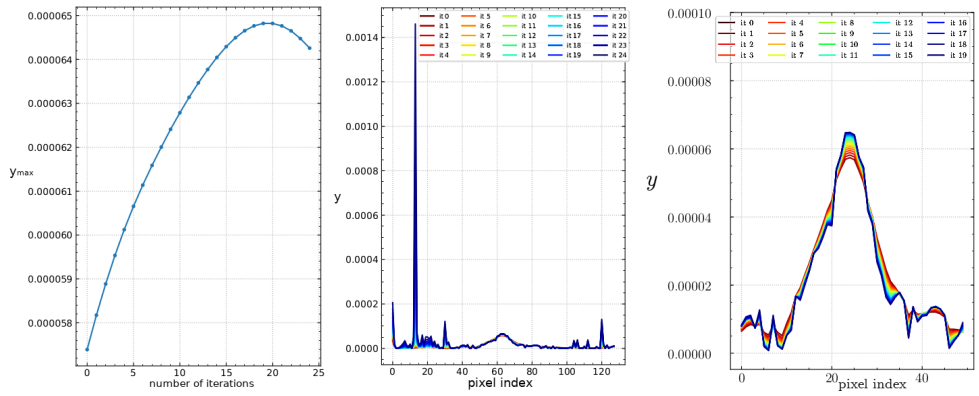

(a) (b) (c)

Figure 3.23. Results from the tests on cluster A2142 with different number of iterations used in the Van Cittert deconvolution implemented in the tSZ imaging algorithm. **(a)** Behaviour of the peak value of the Comptonization parameter across 25 iterations. **(b)** One-dimensional cuts through the maps of the Comptonization parameter as reconstructed with 25 iterations. **(c)** The same as panel (b) up to 20 iterations and with a zoom on the cluster centre.

number of iterations equal to three provides reliable results down to values of the Comptonizaton parameter $y \approx 5 \times 10^{-6}$. Nevertheless, when the expected signal level is not known a priori, as in the case of real targets, this does not necessarily hold.

Referring to cluster A2142 as to a test case, we run the algorithm using up to 25 Van Cittert iterations. The effect of increasing this number has been, as expected, enhancing the features at the peak, and raising its value. Nevertheless we noticed that the algorithm was stable only up to 20 iterations, where the peak reached its maximum value; with further iterations, the algorithm failed to converge. Figure 3.23 shows the one-dimensional horizontal profile passing through the centre of the tSZ maps reconstructed using 25 and 20 iterations, where the sharpening of the peak is clearly visible. Figure 3.23b highlights another drawback of using this deconvolution procedure, which can be seen also from the maps for three iterations shown in Figure 3.24. Specifically, at radial distances $\gtrsim 30$ arcmin from the cluster centre, where the signal is significantly lower, the signal was characterized by pixel-sized artefacts. They correspond to local divergences of the algorithm which manifested at low signal regimes especially when increasing the number of iterations, which produced the amplification of curvelet coefficients. Such a behaviour could thus invalidate the reliability of the reconstructed map in cluster outskirts. On the other hand, a lower number of iterations might lead to an underestimate of the true signal in the central regions.

These aspects led us to introduce a different deconvolution technique, not based on iterative corrections. The stability and reliability of the algorithm have been improved by means of a new *wavelet coefficient-wise* deconvolution [22]. As the name suggests, this method is now applied to the wavelet coefficients, instead of to the curvelet-denoised images. As a consequence, the detection of peaks is more efficient. The

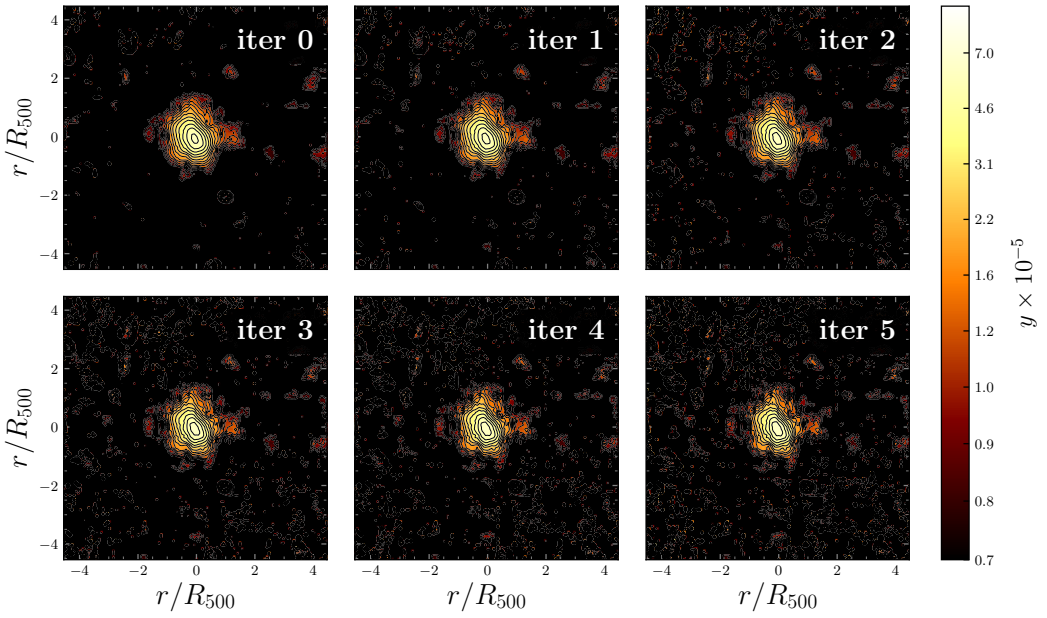

Figure 3.24. Maps of the Comptonization parameter from cluster A2142, as reconstructed using six Van Cittert iterations. It can be seen that in regions corresponding to cluster outskirts the tSZ signal is plagued by diverging artefacts, increasing with number of iterations.

major change to the algorithm introduced by this deconvolution involves the wavelet transform of the residuals entering the chi-square to be minimized. Specifically, the wavelet coefficients of the residuals given in equations (3.90) (approximation level) and (3.91) (detail levels) have been modified, to account for the *Planck* beams, $\mathcal{B}(\nu)$, in the model map. Recalling the full expression of the residuals given in equation (3.87), the new wavelet coefficients become:

$$\begin{aligned}\bar{a}_{j_0,n}(\nu;\boldsymbol{s}) &= \sum_{k}^{N_{\rm pix}} \mathrm{res}^2(\nu,k;\boldsymbol{s})\ \phi^*_{j_0,n}(k) \\ &= \sum_{k}^{N_{\rm pix}} \sigma^{-2}_{\rm HFI}(\nu,k)\{D_{\rm HFI}(\nu,k) - \mathcal{B}(\nu)\otimes[\mathrm{H}\ \mathcal{M}(\nu,k;\boldsymbol{s}+\Delta\boldsymbol{s}) + \\ &+ (1-\mathrm{H})\ \mathcal{M}(\nu,k;\boldsymbol{s}-\Delta\boldsymbol{s})]\}^2\ \phi^*_{j_0,n}(k)\ ,\end{aligned} \tag{3.102}$$

and

$$\begin{aligned}a_{j,n}(\nu;\boldsymbol{s}) &= \sum_{k}^{N_{\rm pix}} \mathrm{res}^2(\nu,k;\boldsymbol{s})\ \psi^*_{j,n}(k) \\ &= \sum_{k}^{N_{\rm pix}} \sigma^{-2}_{\rm HFI}(\nu,k)\{D_{\rm HFI}(\nu,k) - \mathcal{B}(\nu)\otimes[\mathrm{H}\ \mathcal{M}(\nu,k;\boldsymbol{s}+\Delta\boldsymbol{s}) + \\ &+ (1-\mathrm{H})\ \mathcal{M}(\nu,k;\boldsymbol{s}-\Delta\boldsymbol{s})]\}^2\ \psi^*_{j,n}(k)\ ,\end{aligned} \tag{3.103}$$

for the last smooth and the detail levels, respectively, where H is Heaviside step function, needed to preserve positivity. The convolution of the model map with the

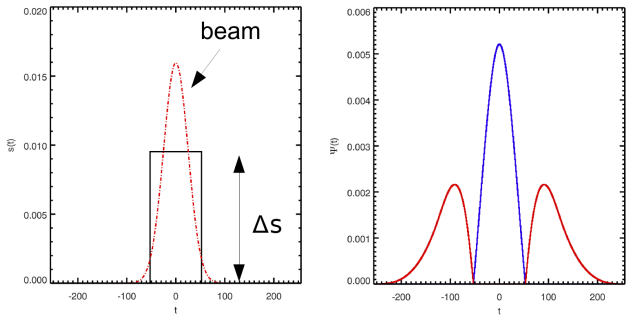

(a) Without convolving with the beam

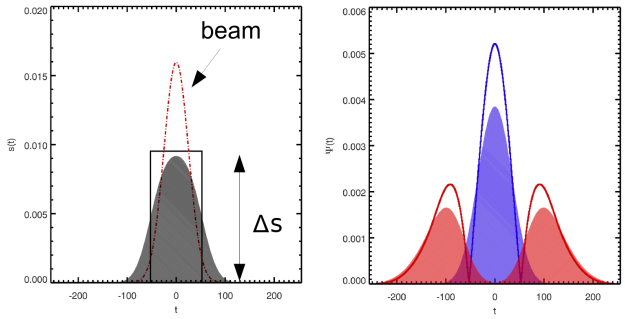

(b) Convolving with the beam

Figure 3.25. Illustration of the new wavelet coefficient-wise deconvolution. **Left panels.** Step-like spatial variation of the parameter, $\Delta \boldsymbol{s}$ (solid black line), and instrumental Gaussian beam (dashed red line). **Right panels.** Effective spatial variation of the parameter encoded in the B_3 spline kernel. Blue and red lines represent the absolute value of the positive and negative parts of the wavelet, respectively. The envelopes of the shaded areas in the bottom panels coincide with the convolution of the instrumental beam with $\Delta \boldsymbol{s}$ (a), and with the support of the positive and negative parts of the kernel (b). It can be seen that the latter are now correlated, thus the decomposition cannot be separated as in B15.

beam does not allow the splitting of the wavelet into a positive and a negative part, differently from the case in which the deconvolution was performed a posteriori. This is because now the positive and negative spatial variations of the best-fit parameters (noted here as $\boldsymbol{s} + \Delta \boldsymbol{s}$ and $\boldsymbol{s} - \Delta \boldsymbol{s}$) are not mutually independent. Figure 3.25 better illustrates this concept. Solid lines refer to the case without beam smoothing, while shaded areas show the effect of the beam. Here the spatial variation $\Delta \boldsymbol{s}$ of the searched parameters is assumed to be positive. The blue and red curves represent ψ_+ and $-\psi_-$, which correlate with $\Delta \boldsymbol{s}$ and $-\Delta \boldsymbol{s}$, respectively. When the convolution is introduced, the blue and red shaded areas overlap, therefore it is not possible to separate the chi-square minimization in two steps, one for each sign of the wavelet. Coefficients are soft-thresholded, and the chi-square to be minimized is now:

$$\chi^2_\psi = \sum_{\nu}^{N_\nu} \sum_{k}^{N_{\rm pix}} \mathrm{res}^2_{\psi,\mathcal{B}}(\nu, k; \boldsymbol{s}) \ , \tag{3.104}$$

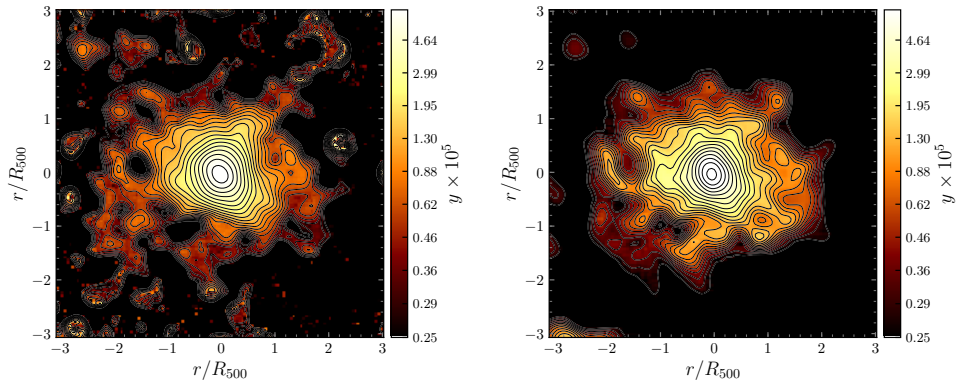

(a) Van Cittert deconvolution **(b)** New deconvolution

Figure 3.26. Maps of the tSZ effect from A2319 as reconstructed from B15's original algorithm featuring Van Cittert deconvolution (left panel), and from the new version with the wavelet coefficient-wise deconvolution (right panel). The color scale is logarithmic and contours are logarithmically spaced by a factor of $\sqrt[4]{2}$.

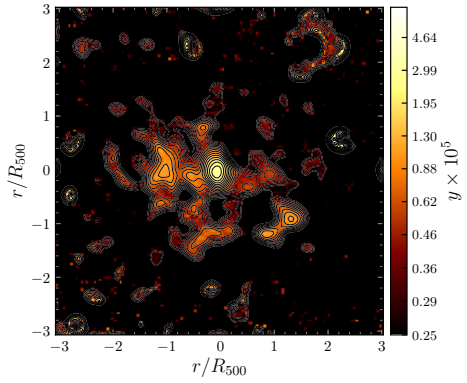

Figure 3.27. Absolute value of the pixel-to-pixel difference between the tSZ maps of cluster A2319 shown in Figure 3.26.

with best-fit parameters estimated as

$$\tilde{\boldsymbol{s}} = \underset{\boldsymbol{s}}{\operatorname{argmin}}(\chi^2_\psi) \ . \tag{3.105}$$

The effects of the new wavelet coefficient-wise deconvolution on the reconstructed tSZ maps can be seen from Figure 3.26, in the example case of cluster A2319. The absolute value of the pixel-to-pixel difference between the two maps is shown in Figure 3.27 instead. The result in Figure 3.26a is obtained with three iterations, and with the convergence parameter α set to 0.25 (see equation (3.96)). It can be seen that this map, similarly to the case of cluster A2142 shown in Figure 3.24, is affected by a number of pixel-sized outliers, which plague regions where the level of the signal is $y \lesssim 7.5 \times 10^{-6}$. The map in Figure 3.26b shows instead that the result from the new wavelet coefficient-wise deconvolution is cleaner, while the mildly ellipsoidal shape of the signal in the centre is still well recovered. It is worth stressing again

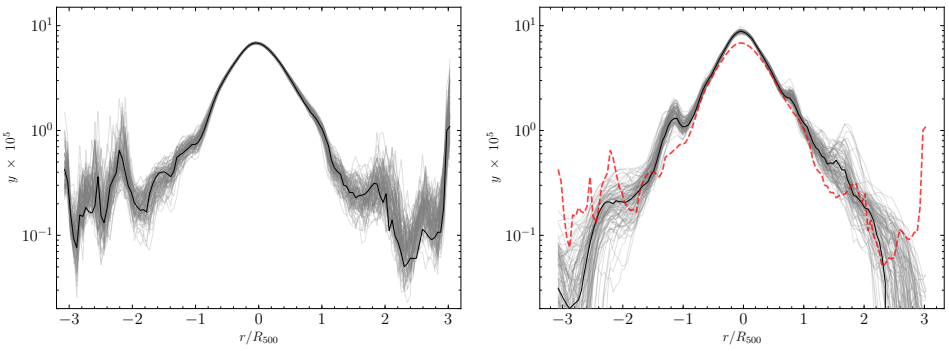

(a) Van Cittert deconvolution **(b)** new deconvolution

Figure 3.28. Profiles of the Compton y-parameter extracted from a 10 arcmin-wide vertical cut passing through the centre of the tSZ maps of cluster A2319, produced with the two versions of the imaging algorithm. Solid black lines in each plot represent the signal estimated from the original HFI maps, while light grey lines are the cuts across each of the $N_{\rm tot} = 100$ tSZ mock maps from the bootstrap-based procedure detailed in section. 3.3.2. The solid black curve of panel (a) is superimposed as a dashed red line to the cuts in panel (b) for comparison purposes.

here that both techniques are sensitive to the basis functions used to project the deconvolved signal. To be specific, Van Cittert method is particularly suitable in highlighting ellipsoidal and elongated features, since it is a regularization of curvelet coefficients. The wavelet coefficient-wise deconvolution, on the contrary, is applied to wavelet coefficients, thus it provides a better localization and detection of peaks. This is evident from Figure 3.26b, where the signal in the cluster centre is recovered more efficiently, with respect to Figure 3.26a. Another important element that improves peak localization is the larger wavelet support which enters the chi-square minimization in the new deconvolution (see Figure 3.25), as a consequence of taking the modulus of the wavelet function to decompose the residuals. Practically, this corresponds to computing wavelet coefficients over a larger sky region, thus enhancing the SNR of the detection.

To better illustrate the improvement of the stability in cluster outskirts, we show as solid black lines in Figure 3.28, the profiles of the Compton y-parameter extracted from a 10 arcmin-wide vertical cut passing through the centres of the images in Figure 3.26. Superimposed light grey lines are the same cuts from $N_{\rm tot} = 100$ different maps of the Comptonization parameter obtained with the bootstrap-based procedure (see section 3.3.2). It can be seen from Figure 3.28b that the non-iterative nature of the new deconvolution improves significantly the stability in low-signal regimes, allowing us to reach a minimum level of y of the order of 10^{-6}, which is consistent with the sensitivity of HFI. On the other hand, the diverging artefacts which hampered the reliability of the detection of substructures in the outskirts with Van Cittert deconvolution, are clearly visible in several realizations of the signal in Figure 3.28a. Moreover, the dispersion of the bootstrap profiles at radii $r \gtrsim 2R_{500}$ is on average 50 per cent lower with the new procedure, corresponding to a lower error in the reconstructed signal in these regions. The different characterization of

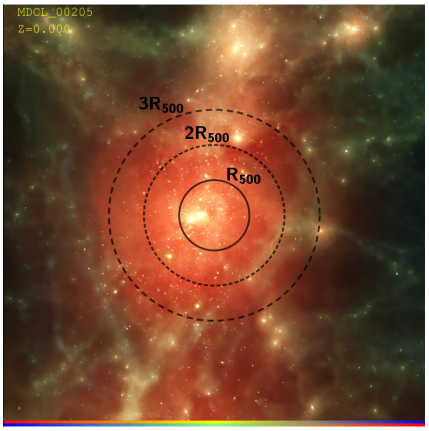

Figure 3.29. Distribution of the gas in a galaxy cluster extracted from the MUSIC CSF data set. The box is $12h^{-1}$Mpc on each side, covering $\approx 6R_{500}$ from the centre of the cluster. Multiples of the R_{500} radius are marked in the figure [taken from http://music.ft.uam.es].

the central peak discussed above is also clear from Figure 3.28b, where the value recovered with Van Cittert deconvolution is ≈ 23 per cent lower with respect to the value obtained with the new one based on wavelet coefficients. Such a difference is due to the joint effect of both the larger SNR provided by the absolute value of the wavelet kernel, and the number of iterations (three) used in Van Cittert deconvolution, as shown e.g. in Figure 3.23.

The following section is dedicated to an interesting science case which can be investigated with our new procedure: the structure of thermal pressure as derived from the tSZ maps in the outermost regions of galaxy clusters.

3.4 Unveiling the outskirts of galaxy clusters

The *outskirts* of galaxy clusters are of particular interest for astrophysics and cosmology. Indeed, they "mark the transition from the cosmic web to the ICM" [16], and they host several complex physical phenomena driven by the continuous accretion of matter onto the cluster centre. Figure 3.29 shows the gas distribution at $z = 0$ in a region enclosing a sphere of $6h^{-1}$Mpc radius centred on a galaxy cluster extracted from MUSIC hydrodynamical simulations [403] (see also section 4.2). It can be clearly seen how the ongoing process of cluster formation shapes the gas distribution, which highlights accretion along filaments from the outer regions, at radii $r \gtrsim 3R_{500}$. Cluster outskirts correspond to the radial range [367]:

$$R_{500} < r < 3R_{200} \ ,$$

where the lower end corresponds to the maximum radius accessible to current X-ray observations of moderate exposure time, while the higher end is the radius which marks the transition to the warm-hot intergalactic medium.
The outskirts region encompasses a number of characteristic radii related to interesting physical processes. They are:

i. the turn around radius from the spherical collapse: $r \simeq 2R_{200}$ (see also section 1.4.2);

ii. the infall region (with radii of the order of several Mpc) where caustics in galaxy redshift space are observed;

iii. the region which is expected to host most of the accretion shocks (between $R_{\rm vir}$ and $3R_{\rm vir}$) [292];

iv. the few-Mpc region where the two-halo term starts dominating over the one-halo term [113].

The understanding of such a variety of phenomena is extremely important, as they can significantly affect the thermodynamic structure of the ICM, possibly leading to observational results which are in disagreement with the theoretical predictions based on self-similarity. In this respect, cosmological simulations are undoubtedly a useful tool to investigate the physics of cluster outskirts. Indeed, numerical studies revealed that hydrostatic equilibrium does not hold in these regions. Moreover, the gas distribution is characterized by clumps and inhomogeneities, with filamentary structures or diffuse "bridges" possibly connecting the virial regions of neighbouring clusters. Also, a significant injection of turbulence from accretion shocks is present [e.g. 450]. All these features introduce biases in the estimate of cluster masses relying on thermodynamic quantities under the assumption of hydrostatic equilibrium, and this can potentially affect the derivation of the related cosmological parameters [381, 17, 256, 16].

From an observational point of view, the combination of complementary data in the X-ray and microwave bands is an optimal strategy to reconstruct the radial profiles of thermodynamic quantities from the cluster centre to the outskirts. As discussed in section 2.1.3, the X-ray signal suffers from low statistics at large cluster-centric distances, mainly due to the contamination from the particle background, while providing a detailed mapping of the ICM in cluster cores. Spectroscopic measurements in this band are often limited to radii $r \simeq R_{500}$. Nevertheless, it is worth mentioning that the low-background *Suzaku* X-ray satellite [249] recently allowed measurements up to $r \simeq R_{200} \approx R_{\rm vir}$ on a sample of four nearby relaxed clusters [318].

Despite such a promising achievement, the tSZ effect remains the best observable to probe cluster outskirts. This is testified e.g. by hydrodynamical simulations, which showed that the fluctuations of the tSZ signal at $r = R_{200}$ are about three times smaller than those of the X-ray signal detected at the same radius [381].

In this perspective, the recent X-COP (*XMM Cluster Outskirts Project*[3]) represents a reference study [144]. The project focusses on a sample of twelve massive objects ($M_{500} > 3 \times 10^{14} {\rm M}_{\odot}$) located at low to intermediate redshifts, $0.04 < z < 0.10$, observed in X-ray by *XMM-Newton* [441, 422] and at millimetre wavelengths by *Planck*. The sample objects have been selected imposing that the SNR of the *Planck* detection is larger than 12. Furthermore, the characteristic angular size θ_{500}, i.e. the angle subtended by the R_{500} radius of each cluster, is larger than 10 arcmin, so that they are well-resolved by *Planck* (see Table 3.2).

[3] https://dominiqueeckert.wixsite.com/xcop

Table 3.3. Identifiers, SNR of the *Planck* detection, redshifts, physical properties and galactic coordinates of the twelve galaxy clusters in the X-COP sample [taken from 173]. Galactic coordinates are taken from the NASA/IPAC Extragalactic Database (https://ned.ipac.caltech.edu).

Cluster name	*Planck* SNR	z	M_{500} ($\times 10^{14} M_\odot$)	R_{500} (kpc)	θ_{500} (arcmin)	l (deg)	b (deg)
A2319	30.8	0.0557	7.31	1346	20.8	75.70	13.51
A3266	27.0	0.0589	8.80	1430	21.0	272.13	-40.13
A2142	21.3	0.0909	8.95	1424	14.1	44.22	48.68
A2255	19.4	0.0809	5.26	1196	13.1	93.97	34.95
A2029	19.3	0.0766	8.65	1414	16.3	6.44	50.53
A85	16.9	0.0555	5.65	1235	19.2	115.23	-72.03
A3158	17.2	0.0597	4.26	1123	16.3	265.05	-48.93
A1795	15.0	0.0622	4.63	1153	16.1	33.82	77.18
A644	13.9	0.0704	5.66	1230	15.3	229.93	15.29
A1644	13.2	0.0473	3.48	1054	19.0	304.88	45.45
RXCJ1825‡	13.4	0.0650	4.08	1105	14.8	58.31	18.54
ZW1215‡	12.8	0.0766	7.66	1358	15.7	282.50	65.19

‡The full identifiers for these two clusters are RXC J1825.3+3026 and ZwCl 1215.1+0400, respectively.

The main physical properties of the X-COP clusters are summarized in Table 3.3. The details on the joint analysis of these data can be found in [173], while Figure 3.30 provides an overview of some thermodynamic profiles in the radial range $0.01 < r/R_{500} < 2$. Results indicate that the density and pressure profiles are in agreement with previous findings. Specifically, their behaviour is consistent with that of an ideal gas in hydrostatic equilibrium within the potential well of a NFW dark matter density profile. Self-similarity is fulfilled at radii beyond $0.3R_{500}$, with no significant differences between the cool core and the non-cool core clusters. Also, the entropy profiles beyond $0.5R_{500}$ are consistent with a purely gravitational generation of entropy, as predicted theoretically. From a comparison of the measured values of the gas fraction with the cosmic baryon fraction, the median amount of non-thermal pressure relative to the total pressure is found to be of the order of 6 per cent at R_{500} and of 10 per cent at R_{200}. The only exception is represented by cluster A2319 [145], which is a noticeable outlier in the sample [see the dedicated work 172].

3.4.1 TSZ imaging of X-COP galaxy clusters

Our aim is to complement the exquisite analysis of the X-COP clusters with an improved mapping of the Compton y-parameter. To this end, we applied the algorithm detailed in section 3.3 to the latest frequency maps by *Planck* 2018 release. Figure 3.31 shows our maps of the tSZ effect for the twelve clusters in the sample. In the majority of cases, the algorithm highlights the presence of blobs or extended filamentary structures at radial distances $r \gtrsim R_{500}$ from the cluster centre. The average minimum values of the Compton y-parameter we can recover from the faintest resolved structures are 2.0×10^{-6} and 4.2×10^{-6}, with a minimum significance of $3\sigma_y$ and $5\sigma_y$, respectively. This represents an improvement of a factor of 2.5 in sensitivity with respect to the version of the algorithm presented in B15, where the minimum signal for a 3σ detection is $y = 5 \times 10^{-6}$. It is important to

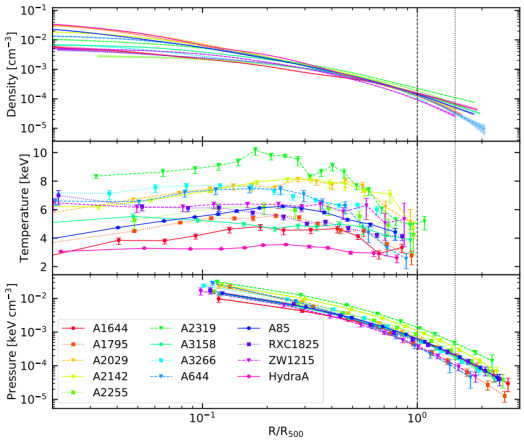

Figure 3.30. Radial profiles of the ICM density, temperature and pressure (from the top to the bottom panel, respectively) of the clusters in the X-COP sample, as derived from the joint analysis of *XMM* and *Planck* data [taken from 154].

stress that, thanks to the deconvolution, the algorithm is capable to recovering the elongated structure of the signal in the cluster central regions (see e.g. the cases of A2142 and A1644).

A particular cluster case which is worth mentioning is that of A2319, which is known to be a complex merging system that behaves as an outlier with respect to the other clusters in the sample [see 172, 145, 173]. The tSZ map of this object shows a number of blobs located in the virial region, which may be due to either substructures or clumpy ICM patches. The detailed study of these features and of their impact on the thermodynamic properties of this system is still in progress.

3.4.2 The cases of A2029 and RXCJ1825

Clusters A2029 and RXCJ1825 are two interesting targets for testing the algorithm. Among the X-COP clusters, they have been detected by *Planck* with intermediate (19.3) and low (13.4) SNR, respectively. A2029 has been widely studied in X-rays [see e.g. 260, 105, 66, 460]; on the contrary, RXCJ1825 has been poorly investigated in this band since its discovery [141]. Both clusters may be interacting with two known neighbouring systems, as suggested by the *Planck* Collaboration in [335]. Nevertheless, given the low significance of the data, no further analysis on the tSZ signal from possible connecting filaments has been explored in their work.

A2029

We show in Fig. 3.32a the contours from our map of the tSZ effect, superimposed to the X-ray surface brightness of A2029. We report the data from the *ROSAT* satellite, which allows the detection of the X-ray emission at larger radii than those probed by *Chandra* or *XMM-Newton*, thanks to its low particle background [440, 452]. The raw data have been denoised via the adaptive smoothing technique [142]. It can be seen that the tSZ signal in the central region matches fairly well with the X-ray surface brightness. Thanks to the deconvolution, we are able to detect the tSZ

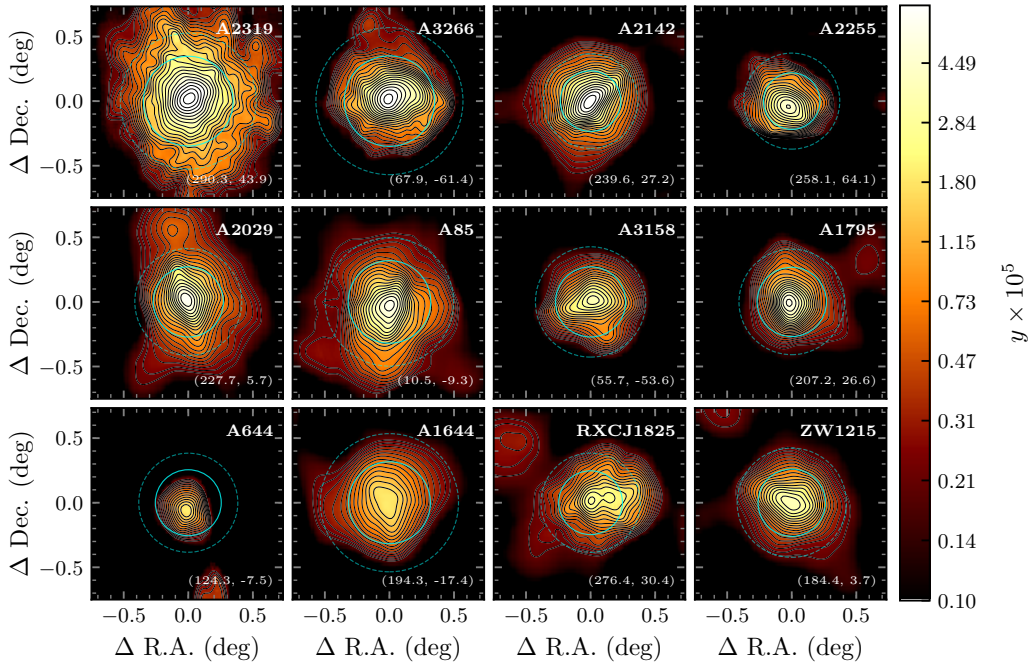

Figure 3.31. Zoomed maps of the Comptonization parameter of all the X-COP clusters, as obtained with our spectral imaging algorithm. Solid and dashed cyan circles on top of the images mark the R_{500} and R_{200} radii, respectively. The color scale is logarithmic and contours are logarithmically spaced by a factor of $\sqrt[4]{2}$, starting from 2×10^{-6}. The J2000 Equatorial coordinates of the cluster centres are reported in the bottom right corner of each map.

emission corresponding to the neighbouring cluster A2033 with a significance of $8\sigma_y$, which together with A2029 belongs to a small supercluster [147]. The X-ray and the tSZ peaks of A2033 show an offset which is, in any case, smaller than the best resolution of 5 arcmin provided by *Planck*. Our tSZ map clearly highlights an elongated projected structure that connects the two clusters. As testified by the image showing y/σ_y in Fig. 3.33a, this elongated excess of signal is significant to better than $5\sigma_y$. X-ray images do also show such an elongated morphology in the peripheral regions to the north-east, pointing to A2033. This suggested a possible ongoing merger between the two objects [see e.g. 142, 460]. However, recent analyses of the reconstructed density field through gravitational lensing, indicate that this signal is likely due to the gas in the overlapping outskirts of the two clusters at R_{200}, rather than to a filament connecting them [179]. Our tSZ imaging does represent an improvement with respect to the map shown in fig. 1 of [335], where the emission from A2033 is barely detected, as well as the signal between the two clusters. However, we cannot favour any of the two hypothesised processes. On the other hand, our maps may help in discriminating among possible scenarios proposed to explain the observed excess, for instance in future works combining microwave and X-ray data to model the three-dimensional thermodynamic properties of the ICM in each component of the system.

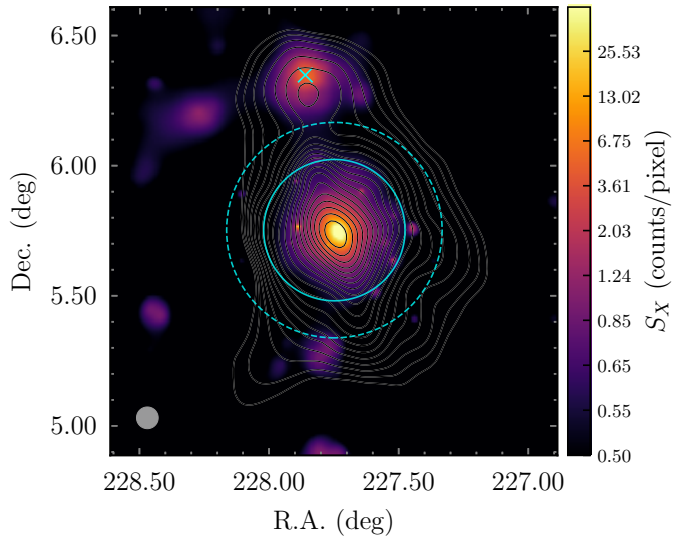

(a) A2029 from *ROSAT*/PSPC

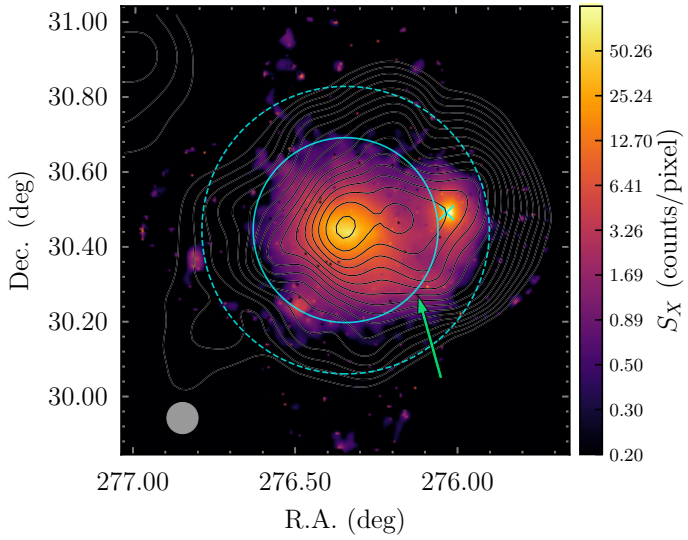

(b) RXCJ1825 from *XMM-Newton*

Figure 3.32. X-ray and tSZ signals of clusters A2029 and RXCJ2815. The maps show the vignetting-corrected and background-subtracted surface brightness in the X-ray energy band 0.5-2.5 keV. The superimposed contours represent the Compton y-parameter from our algorithm. The solid and dashed cyan circles on top of the images are drawn at R_{500} and R_{200}, respectively. The shaded circles in the bottom left corner of the maps represent the 5 arcmin beam of the tSZ maps. **(a)** Cluster A2029 mapped by *ROSAT*/PSPC. The cyan cross indicates the position of the neighbour cluster A2033. **(b)** Cluster RXCJ1825 mapped by *XMM-Newton*. The cyan cross marks the position of cluster CIZAJ1824, while the green arrow identifies a significant elongation which may be associated with stripped gas from a nearby group of galaxies.

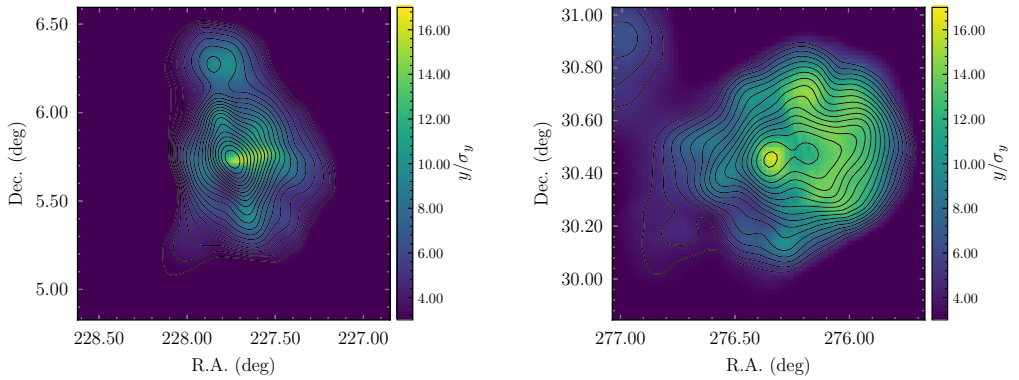

(a) A2029 **(b)** RXCJ1825

Figure 3.33. Maps of y/σ_y from a bootstrap run on clusters A2029 and RXCJ1825. The overlapped contours represent the tSZ signal.

RXCJ1825

In Fig. 3.32b, we show the X-ray surface brightness of RXCJ1825 from *XMM-Newton*, featuring wavelet denoising. The tSZ contours from our algorithm are superimposed to the image. As in the case of A2029, the tSZ emission follows pretty well the X-ray surface brightness. In particular, we notice that the peaks of the signal in the two bands coincide within 1 arcmin. The tSZ signal shows a significant elongation towards the neighbouring cluster CIZA J1824.1+3029 (CIZAJ1824 hereafter), even if the peak corresponding to this object is not clearly visible. A recent analysis based on the kinematics of their member galaxies, suggests that RXCJ1825 and CIZAJ1824 are in a pre-merger state [177]. Thus, also in this case, our maps may shed a new light on the hypothesis of a possible interaction in future analyses. Interestingly, our tSZ map shows a $14\sigma_y$-significant elongation to the south-west of the cluster, highlighted with a green arrow in Fig. 3.32b, which agrees with the excess in the X-ray surface brightness detected with *XMM-Newton*. Such an emission may be due to gas stripped from the past interaction between RXCJ1825 and a small, disrupted group of galaxies, which have been detected at the same redshift in the optical band [106]. This scenario is also supported by the recent finding of a radio halo extending in the same direction of the X-ray elongation [63]. Another feature we notice in the signal is the presence of a third structure located within R_{500}, that contributes at a level of $y \approx 5 \times 10^{-5}$, and which is not detected in X-rays. Nevertheless, the significance of this detection is 35 per cent lower with respect to the signal in the centre, as demonstrated by the map in Fig. 3.33b, constructed from a bootstrap run. Therefore, its detection is likely due to some localised irregularity in the instrumental noise in the raw HFI data.

To further quantify the significance of the signal reconstructed with our algorithm as a function of the radius, we computed the profiles of the ratio σ_y/y that is the inverse of the effective SNR. Specifically, we show in Fig. 3.34 the average of the vertical cuts passing through the centre of the maps of σ_y/y within a 10 arcmin-wide band, for the clusters A2029 and RXCJ1825. It can be seen that our algorithm

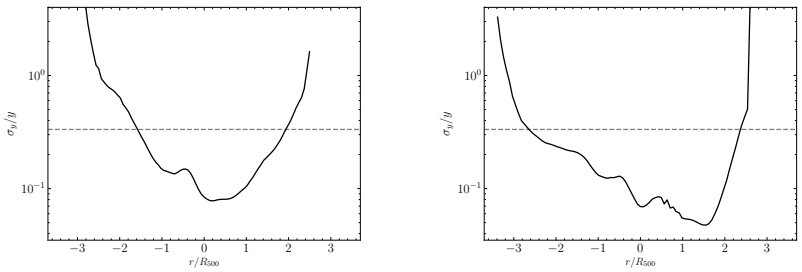

(a) A2029 **(b)** RXCJ1825

Figure 3.34. Profiles of σ_y/y of clusters A2029 and RXCJ1825. The purple dashed lines correspond to an effective SNR of 3 ($\sigma_y/y = 1/3$, see text for details).

provides a reconstruction of the signal with an effective SNR > 3 (marked with a dashed purple line in the plots), up to radii $r \simeq 2R_{500}$ for both clusters.

3.4.3 Impact of tSZ substructures on pressure profiles

As anticipated in section 2.2, accurate maps of the SZ signal are extremely valuable to derive the pressure of the gas and – when combined with spectroscopic and photometric data in X-ray – its temperature and density. As for the pressure, X-ray data are extremely useful to constrain the innermost regions of the profiles, whose reconstruction from tSZ measurements is often less reliable, since it is limited by a lower angular resolution. Thus, a number of joint analyses of SZ and X-ray data have been proposed to explore pressure profiles across a wide radial range [see e.g. 297, 54, 334, 143, 68, 173]. In any case, pressure profiles along the cluster radius from the deprojection of SZ data alone have also been extensively investigated in the literature [see e.g. 332, 393, 3, 379, 394, 380, 385].
In the majority of cases, there is an agreement in describing pressure profiles as self-similar, referring to the gNFW analytical model [303] introduced in equation (2.11). Also, following [303], the ICM pressure along the cluster radius has been characterized in many numerical works, e.g. with the aim of assessing the impact of different prescriptions for the gas physics, sometimes with the proposal of alternative models [see.g. 233, 30, 351, 185].
We mention here two reference parametrizations proposed in the literature.
The first one has been introduced by Arnaud and collaborators for a representative sample of galaxy clusters [14]. This parametrization, which defines the so-called *universal pressure profile*, has been determined using X-ray data up to R_{500}, and data from three different sets of hydrodynamical simulations at larger radii.
The second parametrization refers to the pressure profiles derived from the stacked tSZ maps of a sample of 62 galaxy clusters observed with *Planck*, which use pressure data derived from *XMM-Newton* observations in the innermost regions [334].
Figure 3.35 shows the fit to the gNFW model of pressure profiles from two samples of clusters detected by the *Planck* satellite in two redshift ranges, namely $z < 0.5$ and $z > 0.5$. It can be seen that self-similarity holds at intermediate radii, while the core and the outskirts are characterized by larger scatters. This feature has also

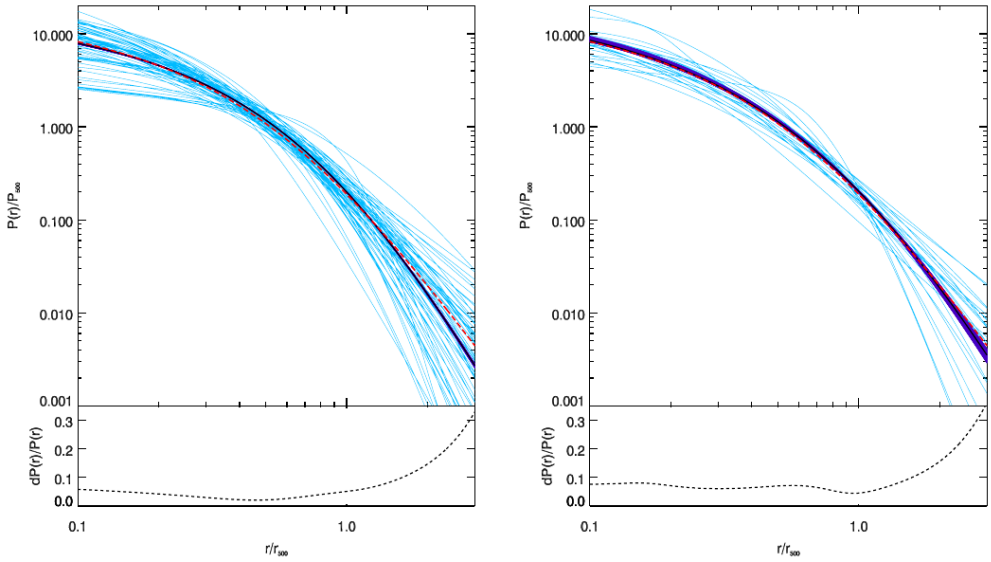

Figure 3.35. Fit to the gNFW model of pressure profiles for single clusters (solid cyan lines). The left panel refers to nearby objects ($z < 0.5$), while the right panel shows the profiles of distant clusters ($z > 0.5$). The dashed red lines represent the profile parametrized by the best-fit values found by the *Planck* Collaboration [334]. The lower panels in each plot show the dispersion of the single pressure profiles relative to the fit to the stacked profiles, given by the solid black lines with purple envelopes at the 68 per cent confidence level [taken from 68].

been found in the X-COP sample, where the intrinsic scatter of the thermodynamic profiles is minimum at radii $0.2R_{500} < r < 0.8R_{500}$ [173].
Generally speaking, the large scatter in the core regions is mostly due to the impact of radiative processes. On the other hand, the behaviour of the profiles at radii $r > R_{500}$ is affected by the complex dynamics and morphology of the outskirts. Specifically, clumps and inhomogeneities in the gas distribution, as well as substructures (see also section 2.1.2) or turbulence injection which are characteristics of these regions, may induce a breaking of the fulfilment of hydrostatic equilibrium, which is one of the underlying assumptions of cluster self-similarity. In this context, high-resolution imaging of clusters with the tSZ effect has an outstanding role to investigate the presence of filamentary structures, anisotropies or the occurrence of shocks in the outskirts, which are hardly detectable through X-ray measurements [see e.g. 5]. For instance, the recent work by [385] shows that overpressure detected with measurements of the tSZ effect at high angular resolution with the NIKA2 camera, produces a non-negligible bias towards higher values in the pressure profile at radii $r \lesssim R_{500}$. This is also expected to have a cosmological impact by means of the estimate of cluster masses based on the self-similar scaling relation linking the mass with the integrated Compton y-parameter. Using our improved tSZ imaging of well-resolved, large systems, we aim at characterizing the impact from pressure substructures beyond R_{500} for the first time.

Recipe for unbiased pressure profiles

In this preliminary analysis, we use *Planck* 2018 data for the X-COP clusters to derive unbiased pressure profiles from the masking of signal features at small scales located beyond R_{500}. To constrain the pressure profiles from our data set, we follow the *forward approach* based on template fitting, proposed in [68].
Pressure profiles from tSZ data are generally inferred from the radial profile of the Comptonization parameter, obtained by averaging the signal in the maps over concentric radial bins as proposed e.g. in [334]. This implies first of all to rely on a specific technique for an efficient extraction of the tSZ signal, but most importantly, it requires to subtract a zero-level offset with the aim of removing the astrophysical and instrumental background in the vicinity of the cluster. Such an offset is generally estimated by averaging the tSZ signal at sufficiently large radial distances from the centre. A major drawback of this procedure is that, depending on the offset value that is subtracted, the resulting profile may appear to be characterized by steep drops, which can mimic the effect of pressure shocks [see for instance the recent work by 213].
The forward approach is based, instead, on fitting the radial profiles of the available data, i.e. the HFI frequency maps. The removal of the astrophysical and instrumental contribution in the selected region is made by means of a wavelet high-pass filter, so that all spatial scales larger than the cluster size are suppressed[4] [see 68, for further details on this procedure]. The model profiles which we compare to the profiles obtained from the data, are constructed assuming the general prescription given in equation (3.78), i.e. properly combining the spectral and physical modelling of the sources of interest (CMB, thermal dust and tSZ effect). The frequency modelling is the same as the one described in section 3.3.1. The spatial modelling for CMB and thermal dust is obtained from the wavelet-denoised frequency maps at 217 and 857 GHz, respectively. The physical component of the tSZ signal is given, as usual, by the Comptonization parameter of equation (3.85).

We rewrite here, for convenience, equation (2.11) giving the gNFW profile, evaluated at the overdensity $\Delta = 500$:

$$p(r) = P_{500}\ \frac{p_0}{(c_{500}r)^{\gamma}[1+(c_{500}r)^{\alpha}]^{(\beta-\gamma)/\alpha}}\ . \tag{3.106}$$

We recall here that, p_0 is a dimensionless normalization factor and c_{500} is the concentration, defined as $c_{500} = R_{500}/r_s$, being r_s the scale radius of the dark matter density profile by [307], as in equation (2.3). The P_{500} scaling factor, which is a function of mass and redshift, is determined from self-similar arguments assuming a perfect gas law, as detailed in [303] and in [14]. It can be written as

$$P_{500} = 1.65\times10^{-3}\ E^{8/3}(z)\ \left[\frac{M_{500}}{3\times10^{14}h^{-1}\mathrm{M}_{\odot}}\right]^{2/3} h^2\ \mathrm{keV\ cm^{-3}}\ , \tag{3.107}$$

being $E(z)$ the Hubble parameter normalized to its present-day value (see equation (1.13)). In the following we will refer to a ΛCDM cosmology, so that $E(z) =$

[4] This relies on the use of HFI maps *not* corrected by any offset, differently from the imaging case.

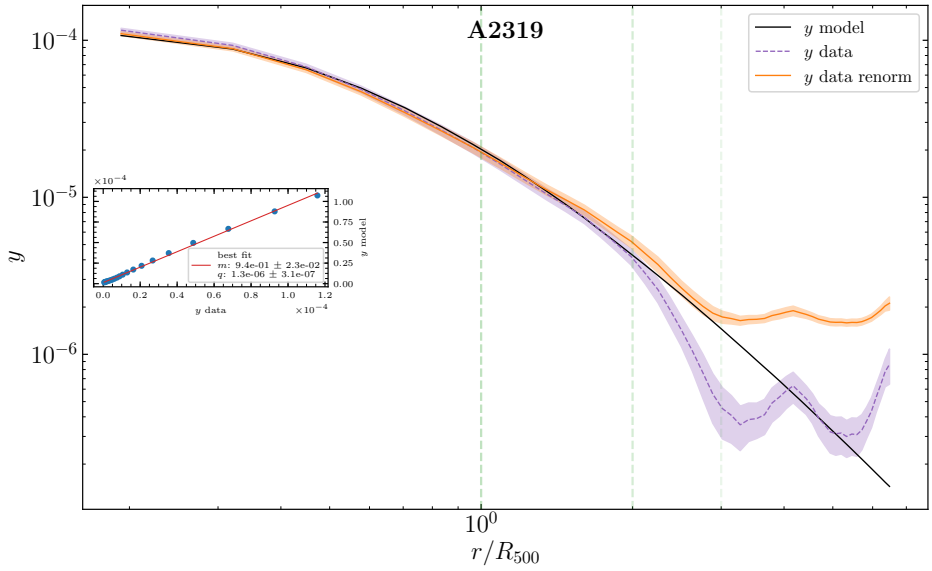

Figure 3.36. Re-normalization of the Compton y-parameter for cluster A2319 (see text for explanation).

$[(1+z)^3\Omega_{m0}+\Omega_\Lambda]^{1/2}$, with parameter values $\Omega_{m0}=0.3$, $\Omega_\Lambda=0.7$ and $h=0.7$, as in [68].

To get the best-fit parameters for the pressure profiles corrected for biases due to substructures, we proceeded as described in the following. We considered three X-COP clusters whose tSZ maps feature interesting substructures, namely: A2319, A2029 and A85. We applied the method by [68] described above to extract the pressure profiles of the clusters from the corresponding unmasked HFI data. We then used the set of parameters of the gNFW profile derived from the above fit, which we list in the top rows of Table 3.4, to evaluate the best-fit maps of the Compton y-parameter. The signal from substructures located in the peripheries of each cluster has been then obtained by evaluating the residuals between the tSZ maps from our spectral imaging algorithm (shown in Fig. 3.31), and the corresponding model maps mentioned above. To avoid zero-level biases, we re-normalized the signal in our tSZ maps, y, to the best-fit signal, $y_{\rm bf}$, as illustrated in Figure 3.36 in the example case of cluster A2319. To this end, we computed the radial profiles across the data and the model maps, represented as the purple and the black lines in Figure 3.36. Then, we calculated a robust linear fit within $3R_{500}$, to retrieve the normalization factor, m and the intercept q, such that the relation between the model map, $y_{\rm bf}$, and the data map y, is: $y_{\rm bf}=my+q$, being m and q constants, as shown in the panel inserted to the left-hand side of the same figure. The re-normalized signal is then calculated as $y_{\rm renorm}=m\ y+q$, as represented by the orange curve. The shaded bands around the profiles of y and of $y_{\rm renorm}$ have been obtained from the radial profiles of the $1\sigma_y$ bootstrap-derived error maps on y, described in section 3.3.2.
After re-normalizing the signal, we computed the residuals $y_{\rm renorm}-y_{\rm bf}$. In particular, we selected only the residual signal located outside the R_{500} radius, and we imposed it to have an amplitude higher than $1\sigma_y$, which is the error on the tSZ maps

Table 3.4. Best-fit parameters to the gNFW model obtained from the procedure described in [68]. The γ parameter has been kept fixed to 0.3081, which is the value by [14]. We distinguish the two cases without and with the masking of tSZ-detected substructures.

Configuration	cluster name	p_0	c_{500}	α	β
Without masks	A2319	9.8 ± 0.5	0.65 ± 0.09	0.88 ± 0.04	5.8 ± 0.2
	A2029	5.7 ± 2.1	2.3 ± 0.4	1.5 ± 1.4	3.6 ± 0.3
	A85	3.5 ± 0.9	3.0 ± 0.3	7.0 ± 1.4	2.7 ± 0.1
With masks	A2319	5.6 ± 0.3	0.39 ± 0.02	1.04 ± 0.02	9.6 ± 0.4
	A2029	2.6 ± 0.6	0.2 ± 0.2	1.0 ± 0.1	25 ± 6
	A85	3.3 ± 0.9	2.5 ± 0.4	4.8 ± 1.6	3.2 ± 0.5

we estimated from the bootstrap technique. The resulting masks that we use to exclude the pixels in the calculation of the profiles are shown in the middle panels of Figure 3.37, together with the un-masked and the masked tSZ signal. Despite the large radial range covered by our maps, we limited the calculation of all radial profiles and of the corresponding best fit to the maximum radius $r = 3R_{500}$, which is a limit imposed by the SNR of the available data. It is important to stress that the mask has been applied to the single frequency maps by *Planck* in the template fitting procedure. Figure 3.38 shows the preliminary results on the gNFW pressure profiles from our method after removing overpressure in the outskirts, in the cases of cluster A2319, A2029 and A85. The corresponding best-fit parameters are listed in the bottom rows of Table 3.4. It can be seen that, as expected, the pressure profiles become steeper in the outskirts in the masked case, because of the removal of pressure from substructures. In the case of cluster A2319, which has been detected by *Planck* with the highest SNR, we find smaller envelopes, and the two profiles are distinguishable at the 68% confidence level beyond R_{500}.
The remarkable aspect that we want to stress here is that the effect of substructures on pressure in the outskirts can be clearly seen in *single* cluster profiles. Clearly, this method can be applied only to well-resolved objects, as in the case of the X-COP sample detections with *Planck*.

Future developments

The robustness of the above procedure for substructure masking is currently under test, with a possible comparison with X-ray photometric data. In particular, we plan to extend this analysis to all the clusters in the X-COP sample and, subsequently, to the stacked data to compare our results with known universal profiles from the literature. A proper treatment of possible cluster asphericities will be also addressed, by means of a refinement of both the adopted theoretical model and the masks.
Also, this assessment could have a significant impact on the general thermodynamic properties of the unique case of cluster A2319, which we are addressing in a work in preparation. In the dedicated study by the X-COP collaboration [see 172], the diverse behaviour of this system with respect to the other clusters in the sample has been interpreted as a consequence of its complex dynamics. Indeed, the support from non-thermal pressure in this cluster has been found to be at the level of 50 per cent

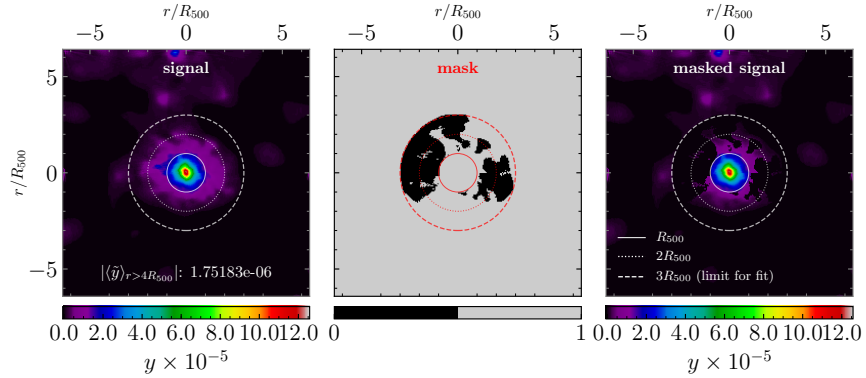

(a) A2319

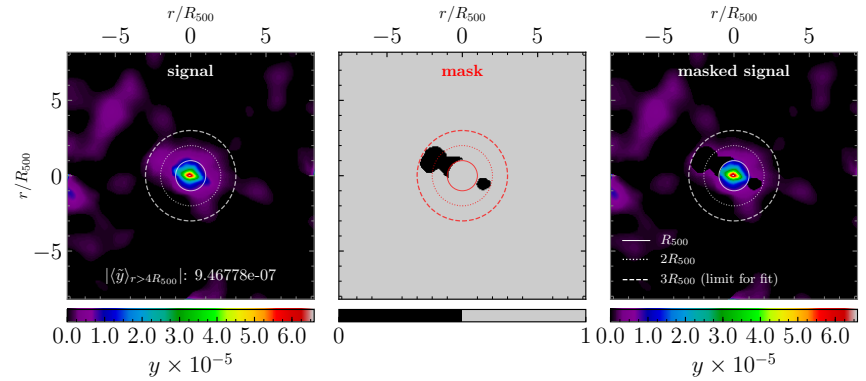

(b) A2029

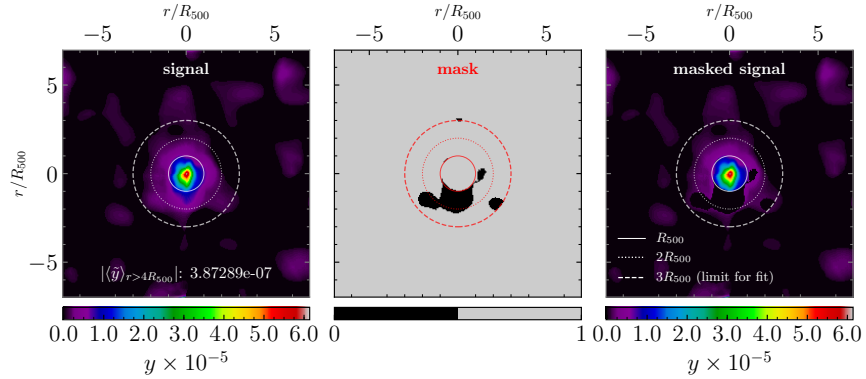

(c) A85

Figure 3.37. Removal of significant substructures from the maps of the Compton y-parameter of clusters A2319, A2029 and A85. **Left panel.** Original signal from the clusters as obtained from the imaging algorithm applied to the six HFI raw data maps. **Middle panel.** Mask applied to the signal to remove substructures (see text for the procedure). **Right panel.** Signal which is actually kept after the masking of substructures. Circles are drawn at 1, 2 and $3R_{500}$.

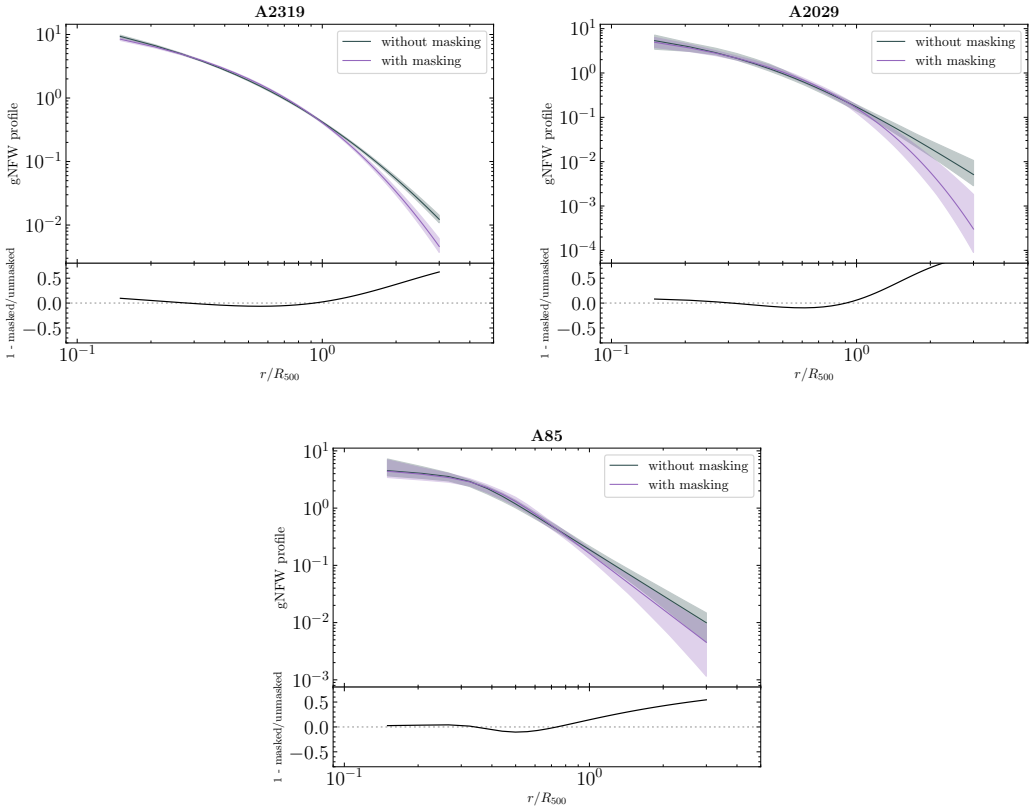

Figure 3.38. Fit to the gNFW pressure profiles using the unmasked and the masked data (i.e. without substructures), for clusters A2319, A2029 and A85. The shaded bands give the 68% confidence limit. The sub-panels to the bottom of each plot show the relative difference between the two profiles.

of the thermal one at the virial radius. Nevertheless, the outlying pressure profile of A2319 may be also explained by accounting for the pressure contribution from small structures, which are clearly detected in our maps of the Compton y-parameter of this object. Such additional pressure may ultimately bias the cluster mass towards higher values, which can have an impact on the rescaling of the pressure profile itself within R_{500}. More generally, a correction of the effect of pressure substructures on the mass of single clusters would have an impact on cluster-based cosmology. Indeed, as discussed in section 1.4.2, it is a central quantity in the cluster mass function, and it can affect the estimate of the related cosmological parameters.

Chapter 4

Clusters rotation and kinetic Sunyaev–Zel'dovich effect

In this Chapter, we introduce the problem of the underestimate of cluster masses descending from the assumption of hydrostatic equilibrium. In this context, we focus on the contribution from non-thermal motions as a possible solution and, in particular, we investigate the rotation of the diffuse medium in clusters. To this end, we provide a summary on the techniques which can be used to detect cluster rotation, focussing on the kSZ effect. Then, we introduce the set of hydrodynamical simulations of clusters that we considered in our analysis, namely the MUSIC catalogue. It follows a study on the properties of the angular momentum vector of the gas and the dark matter components in a selected sample of clusters, which allowed us to introduce a new law for gas rotation along the cluster radius. We then present our study on the recovery of the rotational signal from mock maps of the kSZ effect, assuming the best observational configuration. We conclude with a preliminary investigation of cluster rotation inferred from the velocities of the galaxy members, in the light of possible multi-probe observations of rotation in clusters with future instruments.

4.1 Rotational motions in galaxy clusters

The ICM in galaxy clusters is characterized by ubiquitous non-thermal motions at different scales, as testified by a number of numerical studies [see e.g. the recent review by 413]. On large scales, the continuous process of structure formation induces accretion-driven flows of gas towards the cluster centre, which can be associated with both coherent radial infall and turbulence [e.g. 449]. More complex events, such as merging of smaller clusters, can trigger sloshing motions and they can originate cold fronts, with abrupt gradients of the thermodynamic properties. On the other hand, the small-scale dynamics in the innermost cluster regions are largely influenced by the energy feedback provided by the central AGN.

A possible interesting scenario is that the diffuse matter components in clusters (i.e. the dark matter and the ICM), and possibly also the galaxies, may have coherent *rotational* motions. Large-scale global rotations supposedly originated from tidal

torques have been firstly investigated by Peebles in 1969 [322]. Such rotations can account for the non-zero angular momentum of large structures, given that the contribution to this quantity from non-ordered motions is averagely null. More specifically, the amount of rotational energy can be quantified by the *total* spin parameter:

$$\lambda_{\rm tot} = \frac{L_{\rm tot}|E|^{1/2}}{GM^{5/2}} \ , \tag{4.1}$$

being $L_{\rm tot}$, E and M, the modulus of total angular momentum vector, the total energy and the total mass of the cluster, respectively.
As suggested by numerical simulations, off-axis mergers of clusters can also originate a rotation, with velocities of the order of thousands $\mathrm{km\,s^{-1}}$ [373, 378, 374]. As a consequence, a gradient in the velocity structure of the ICM should be observed, as reported in the analysis by [140] based on X-ray data.

Besides affecting the global evolution of the formed structures, rotational motions of the ICM can impact cluster astrophysics and cosmology. For instance, rotation is expected to induce magneto-rotational instability in cool core clusters [313], and it may decelerate the accretion of matter to the BCG [442].
From a cosmological point of view, rotation can play a significant role in obtaining reliable estimates of cluster masses. The latter are key observables to constrain the parameters concerning with structure formation [see the recent review by 355]. As discussed in section 2.1.3, cluster masses can be derived from different observables. The most widely used method, though, is based on evaluating the radial gradients of the profiles of the thermodynamic properties of the gas, under the assumption of hydrostatic equilibrium within the potential well of dark matter. In a SZ-based approach, the hydrostatic mass within the radius r can be derived from the gradient of the pressure profile, combined with the density profile from ancillary X-ray data. We report here for convenience the corresponding expression as in equation (2.19):

$$M_{\rm he}(<r) = -\frac{rp(r)}{G\rho(r)}\frac{d\ln p(r)}{d\ln r} \ .$$

While being based on more and more precise reconstructions of the thermodynamic profiles of the ICM, the above approximation systematically underestimates the true cluster mass. Indeed, several numerical works indicate that the relative difference between the true and the hydrostatic mass ranges between 10 and 25 per cent [e.g. 363, 304, 232, 221, 330, 10, 283, 403, 42]. Such a discrepancy is then quantified through the *hydrostatic mass bias*:

$$b_{\rm he} = \frac{M - M_{\rm he}}{M} \ , \tag{4.2}$$

where the true mass, M, can be easily obtained from simulations as the sum of the masses of all the particles.
Besides the biases which may be introduced by asphericity, a possible cause of this difference could be a non-negligible contribution from additional non-thermal pressure terms supporting the gas against gravity. These terms can originate from ICM flows associated with turbulence, or to coherent motions such as rotation or radial infall [161, 162, 449, 254, 40, 308, 255, 309, 410]. In this respect, the mass of

a cluster can be written by virtue of Euler's equation and Poisson's equation as [162]

$$M = \frac{1}{4\pi G}\int_{\mathcal{S}}\left[-\frac{1}{\rho}\boldsymbol{\nabla}(p+p_{\rm turb}) - (\boldsymbol{v}\cdot\boldsymbol{\nabla})\boldsymbol{v}\right]\cdot\ d^2\mathcal{S}\ , \tag{4.3}$$

where $\mathcal{S}$ is the surface enclosing the gas, p is the pressure of the gas, ρ is its density, and $\boldsymbol{v}$ is its velocity. The term proportional to the pressure gradient takes into account the contribution from random motions, both thermal and turbulent, which are associated with the corresponding pressure terms p and $p_{\rm turb}$. On the other hand, the velocity term includes the support from ordered motions, i.e. rotation and streaming. Thus, from equation (4.3), the full expression for the mass can be written as

$$M = M_{\rm he} + M_{\rm turb} + M_{\rm stream} + M_{\rm rot}\ , \tag{4.4}$$

which reduces to the hydrostatic one when neglecting the dynamical masses associated with turbulence and ordedred motions.
The explicit expressions of the streaming mass and of the rotational mass follow from the evaluation of $(\boldsymbol{v}\cdot\boldsymbol{\nabla})\boldsymbol{v}$ in spherical coordinates [43]. Denoting the polar and the azimuthal angles as θ and ϕ, respectively, one has:

$$M_{\rm stream} = \frac{1}{4\pi G}\int_{\mathcal{S}}\left(\frac{v_\theta^2+v_\phi^2}{r}\right)\cdot\ d^2\mathcal{S} \tag{4.5}$$

$$M_{\rm rot} = -\frac{1}{4\pi G}\int_{\mathcal{S}}\left(v_r\frac{\partial v_r}{\partial r} + \frac{v_\theta}{r}\frac{\partial v_r}{\partial\theta} + \frac{v_\phi}{r\sin\theta}\frac{\partial v_r}{\partial\phi}\right)\cdot\ d^2\mathcal{S}\ . \tag{4.6}$$

Figure 4.1 shows the radial profiles of the mass terms of equation (4.4), evaluated separately for a relaxed and a disturbed cluster taken from the simulations analysed in [162]. The top panels illustrate that the hydrostatic mass alone (solid red lines) clearly underestimates the true mass (solid black lines). On the contrary, the true mass is better recovered when the dynamical terms (dashed red lines) are taken into account, as illustrated by the solid green line. Specifically, the correction is more relevant in the innermost regions (below $r \lesssim 0.3R_{500}$), where a larger rotational support is expected. As highlighted in the bottom panels of Figure 4.1, the streaming mass term, $M_{\rm stream}$, is generally found to be less important in the total mass budget with respect to the rotation term, especially in a relaxed cluster. In any case, its contribution increases in the cluster outskirts, which are dominated by radial infall. Such findings suggest that accounting for the mass terms arising from non-thermal pressure could be a promising solution to the problem of mass bias.
In the recent work by [145], a quantitative estimate of the non-thermal pressure support in the ICM based on observations is addressed for the first time, in the case of the X-COP cluster sample (see section 3.4 for a description). In particular, the amount of non-thermal pressure support is evaluated by measuring the deviations of the universal gas fraction from the predictions based only on gravitational collapse. The median value of the non-thermal vs thermal pressure ratio is found to be of the order of 6 per cent at R_{500}, and of 10 per cent at the virial radius. These values are smaller than the predictions from numerical simulations, which may be explained in terms of a faster and more efficient thermalisation of the kinetic energy in real clusters. However, in the case of cluster A2319 the above ratios take the values of 42

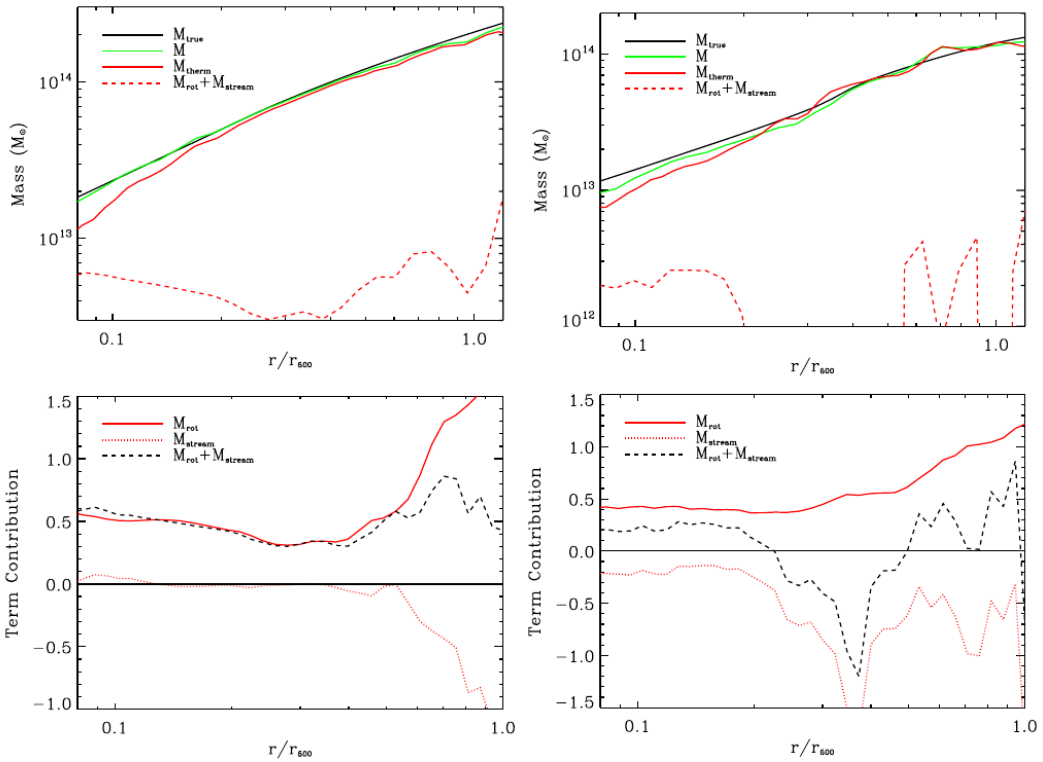

(a) relaxed cluster **(b)** disturbed cluster

Figure 4.1. Radial profiles of the mass terms appearing in equation (4.4). Left (right) panels illustrate the case of a simulated relaxed (disturbed) cluster. **Top panels.** Profiles of the mass from the sum of the rotational and the streaming terms, the thermal mass ($M_{\rm therm}$, corresponding to $M_{\rm he}$), the sum of the above three terms (M), and true mass from the simulation data ($M_{\rm true}$). **Bottom panels.** Profiles of the contribution to the total mass profile from the rotational and streaming masses, in units of $10^{13}\mathrm{M}_{\odot}$ [taken from 162].

and ~ 50 per cent at the same radii. This may be due to the very complex structure and not yet fully unveiled dynamics of this system. In any case, observations tailored to unveiling the dynamics within clusters are fundamental to address this problem.

4.1.1 Observational probes

Observationally speaking, the presence of rotational motions in clusters of galaxies is very challenging to be assessed. However, several methods can be applied to multi-wavelength cluster data to reach this goal, as reviewed in [189]. Indeed, global rotation can be investigated from spectroscopic measurements towards the galaxy members at optical wavelengths [216, 437, 271], or from observations of the diffuse ICM in the X-ray band [39, 266] and in the millimetre band through the kSZ effect [112, 101]. We provide below a short overview of the approaches exploiting optical and X-ray observations, and we will discuss the case of the kSZ effect in more detail in the dedicated section 4.1.2.

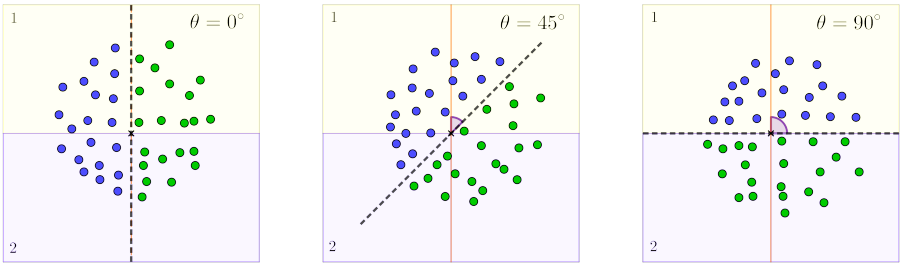

Figure 4.2. Schematic view illustrating the construction of the rotation curve proposed by MP17. Blue (green) points represent the projected positions of the galaxies within a cluster, having a positive (negative) projected velocity along the line of sight. The dashed line corresponds to the projected axis of rotation of the galaxies. The three panels show the example configurations with $\theta = 0°$, $45°$, $90°$, respectively, where θ is the angle between the rotation axis and the axis pointing to the North (orange line). Subscripts 1 and 2 in the definition of the velocity difference given in equation (4.7) refer to the corresponding half-planes shown here.

Optical band

Spectroscopy-based measurements of the velocity of the member galaxies can be used to establish the presence of a global rotation in clusters, under the assumption of a co-rotation of the baryonic components. A possible method consists in evaluating the spatial correlation between the velocities of the galaxy members [317]. However, the most used technique is based on measuring velocity gradients of galaxy velocities across the cluster [277, 216]. For instance, in [437] the rotational state is inferred from the spatial distribution of member galaxies having higher or lower velocities with respect to the mean global velocity. With this method, 26 per cent of the analysed clusters are found to be rotating.

The recent work by Manolopoulou & Plionis (2017) [271] (MP17 hereafter), proposes an improved variant of the velocity gradients technique. It is based on identifying rotating clusters from the inspection of a *rotation diagram*, which is constructed considering the projection of the velocity of the single galaxies along the line of sight. More specifically, referring to Figure 4.2 for a schematic visualization, the observed plane of the sky is divided in two half-planes, labelled here as 1 and 2, by means of a horizontal axis, which is kept fixed. From the projected velocities of the galaxies located in the two half-planes, it is possible to compute the average values, $\langle v_{\rm los}\rangle_1$ and $\langle v_{\rm los}\rangle_2$. The curve in the rotation diagram is a plot of the velocity $v_{\rm diff}$:

$$v_{\rm diff}(\theta) = \langle v_{\rm los}\rangle_1 - \langle v_{\rm los}\rangle_2 \ , \tag{4.7}$$

for varying orientations of the rotation axis of the galaxies projected on the plane of the sky, relatively to the vertical axis pointing to the North (θ, see Figure 4.2). If the projected rotation axis coincides with the vertical axis, as in the initial configuration shown in the left panel of Figure 4.2, the average velocities in the two half-planes should both cancel to zero. To construct the rotation diagram, all the projected galaxy positions are rotated by an angle θ in the clockwise direction. In this way,

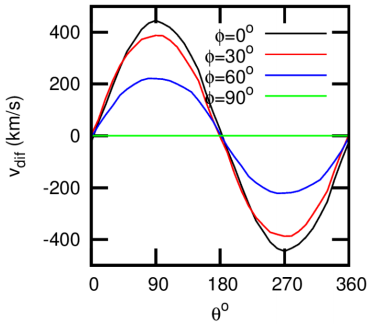

Figure 4.3. Example of rotation diagram for the member galaxies of a simulated cluster rotating at $450\,\mathrm{km\,s^{-1}}$. The ϕ angle in the legend gives the complementary angle to the orientation between the line of sight and the rotation axis. In this case, the maximum rotational signal, corresponding to the two axes being orthogonal, occurs when $\phi = 0°$ [adapted from MP17].

also the rotation axis is rotated by θ with respect to the vertical axis of the figure. If $\theta = 90°$, the two half-planes will contain only positive or negative projected velocities, respectively. Therefore, the velocity difference $v_{\mathrm{diff}}(90°)$ will be about twice the average velocity, which is ideally the same in both half-planes. The final curve of v_{diff} is expected to be a sinusoid as a function of the rotation angle θ, as illustrated in Figure 4.3 for different orientations of the line of sight. The projected rotation axis is inferred as the one corresponding to the value of θ which provides the highest amplitude in the rotation diagram. If the rotation axis is not oriented perpendicularly to the line of sight, the rotational signal gets dimmed, becoming almost undetectable for mutual orientations smaller than $\sim 30°$ (corresponding to $\phi \gtrsim 60°$ in Figure 4.3). Thus, the expected random orientation of the possible rotation axes of clusters with respect to the line of sight, clearly puts an intrinsic limit on the fraction of observable rotating clusters.
In MP17, two criteria are used to establish whether a cluster is rotating or not. They are based on (*i*) the value of the chi-square relative to the expected ideal rotation diagram, and (*ii*) the value of the Kolmogorov–Smirnov probability calculated from the distributions of v_{los} in the two half-planes. By applying this procedure to a total sample of ∼50 clusters, the authors find a fraction of 23 per cent rotating candidates, with galaxy rotational velocities of the order of a few thousand $\mathrm{km\,s^{-1}}$. Nevertheless, it should be stressed that the above method is largely prone to suffer from projection effects. Furthermore, since the dynamical evolution of the galaxies and of the ICM are significantly different, the assessment of a global rotation of the baryonic components of clusters is not straightforward. Indeed, as discussed in the upcoming sections, the results obtained from the study of the velocities of the member galaxies and those derived from the X-ray signal of the same cluster can be controversial.

X-ray band

One of the most direct ways to measure the rotation of the gas in clusters is based on X-ray spectroscopy, since any gas motion induces the shift and the broadening of

spectral lines [217]. In particular, the spatial distribution of the radial velocity is an important indicator, which can be inferred from a fit to the position of the spectral lines. Also, the line width resulting from the impact of gas motions is expected to be dominant with respect to the width due to thermal broadening.
As discussed also in section 2.1.3, the iron K_α line at 6.7-6.9 keV is the most prominent emission line in X-ray spectra of clusters; therefore, the corresponding energy band would be the optimal one to investigate the presence of a rotation. However, at present these measurements are not feasible because of the insufficient spectral and angular resolutions of currently available instruments. Indeed, the high angular resolution needed to map the velocity structure requires the use of CCD cameras, with a consequent loss in spectral resolution [266]. The latter, on the other hand, should be as high as the one needed to detect temperature variations $\lesssim 20\,\mathrm{eV}$, for rotational velocities of the order of $1000\,\mathrm{km\,s^{-1}}$. In this respect, upcoming X-ray missions, e.g. *Athena* [23, 382] and *XRISM* [433], can potentially shed new light on the kinematic properties of the ICM, thanks to their improved sensitivity and unprecedented spectral resolutions.

Despite the difficulties mentioned above, the measurement of the velocity gradients in Perseus cluster reported by [140] provides one of the first attempts to constrain rotation in clusters with X-ray data. More recent observations of the same cluster with the *Hitomi* satellite, indicate that the velocity dispersion in the core regions are compatible with a relatively low amount of turbulent motions, suggesting a quiescent dynamics [199].
Another interesting study tailored to the investigation of the ICM rotation by means of X-ray data has been recently proposed by [265]. They focus on cluster A2107, which has been found to be possibly rotating based on the results from recent studies of the velocities of the member galaxies in the optical band. To assess a possible rotation of the ICM, the authors produce a velocity map from the emission-weighted shift of the iron K_α line, as measured from *Chandra* CCD spectra. The maps are then fitted to a model which has been constructed following the prescriptions by [39], which follow from simulations. While being based on a promising approach, the results show that it is not possible to establish whether the ICM in A2107 is rotating or not. Moreover, the direction of the projected axis of rotation inferred from X-ray spectroscopy is significantly different from the one derived with the method by MP17 applied to galactic velocities. The angle between the two axes is indeed $\approx 144°$, with momentum vectors pointing in opposite directions. This fact suggests that, even in the presence of a global rotation within the same cluster, the baryonic components do not necessarily co-rotate. In this respect, the comparison with the results from data at millimetre wavelengths, namely via the kSZ effect, represent the ideal probe to confirm the rotational state of the diffuse gas in clusters.
A further X-ray observable which has been argued as a possible signature of gas rotation is the flatness of the isophotes tracing the surface brightness maps, as suggested by [162, 39]. Nevertheless, this indicator is likely less reliable than spectroscopy-based tracers. For instance, mock maps from hydrodynamical simulations of clusters showing a significant amount of rotational support do not feature evident flattening of X-ray isophotes [see 40].

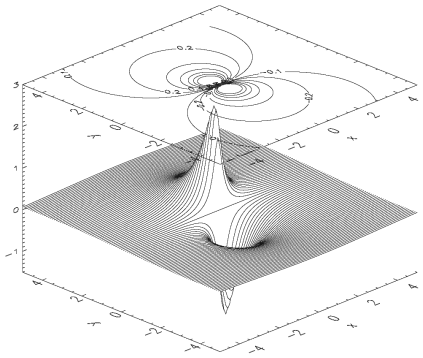

Figure 4.4. Temperature anisotropy in μK produced by the rotational kSZ effect from a massive cluster, according to equation (4.9). Axes labels are in units of the NFW scale radius of the cluster [taken from CC02].

4.1.2 Rotational kSZ effect

The kSZ effect is, in principle, another direct probe of the gas velocity projected on the line of sight (see equation (2.34)). Therefore, it may potentially be used to investigate ICM rotation.
Such a possibility was explored for the first time in the pioneering works by Cooray & Chen (2002) [112] (CC02 hereafter), and by Chluba & Mannheim (2002) [101].
For the sake of completeness, we rewrite here equation (2.34) in the following form:

$$\frac{\Delta T_{\rm kSZ}(\hat{n})}{T_{\rm CMB}} = -\frac{\sigma_T}{c}\int_{\rm los} n_e v_p \; dl \; , \tag{4.8}$$

which gives the temperature shift produced by the kSZ in the non-relativistic regime, observed along the direction identified by the vector $\hat{n}$. Here v_p is the projection of the gas velocity on the line of sight (los) which, in the simplest case, has a constant value.
If the gas rotates according to a law described by a generic angular velocity $\omega(r)$ along the cluster radius, equation (4.8) for such a rotational component becomes:

$$\frac{\Delta T_{\rm kSZ,r}(R,\phi)}{T_{\rm CMB}} = -\frac{\sigma_T}{c} R\cos\phi\sin i \int_R^{R_{\rm vir}} n_e(r)\;\omega(r)\;\frac{2r\;dr}{\sqrt{r^2-R^2}} \; , \tag{4.9}$$

as prescribed in CC02. R and ϕ in equation (4.9) are the polar coordinates of the map in the plane of the sky, while r is the three-dimensional radial distance from the cluster centre of mass. The $\sin i$ factor accounts for the orientation, given by the angle i, of the line of sight with respect to the rotation axis of the gas. If the line of sight is orthogonal or parallel to the rotation axis, the amplitude of the signal will be therefore maximum or null, respectively.
Figure 4.4 illustrates the temperature signal of equation (4.9) in the case of the best observational configuration, corresponding to $i = 90°$, for a cluster having $M_{\rm vir} = 5 \times 10^{14} {\rm M}_\odot$ at $z = 0.5$. It can be seen that the map features a dipole-shaped pattern, with two symmetric peaks having opposite sign. The rotation is here assumed to follow a solid body law, with a constant $\omega(r) = \omega_{\rm sb}$. The positive peak is

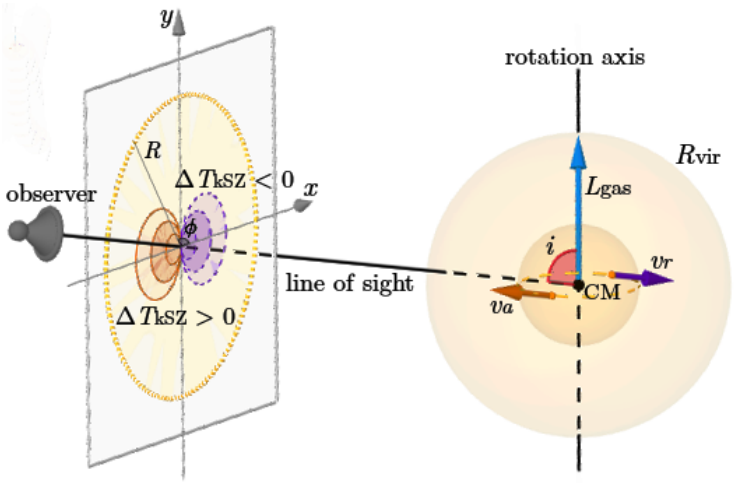

Figure 4.5. Schematic view illustrating the expected kSZ map from a rotating cluster, assuming the best observational configuration (i.e. with the line of sight orthogonal to the axis of rotation). The gas distribution in the cluster is assumed to be spherically symmetric, with the rotation axis aligned with the angular momentum vector of the gas as measured at the virial radius ($\boldsymbol{L}_{\rm gas}$). The velocity vectors, $\boldsymbol{v}_a$ and $\boldsymbol{v}_r$, indicate respectively the approaching and receding velocity components along the line of sight for two generic gas particles, located at the same radial distance from the cluster centre of mass.

produced by the projected velocity of the gas approaching to the observer; vice-versa, the negative one is due to the receding gas. A simple view of the same observational configuration is shown in Figure 4.5. In particular, this scheme clearly highlights that in this case the dipole is aligned horizontally with respect to the projected axis of rotation, supposedly coincident with the direction of the angular momentum vector of the gas at the virial radius.

In a more realistic case, the kSZ signal from a cluster is not only due to a pure rotational motion. Indeed, the contribution from the cluster bulk velocity is also present, and it may be dominant with respect to the rotation, depending on the projection of the bulk velocity itself on the line of sight.
The full signal describing the theoretical kSZ due to a possible rotation plus the bulk motion is therefore:

$$\frac{\Delta T_{\rm kSZ}(R,\phi)}{T_{\rm CMB}} = \frac{\Delta T_{\rm kSZ,r}(R,\phi)}{T_{\rm CMB}} - \frac{\sigma_T}{c}\, v_{\rm bulk} \int_R^{R_{\rm vir}} n_e(r)\, \frac{2r\ dr}{\sqrt{r^2 - R^2}}\ , \tag{4.10}$$

where the $\Delta T_{\rm kSZ,r}(R,\phi)/T_{\rm CMB}$ term for the rotational component is given in equation (4.9), while $v_{\rm bulk}$ denotes the projection of the cluster bulk velocity of the gas on the line of sight. In this case, the expected signal is characterized by an asymmetric dipolar pattern, depending on the dominating approaching or receding $v_{\rm bulk}$ for a given line of sight. If the projected bulk motion is significantly dominant with respect to the projected rotational motion, then the signal will reduce to the "classical" kSZ effect, with a single peak at the cluster centre, which is illustrated in the left panel of Figure 4.6.

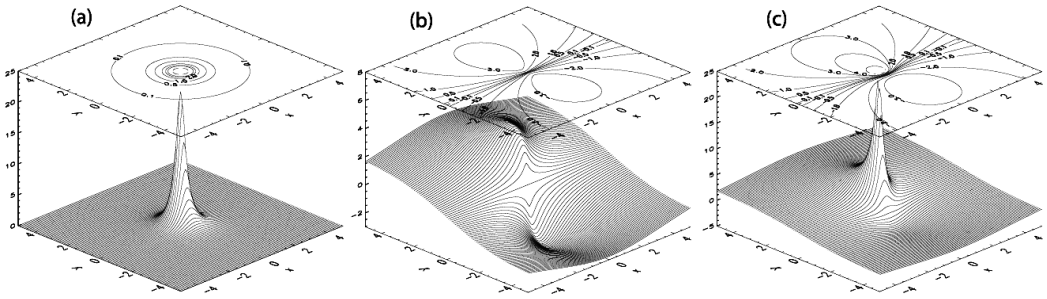

Figure 4.6. Possible contaminations of a purely-rotational dipole in CMB temperature anisotropies. **(a)** KSZ signal from the cluster bulk motion. **(b)** Dipole induced by gravitational lensing on the CMB. **(c)** Total signal, from the sum of the kSZ component from the bulk, the kSZ due to ICM rotation, and CMB lensing, supposedly aligned to the axis of rotation.

In [101], assuming the results of CC02 as a starting basis, they report a detailed analytical development of the characteristics of the rotational signal (e.g. the position of the peaks and the spatial extension of the dipole) as a function of cluster physical parameters, still referring to the case of a solid body rotation. By assuming a β-model for the electron number density (see equation (2.8)), some estimates of the expected amplitude are provided, in the perspective of a future detection with interferometric methods towards a set of nearby candidate clusters. In both CC02 and [101], the amplitude of the signal at the dipole peak is estimated to range between a few µK and tens of µK. Such estimates mainly depend on the mutual orientation between the line of sight and the ICM rotation axis, and on the dynamical state of the observed cluster. Specifically, since rotation may originate from merger events, it is reasonable to expect larger angular velocities in clusters involved in recent mergers.

The rotation of the ICM is not the only physical process which originates a dipole pattern in CMB anisotropies as photons propagate through galaxy clusters. Indeed, the gravitational lensing from the gradient of the dark matter potential in clusters can produce a dipole, which is aligned with the CMB large-scale gradient [402]. In addition to this, the transverse component of the bulk velocity of the cluster with respect to the line of sight produces a further lensing term, that is the moving-lens effect [291] originating from the non-linear Rees–Sciama effect. Both these lensing contributions have different orientations and amplitudes, which are expected to be of the order of ≈ 10 and a few µK, respectively. The imprint from lensing on CMB temperature anisotropies is illustrated in the middle panel of Figure 4.6, for the same cluster used to produce Figure 4.4. The right panel of Figure 4.6 shows instead the total signal coming from ICM rotation, plus the cluster bulk motion, plus the CMB lensing effect. In principle, the different dipole patterns can be separated by means of their different orientations and spatial extensions. Indeed, the CMB large-scale gradient is unlikely to be aligned with the rotation axis of gas in clusters. On the other hand, the rotational kSZ effect occurs mostly in the cluster innermost regions, (as testified by Fig 4.4), while the spatial extension of lensing dipoles covers larger scales. A classical approach to the problem of disentangling the lensing signal from the SZ effect has been discussed in [402], through suitable matching filters. On

the other hand, the more recent work by [360] proposes a novel procedure based on inpainting.

At present, a significant detection of the rotational kSZ with the available instrumentation has not yet been achieved. Besides lensing, also the contamination from the CMB itself, as well as from either foregrounds or instrumental effects, must be properly addressed (see also the paragraph dedicated to kSZ observations in section 2.2.4). Another important aspect is to reduce as much as possible the uncertainties affecting the reconstruction of complementary ICM properties (e.g. the temperature) based on X-ray observables, which are needed to disentangle the velocity. In this respect, the X-COP study (see section 3.4.1) provides an efficient approach for unveiling cluster properties, which points to interesting future perspectives. Furthermore, it is fundamental to have an exquisite angular resolution to observe the kSZ. The recent significant detection of the kSZ signal from the NIKA camera at 260 GHz with an effective angular resolution of 22 arcseconds [4], undoubtedly represents a promising result.

Towards a possible multi-wavelength detection of rotational motions in real clusters with future instruments, modern high-resolution gas-dynamical simulations are extremely valuable tools for preliminary analyses. A very first assessment of the detectability of turbulent and ordered motions through the kSZ is reported in [423]. The authors consider a large, isolated galaxy cluster from a cosmological simulation populated with dark matter and non-radiative gas physics. The kSZ map of this object shows the presence of a possible coherent rotation, that can be deduced from two clearly distinguishable spots of opposite sign in the innermost regions of the cluster.
In the following, we take a step forward, making use of more realistic high-resolution cluster simulations to improve the estimate of the rotational kSZ signal, and to possibly describe the ICM rotation with a more suitable model for the rotational velocity, different from the simple solid body.

4.2 The MUSIC data set

MUSIC (*Marenostrum-mUltidark SImulations of galaxy Clusters*[1]) is among the largest data set of high-resolution hydrodynamical simulations of clusters of galaxies [403]. It consists of more than 700 clusters and more than 2000 groups of galaxies, populating the MUSIC-1 and MUSIC-2 sub-sets. The latter have been built from the re-simulation of two parent N-body simulations: *MareNostrum Universe* [180] and *MultiDark* [354], respectively. Gas physics is treated according to both a purely gravitational prescription (NR run, see also section 2.1.1) and two modellings including radiative feedback from cooling and star formation mechanisms (CSF run), plus feedback from AGN (AGN run).

MareNostrum Universe is a non-radiative SPH simulation with two billion gas and dark matter particles (2×1024^3), in a cubic box of $500h^{-1}$ Mpc on a side. The adopted cosmological model in this simulation takes the parameter values from *WMAP1* results, i.e. $\Omega_{m0} = 0.3$, $\Omega_{b0} = 0.045$, $\Omega_\Lambda = 0.7$, $\sigma_8 = 0.9$, $n_s = 1.0$,

[1] http://music.ft.uam.es

$h = 0.7$ [245]. The MUSIC-1 sub-set consists in the re-simulation of 164 clusters from the MareNostrum Universe data set. They are selected according to their dynamical state, to re-simulate 82 relaxed objects, and 82 bullet-like clusters (referring to the case of cluster 1E0657-556 in Carena constellation, known as *bullet cluster*).
MultiDark is a dark matter-only simulation run in a cubic box of $1h^{-1}$ Gpc on each side, containing 2048^3 particles. The cosmological model used in this simulation takes the values from the joint fit of *WMAP7*+BAO+SNI data: $\Omega_{m0} = 0.27$, $\Omega_{b0} = 0.0469$, $\Omega_\Lambda = 0.73$, $\sigma_8 = 0.82$, $n_s = 0.95$, $h = 0.7$ [245]. The clusters chosen for MUSIC-2 re-simulations are those having virial masses $M_{\rm vir} > 10^{15}h^{-1}\mathrm{M}_\odot$ at redshift $z = 0$, for a total of 282 objects.

4.2.1 Code and re-simulation technique

MUSIC re-simulations have been generated using the GADGET-3 code [415]. It is a massively parallel, hybrid TreePM+SPH entropy-conserving code, where the gravitational force is computed using a hierarchical multipole expansion (see also section 2.1.1). Specifically, Poisson's equation is solved by splitting the gravitational potential in two terms: a long-range term whose solution is computed as prescribed by the PM procedure, and a short-range term solved by the Tree algorithm, which divides the space into smaller cells. The main physical quantities are derived from the interpolation of discrete values with the following spline kernel:

$$W(r, h_s) = \frac{8}{\pi h_s^3} \begin{cases} 1 - 6(r/h_s)^2 + 6(r/h_s)^3 & \text{for} \quad 0 \leq r/h_s \leq 0.5 \\ 2[1 - (r/h_s)]^3 & \text{for} \quad 0.5 < r/h_s \leq 1 \\ 0 & \text{for} \quad r/h_s > 1 \end{cases}, \tag{4.11}$$

proposed by [293], where r is the comoving distance between two fluid particles. The comoving smoothing length, h_s, varies according to the resolution, being equal to $6h^{-1}$ kpc in the high-resolution areas.

To re-simulate the clusters from the parent simulations with higher resolution, especially in the view of including radiative processes, MUSIC simulations employ the zooming technique of [239], implemented in a number of numerical works [e.g. 468, 365, 25, 116]. This procedure consists in filling the simulation box with particles of decreasing mass resolution (increasing mass value) with increasing distance from the centre of the box.
More specifically, each cluster selected from the two parent simulations at $z = 0$ is enclosed in a cubic box of $1h^{-1}$ Gpc-side, centred on the cluster centre of mass. The high-resolution region is chosen to coincide with the spherical volume of radius $6h^{-1}$ Mpc, $\mathcal{S}_{\rm hr}$, centred on the cluster, which encloses the outskirts region of massive objects ($\sim 3R_{\rm vir}$ for $M_{\rm vir} \simeq 10^{15}h^{-1}\mathrm{M}_\odot$). To create new initial conditions, all the particles within $\mathcal{S}_{\rm hr}$ extracted from a low-resolution version of the two parent simulations (filled with 256^3 particles), are mapped back to the highest considered redshift ($z = 9$ in MUSIC), to identify the corresponding Lagrangian region which will evolve into the $\mathcal{S}_{\rm hr}$ region around the cluster at $z = 0$. Once the new initial conditions are provided, the high-resolution sphere is filled with 2048^3 and 4096^3 particles for MareNostrum Universe and MultiDark clusters, respectively. In MUSIC-1 re-simulations the mass is fixed to $m_{\rm DM} = 1.03 \times 10^9 h^{-1}\mathrm{M}_\odot$ for dark matter

particles, and to $m_{\rm gas} = 1.82 \times 10^8 h^{-1}{\rm M}_\odot$ for gas particles. On the other hand, the corresponding values in the case of MUSIC-2 are $m_{\rm DM} = 9 \times 10^8 h^{-1}{\rm M}_\odot$ and $m_{\rm gas} = 1.9 \times 10^8 h^{-1}{\rm M}_\odot$, respectively. The value of gas particle masses varies in radiative runs, always being of the order of a few $10^8 h^{-1}{\rm M}_\odot$. In any case, the values of the masses $m_{\rm DM}$ and $m_{\rm gas}$ are chosen to be consistent with the assumed baryon fraction in the corresponding sub-set. The remaining volume of the box is filled with shells of dark matter particles with decreasing resolution down to 256^3, with a total of 4 shells for MUSIC-1 clusters and 5 shells for MUSIC-2 clusters, corresponding to as many mass refinements. It is worth to stress that SPH gas particles are included only at the highest refinement level. This procedure allows to save considerable computational time, while following the evolution of small-scale processes with appropriate resolution, over a large cosmological box.
The identification of virialized structures formed in each simulation box is made through the parallel *Amiga Halo Finder* (AHF) algorithm [242]. It automatically finds haloes, sub-haloes, and minor structures formed in the simulations which enclose a minimum of 20 particles [241]. The strategy adopted by the AHF is to find density peaks in a hierarchy of grids having a higher refinement in over-dense regions. It also provides the removal of unbound high-velocity particles causing perturbations in cluster dynamics.

Prescriptions for baryon physics

The modelling of the sub-grid physics of the CSF and AGN subsets in MUSIC accounts for the effects of radiative cooling, ultraviolet photoionization, star formation and supernova feedback, including the effects of strong winds from supernovae, as described in [417]. Stars are assumed to form from cold gas clouds on a characteristic timescale $t_\star$, and a stellar mass fraction $\beta_\star = 0.1$ is instantaneously released due to supernovae from massive stars ($M > 8{\rm M}_\odot$). This is consistent with assuming an universal Salpeter initial mass function with a slope of -1.35. In addition to this mass injection of hot gas, thermal energy is also released to the interstellar medium by the supernovae. The number of collisionless star particles spawned from each SPH parent gas particle is fixed to 2. Kinetic feedback is also included: gas mass losses due to galactic winds, $\dot{M}_{\rm w}$, is assumed to be proportional to the star formation rate $M_{\rm SFR}$, i.e. $\dot{M}_{\rm w} = \eta_\star M_{\rm SFR}$ with $\eta_\star = 2$. Additionally, the wind contains a fixed fraction $\epsilon_w = 0.5$ of the total supernova energy. SPH particles near the star formation region are subject to enter in the wind in an stochastic way, given an isotropic velocity kick of $v = 400\,{\rm km\,s^{-1}}$. Figure 4.7 shows pictures from 6 out of the total 14 snapshots, illustrating the gas density across the evolution of a massive cluster from the CSF run.
The simulations including AGN feedback have been carried with the same version of the GADGET-3 code that has been used for the simulations presented in [350]. This model is based on the original implementation by [416] (SMH model), with feedback energy released as a result of gas accretion onto supermassive black holes (BH). In this AGN model, BHs are described as sink particles, which grow their mass by gas accretion and merging with other BHs. The seeding of BH particles has been modified with respect to the original SMH model, and occurs only in haloes where star formation took place. A minimum mass of $5 \times 10^6 h^{-1}{\rm M}_\odot$ is assumed for

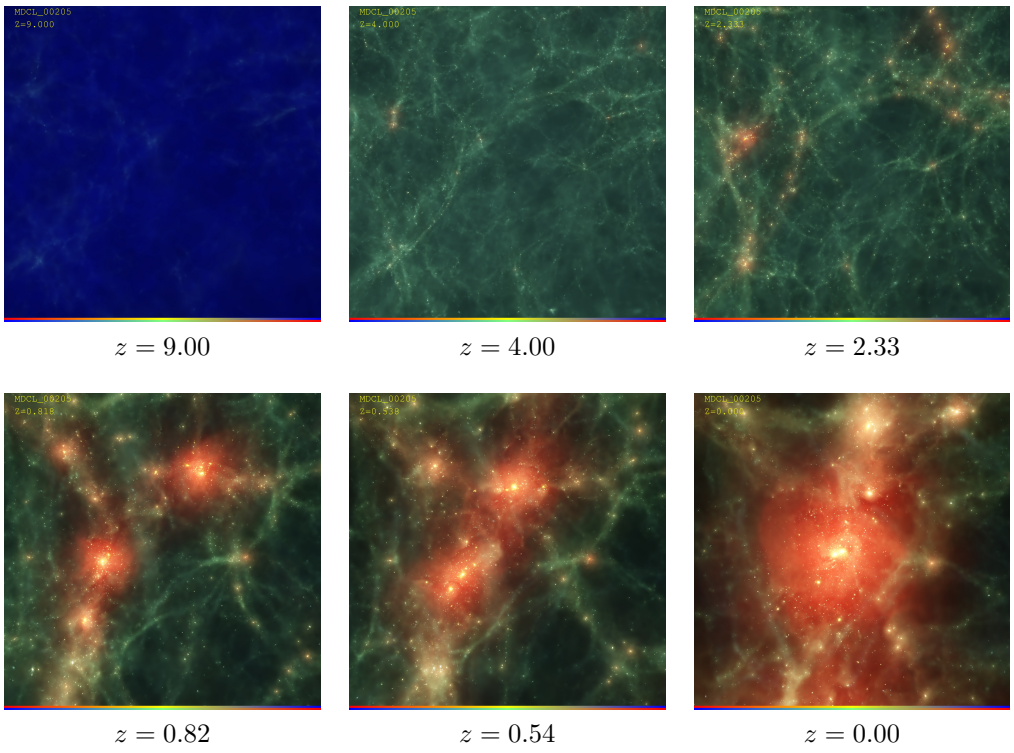

Figure 4.7. Snapshots of cluster 205 from MUSIC radiative run (CSF), within a box of $6h^{-1}$ Mpc on each side. Each image shows the gas density, and yellow dots represent stars [taken from http://music.ft.uam.es].

a friends-of-friends (FoF) group of star particles to be seeded with a BH particle. Seeded BHs are located at the potential minimum of the FoF group, instead of at the density maximum, as originally implemented by SMH. The pinning of the BH is regulated at each time-step to avoid advection. In this way a BH particle remains within the host galaxy, when this becomes a satellite of a larger halo. A more strict momentum conservation during gas accretion and BH merger is also set. Two BHs now merge when they are located at a distance from each other that is less than the gravitational softening and when their relative velocity is less than half of the sound speed. Finally, the AGN feedback is provided via thermal energy to the surrounding gas particles. Eddington-limited Bondi accretion produces a radiated energy which corresponds to a fraction $\epsilon_r = 0.1$ of the rest-mass energy of the accreted gas. A fraction of this radiated energy is thermally coupled to the surrounding gas with feedback efficiency $\epsilon_f = 0.1$. This parameter is regulated to reproduce the observed relation between the BH mass and stellar mass of the hosting halo [361]. Special care is devoted to the treatment of multi-phase and star forming particles to avoid loosing the AGN energy [see 350, for details]. No mechanical feedback is implemented in these runs, therefore jets and raising bubbles are not described. The transition from a 'quasar' phase to a 'radio' mode of the BH feedback happens when the accretion rate onto the BH becomes smaller than 1 per cent of the Eddington accretion [see also 411, 159]. At that instant, the efficiency of the AGN feedback is 4 times larger.

4.2.2 The Three Hundred project

The MUSIC code and data set constitute the benchmark used to assess the properties of the simulated clusters constituting the recent data set of *The Three Hundred*[2] project [116]. It consists in state-of-the-art hydrodynamical simulations of galaxy clusters with high mass resolution, run as a zooming-based re-simulation of objects extracted from *MultiDark PLanck2* (MDPL2) [240]. The latter is a dark matter-only simulation run in a cubic box of $1h^{-1}$ Gpc side, containing 3840^3 particles with mass $m_{\rm DM,MDPL2} = 1.5 \times 10^9 h^{-1}{\rm M}_\odot$, whose initial conditions are based on the cosmological parameters reported by the *Planck* Collaboration in 2015 [344].
More specifically, The Three Hundred data set consists of 324 spherical regions with a radius of $15h^{-1}$ Mpc having $M_{\rm vir} > 8 \times 10^{14} h^{-1}{\rm M}_\odot$ at $z = 0$, which have been extracted from the parent MDPL2 simulation. The mass resolution for the dark matter and gas particles is the same as in MUSIC, namely $m_{\rm DM} + m_{\rm gas} = 1.5 \times 10^9 h^{-1}{\rm M}_\odot$. On the other hand, the major difference with MUSIC resides in the improved treatment of gas physics. Specifically, The Three Hundred simulations are produced using the GADGET-X code, which features the implementation of a modern SPH scheme, which optimally treats discontinuities between different gas phases, thus overcoming the mixing problem affecting "classical" SPH codes [see e.g. 405]. Moreover, a more realistic modelling of sub-grid physics is also implemented, including feedback from AGN.
The main properties of the re-simulated clusters at $z = 0$ in The Three Hundred catalogue have been compared to the most recent compilations of observational data concerning with the concentration-mass relation, several indicators related to the stellar mass (e.g. the stellar fraction), and the main scaling relations in the optical, X-ray and microwave (SZ) bands. A comparison with the results from the GADGET-MUSIC code run towards the same initial conditions is also performed, as well as with the results from three different semi-analytical models of galaxy formation. The comparisons above show a good overall agreement between The Three Hundred outcomes and observational data. In particular, quantities related to star formation are better recovered with respect to MUSIC-based runs, which are characterized by an unrealistically efficient star formation because of the lack of AGN feedback. Noticeably, the properties of the ICM are consistent between the two numerical schemes and with the reference data. These results represent a very promising basis for future investigations on the dynamical properties of clusters, taking advantage of such improved, more realistic simulations.
In the following, we illustrate our analysis of MUSIC data tailored to unveiling rotational motions of the ICM, which will be possibly extended to the more recent The Three Hundred data set.

4.3 Rotation in MUSIC clusters

The assessment of rotational motions in the diffuse components in galaxy clusters can be addressed in two steps. The first one consists in characterizing the behaviour of the angular momentum vector along the cluster radius. Such an investigation is

[2] http://the300-project.org

possible only by using simulated data, since they allow the reconstruction of the three-dimensional dynamical vectors of all the particles within the clusters. From the characterisation of the specific angular momentum, it is then possible to infer the rotational law describing the tangential velocity as a function of the cluster-centric distance. The second step is to test a possible observational probe to unveil the expected motions. In this respect, the kSZ effect is one of the most promising probes, since rotational motions should imprint a characteristic signature on the temperature anisotropies induced by this effect, namely a dipole pattern.
In the following we apply such a two-step approach to a selected sample of MUSIC clusters.

4.3.1 Selected cluster sample

One of the main advantages of working with simulated data is the absence of possible selection biases which, on the contrary, affect data collected from observations. For instance, X-ray measurements are flux-limited, meaning that objects that are too faint cannot be detected. On the other hand, measurements of the SZ effect are mass-limited, since they are not (ideally) affected by cluster redshift.
To avoid any selection effect, we limited the investigation of rotation in clusters to a mass-selected sample of clusters extracted from the whole MUSIC-2 sub-set. Specifically, we picked all the objects with masses $M_{\rm vir} > 5 \times 10^{14} h^{-1} \mathrm{M}_{\odot}$ at $z = 0$, since they constitute a complete volume-limited sample. In other words, this means that more than 80 per cent of the clusters found in the original MultiDark volume of $(1h^{-1}$ Gpc$)^3$ above this mass limit at the same redshift have been re-simulated in MUSIC-2.
This sample has been considered for a number of ancillary works, e.g. the study of SZ and X-ray scaling relations [403, 41], and the characterisation of the dynamical state by means of X-ray indicators applied to the maps of the tSZ effect [104].

Relaxed clusters

With the aim of unveiling a possible rotation of the ICM, we identified the most relaxed objects in the above selected sample. This choice prevents possible contaminations from the motion of the gas in substructures located within the virial radius of the clusters. Indeed, in the specific case of the kSZ signal, the projected velocity of substructures along the line of sight may mimic the pattern of the expected signal from the rotation of the ICM. Whenever the distinction among relaxed and unrelaxed clusters is quoted in the forthcoming analysis, we refer to the criteria described in the following [20].
To assess the dynamical state of a cluster, we evaluated two dynamical indicators derived from the simulation data, which are largely employed in the literature [see e.g. 310, 353, 235, 284, 404, 240, 42].

Specifically, the first indicator is the normalized offset between the position of the maximum density peak, $\boldsymbol{r}_{\rho_p}$ and the position of the centre of mass, $\boldsymbol{r}_{\rm CM}$, that is

$$\Delta r = \frac{|\boldsymbol{r}_{\rho_p} - \boldsymbol{r}_{\rm CM}|}{R_{\rm vir}} \,. \tag{4.12}$$

The second indicator we consider is the ratio between the mass of the largest substructure within the virial radius and the virial mass of the halo, $M_{\rm sub}/M_{\rm vir}$ [see also 404]. A cluster is classified as relaxed if it simultaneously satisfies both the conditions $\Delta r < 0.10$ [139] and $M_{\rm sub}/M_{\rm vir} < 0.10$ [15, 404, 284]. Using these joint criteria, 57 per cent of the clusters in the total sample have been classified as relaxed. This fraction is consistent with results from observational data [see e.g. 383], from the analysis on the morphology of MultiDark simulated clusters [451], and from estimates for the re-simulated clusters in The Three Hundred catalogue [116].

4.3.2 Analysis of the angular momentum

Spin parameter

As discussed in section 4.1, the rotational state of a halo can be quantified by calculating the spin parameter λ, evaluated at the cluster virial radius. It can be interpreted as the ratio between the angular velocity of the system, and the angular velocity needed to provide rotational support to it [319], which is strictly connected with the circular velocity at the virial radius, $v_{\rm circ} = \sqrt{GM_{\rm vir}/R_{\rm vir}}$.
Besides its classical theoretical definition (see equation (4.1)), several simplified definitions have been introduced in the literature to calculate the spin parameter in simulations [see also 77, 180, 75]. In the following, we adopt the expression introduced by [77]:

$$\lambda_{\rm tot} = \frac{L_{\rm tot}}{\sqrt{2} v_{\rm circ} M_{\rm vir} R_{\rm vir}} \ . \tag{4.13}$$

The main reason for this choice is that the above equation allows us to write the spin parameter of each single matter component (gas or dark matter, DM hereafter), thus allowing for a comparison between their rotational properties. Indexing each component with μ, one has:

$$\lambda_{\mu} = \frac{L_{\mu}}{\sqrt{2GM_{\rm vir}R_{\rm vir}}\ M_{\mu}} \ . \tag{4.14}$$

We found that the values of the DM spin parameter are very close to those derived from the total angular momentum. This is not surprising since the mass of the DM component dominates over the baryonic one. The relation between $\lambda_{\rm tot}$ and $\lambda_{\rm DM}$ is linear, with a slope close to unity for all the three analysed subsets (NR, CSF and AGN). We show in Figure 4.8 the explicit comparison between the spin parameters of gas and DM, indicating a clear linear relation between the two. The corresponding best-fit parameters, obtained from a robust fit to the data using the bisector method [218], are listed in Table 4.1.

If rotation in clusters arises from tidal torques on large scales, then the spin parameter of the DM component is expected to follow a log-normal distribution [97]. Figure 4.9 shows the distributions of the spin parameters for the gas, the DM and the total matter content of the clusters in our sample, for the three different flavours. It can be seen that they are well-described by a log-normal distribution of the kind:

$$\mathcal{P}(\lambda)\ d\lambda = \frac{1}{\lambda\sqrt{2\pi}\sigma} \exp\left(-\frac{\ln^2(\lambda/\lambda_0)}{2\sigma^2}\right) d\lambda \ , \tag{4.15}$$

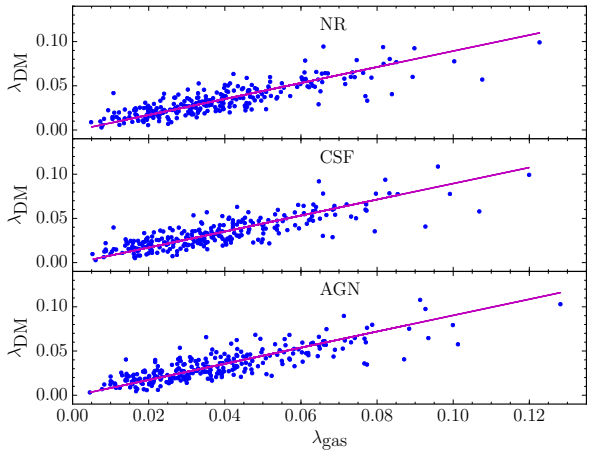

Figure 4.8. Relation between the spin parameters of the DM and ICM components for all the clusters in the sample from the three runs. The solid magenta lines represent the robust linear fits.

Specifically, the scale parameter λ_0 and the shape parameter σ derived from our sample of clusters are reported in Table 4.2. As expected, the similarity between total and DM values is also evident from these results. When comparing our values of the parameters with other works, we find a general agreement [26, 77, 447, 407, 180, 268, 75]. It is worth to stress that these studies refer to galactic or proto-galactic haloes, with the exception of [268], where objects on different scales are considered (from galaxies to clusters), and of [180], which include clusters of galaxies of the MareNostrum gas-dynamical simulation. Therefore, this result suggests that the shape of the distribution does not vary significantly from galaxies to clusters. The values of $\lambda_{0,\mathrm{gas}}$ are typically larger than those of the DM (by 13 per cent in our case), suggesting more rotational support. This may be because tidal interactions with surrounding large-scale structures have had more time to apply torques to the gas accreted at a later time.

Angular momentum profiles

After characterizing the spin computed up to the virial radius, we studied the amplitude and the direction of the specific angular momentum vector along the cluster radius, considering only the relaxed clusters. We produced radial profiles

Table 4.1. Values of the correlation coefficient (c_{corr}) and of the parameters for the linear fits shown in Figure 4.8, performed with the bisector method.

Data set	c_{corr}	Slope	Intercept
NR	0.84	0.90 ± 0.04	-0.001 ± 0.002
CSF	0.83	0.91 ± 0.05	-0.001 ± 0.001
AGN	0.83	0.91 ± 0.04	-0.001 ± 0.001

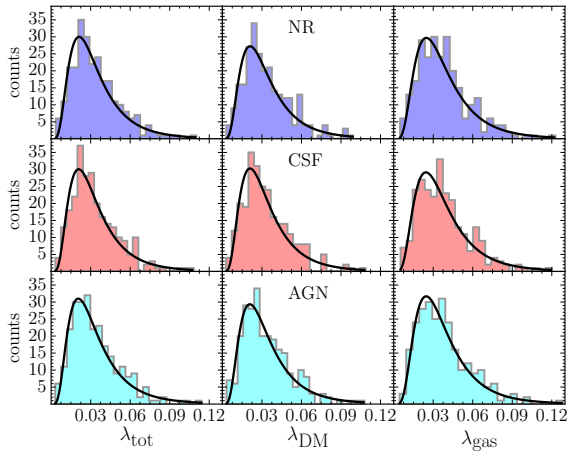

Figure 4.9. Distributions of the spin parameters of each matter component (along columns) for the three analysed subsets (along rows). The solid lines represent the fits to the log-normal distribution.

describing its modulus and orientation with respect to the angular momentum computed at the virial radius. We considered 15 concentric spheres with radius increasing logarithmically, from $r = 0.05R_{\rm vir}$ to $r = R_{\rm vir}$, to have a suitable radial sampling. We did not impose any condition on the number of particles in each sphere, but we would like to remark that the minimum amount of particles in each sphere is always above 10^4, i.e. enough to lead to robust results. For the i-th sphere, the modulus of the specific angular momentum $j(< r_i) = |\boldsymbol{j}(< r_i)|$ has been estimated as

$$j(< r_i) = \frac{|\boldsymbol{L}(< r_i)|}{M(< r_i)} = \frac{|\sum_k^{N_i} \boldsymbol{r}_k \times m_k \boldsymbol{v}_k|}{\sum_k^{N_i} m_k} \,, \tag{4.16}$$

where N_i is the number of particles inside the i-th sphere, $\boldsymbol{r}_k$ is the position of the k-th particle relative to the centre of mass, m_k is its mass, and $\boldsymbol{v}_k$ is its velocity vector subtracted by the velocity of the centre of mass.
The angle $\alpha(< r_i)$ quantifies the orientation between the angular momentum vector within the radius r_i, relative to the direction of the angular momentum vector at

Table 4.2. Values of the parameters λ_0 and σ from the log-normal fits to the spin parameter distributions for DM, gas and the total matter components of the analysed sample.

Data set	$\lambda_{0,\rm tot}$	$\sigma_{\rm tot}$	$\lambda_{0,\rm DM}$	$\sigma_{\rm DM}$	$\lambda_{0,\rm gas}$	$\sigma_{\rm gas}$
NR	0.0292	0.5655	0.0289	0.5674	0.0333	0.5470
CSF	0.0287	0.5641	0.0288	0.5638	0.0330	0.5489
AGN	0.0289	0.5810	0.0289	0.5755	0.0330	0.5416

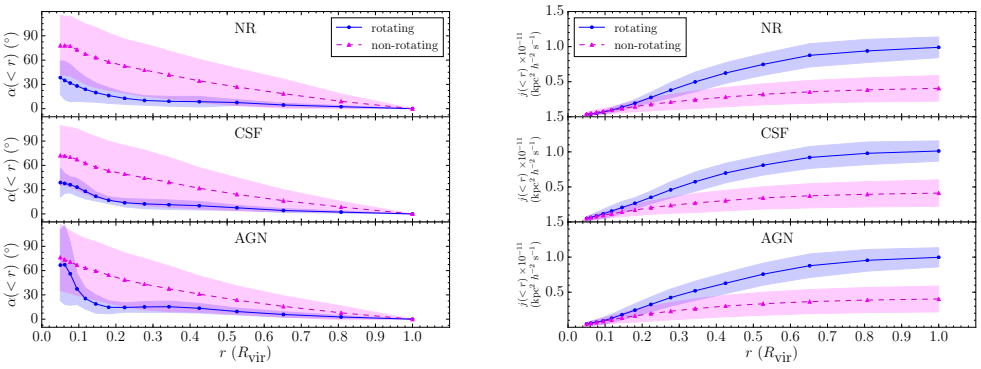

(a) direction **(b)** modulus

Figure 4.10. Radial profiles of the orientation (left panel) and the modulus (right panel) of the specific angular momentum of the gas in the three runs. The two populations of relaxed rotating and relaxed non-rotating clusters have been distinguished. The points in the plots represent the mean values for each population, and the shaded bands indicate the 1σ scatter with respect to the mean.

the virial radius. Thus, it is defined as

$$\alpha(< r_i) = \arccos\left[\hat{j}(< r_i) \cdot \hat{j}(< R_{\rm vir})\right] \ , \tag{4.17}$$

being $\hat{j}(< r) = \boldsymbol{j}(< r)/j(< r)$. In the case of a simple solid body rotation, $\alpha(< r_i)$ is expected to be always null along the cluster radius.

To define the rotational state of a relaxed cluster, we considered the value of the spin parameter of the gas as the discriminant indicator, since it quantifies the contribution of the gas rotational energy to the total energy of the cluster, by definition. We classify a cluster as rotating if it satisfies the condition $\lambda_{\rm gas} > \lambda_{\rm gas,crit}$, where $\lambda_{\rm gas,crit}$ is the threshold that separates the total sample in two sub-samples showing distinguishable profiles of the tangential velocity (see next paragraph for details). In our case, $\lambda_{\rm gas,crit} = 0.07$, according to which about 4 per cent of the relaxed clusters can be classified as rotating. In separating the population of the relaxed and rotating clusters, the corresponding conditions have been imposed to be valid for all the three subsets (NR, CSF and AGN). To verify whether the most massive clusters have the largest rotational support, we investigated the correlation between $M_{\rm vir}$ and $\lambda_{\rm gas}$, finding that the clusters classified as rotating are not the most massive objects in the sample. It is worth to stress, however, that the statistics of objects having large masses is intrinsically limited, given that the sample is volume-limited. This may explain the relatively small number of massive rotating clusters we found.

The ICM mean profiles of $j(< r)$ and $\alpha(< r)$ for the two classes of rotating and non-rotating clusters, are shown in Figure 4.10a and Figure 4.10b respectively; the profiles for DM are characterized by similar features.
Some general trends are evident, as described in the following. On average, the direction of $j(< r)$ reaches more than 60° in the core of non-rotating clusters and it is still above 30° at half of the virial radius. It is also noticeable that several objects

register a variation equal or larger than 90° from the core to the outskirts. The rotating clusters show a much smaller variation: for $r \gtrsim 0.3R_{\rm vir}$ we find that $\alpha(< r)$ is less than $\sim 20°$, pointing out that the orientation is almost fixed. The profiles of the modulus increase from the centre up to the virial radius and flatten in the outskirts, reaching larger values in the rotating clusters, as expected. A similar behaviour has also been found in [77], who analysed only the DM component of galaxy-sized haloes. They find a power-law relation of the type $j(< r) \propto r^{\beta_j}$ with $\beta_j = 1.1 \pm 0.3$. In our sample we perform a similar fit to a power-law $j(< r)/j(< R_{\rm vir}) \propto r^{\beta_j}$ to the profiles over spherical shells, normalized at virial radius for the gas and DM components in the rotating clusters. The mean values of β_j with the corresponding standard deviations are listed in Table 4.3. The power-law profiles of the DM are in agreement with [77], while the values of the gas are 20 per cent lower.

Our results lead to the conclusion that the coherent rotational motions of ICM and DM in our cluster sample are not properly described by a simple solid body model. A further confirmation of this fact is given by the angles between the angular momentum vector and the three semi-axes describing the ellipsoids that approximate the shape of the matter distribution of gas and DM. Indeed, considering only the case of rotating clusters, these angles range from tens, up to 180 degrees, suggesting a misalignment that is not compatible with a rigid rotation.

Finally, we computed $\alpha(< r)$ and $j(< r)$ for the total angular momentum, and through a comparison of the profiles with those obtained for the gas and the DM we found a very close similarity with the latter, reflecting the predominance of this component on the ICM. The dominating role of DM in the cluster dynamics can also be inferred from the lack of significant differences between the results obtained for the three physical flavours of the simulations used to describe the ICM. The only marked difference is the higher average value of gas $\alpha(< r)$, associated with a significant dispersion in the core of the AGN runs ($r < 0.1R_{\rm vir}$). In this case the AGN feedback likely influences the motion of the gas that, receiving extra energy from the central source, buoyantly raises without any pre-selected orientation. The effect in real clusters might be even more intense for the presence of the AGN jets which are not included in our model.

Co-rotation of ICM and DM

The correlation we found between the spin parameters of gas and DM, as well as their similar log-normal distributions, suggest that these two components are possibly co-rotating. To investigate this point in more detail, we compared the specific angular

Table 4.3. Mean values and standard deviations of the power-law exponent β_j as derived from the fits of $j(< r)/j(< R_{\rm vir})$ for the rotating clusters.

Data set	β_j	
	gas	DM
NR	0.78 ± 0.13	0.96 ± 0.13
CSF	0.69 ± 0.10	0.92 ± 0.15
AGN	0.75 ± 0.13	0.90 ± 0.14

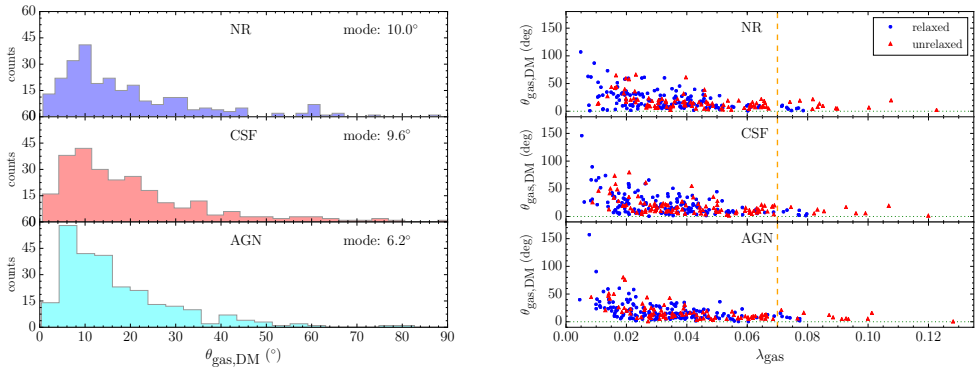

(a) Distribution of $\theta_{\rm gas,DM}$ **(b)** $\theta_{\rm gas,DM}$ vs $\lambda_{\rm gas}$

Figure 4.11. Angles $\theta_{\rm gas,DM}$ between the specific angular momentum vectors of gas and DM at virial radius. **(a)** Distribution of the angle values across the cluster sample. For $\theta_{\rm gas,DM} > 90°$ there are only few isolated clusters. **(b)** Relation between $\theta_{\rm gas,DM}$ and the spin parameter of the gas, with the distinction of relaxed and unrelaxed clusters. The dashed orange line indicates the threshold value for the separation of the rotating clusters from the non-rotating ones (at 0.07).

momentum vectors of these two components, evaluated at the virial radius. We drop here the distinction between relaxed and unrelaxed objects, unless differently specified. Using the direction vectors, $\hat{j}_{\rm gas} = \boldsymbol{j}_{\rm gas}/j_{\rm gas}$ and $\hat{j}_{\rm DM} = \boldsymbol{j}_{\rm DM}/j_{\rm DM}$ (being $j_{\rm gas} = |\boldsymbol{j}_{\rm gas}|$ and $j_{\rm DM} = |\boldsymbol{j}_{\rm DM}|$), the angle between the two angular momenta at virial radius is computed as

$$\theta_{\rm gas,DM} = \arccos\left[\hat{j}_{\rm gas}(R_{\rm vir}) \cdot \hat{j}_{\rm DM}(R_{\rm vir})\right] \ . \tag{4.18}$$

For our goal, we consider that two vectors could be assumed aligned if $\theta_{\rm gas,DM} < 10°$. Under this condition the gas and DM particles are co-rotating, and the motions of DM could be inferred by measuring the gas.

The distribution of $\theta_{\rm gas,DM}$ for all the clusters in the sample is reported in Figure 4.11a. Around 40 per cent of the sample (corresponding to ~ 100 objects) shows $\theta_{\rm gas,DM} < 10°$. In Figure 4.11b we plot the angle $\theta_{\rm gas,DM}$ as a function of $\lambda_{\rm gas}$. We highlight the relaxation state of the clusters with different colours, finding that it does not seem to have an impact on the alignment between gas and DM. The values of $\theta_{\rm gas,DM}$ are below 20° for relatively high values of $\lambda_{\rm gas}$. In the clusters classified as rotating (having $\lambda_{\rm gas} > 0.07$) the angle values are about 10°. This leads to the conclusion that a larger cluster rotation is linked to a larger alignment of the angular momenta of gas and DM. Such alignment can be seen as the evidence for a co-rotation of these two components, considering that the orientation of the angular momentum for radial values $r \gtrsim 0.3R_{\rm vir}$ (see Figure 4.10a) is almost constant.

As in the case of the orientation, we also expect a correlation in the absolute values of the angular momentum of the two components. The absolute values show indeed a linear relation, and the parameters of the fits to the data performed with the bisector method are listed in Table 4.4. It is worth noting that the slope value of ~ 0.94 is consistent within the error with the value obtained from the correlation

between the spin parameters of the DM and gas component (see Table 4.1). From this result we find that the ICM specific angular momentum is a factor of ~ 1.06 larger than that of DM. However, we also find that the gas angular momentum fraction $\ell_{\rm gas} = L_{\rm gas}/L_{\rm DM} \sim 0.17$ at virial radius, meaning that when masses are taken into account, the DM contribution to the angular momentum is dominant.

Velocity profiles

We studied the radial profiles of the tangential (or rotational) velocity of gas and DM particles, expressed as follows:

$$v_{\rm tan}(r_i) = \frac{|\sum_k^{N_i} \frac{\boldsymbol{r}_k \times m_k \boldsymbol{v}_k}{|\boldsymbol{r}_k|}|}{\sum_k^{N_i} m_k} \,, \tag{4.19}$$

where the sums are extended to the N_i particles located within the 15 spherical shells enclosed between the radii r_{i-1} and r_i, and not to the spheres used above. In this way we get the local values of the tangential velocity, that we use to test possible rotational behaviours. We can derive the tangential velocity from the specific angular momentum, by approximating equation (4.19) using $v_{\rm tan}(r_i) \sim \langle |\boldsymbol{j}(r_i)| \rangle / r_i$. In the second term, the contribution from random turbulence motions is averagely null by definition, thus the average angular momentum computed in a given shell accounts only for the contribution from rotational coherent motions [15].

The velocity component associated with macroscopic random motions will be referred hereafter as turbulence, denoted with $v_{\rm turb}$. We quantified it from the dispersion with respect to the average tangential velocity as in equation (4.19):

$$v_{\rm turb}(r_i) = \left[\sum_k^{N_i} m_k \left(\frac{|\boldsymbol{r}_k \times \boldsymbol{v}_k|}{|\boldsymbol{r}_k|} - v_{\rm tan}(r_i) \right)^2 / \sum_k^{N_i} m_k \right]^{\frac{1}{2}} \,, \tag{4.20}$$

where the sums are extended to spherical shells for gas and DM particles.

Both velocity profiles (equations (4.19) and (4.20)) are normalized to the circular velocity $v_{\rm circ}$ of each cluster at $R_{\rm vir}$. In our sample we have an average value of $\langle v_{\rm circ} \rangle = (1365 \pm 145)\,{\rm km\,s^{-1}}$, and the distributions are shown in Figure 4.12. Due to the tight correlation between the total mass and the circular velocity [157], these distributions emphasize that there is no mass segregation for relaxed clusters.

The mean profiles of the tangential and turbulent velocity have been calculated for both classes of rotating and non-rotating clusters, for all the radiative prescriptions.

Table 4.4. Parameters of the robust linear fits to the $j_{\rm DM}(R_{\rm vir})$ vs $j_{\rm gas}(R_{\rm vir})$ data. The value of $c_{\rm corr}$ gives the correlation coefficient.

Data set	$c_{\rm corr}$	Slope	Intercept ($\rm kpc^2 h^{-2} s^{-1}$)
NR	0.85	0.94 ± 0.04	$(-4 \pm 2) \times 10^{-13}$
CSF	0.84	0.94 ± 0.04	$(-3 \pm 2) \times 10^{-13}$
AGN	0.83	0.93 ± 0.04	$(-3 \pm 2) \times 10^{-13}$

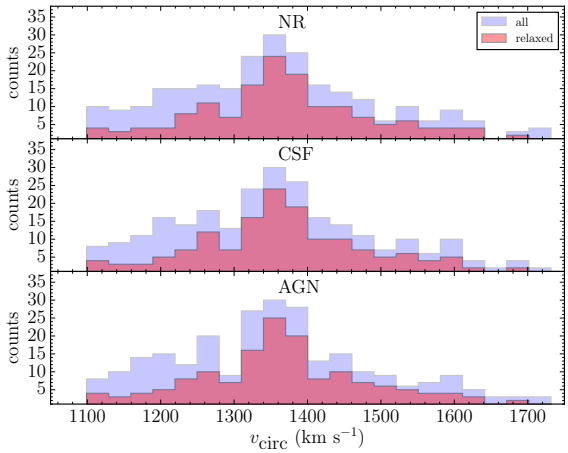

Figure 4.12. Distribution of the circular velocity as calculated at the virial radius for all the clusters in the analysed sample, and with the discrimination of the relaxed ones.

Since the tangential velocity is derived from the specific angular momentum, whose direction changes significantly along the radius (Figure 4.10a), we multiply its value by the cosine of the mean angle $\alpha(r)$, in the central region ($r < 0.3R_{\rm vir}$). In this way we fix the orientation, and we assume the same rotational plane.

By comparing the radial profiles of the mean tangential and turbulent velocity for the rotating clusters, as shown in Figure 4.13a for the ICM and in Figure 4.13b for the DM, we find a significant difference between these two matter components. For the DM there is a net distinction between the two velocities: the turbulent velocity dominates over the tangential one, with a decrease of ~ 30 per cent from the centre to the outskirts. In the profiles of ICM velocities instead, there is a comparable contribution from turbulence and coherent rotation in the region between ~ 0.15 and $\sim 0.65R_{\rm vir}$. Turbulence is still dominant in the innermost and in the outer regions, with a tendency to increase for radial values between 0.1 and $0.4R_{\rm vir}$, and a flattening for higher radii. Along the whole radial range, values vary between 0.2 and $0.3v_{\rm circ}$, corresponding to ~ 273 and $\sim 410\,{\rm km\,s^{-1}}$. The larger values of the DM velocity dispersion with respect to the gas can be explained in terms of the absence of radiative mechanisms that remove kinetic energy of particles transforming it into thermal energy, as in the case of gas particles.

From the comparison of our profiles of the velocity dispersion with other works, we find a general consistency. In particular there is a fairly good agreement for the DM profiles, that typically show a decreasing trend and have larger values with respect to the gas [see 423, 362, 161]. A remarkable agreement can be found with [15], as the values are compatible within the errors over all the considered radial range. Values are generally around a thousand of ${\rm km\,s^{-1}}$ in the central regions, and differ more significantly in the outskirts.

The profiles of ICM turbulence show less regular behaviours. A recurring trend is the flattening for radii $r \gtrsim 0.75R_{\rm vir}$, and values typically span a relatively narrow range. In particular our values are compatible with [161] in the innermost regions ($r \sim 0.10R_{\rm vir}$), and with [362] and [254] at intermediate radii. The agreement with

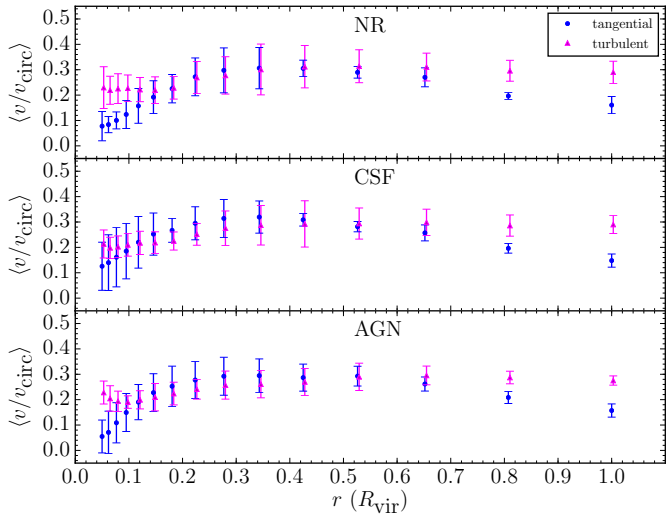

(a) gas

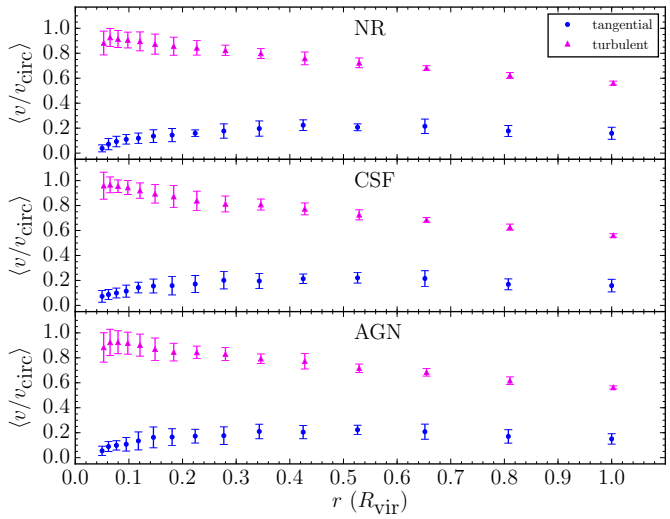

(b) DM

Figure 4.13. Radial profiles of the mean tangential and turbulent velocity of ICM (upper panel) and DM (lower panel) for the rotating clusters only. The error bars indicate the standard deviation.

the latter is of particular interest, since they take into account the dynamical state of the clusters, thus only the profiles of the relaxed ones have been compared here. We find more marked differences with [423], possibly because only a cluster is considered in their analysis, thus they are more sensitive to single-cluster properties.

The radial profiles of the tangential velocity for the rotating and the non-rotating clusters are shown in Figure 4.14a and in Figure 4.14b, for the ICM and the DM respectively. Differently from the case of the turbulent velocity profiles, there is a common trend for both the gas and the DM, that is the increase of the values in the innermost regions up to $0.3 - 0.4 R_{\rm vir}$, where they reach $\sim 400\,{\rm km\,s^{-1}}$ for the ICM and $\sim 250\,{\rm km\,s^{-1}}$ for the DM, and a smooth decrease in the outskirts. Values at virial radius are around 16 per cent of the circular velocity in the rotating clusters, and 8 per cent in the non-rotating clusters (with no substantial differences between ICM and DM). These results are in fairly good agreement with the values reported in [15] for the DM and in [254] for the gas. The plots in Figure 4.14 clearly show that single profiles are affected by relatively large scatters, because of the different intrinsic behaviours of individual clusters.

To check whether our mean profiles of the tangential velocity can be described by an analytical rotational model, we fit them to the two models introduced by Bianconi et al. (2013) [39]. We neglected the simple solid body model, since we can see from the angular momentum profiles shown at page 136. that it is not appropriate to describe the rotational motions in our cluster sample. The two models that we consider refer to the case of a non-rigid rotating ICM, whose contribution to the gravitational potential of the cluster is negligible. The first proposed model, referred hereafter as vp1, is the circular velocity of the gas in a NFW distribution of the DM density [307], as a function of the radial distance from the centre:

$$v_{\rm circ}(r) = v_{c0} \left[\frac{\ln(1 + r/r_0)}{r/r_0} - \frac{1}{1 + r/r_0} \right]^{\frac{1}{2}} , \tag{4.21}$$

where the radius r_0 corresponds to the peak value of the velocity. Since it represents the circular velocity along the cluster radius, this profile is not fully appropriate to fit our tangential velocity. The second model proposed by [39] is an alternative to the circular velocity profile, characterized by a steeper increase in the core regions and a deeper decrease in the outskirts:

$$v_{\rm tan}(r) = v_{t0} \, \frac{r/r_0}{(1 + r/r_0)^2} \tag{4.22}$$

that will be referred hereafter as vp2 model. We also introduce a modified version of vp2, the vp2b model, of equation:

$$v_{\rm tan}(r) = v_{t0} \, \frac{r/r_0}{1 + (r/r_0)^2} \, . \tag{4.23}$$

The fits of the mean tangential velocity profiles to the vp2 and vp2b models can be seen in Figure 4.14a for the gas and in Figure 4.14b for the DM. The v_{t0} and r_0 parameters which best fit equations (4.22) and (4.23) are listed in Table 4.5. Both models are in agreement with the data within one standard deviation. Nevertheless, the residuals are lower for the vp2b, that better fits the ICM data, especially around the bump observed at $r \sim 0.3 R_{\rm vir}$ and in the external regions.

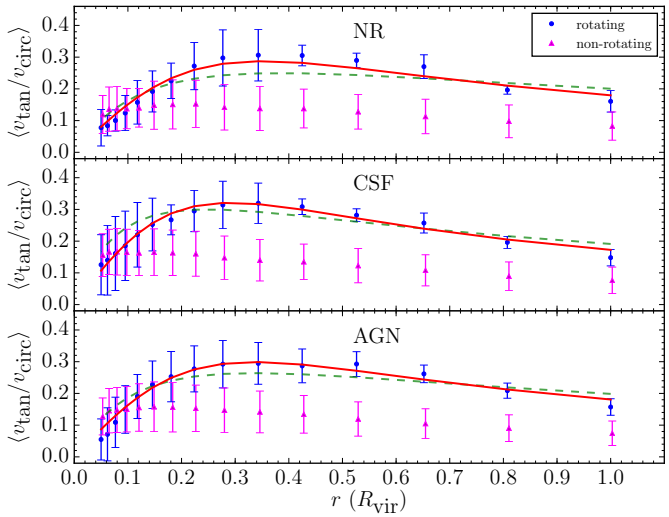

(a) gas

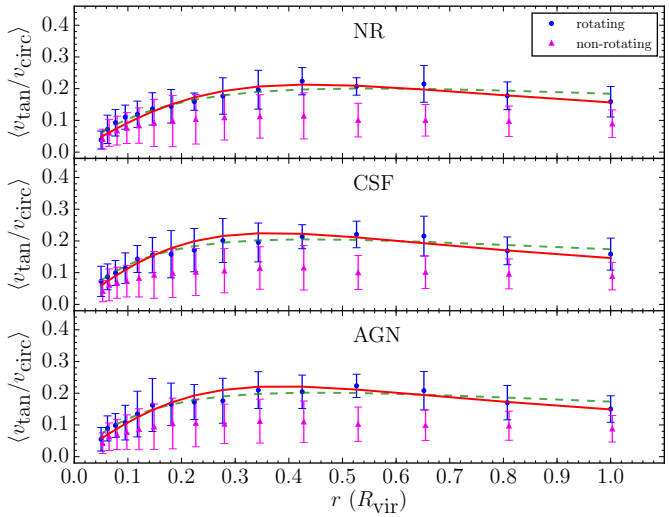

(b) DM

Figure 4.14. Radial profiles of the mean rotational velocity of ICM (upper panel) and DM (lower panel) for the rotating and the non-rotating clusters. The error bars indicate the standard deviation of the single profiles with respect to the mean profiles. The dashed green line is the fit with the vp2 model, while the red solid line is the fit to the model of equation (4.23) (see text).

Table 4.5. Parameters of the fit to the vp2 and vp2b models of equations (4.22) and (4.23), for the mean tangential velocity of gas and DM in rotating clusters.

Component	Data set	vp2 model		vp2b model	
		v_{t0} ($v_{\rm circ}$)	r_0 ($R_{\rm vir}$)	v_{t0} ($v_{\rm circ}$)	r_0 ($R_{\rm vir}$)
gas	NR	1.00 ± 0.04	0.38 ± 0.05	0.58 ± 0.03	0.35 ± 0.03
	CSF	1.21 ± 0.07	0.24 ± 0.04	0.65 ± 0.04	0.29 ± 0.03
	AGN	1.07 ± 0.07	0.33 ± 0.05	0.60 ± 0.04	0.33 ± 0.04
DM	NR	0.80 ± 0.06	0.55 ± 0.12	0.42 ± 0.03	0.44 ± 0.06
	CSF	0.82 ± 0.07	0.44 ± 0.09	0.45 ± 0.03	0.37 ± 0.05
	AGN	0.81 ± 0.07	0.45 ± 0.10	0.44 ± 0.04	0.38 ± 0.06

Table 4.6. Threshold values for the gas spin parameter and corresponding percentage of rotating clusters with respect to the number of relaxed clusters, $N_{\rm rot}/N_{\rm rel}$. The d_{vm} value is also shown (see text).

$\lambda_{\rm gas,crit}$	$N_{\rm rot}/N_{\rm rel}$	d_{vm}
0.03	49%	0.49
0.05	10%	0.85
0.07	4%	1.11

Critical value of the spin parameter for rotating clusters

Since there is not a universal critical value for $\lambda_{\rm gas}$ that can be adopted to discriminate rotating objects, we choose the threshold by inspecting the radial average profiles of the tangential velocity of the two populations of rotating and non-rotating clusters, ($v_{\rm tan}^{rot}(r)$ and $v_{\rm tan}^{nonrot}(r)$, respectively). We take the value for which these profiles are separated more than the corresponding standard deviations over $r \gtrsim 0.3R_{\rm vir}$, that is the radial range where the angular momentum orientation is almost fixed. To quantify the separation of the profiles at a radius r, indicating with $\sigma_{\rm tan}^{rot}(r)$ and $\sigma_{\rm tan}^{nonrot}(r)$ the corresponding standard deviations (represented by the error bars in the profile plots), we introduce the following estimator

$$d_v(r) = \frac{|v_{\rm tan}^{rot}(r) - v_{\rm tan}^{nonrot}(r)|}{\sigma_{\rm tan}^{rot}(r) + \sigma_{\rm tan}^{nonrot}(r)} \ , \tag{4.24}$$

so that they can be considered as separated when $d_v(r) > 1$. The best $\lambda_{\rm gas,crit}$ is the one for which the minimum value of $d_v(r)$, d_{vm}, is larger than one in the range $r \gtrsim 0.3R_{\rm vir}$. The fraction of relaxed clusters which, according to our criterion, can be defined as rotating is listed in Table 4.6 for some values of $\lambda_{\rm gas,crit}$, together with d_{vm}. It turns out that the $\lambda_{\rm gas,crit}$ having $d_{vm} > 1$ in the chosen radial range is 0.07, therefore we adopt this value as the discriminating one. Fig. 4.15 shows the profiles for $\lambda_{\rm gas,crit} = 0.03$, where the overlapping of the two classes for $r \lesssim 0.5R_{\rm vir}$ is evident. Values of $\lambda_{\rm gas,crit}$ larger than 0.07 cannot be tested, since the maximum spin parameter of the gas in the sub-sample of relaxed clusters is ~ 0.078. It can be seen from Fig. 4.9 that these values correspond to the tails of the spin parameter distributions.

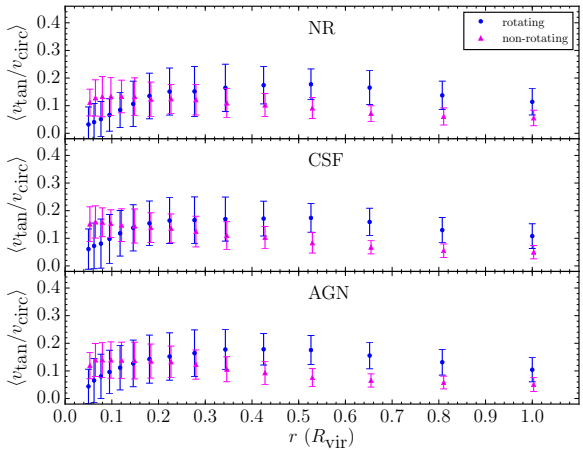

Figure 4.15. Radial profiles of the tangential velocity of the gas for the rotating and the non-rotating clusters, assuming $\lambda_{\rm gas,crit} = 0.03$. See the caption of Fig. 4.14 for a detailed description of the plots.

Table 4.7. Identifier, virial mass, virial radius, and spin parameter of the gas of the six relaxed and rotating clusters in the volume-limited MUSIC-2 sample from the NR run at $z = 0$.

Cluster ID	$M_{\rm vir}$ ($\times 10^{15}$ M$_\odot$)	$R_{\rm vir}$ (kpc)	$\lambda_{\rm gas}$
46	1.17	2756	0.0785
93	1.90	3241	0.0769
98	1.61	3071	0.0735
103	1.02	2633	0.0746
205	1.24	2813	0.0763
256	1.31	2867	0.0714

4.3.3 KSZ effect in MUSIC rotating clusters

To check whether we can probe observationally the above results based on the analysis of the angular momentum, we produced the mock temperature anisotropy maps of the kSZ effect [21]. We focussed only on the relaxed and rotating clusters selected from the NR data, whose properties are summarised in Table 4.7.

Simulated kSZ maps

The kSZ maps of the synthetic clusters in our data set have been produced using the publicly available `pymsz`[3] package, which provides mock observations of both the thermal and kinetic SZ effects. The kSZ temperature signal has been computed as

$$\frac{\Delta T_{\rm kSZ}(\hat{n})}{T_{\rm CMB}} = -\frac{\sigma_T}{cD_A^2}\sum_i^{N_P} N_{e,i}\ v_{p,i}\ W_p(r_i, h_s)\ , \tag{4.25}$$

[3] https://github.com/weiguangcui/pymsz

where D_A is the angular diameter distance of the cluster. The sum extends over the total number of particles along the line of sight, N_P, each being located at a distance r_i from the centre of mass, having projected velocity $v_{p,i}$ and containing $N_{e,i}$ electrons. The W_p function is the SPH smoothing kernel of the simulation (see equation (4.11)). Here it is used to smear the kSZ from each gas particle to the projected image pixels, being h_s the smoothing length of the gas particles.
We computed the maps as in equation (4.25) in two different versions, to match the only rotational and the rotational+bulk cases (corresponding to the theoretical prescriptions of equations (4.9) and (4.10), respectively). To separate the rotational component, we simply subtracted the cluster bulk velocity, estimated as the average gas particle velocity, from the velocity of all single gas particles. In this way we could fit separately the kSZ maps computed from the data to the corresponding model in the two configurations. This would allow us in the first place to establish whether it is possible to recover the expected rotational properties and, secondly, to assess the maximum contribution to the total kSZ coming from rotation. Clearly, this is a simplification that cannot be used when dealing with real data, since it is not possible to separate the bulk component from the total signal, though some complementary methods to estimate the peculiar velocity could be used, e.g. the Tully–Fisher relation in the case of nearby clusters [see 229].

With the aim of maximising the rotational signal, we set the best observational configuration to detect the dipole, that corresponds to keeping the angle between the line of sight and the rotation axis fixed to $i = 90°$ (edge-on with respect to the rotation axis). To get the corresponding projection, we performed a change of coordinate system, by transforming all the particle positions and velocities according to a suitable rotation matrix. As zero-th order approximation, we assumed the rotation axis to be coincident with the direction of the angular momentum vector of the gas computed at the virial radius. Therefore, we constructed the rotation matrix in such a way that the z axis of the rotated reference frame coincided with this vector. With this choice the x axis of the map is aligned with the dipole spots, while the y axis corresponds to the projection of the rotation axis on the plane of the sky, as also illustrated in Figure 4.5 on page 125. We want to stress here that we adopted these simplifications only to investigate the detectability of the rotation in suitable candidate clusters (relaxed with large spin parameter) using the kSZ at the best observational configuration.

To validate the effective rotational origin of the dipole pattern, we produced different projections for each cluster. Specifically, we selected different lines of sight, all lying on the orthogonal plane to the rotation axis, always fulfilling the edge-on condition. Each line of sight is identified by the angle $\theta_{\rm los}$, that indicates the separation with respect to the reference line of sight, having $\theta_{\rm los} = 0°$. We took a total of six lines of sight, separated by uniform steps of $\Delta\theta_{\rm los} = 30°$, so that $0° \leq \theta_{\rm los} \leq 150°$. If a dipole originated by ICM rotation is present, its approaching and receding spots should show the same sign and orientation across the maps, regardless of the particular line of sight chosen for the projection. As in the case of the subtraction of the cluster bulk velocity, this simplification in the interpretation of the results is possible only when dealing with data from simulations, since observations can be made along only one line of sight.

The maps of each cluster extend over $2.5R_{\rm vir}$ on a side, with a pixel size $d_{\rm pix} =$

$5 \times 10^{-3} R_{\rm vir}$ that is of the order of ≈ 10 kpc. For practical reasons, we assume the analysed clusters to be located at $z = 0.05$, instead of $z = 0$. With this choice, according to the cosmological model adopted in the simulation, the angular diameter distance is 200.7 Mpc. The angular size of each pixel is therefore of the order of 10 arcsec, and the maps span a few degrees on each side. To get results that can be useful for possible future applications to data from real experiments, we reduced the angular resolution of our simulated maps. To this end, we applied a smoothing with a Gaussian filter having full width at half maximum equal to 20 arcsec, which is compatible with the resolution of currently operating microwave instruments (e.g. NIKA2 at 260 GHz).

Figure 4.16 shows the kSZ maps for cluster 93 – which is the most massive cluster in the sample – smoothed at 20 arcsec, for different lines of sight, as described above. The left panels show the maps generated after the subtraction of the cluster bulk velocity which, on the contrary, is included in the maps shown in the right panels. It can be seen that, in general, all maps for cluster 93 reported in Figure 4.16 show a dipole-like feature with horizontal alignment, and with spots having the same sign at all different projections. These characteristics confirm that cluster 93 is a good candidate for the inspection of a possible rotation of the ICM through the kSZ maps. In the maps in the right panels in Figure 4.16 it is possible to see how the dipole gets distorted because of the dominating approaching component of the bulk velocity with respect to the observer for lines of sight having $\theta_{\rm los} \leq 90°$. The cluster bulk velocity projection is almost null for $\theta_{\rm los} \geq 120°$ instead, so that the rotational signal remains practically unaffected in this projection. A number of small-scale features can be identified in all the maps in Figure 4.16, because of the presence of sub-structures. In any case, according to the relaxation criteria that we imposed to select the clusters in our sample (see subsection 4.3.1 for details), the masses of these sub-structures are smaller than ten per cent of the mass of the main halo. They may produce, in some cases, significant outliers in the kSZ temperature maps due to their high velocity projected on the line of sight. Despite that, since they extend over scales much smaller than the dipole scale, their presence does not affect dramatically the results from the fit to the theoretical maps of the rotational component of the kSZ. For this reason, the $\Delta T_{\rm kSZ}$ range in the figures is set to $\pm 30\,\mu$K, to accommodate the dynamic range of the dipole without being affected by substructure outliers. The other five clusters in the sample show maps with very similar features, as illustrated in Figures 4.17 and 4.18.

To highlight the impact of different orientations of the line of sight with respect to the rotation axis, we show in Figure 4.19 the maps of cluster 93 at $\theta_{\rm los} = 0°$, for different values of the angle i. We verify that the dipole is clearly visible in the case of orthogonal line of sight with respect to the rotation axis, with decreasing amplitude for decreasing values of i, consistently with the expectations. Unfortunately, the contribution from the $\sin i$ term and the velocity cannot be discriminated in the observed signal. For this reason we set $i = 90°$ in the rest of the analysis.

Theoretical kSZ maps

The synthetic maps described above have been compared to suitable model maps, to recover the parameters describing the ICM rotation. As can be seen from

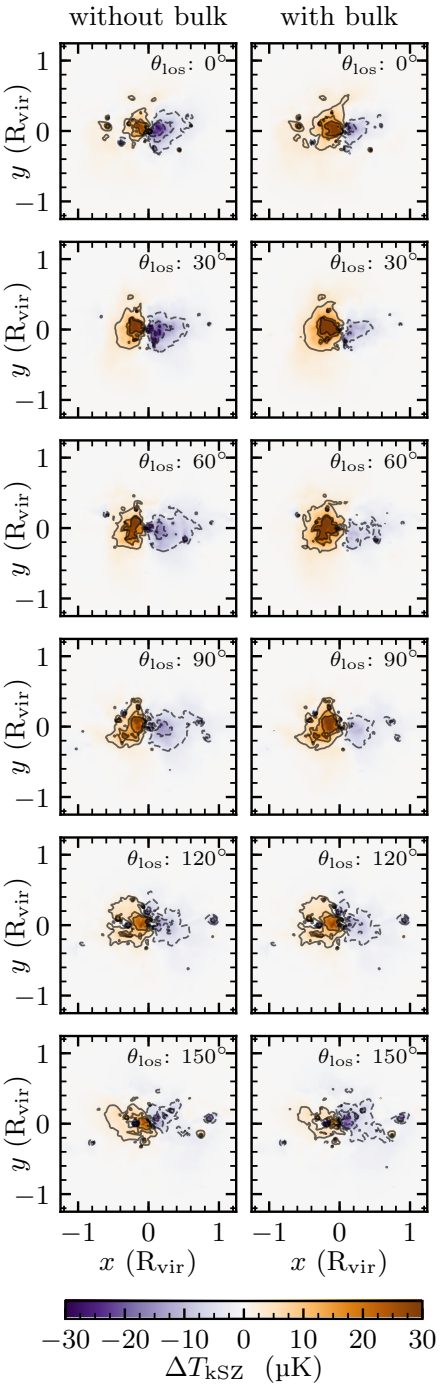

Figure 4.16. Maps of the temperature shift produced by the kSZ effect for cluster 93, obtained from different projections as described in the text, and smoothed at 20 arcsec. Left and right panels show the maps obtained without and with the addition of the cluster bulk velocity, respectively. The angles $\theta_{\rm los}$ of the corresponding lines of sight are specified on top of each map. The contours are plotted from -5σ to 5σ, with dashed (solid) lines for negative (positive) values. The maximum and minimum values in the maps have been set to ±30 μK for displaying purposes.

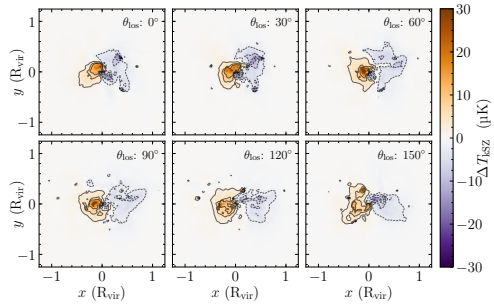

(a) cl. 46

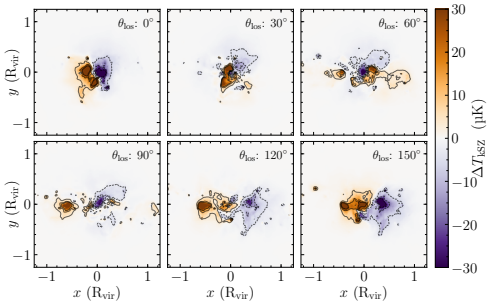

(b) cl. 98

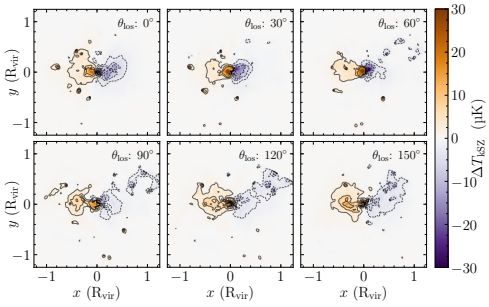

(c) cl. 103

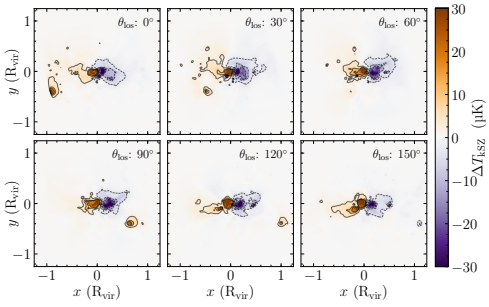

(d) cl. 205

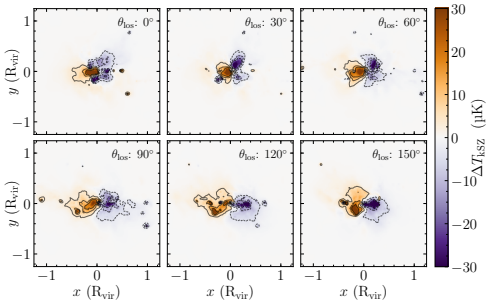

(e) cl. 256

Figure 4.17. Maps of the kSZ effect for the clusters in the sample at the different projections. The contours are plotted from -5σ to 5σ, with dashed (solid) lines for negative (positive) values.

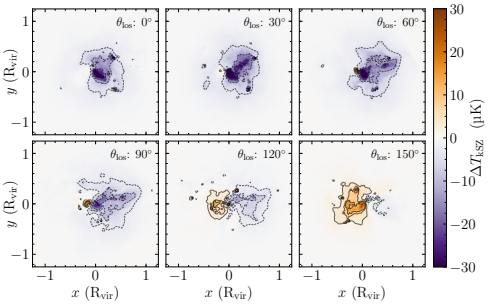

(a) cl. 46

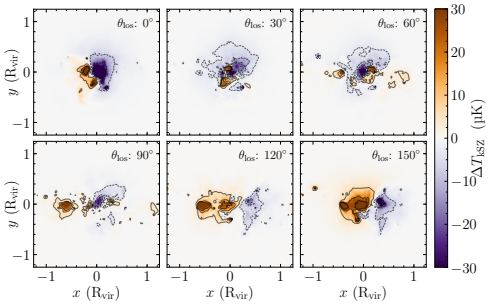

(b) cl. 98

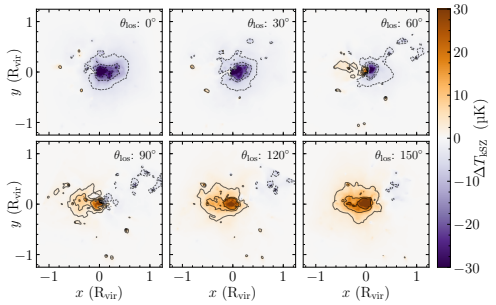

(c) cl. 103

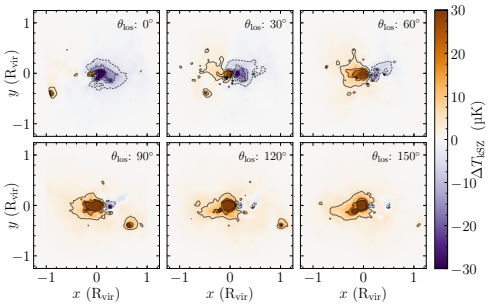

(d) cl. 205

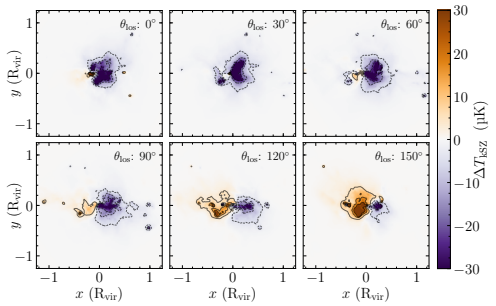

(e) cl. 256

Figure 4.18. Same maps as in Figure 4.17, with the contribution from bulk motion.

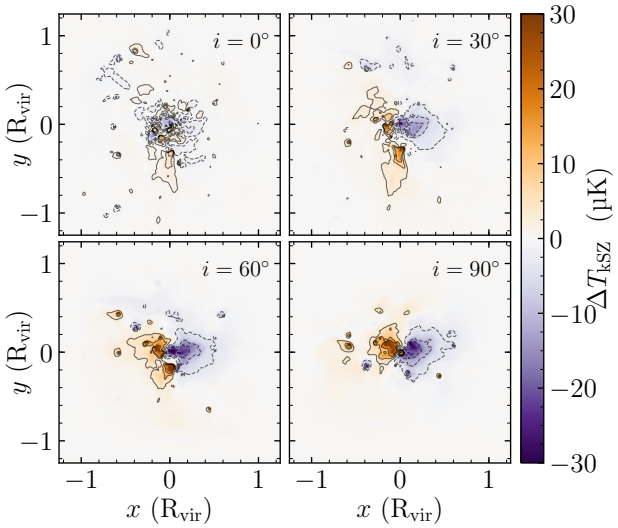

Figure 4.19. Maps of the kSZ effect of cluster 93, for different values of the angle i, without accounting for the contribution of the bulk motion. The dipole pattern weakens from edge-on to face-on with respect to the rotation axis.

equations (4.9) and (4.10), the calculation of the theoretical kSZ maps corresponds to the integration along the line of sight of the radial profiles of the electron number density, $n_e(r)$, and of the angular velocity, $\omega(r)$.

In real-life observations of clusters, the SZ effect alone cannot be used to constrain all the thermodynamic and dynamical properties of the ICM. Thus, to derive the parameters characterizing the rotational velocity it is necessary to have an independent measurement of the electron number density, and a possible estimate of the analytical model describing its radial profile, $n_e(r)$. This information has to be provided by ancillary X-ray observations, which may allow the reconstruction of cluster densities at radii up to the virial radius. In our case, instead of using mock X-ray data, we used the numerical profiles derived from the cluster data provided by the simulation, and we fit them to a suitable theoretical model. The numerical profiles have been computed as described in [403], following:

$$n_e(r) = N_e(r)\ \rho_{\rm gas}(r)\ \frac{Y_H}{m_p}\ , \tag{4.26}$$

where $N_e(r)$ and $\rho_{\rm gas}(r)$ are the number of electrons and the gas density at the cluster radius r, $Y_H = 0.76$ is the hydrogen abundance referred to the gas particle, and m_p is the proton mass. The model we use to describe $n_e(r)$ is a six-parameter, *simplified* Vikhlinin model [453] (see also equation (2.10)), that is

$$n_e(r) = n_0\ \frac{(r/r_c)^{-\alpha/2}}{[1+(r/r_c)^2]^{3\beta/2-\alpha/4}}\ \frac{1}{[1+(r/r_s)^\gamma]^{\varepsilon/(2\gamma)}}\ , \tag{4.27}$$

where n_0 is the central density, r_c and r_s are scale radii, and α, β and ε control the slopes of the profile at different radii. To determine the best-fit values of the free parameters (n_0, r_c, α, β, r_s and ε), we used a Monte Carlo Markov chain procedure.

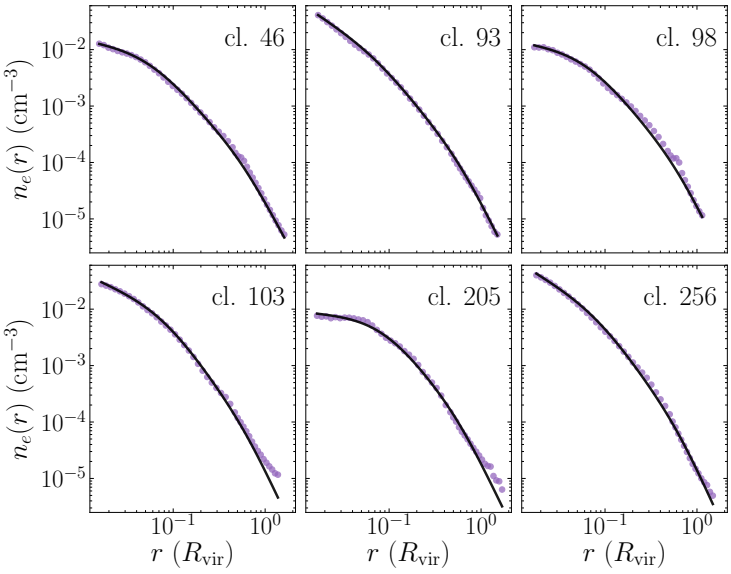

Figure 4.20. Radial profiles of the electron number density of the clusters in our sample. Purple dots are the median values computed according to equation (4.26); solid black lines represent the best-fit curves described by the simplified Vikhlinin model of equation (4.27) with the parameters listed in Table 4.8.

The slopes α, β and ε, have been all constrained to be positive, with the additional condition $\varepsilon < 5$; the γ parameter, instead, has been kept fixed to 3.0 [453]. We summarize the results in Table 4.8, where we list the parameter values with the corresponding 68% errors, and in Figure 4.20, showing the data and the best-fit curves.

As for the angular velocity, we showed in section 4.3.2 that the possible rotation of the gas in our cluster sample can be described by a generalized radial profile of the tangential velocity, rather than by a solid body model (differently from CC02). We called this law vp2b model [20]; the corresponding radial profile of the angular velocity is then

$$\omega(r) = \frac{\mathrm{vp2b}(r)}{r} = \frac{v_{t0}/r_0}{1 + (r/r_0)^2} \ , \tag{4.28}$$

being r_0 and v_{t0} the parameters of the vp2b model, i.e. the scale radius and half of

Table 4.8. Parameter values from the fit of radial profiles of the electron number density derived from the simulation to the simplified Vikhlinin model of equation (4.27). The γ parameter has been kept fixed to 3.0 for all the clusters.

Cluster ID	n_0 (cm^{-3})	r_c ($R_{\rm vir}$)	α	β	r_s ($R_{\rm vir}$)	ε
46	0.019 ± 0.004	0.056 ± 0.004	0.6 ± 0.3	0.63 ± 0.08	0.59 ± 0.08	2.3 ± 1.2
93	0.019 ± 0.005	0.070 ± 0.005	2.1 ± 0.2	0.69 ± 0.07	0.61 ± 0.07	2.5 ± 1.3
98	0.018 ± 0.004	0.064 ± 0.004	0.5 ± 0.3	0.7 ± 0.1	0.6 ± 0.1	2.6 ± 1.5
103	0.021 ± 0.004	0.078 ± 0.004	1.4 ± 0.2	0.79 ± 0.09	0.63 ± 0.09	2.3 ± 1.4
205	0.014 ± 0.002	0.088 ± 0.002	0.2 ± 0.2	0.7 ± 0.1	0.6 ± 0.1	2.5 ± 1.4
256	0.020 ± 0.005	0.082 ± 0.005	1.9 ± 0.2	0.79 ± 0.08	0.64 ± 0.08	2.6 ± 1.4

the velocity at this radius, $v_{t0} = \mathrm{vp2b}(r_0)/2$ (see also equation (4.23)).

Figure 4.21 shows the central cuts along an example of theoretical kSZ map computed according to equation (4.9), using the solid body model – with constant angular velocity ω – and the vp2b model, for a fixed profile of the electron number density. These cuts show that the dipole spots, which have here the same amplitude for comparison purposes, are more broadened in the case of a constant angular velocity. The spatial scale of the dipole, that can be estimated as the distance between the maximum and the minimum peaks, is of the order of $\approx 0.2 R_{\mathrm{vir}}$ for both models. This is because this separation has a stronger dependence on the parameters setting the slopes of the electron number density profile (which has been kept fixed here) rather than on the velocity profile, in agreement with the results from [101].

Results from the fit

To recover the rotational properties of our test clusters, we used the Levenberg–Marquardt least-square algorithm [296] to compare the simulated maps with the theoretical ones. We treated separately the purely rotational case, referring to the theoretical model given by equation (4.9), and the full case accounting also for the cluster bulk motion, referring to the model of equation (4.10). The six parameters of the radial profile of the electron number density are kept fixed, with the values listed in Table 4.8. The free parameters we recovered from the fit to the kSZ maps are the scale radius, r_0, and the scale velocity, v_{t0}, introduced in equations (4.23) and (4.28). In the full case including the bulk motion, we treated the cluster bulk velocity projected on the line of sight (v_{bulk}) as an additional free parameter.

Figure 4.22 shows our simulated kSZ maps with the corresponding best-fit theoretical maps, all smoothed at 20 arcsec, without (left panel) and with (right panel) the bulk motion, in the case of cluster 93. Similar maps for the other clusters in the sample showing the results only for the best lines of sight are reported in Figure 4.23. We also show in Figure 4.24, again for cluster 93, the central cuts through the same maps of Figure 4.22, to better highlight how our procedure recovers the features of the signal. It can be seen that, in general, the theoretical model is appropriate to describe the data in both cases of subtraction and adding of the cluster bulk velocity. The signal in the data maps may be larger of a factor of ≈ 3 at

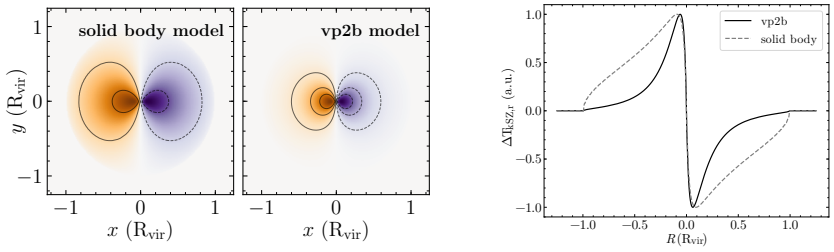

(a) map **(b)** central cut

Figure 4.21. Normalized theoretical maps (left panel) and corresponding central cuts (right panel). The signal has been computed using equation (4.9), with the vp2b and the solid body models.

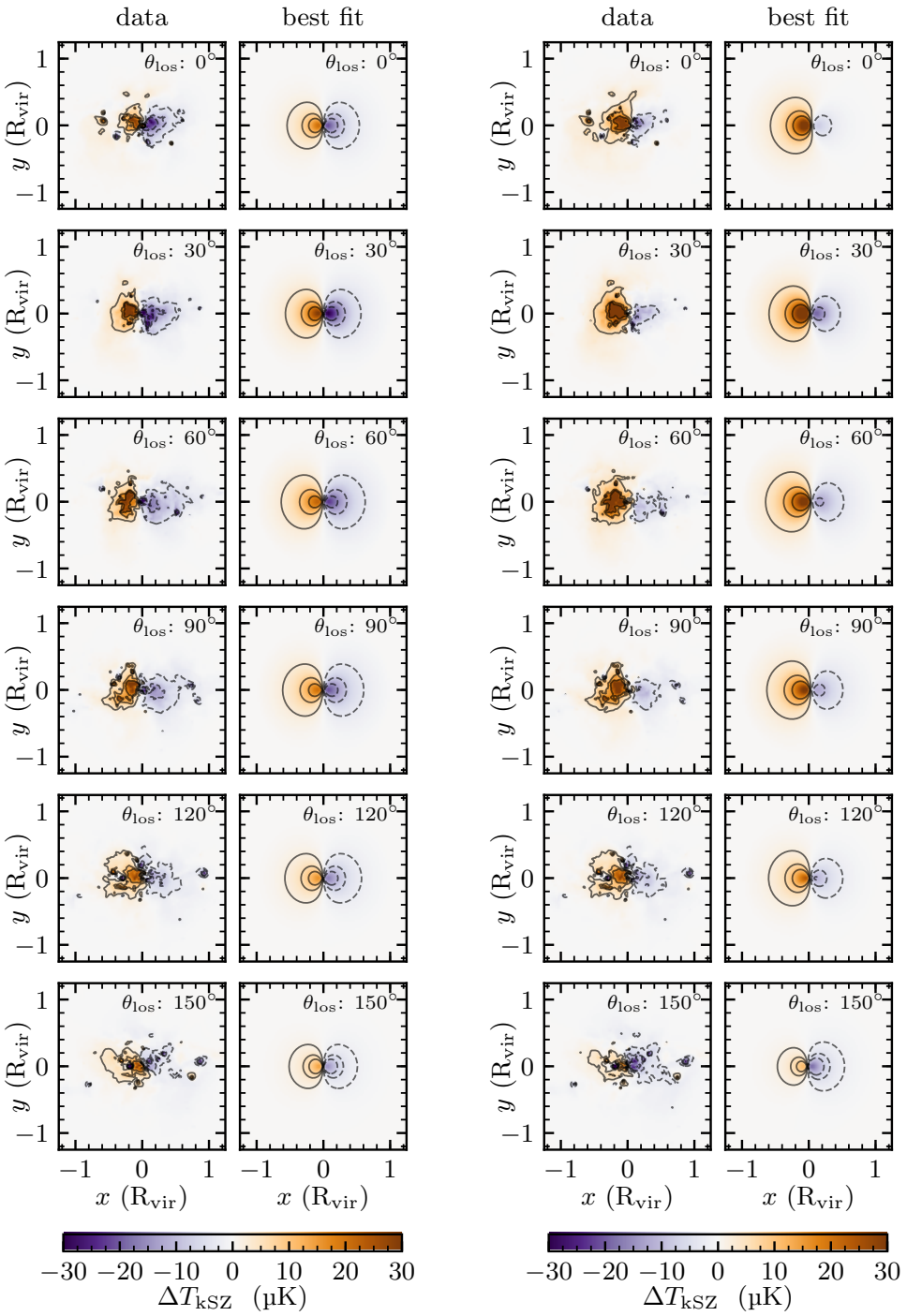

(a) without bulk motion **(b)** with bulk motion

Figure 4.22. Comparison between the kSZ temperature maps of cluster 93 and the corresponding best-fit maps, without and with accounting for the cluster bulk velocity (left and right panels, respectively). The contours are plotted from -5σ to 5σ, with dashed (solid) lines for negative (positive) values. The colorbar is set to ±30 μK for displaying purposes.

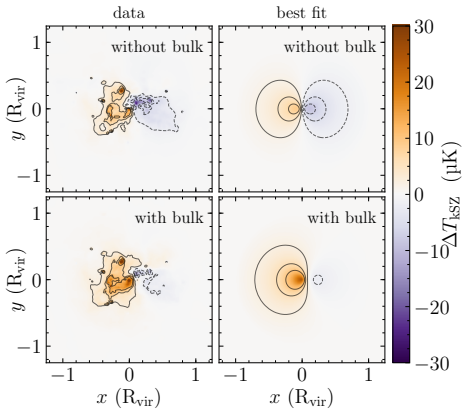

(a) cl. 46

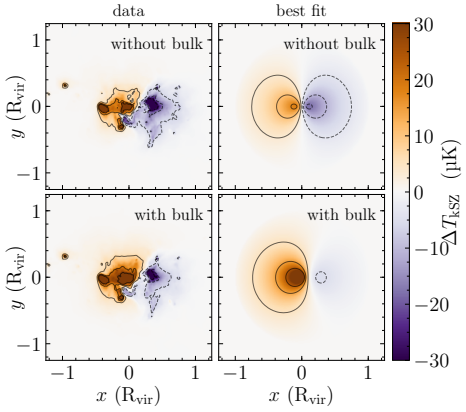

(b) cl. 98

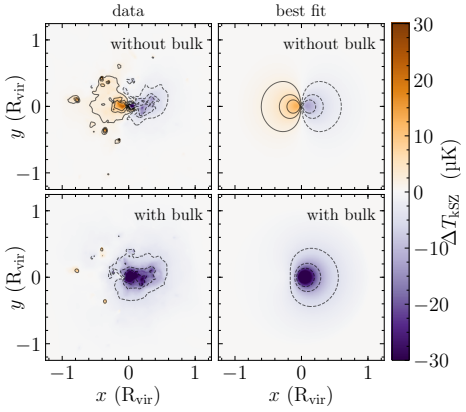

(c) cl. 103

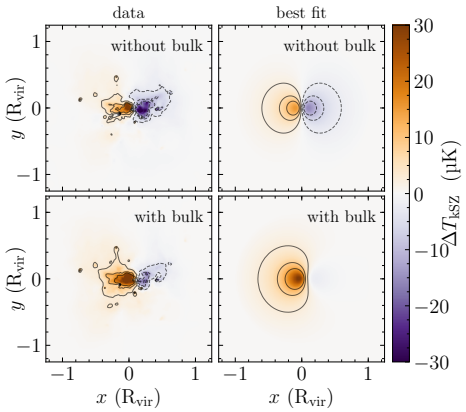

(d) cl. 205

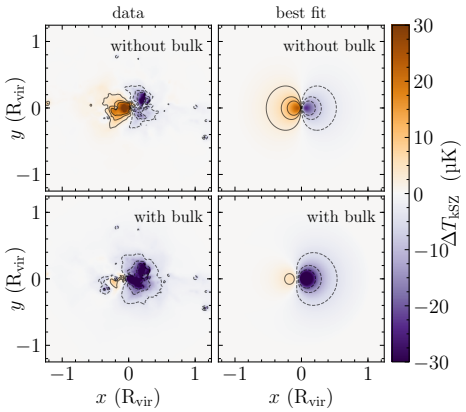

(e) cl. 256

Figure 4.23. Maps of the kSZ effect and corresponding best fits for the full cluster sample. The cases accounting only for rotation and for rotation plus bulk motion are reported in the top and bottom panels, respectively. The contours are plotted from -5σ to 5σ, with dashed (solid) lines for negative (positive) values.

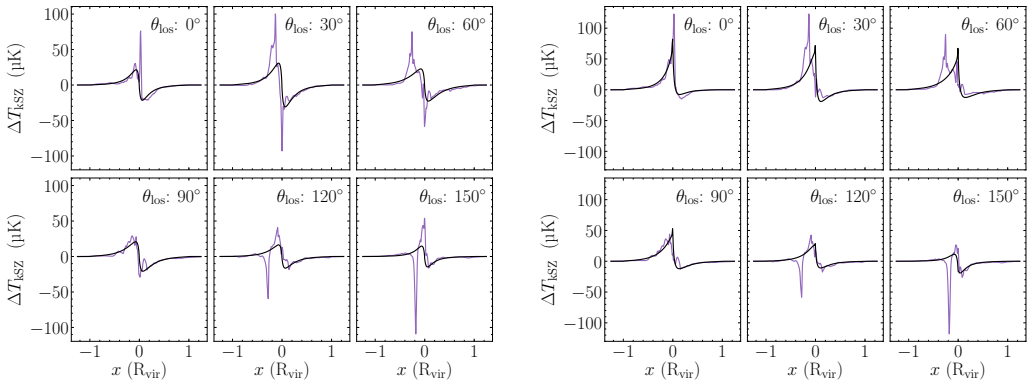

(a) without bulk motion **(b)** with bulk motion

Figure 4.24. Central cuts along the kSZ maps of cluster 93, without (left panel) and with (right panel) the cluster bulk velocity, for different lines of sight. The purple curves represent the cut through the data maps, while the black curves represent the cut through the best-fit maps. The presence of high-velocity particles can be seen as outliers at small scales.

most with respect to the best-fit maps in some regions, because of small-scale outliers due to sub-structures (that can be clearly seen in the plots of Figure 4.24), whose contribution generally changes from one line of sight to another (see also Figure 4.16). Similar plots for the other clusters in the sample are shown in Figures 4.25 and 4.26, without and with the bulk velocity, respectively.

Table 4.9 lists the r_0 and v_{t0} parameters estimated from the fit. Since they should have consistent values independently on the observed projection, we report the average and standard deviation over the different lines of sight we considered. We find that the values of both parameters are in agreement within one standard deviation when comparing the two cases without and with the bulk term, which are listed in the left and centre columns of Table 4.9, respectively. This indicates that, in principle, our procedure is able to disentangle the signal produced by rotation from the signal produced by the bulk motion. To further assess the impact of the cluster bulk velocity on the determination of the parameters describing the rotational law, we inspected the parameter covariance matrix, finding no significant correlation between $v_{\rm bulk}$ and both r_0 and v_{t0}.

The right columns of Table 4.9 report the values of the r_0 and v_{t0} parameters as derived from the fit to the rotational velocity inferred directly from the simulation data, namely from the $v_{\rm tan}$ velocity of equation (4.19). It can be seen that the values of the scale radius r_0 estimated from the fit to the kSZ maps are consistent with the expected ones within one standard deviation. The values of the v_{t0} parameter, instead, are overestimated by a factor of ~ 1.5 (1.6) on average, when performing the fit without (with) the bulk motion. Indeed, they reach values larger than 80 per cent of the circular velocity at the virial radius (which is $\gtrsim 1200\,{\rm km\,s^{-1}}$ for all the clusters, see also Figure 4.12). Nevertheless, there is agreement within one standard deviation for almost all the clusters. A noticeable exception is given by cluster 98, for which we get a larger overestimate (of factors of 3.1 and 2.8 without and with the

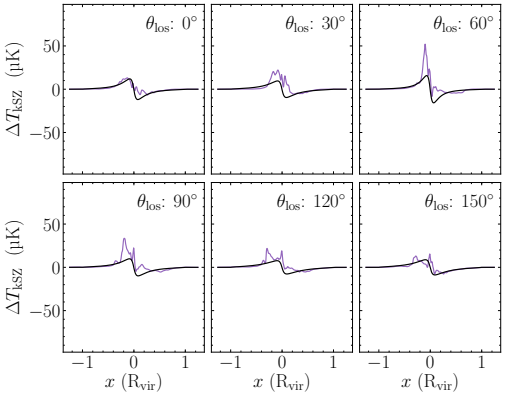

(a) cl. 46 without bulk

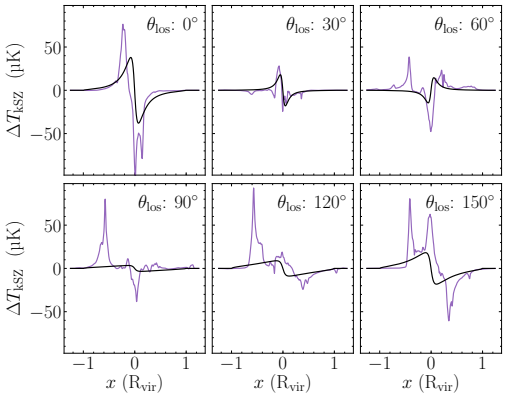

(b) cl. 98 without bulk

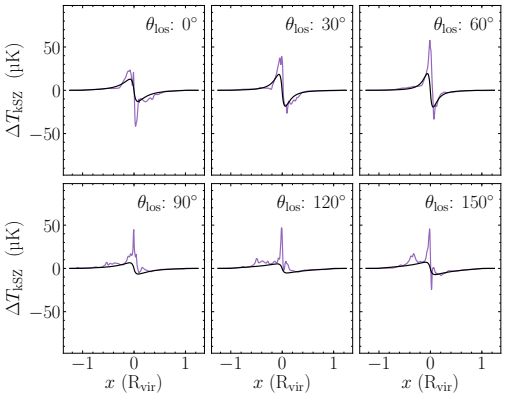

(c) cl. 103 without bulk

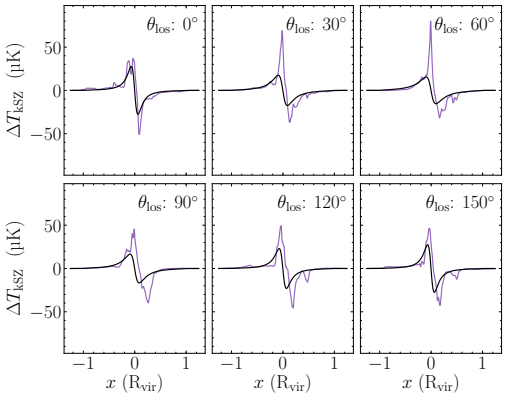

(d) cl. 205 without bulk

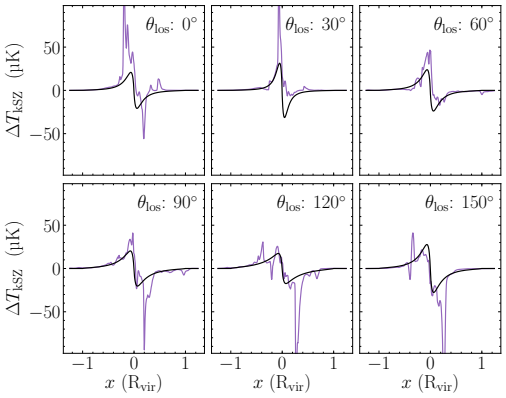

(e) cl. 256 without bulk

Figure 4.25. Same plots as in Figure 4.24a for the other clusters in the sample.

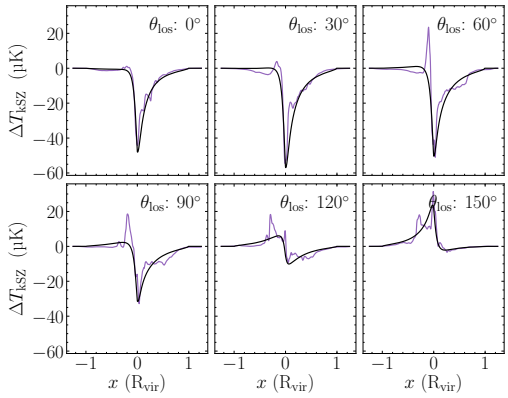

(a) cl. 46 with bulk

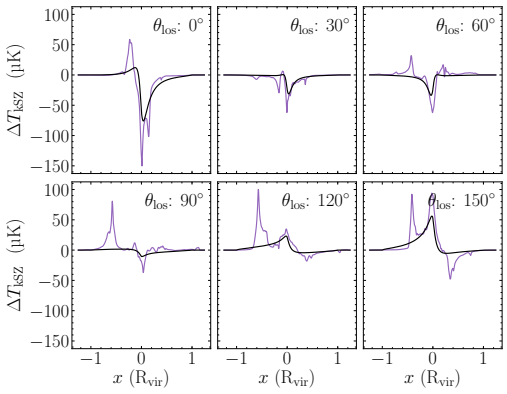

(b) cl. 98 with bulk

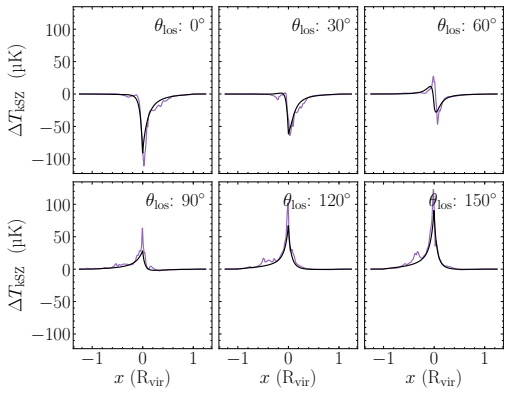

(c) cl. 103 with bulk

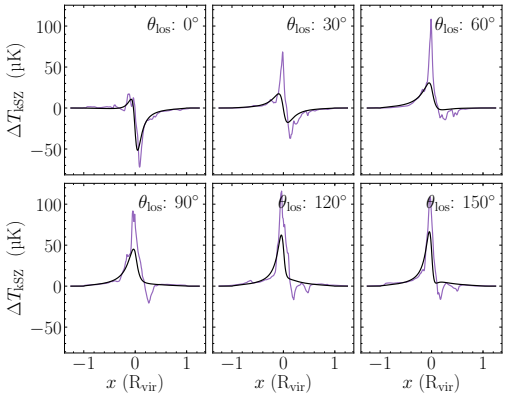

(d) cl. 205 with bulk

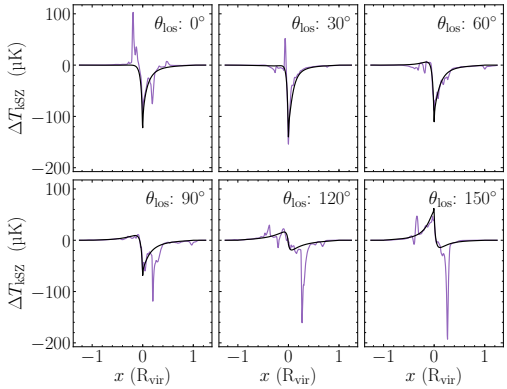

(e) cl. 256 with bulk

Figure 4.26. Same plots as in Figure 4.24b for the other clusters in the sample.

Table 4.9. Best-fit values of the free parameters r_0 and v_{t0} of equation (4.28). The left and middle columns report the average values with their standard deviation computed over all the lines of sight The right columns lists the expected values for the parameters, derived from the fit to the tangential velocity data, $v_{\rm tan}$, extracted from the simulation.

Cluster ID	fit to kSZ without bulk		fit to kSZ with bulk		fit to $v_{\rm tan}$ data	
	r_0 ($R_{\rm vir}$)	v_{t0} ($v_{\rm circ}$)	r_0 ($R_{\rm vir}$)	v_{t0} ($v_{\rm circ}$)	r_0 ($R_{\rm vir}$)	v_{t0} ($v_{\rm circ}$)
46	0.34 ± 0.09	0.84 ± 0.04	0.37 ± 0.05	0.95 ± 0.17	0.36 ± 0.22	0.56 ± 0.17
93	0.34 ± 0.08	0.87 ± 0.27	0.34 ± 0.07	0.88 ± 0.28	0.49 ± 0.27	0.58 ± 0.20
98	0.38 ± 0.30	1.53 ± 0.67	0.33 ± 0.25	1.39 ± 0.65	0.57 ± 0.62	0.49 ± 0.29
103	0.29 ± 0.13	0.82 ± 0.09	0.28 ± 0.11	0.83 ± 0.09	0.47 ± 0.35	0.52 ± 0.19
205	0.20 ± 0.08	0.96 ± 0.08	0.24 ± 0.09	0.86 ± 0.19	0.27 ± 0.14	0.65 ± 0.17
256	0.32 ± 0.12	1.00 ± 0.23	0.33 ± 0.11	1.02 ± 0.24	0.37 ± 0.20	0.61 ± 0.22

cluster bulk, respectively), and significantly larger errors. Such discrepancies may be due, in general, to a less efficient reconstruction of the dipole because of a higher impact from irregularities in the gas density distribution, and from high-velocity sub-structures, especially in the outer regions (see e.g. Figure 4.17b).

To give a quantitative indication of the kSZ signal produced only by the rotation, we measure the amplitude of the dipole from the best-fit theoretical maps in the rotation-only case. The values are listed in Table 4.10, as derived from the average over all the explored projections. It can be seen that the dispersion across different lines of sight is of the order of 38 per cent at most, while average values are of the order of a few tens of µK. This result is in agreement with the predictions by [101], that indicate dipole amplitudes ranging between ~ 4 and $\sim 30\,\mu$K (assuming a solid body rotation). Table 4.10 reports also the maximum amplitude, $A_{\rm bulk}$, measured in the best-fit maps accounting for the cluster bulk motion. We verify that, as expected, this quantity is linearly proportional to the projected bulk velocity, $v_{\rm bulk}$. Using these values it is possible to compute the ratio $A_{\rm dip}/A_{\rm bulk}$, to estimate how much does the rotation contribute to the total kSZ signal, when the projection of the cluster bulk velocity takes its maximum value. The average value of this ratio is ~ 0.23, confirming that very high sensitivities are needed to measure the effect of a rotation, provided the best observational conditions. The recovered

Table 4.10. Amplitude of the kSZ temperature signal measured from the best-fit maps. The $A_{\rm dip}$ column refers to the amplitude of the dipole averaged over all the lines of sight, as derived from the fit to the maps without the bulk motion. $A_{\rm bulk}$ refers instead to the maximum amplitude of the best fit to the maps accounting for the cluster bulk motion.

cluster ID	$A_{\rm dip}$ (µK)	$A_{\rm bulk}$ (µK)
46	10.8 ± 2.5	-57.5
93	21.1 ± 5.2	82.1
98	24.4 ± 9.2	-77.9
103	16.5 ± 2.9	-99.4
205	20.9 ± 5.1	68.8
256	24.4 ± 4.3	-143.1

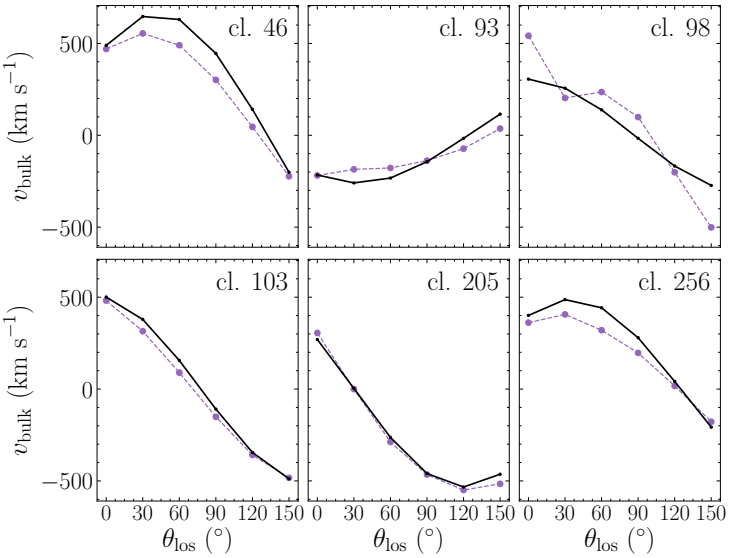

Figure 4.27. Values of the projected cluster bulk velocity, $v_{\rm bulk}$, as a function of the angle $\theta_{\rm los}$ identifying the different lines of sight. The purple dots with the dashed line represent the estimate from the fit to the maps with the bulk term. The black dots with the solid line are the true values extracted from the simulation.

values of $v_{\rm bulk}$ are of the order of hundreds of km s^{-1}, and they are fairly compatible with the true values from the simulation. We show the comparison between these values in Figure 4.27, where the sinusoidal behaviour of the different projections with varying $\theta_{\rm los}$ can also be seen. In Table 4.11 we report the differences between $v_{\rm bulk}$ recovered from the fit to the kSZ maps and the true value from the simulation, $v_{\rm bulk,sim}$, normalized to $v_{\rm bulk,sim}$ itself. Values are generally underestimated by a few tens of per cent for most of the projections. The differences are more significant for lines of sight for which the projected bulk velocity takes absolute values smaller than 100 km s^{-1}. The possibility of recovering the bulk velocity term with this procedure is an important result of this work. Indeed, the use of the rotational kSZ effect with

Table 4.11. Normalized difference between the recovered $v_{\rm bulk}$ and the true one extracted from the simulation, $v_{\rm bulk,sim}$. The values along the columns refer to the six different lines of sight.

cluster ID	$v_{\rm bulk}/v_{\rm bulk,sim} - 1$					
	$\theta_{\rm los}$					
	0°	30°	60°	90°	120°	150°
46	-0.04	-0.14	-0.22	-0.32	-0.68	-0.11
93	-0.01	0.28	0.24	0.04	-3.39	-0.68
98	0.77	-0.21	0.70	-4.96	-0.20	-0.84
103	-0.04	-0.17	-0.43	-0.38	-0.04	0.01
205	0.13	-0.92	-0.09	-0.01	-0.03	-0.11
256	-0.10	-0.17	-0.28	-0.30	-0.61	0.14

complementary observables, e.g. higher order corrections terms to the Kompaneets' approximation, or the degree of CMB polarization induced by the kSZ, could give an estimate of the three-dimensional cluster velocity [45].

The simplifying assumptions we have made, e.g. the orthogonal orientation of the los with respect to the rotation axis, and the poor error constraints we get in the final estimates of the parameters could be limiting factors for this analysis. Nevertheless, this study is intended to quantify the amount of kSZ signal that would be produced by ICM rotation at the best observational conditions, also to get a possible validation of the vp2b model. Some enhancements to get more robust results can include e.g. a proper modelling of the sub-structures to be included in the theoretical map for a more accurate fit.

An interesting recent study on cluster rotation from the kSZ effect has been performed by [34]. They use the *Planck* CMB data cleaned for the thermal SZ effect to look for the signature from the rotational dipole in a set of stacked maps, centred on thirteen low-redshift massive clusters. The rotational signal is assessed using the galaxy members as proxies, and via a geometric indicator based on the asymmetry of the negative and positive spots occurring in the maps, and it is also determined via a model fitting. The results indicate a possible rotation from the stacked kSZ signal with a significance of 2σ, which is consistent with our findings presented in this section. Nevertheless, there is no evidence for rotation from the analysis of the maps of the single clusters, at least with the sensitivity and the resolution provided by *Planck*. This first experimental assessment of the rotational kSZ signal is undoubtedly promising. Future experiments (e.g. *MILLIMETRON* [414]) will certainly deliver more reliable and precise data which will allow deeper investigations on this fascinating topic.

4.3.4 Co-rotation of ICM and galaxies in the selected sample

The study of the rotational kSZ effect presented in the above sections is part of a larger project on the feasibility of the detection of ICM rotation, that will include the complementary analysis of multi-frequency mock signals generated from MUSIC cluster data.

In this respect, we addressed the study of the dynamics of the galaxy members, focussing on our sample of relaxed and rotating clusters (see Table 4.7), to investigate the possible co-rotation between the baryonic components. To check for the rotation of the galaxies, we used the same method introduced by MP17. We refer the reader to the paragraph dedicated to optical probes of rotation in section 4.1.1, for a synthetic description of the method.

When applying this procedure to MUSIC clusters, we did not emulate spectroscopic measurements of the galaxy velocities based on mock optical data. Taking advantage of the simulations, instead, we used directly the three-dimensional vectors giving the positions and the velocities of all the "galaxy particles". This leads to more general results, since they do not refer to any particular instrument. As in the case of the rotational kSZ effect, the aim of this analysis is to check whether we could recover the global cluster rotation setting the best, noiseless observational configuration.

The galaxy particles that we considered for the analysis have been selected as those sub-haloes having masses $M_{\rm vir} < 5 \times 10^{12} h^{-1} {\rm M}_{\odot}$ from the CSF run, located within

the virial radius of each cluster. Moreover, we checked whether this technique gives consistent results relative to the analysis of the angular momentum, concerning with the rotational state of gas and DM particles. To this end, we also randomly extracted as many particles of gas and DM as the galaxies, to use them to run the algorithm.

Since MP17's method applies to the projected velocities along the line of sight, we explored different possible configurations by suitably rotating all the particle positions and velocity vectors. Under the assumption that the galaxies co-rotate with the gas (and with the DM), we identified the axis of rotation with the direction of the angular momentum vector of the gas at the virial radius, $\boldsymbol{L}_{\rm gas}(R_{\rm vir})$, as in our previous analyses. By construction, we imposed this vector to coincide with the $\hat{z}$ axis of the rotated three-dimensional reference frame. The rotation of the particles has been checked on five different observational planes of the sky (see Figure 4.2 for a representation of the observational plane). This corresponds to choosing five different lines of sight orthogonal to these planes. More specifically, such planes are denoted in the new (rotated) reference frame as: $\hat{x}\hat{y}$, $\hat{x}\hat{z}$, $\hat{y}\hat{z}$, $\hat{x}\hat{z}_{45}$, and $\hat{y}\hat{z}_{45}$; the latter are oriented 45° with respect to the $\hat{x}\hat{z}$ and the $\hat{y}\hat{z}$ planes, respectively. The corresponding lines of sight coincide with the $\hat{z}$, $\hat{y}$, $\hat{x}$, $\hat{y}_{45}$ and $\hat{x}_{45}$ axes, respectively. Given the alignment of $\hat{z}$ with $\boldsymbol{L}_{\rm gas}(R_{\rm vir})$, we expect that there is no rotation when considering the $\hat{x}\hat{y}$ observational plane, if all the particle species (galaxies, gas and DM) co-rotate. On the contrary, the signal should be maximised when observed along the $\hat{x}$ or the $\hat{y}$ lines of sight (corresponding to the $\hat{x}\hat{z}$ and $\hat{y}\hat{z}$ planes).

The results from the run of the algorithm towards our most rotating clusters indicate that, for the majority of the objects, the galaxy particles seem to show a rotation in the observational planes containing the $\hat{z}$ axis. This fact is expected in the case of a co-rotation with the gas; nevertheless, we found hints for a strong rotation also in the $\hat{x}\hat{y}$ plane, in some cases, which is difficult to be interpreted. Interestingly, the largest contribution to the rotation comes from the most massive galaxies (with stellar masses $M_{\rm star} > 10^{10}h^{-1}{\rm M}_{\odot}$), located at radii $r > 0.75R_{\rm vir}$, which is in disagreement with our findings on the tangential velocity profiles (peaked at about $0.3R_{\rm vir}$).

For the sake of completeness, we also tested the same procedure using the five least rotating clusters in the MUSIC-2 selected sub-sample, namely those having $\lambda_{\rm gas} < 0.01$. The results are puzzling, since a strong rotational signal is found in at least one projection for all these clusters, despite they should not be rotating at all. Figure 4.28 provides the rotation diagrams for the example cases of an expected rotating (left panel) and a non-rotating cluster (right panel). The data points represent the $v_{\rm diff}$ velocity defined in equation (4.7) on page 121, as a function of θ. The latter is defined as the angle between the line of sight – which is orthogonal to the observational plane indicated at the top of the figures – and the projected rotation axis (see also Figure 4.2). The red curves give the best fit to the data, which should ideally follow a sinusoidal behaviour if the galaxies rotate, as illustrated also in Figure 4.3. The blue lines highlight the limit on $v_{\rm diff}$ set by random motions. It can be seen that in the case of cluster 98 (which rotates according to the spin parameter of the ICM), we find that also galaxies rotate, when considering an observational plane containing the rotation axis. Cluster 174, instead, which is expected to be non-rotating, shows contradictory results. Indeed, data seem to indicate a rotation when

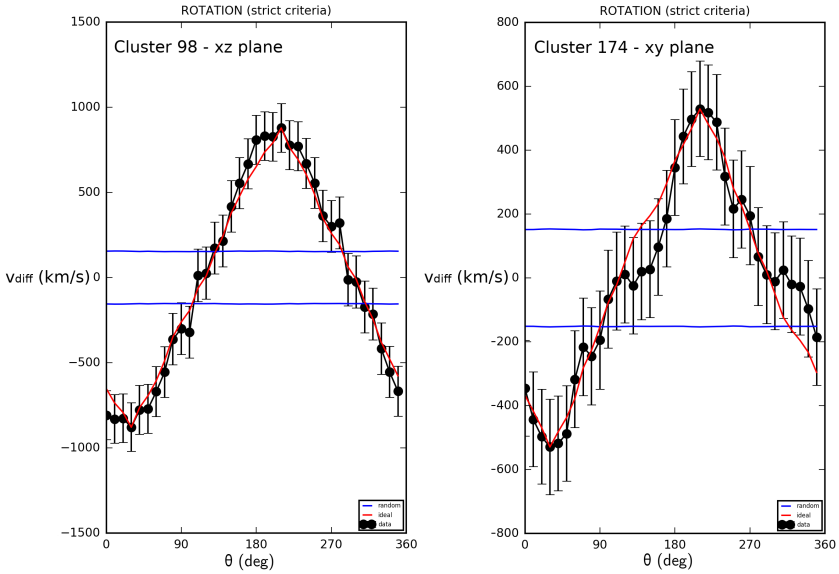

Figure 4.28. Rotation diagrams from the galaxy velocities of a supposedly rotating cluster ($\lambda_{\rm gas} > 0.07$) and a non-rotating one ($\lambda_{\rm gas} < 0.01$), extracted from the MUSIC-2 sub-sample of massive relaxed objects. See text for the explanation.

observing the cluster along a line of sight which is parallel to the expected rotation axis, although with large errors. This may indicate that neither the orientation of the rotation axis, nor the rotational state itself are necessarily consistent between the gas and the galaxies in the same cluster.

The results on the rotational state of gas and DM particles recovered with MP17 show, on the other hand, an overall agreement with the values of the spin parameters. For instance, in the test case of cluster 93 (which is expected to be rotating), no rotation is found, as expected, when considering the $\hat{x}\hat{y}$ observational plane. Instead, there are indications for a rotation in the remaining projections, in agreement with the orientation of the expected rotation axis of the gas.

With the aim of getting a statistics on the detection of rotating clusters, and to avoid single-cluster effects, we also extended the above study to all the relaxed clusters in the MUSIC-2 CSF sub-sample, dropping the prior distinction between rotating vs non-rotating clusters. We find that, with MP17's method, the rotation of the galaxies poorly correlates, in general, with the rotation of the gas and of the DM as inferred with the same method. Indeed, the values of the Spearman correlation coefficients are -0.05 and 0.03, respectively. Gas and DM themselves are correlated, instead, in agreement with the results presented in section 4.3.2. When comparing the outcomes of this method for the galaxies with the values of the spin parameters of gas and DM, there is only a weak correlation, with coefficients of 0.15 and 0.26, respectively. The larger correlation with the DM suggests that this component likely dominates the dynamics in clusters, as already pointed out in section 4.3.2.

To conclude, the tests we made using MP17's algorithm indicate that the galaxies are not good tracers of a possible global rotation in clusters. The results are, indeed, controversial and sometimes difficult to interpret. This has been also confirmed experimentally, from the recent findings reported in [265] for cluster A2107. A

possible reason for these discrepancies may reside in the very different dynamical evolution and nature of galaxies, compared to the ICM and to the DM.
The global statistics on the 154 relaxed clusters from the CSF run reports ≈ 11 per cent of rotating clusters according to the galaxies, which raises to ≈ 73 per cent if considering gas and DM. These values are significantly larger than the fraction of rotating clusters we found in the same relaxed sample, according to the value of the spin parameter of the gas (which is about 4 per cent). This fact may suggest that MP17's method may largely overestimate the fraction of rotating clusters because of projection effects, which lead to a non-negligible number of false detections (as in the case of the supposedly non-rotating clusters).

Future developments

The mild agreement we got with the two different approaches on the sample of rotating objects under study, is not enough to undoubtedly establish the co-rotation of baryonic components in clusters. Nevertheless, this challenging problem, which we are addressing in a paper in preparation, deserves further investigations, possibly with more rigorous methods, or with a different cluster sample. In this respect, in particular, we plan to apply our ongoing analysis to the new data set of The Three Hundred project, especially to study the possible impacts of the state-of-the-art gas physics which has been implemented.
Another interesting study based on multi-wavelength data which would be feasible with The Three Hundred data set, would consist in analysing the correlation between the gas kinematics inferred from the kSZ, and the rotational motion of stars in the BCG. Such an information would be extremely useful to identify good real candidate clusters to search for the kSZ rotational signal in future observational campaigns.
Furthermore, a deeper approach focused on a more quantitative assessment of the feasibility of such challenging detection at millimetre wavelengths is ongoing, with the aim of applying this study to observations of real clusters. Specifically, we will refer to the full pipeline of the NIKA2 camera at the IRAM telescope, to properly account for the full instrumental effects and for the contamination from both astrophysical sources and the SZ background.

Conclusions and future perspectives

In this Thesis, we presented our work dedicated to the study of cluster astrophysics with the Sunyaev–Zel'dovich (SZ) effect. In particular, we exploited both the thermal and the kinetic components of the above effect in two works. The first one aims at an improved mapping of the thermal pressure in cluster outskirts via the thermal Sunyaev–Zel'dovich (tSZ) effect. The second one is dedicated to the investigation of a possible rotation of the gas, by means of the analysis of the properties of the angular momentum and of the maps of the kinetic Sunyaev–Zel'dovich (kSZ) signal. The underlying motivation of these two works is to consider a possible way of estimating cluster masses more accurately. Indeed, overpressure in the outskirts can lead to biases in the mass as derived from the thermodynamic properties of the intra-cluster medium, or from the scaling relation involving the integrated signal from the tSZ effect. On the other hand, the support from non-thermal motions (e.g. rotation) can be associated to an additional, dynamical mass term which is usually neglected, under the hypothesis of hydrostatic equilibrium.
We summarise our methods and our main findings in the following.

In the first part of the Thesis, we presented an improved version of an existing spectral imaging algorithm for parametric component separation, which is based on wavelet and curvelet decompositions. The enhancements we discussed are, specifically: (*i*) a double grey body spectral energy density to model the emission from Galactic thermal dust; (*ii*) the cleaning of residual contamination from dust on large scales, and from bright point sources; (*iii*) a new, non-iterative wavelet coefficient-wise deconvolution of the *Planck* beams within the calculation of the wavelet transform. Moreover, we introduced a new method to estimate the error on the reconstructed signal based on bootstrap extractions of *Planck* noise maps. Using these error maps, we assessed an equivalent signal-to-noise ratio to establish the significance of the detected features. The procedure has been applied to the latest *Planck* frequency maps centred on twelve nearby, massive galaxy clusters constituting the X-COP sample. The comparison between the new version of the imaging procedure and the original one highlights a significant improvement. This concerns primarily with the stability of the algorithm, which was hampered by local divergences in low-signal regimes. Furthermore, the reconstruction of the signal in the outskirts is more precise, down to values of the Compton y-parameter of a few 10^{-6}, and the recovery of the peak value is more reliable. Our maps of the Compton y-parameter for the whole cluster sample show that we are able to reconstruct the signal from anisotropies

– such as elongations, diffuse filaments and small substructures – located beyond R_{500}. Indeed, we detected interesting features in the outskirts of the majority of the clusters under study. In particular, we highlighted significant diffuse elongations in the cluster systems A2029 and RXCJ1825. These findings are consistent with ancillary surface brightness maps in the X-ray band.
As for the future perspectives, one of the most direct application of our maps of the Compton y-parameter is the assessment of the impact of thermal pressure from the aforementioned anisotropic signal structures in cluster peripheral regions. We started indeed to explore this possibility, by applying a preliminary technique based on a simple masking of the pixels corresponding to significant signal anisotropies, according to our bootstrap-derived error maps. We found encouraging results from the fit to the pressure profiles of a few single clusters, where we clearly see that the pressure contribution in the outskirts is smaller when the masks are applied. The final step would be that of combining all the maps together to get the stacked profile, which could be compared to similar profiles in the literature, and possibly provide a more consistent, less scattered behaviour beyond the R_{500} radius. Such a study could be very promising in correcting the mass estimate of clusters, which is connected with their thermal pressure budget. An improved mapping of the pressure, combined with X-ray information, may point to the need for a correction of the estimated mass, accounting for the contribution from poorly resolved structures within the virial region. In this context, a further development of this work, will be the detailed study of a particularly interesting system in the X-COP sample, namely cluster A2319, which we will develop in a forthcoming paper.

In the second part of the Thesis, we investigated rotational motions, which are expected to contribute to the hydrostatic support in clusters. We focussed on a sub-sample of massive clusters extracted from the MUSIC hydrodynamical simulations. First, we studied the properties of the specific angular momentum and of the tangential and random velocity components of gas and dark matter (DM). We produced the profiles of these quantities along the cluster radius, considering data from all the three available gas modellings adopted in the simulations: non-radiative, with cooling and star formation and with AGN feedback. To avoid the impact of possible merging processes and of the motions of large substructures, we focussed on the most relaxed objects. Then, we classified them as rotating or not according to the value of the spin parameter of the gas at the virial radius, with the threshold value of 0.07. We found that the overall dynamics of the clusters is dominated by the DM component, since there are no significant differences among the three flavours of the gas physics. The sample of rotating clusters consists in a relatively small number of objects, which is 4 per cent of the relaxed sample. The average profiles for these clusters show that the rotation is not well described by a solid body, which motivated us to introduce a new model for the radial profile of the tangential velocity (which we call vp2b model), based on previous works. The rotational support to the circular velocity is found to be of the order of 16 per cent at the virial radius, but yet non null. Interestingly, we found that in a non-negligible fraction of the total sample (about 40 per cent) the angular momentum vectors of gas and DM are aligned, suggesting a co-rotation of the two components. This holds true especially for increasing values of the spin parameter of the gas, i.e. for the most rotating objects.

Subsequently, referring only to the case of non-radiative simulations, we tried to reconstruct the rotation described by the tangential velocity profile of the six relaxed and rotating clusters by means of the kSZ effect. We treated both a simplified case not accounting for the cluster bulk motion, and the complete case including the additional term depending on the cluster bulk velocity projected on the line of sight. We also explored six different lines of sight for both cases, picking them all orthogonal to the expected rotation axis, to maximize the amplitude of the rotational signal. The mock maps from our rotating clusters have been fit to the theoretical ones, which we modelled using the vp2b rotational law descending from the analysis of the angular momentum. The results from the fit indicate that, provided the best observational conditions, it is possible to recover the parameters of the radial profile of the rotational velocity within one standard deviation in the case of the scale radius, and within two standard deviations at most in the case of the scale velocity, by averaging across the considered lines of sight. These results are poorly affected by the small-scale outliers produced by high-velocity substructures located within the cluster virial radius, at most projections. The amplitude of the best-fit dipole is consistent with the estimates found in the literature for relaxed systems. From a comparison between the amplitude derived without and with the bulk motion, we estimate that the rotational contribution to the total kSZ signal is, on average, at most of the order of 23 per cent.
We can conclude that, when present, rotational support is undoubtedly small, thus it is challenging to detect it with the currently available instruments. In any case, ancillary data from measurements in the X-ray and optical bands are mandatory to validate possible future observations. Future experiments with high resolution and sensitivity will surely provide a significant improvement over the current capabilities of addressing such a challenging measurement. In this future perspective, high-resolution hydrodynamical simulations are still indispensable for feasibility analyses. For instance, an interesting study would consist in taking into account the instrumental effects of an optimal candidate observatory (e.g. the NIKA2 camera at the IRAM telescope), to provide a more realistic assessment of the detectability of the signal. Another useful way to exploit simulations is to use mock data at ancillary wavelengths, to see whether we get a consistent picture from all observables in the same cluster sample. In this respect, we started a study on the velocities of the member galaxies, based on the method proposed in the recent work by MP17. Despite we found a mild agreement on the rotational state inferred from both the gas and the galaxies in some of the most rotating clusters, it seems that the motion of galaxies is not an adequate indicator. Most notably, all the proposed methods so far are particularly sensitive to projection effects which bias-high the statistics of rotating clusters. While being still very challenging in the context of observational perspectives, cluster rotation is definitely a topic of interest, as testified by recent works. This encourages further developments, possibly with novel methods or new, high-quality synthetic data sets.

As a general conclusion, the noticeable progresses in the study of galaxy clusters are extremely valuable for astrophysics and cosmology. The upcoming large surveys and the refined theoretical picture provided by cosmological simulations will offer promising possibilities to improve our understanding of the universe. In this respect, the SZ effect is undoubtedly an indispensable probe to pursuit this knowledge.

Acknowledgments

Part of this Thesis work has been awarded funding from Sapienza Università di Roma as "Progetti per Avvio alla Ricerca - Tipo 1" in the Academic Years 2017/2018 (prot. AR11715C82402BC7), and 2018/2019 (prot. AR11816430D9FBEA).

Bibliography

[1] Abazajian, K. N. et al. Neutrino physics from the cosmic microwave background and large scale structure. Astroparticle Physics, **63** (2015), 66.

[2] Abel, T., Bryan, G. L., and Norman, M. L. The Formation and Fragmentation of Primordial Molecular Clouds. ApJ, **540** (2000), 39.

[3] Adam, R. et al. Pressure distribution of the high-redshift cluster of galaxies cl j1226.9+3332 with nika. A&A, **576** (2015), A12.

[4] Adam, R. et al. Mapping the kinetic Sunyaev-Zel'dovich effect toward MACS J0717.5+3745 with NIKA. A&A, **598** (2017), A115.

[5] Adam, R. et al. Substructure and merger detection in resolved NIKA Sunyaev-Zel'dovich images of distant clusters. A&A, **614** (2018), A118.

[6] Aghanim, N. et al. PACT I: Combining ACT and Planck data for optimal detection of tSZ signal. Preprint (arXiv:1902.00350), (2019).

[7] Allen, S. W., Evrard, A. E., and Mantz, A. B. Cosmological Parameters from Observations of Galaxy Clusters. ARA&A, **49** (2011), 409.

[8] Alma Consortium. The Atacama Large Millimeter Array (ALMA). In *European Southern Observatory Press Release* (1999).

[9] Alpher, R. A., Follin, J. W., and Herman, R. C. Physical Conditions in the Initial Stages of the Expanding Universe. PhRv, **92** (1953), 1347.

[10] Ameglio, S. et al. Reconstructing mass profiles of simulated galaxy clusters by combining Sunyaev-Zeldovich and X-ray images. MNRAS, **394** (2009), 479.

[11] Ami Consortium. High-significance Sunyaev-Zel'dovich measurement: Abell 1914 seen with the Arcminute Microkelvin Imager. MNRAS, **369** (2006), 1.

[12] Anders, E. and Grevesse, N. Abundances of the elements: Meteoritic and solar. Geochim. Cosmochim. Acta, **53** (1989), 197.

[13] Armendariz-Picon, C., Mukhanov, V., and Steinhardt, P. J. Dynamical Solution to the Problem of a Small Cosmological Constant and Late-Time Cosmic Acceleration. Phys. Rev. Lett., **85** (2000), 4438.

[14] Arnaud, M. et al. The universal galaxy cluster pressure profile from a representative sample of nearby systems (rexcess) and the ysz-m500 relation. A&A, **517** (2010), A92.

[15] Ascasibar, Y. et al. On the physical origin of dark matter density profiles. MNRAS, **352** (2004), 1109.

[16] Avestruz, C., Nagai, D., and Lau, E. T. Stirred, Not Clumped: Evolution of Temperature Profiles in the Outskirts of Galaxy Clusters. ApJ, **833** (2016), 227.

[17] Avestruz, C. et al. Non-equilibrium Electrons in the Outskirts of Galaxy Clusters. ApJ, **808** (2015), 176.

[18] Bagla, J. S. TreePM: A Code for Cosmological N-Body Simulations. Journal of Astrophysics and Astronomy, **23** (2002), 185.
[19] Balantekin, A. B. and Kayser, B. On the properties of neutrinos. ARNPS, **68** (2018), 313.
[20] Baldi, A. S. et al. On the coherent rotation of diffuse matter in numerical simulations of clusters of galaxies. MNRAS, **465** (2017), 2584.
[21] Baldi, A. S. et al. Kinetic Sunyaev-Zel'dovich effect in rotating galaxy clusters from MUSIC simulations. MNRAS, **479** (2018), 4028.
[22] Baldi, A. S. et al. Spectral imaging of the thermal Sunyaev-Zel'dovich effect in X-COP galaxy clusters: method and validation. A&A, **630** (2019), A121.
[23] Barcons, X. et al. Athena: the X-ray observatory to study the hot and energetic Universe. JPhCS, **610** (2015), 012008.
[24] Bardeen, J. M. et al. The Statistics of Peaks of Gaussian Random Fields. ApJ, **304** (1986), 15.
[25] Barnes, D. J. et al. The Cluster-EAGLE project: global properties of simulated clusters with resolved galaxies. MNRAS, **471** (2017), 1088.
[26] Barnes, J. and Efstathiou, G. Angular Momentum from Tidal Torques. ApJ, **319** (1987), 575.
[27] Barnes, J. and Hut, P. A hierarchical O(N log N) force-calculation algorithm. Nature, **324** (1986), 446.
[28] Bartelmann, M. The dark Universe. RvMP, **82** (2010), 331.
[29] Bartelmann, M. TOPICAL REVIEW Gravitational lensing. CQGra, **27** (2010), 233001.
[30] Battaglia, N. et al. On the Cluster Physics of Sunyaev-Zel'dovich and X-Ray Surveys. I. The Influence of Feedback, Non-thermal Pressure, and Cluster Shapes on Y-M Scaling Relations. ApJ, **758** (2012), 74.
[31] Battistelli, E. S. et al. Cosmic Microwave Background Temperature at Galaxy Clusters. ApJ, **580** (2002), L101.
[32] Baugh, C. M. A primer on hierarchical galaxy formation: the semi-analytical approach. RPPh, **69** (2006), 3101.
[33] Baumann, D. and McAllister, L. *Inflation and String Theory*. Cambridge University Press (2015).
[34] Baxter, E. J., Sherwin, B. D., and Raghunathan, S. Constraining the rotational kinematic Sunyaev-Zel'dovich effect in massive galaxy clusters. J. Cosmology Astropart. Phys., **2019** (2019), 001.
[35] Bennett, C. L. et al. First-Year Wilkinson Microwave Anisotropy Probe (WMAP) Observations: Preliminary Maps and Basic Results. ApJS, **148** (2003), 1.
[36] Benson, B. A. et al. SPT-3G: a next-generation cosmic microwave background polarization experiment on the South Pole telescope. In *Millimeter, Submillimeter, and Far-Infrared Detectors and Instrumentation for Astronomy VII*, vol. 9153 of Proc. SPIE, p. 91531P (2014).
[37] Bergamini, P. et al. Enhanced cluster lensing models with measured galaxy kinematics. Preprint (arXiv:1905.13236), (2019).
[38] Bialek, J. J., Evrard, A. E., and Mohr, J. J. Effects of Preheating on X-Ray Scaling Relations in Galaxy Clusters. ApJ, **555** (2001), 597.

[39] Bianconi, M., Ettori, S., and Nipoti, C. Gas rotation in galaxy clusters: signatures and detectability in X-rays. MNRAS, **434** (2013), 1565.
[40] Biffi, V., Dolag, K., and Böhringer, H. Velocity structure diagnostics of simulated galaxy clusters. MNRAS, **413** (2011), 573.
[41] Biffi, V. et al. The MUSIC of Galaxy Clusters - II. X-ray global properties and scaling relations. MNRAS, **439** (2014), 588.
[42] Biffi, V. et al. On the Nature of Hydrostatic Equilibrium in Galaxy Clusters. ApJ, **827** (2016), 112.
[43] Binney, J. and Tremaine, S. *Galactic dynamics*. Princeton university press (2011).
[44] Birkinshaw, M. The Sunyaev-Zel'dovich Effect towards three clusters of galaxies. Natur, **309** (1984), 34.
[45] Birkinshaw, M. The Sunyaev-Zel'dovich effect. Phys. Rep., **310** (1999), 97.
[46] Blasi, P., Olinto, A. V., and Stebbins, A. The Effect of a Nonthermal Tail on the Sunyaev-Zeldovich Effect in Clusters of Galaxies. ApJ, **535** (2000), L71.
[47] Bleem, L. E. et al. Galaxy Clusters Discovered via the Sunyaev-Zel'dovich Effect in the 2500-Square-Degree SPT-SZ Survey. ApJS, **216** (2015), 27.
[48] Bobin, J. et al. SZ and CMB reconstruction using generalized morphological component analysis. StMet, **5** (2008), 307.
[49] Bobin, J. et al. Sparse component separation for accurate cosmic microwave background estimation. A&A, **550** (2013), A73.
[50] Bocquet, S. et al. Halo mass function: baryon impact, fitting formulae, and implications for cluster cosmology. MNRAS, **456** (2016), 2361.
[51] Böhringer, H. and Werner, N. X-ray spectroscopy of galaxy clusters: studying astrophysical processes in the largest celestial laboratories. A&A Rev., **18** (2010), 127.
[52] Bolliet, B. et al. Including massive neutrinos in thermal Sunyaev Zeldovich power spectrum and cluster counts analyses. Preprint (arXiv:1906.10359), (2019).
[53] Bonamente, M. et al. Determination of the Cosmic Distance Scale from Sunyaev-Zel'dovich Effect and Chandra X-Ray Measurements of High-Redshift Galaxy Clusters. ApJ, **647** (2006), 25.
[54] Bonamente, M. et al. Comparison of pressure profiles of massive relaxed galaxy clusters using the Sunyaev-Zel'dovich and x-ray data. NJPh, **14** (2012), 025010.
[55] Bond, J. R., Kofman, L., and Pogosyan, D. How filaments of galaxies are woven into the cosmic web. Nature, **380** (1996), 603.
[56] Bond, J. R. et al. Excursion Set Mass Functions for Hierarchical Gaussian Fluctuations. ApJ, **379** (1991), 440.
[57] Bondi, H. On spherically symmetrical accretion. MNRAS, **112** (1952), 195.
[58] Borgani, S. and Guzzo, L. X-ray clusters of galaxies as tracers of structure in the Universe. Nature, **409** (2001), 39.
[59] Borgani, S. and Kravtsov, A. Cosmological Simulations of Galaxy Clusters. ASL, **4** (2011), 204.
[60] Borgani, S. et al. The effect of non-gravitational gas heating in groups and clusters of galaxies. MNRAS, **336** (2002), 409.

[61] Borgani, S. et al. X-ray properties of galaxy clusters and groups from a cosmological hydrodynamical simulation. MNRAS, **348** (2004), 1078.
[62] Bose, S.N. Plancks Gesetz und Lichtquantenhypothese. ZPhy, **26** (1924), 178.
[63] Botteon, A. et al. Particle acceleration in a nearby galaxy cluster pair: the role of cluster dynamics. A&A, **630** (2019), A77.
[64] Boulanger, F. et al. The dust/gas correlation at high Galactic latitude. A&A, **312** (1996), 256.
[65] Bourdin, H. *Imagerie et spectro-imagerie X appliquees a l'etude des proprietes du milieu inter- galactique dans les amas de galaxies en cours de coalescence.* PhD Thesis, Ecole Doctorale d'Astronomie et Astrophysique d'Ile de France - Université Pierre et Marie Curie (A.A. 2004).
[66] Bourdin, H. and Mazzotta, P. Temperature structure of the intergalactic medium within seven nearby and bright clusters of galaxies observed with XMM-Newton . A&A, **479** (2008), 307.
[67] Bourdin, H., Mazzotta, P., and Rasia, E. Spectral imaging of galaxy clusters with *Planck*. ApJ, **815** (2015), 92.
[68] Bourdin, H. et al. Pressure Profiles of Distant Galaxy Clusters in the Planck Catalogue. ApJ, **843** (2017), 72.
[69] Bower, R. G., McCarthy, I. G., and Benson, A. J. The flip side of galaxy formation: a combined model of galaxy formation and cluster heating. MNRAS, **390** (2008), 1399.
[70] Bracewell, R. N. *The Fourier transform and its applications.* McGraw-Hill New York (1986).
[71] Bradt, H. *Astrophysics Processes: The Physics of Astronomical Phenomena.* Cambridge University Press (2008).
[72] Bridle, S. L. et al. Reconstructing the primordial power spectrum. MNRAS, **342** (2003), L72.
[73] Bryan, G. L. and Norman, M. L. Statistical Properties of X-Ray Clusters: Analytic and Numerical Comparisons. ApJ, **495** (1998), 80.
[74] Bryan, G. L. et al. X-Ray Clusters from a High-Resolution Hydrodynamic PPM Simulation of the Cold Dark Matter Universe. ApJ, **428** (1994), 405.
[75] Bryan, S. E. et al. The impact of baryons on the spins and shapes of dark matter haloes. MNRAS, **429** (2013), 3316.
[76] Buchdahl, H. A. General Relativistic Fluid Spheres. Physical Review, **116** (1959), 1027.
[77] Bullock, J. S. et al. A universal angular momentum profile for galactic halos. ApJ, **555** (2001), 240.
[78] Calvo, M. et al. The NIKA2 Instrument, A Dual-Band Kilopixel KID Array for Millimetric Astronomy. JLTP, **184** (2016), 816.
[79] Caminha, G. et al. Strong lensing models of eight CLASH clusters from extensive spectroscopy: accurate total mass reconstructions in the cores. A&A, **632** (2019), A36.
[80] Candès, E. J. Harmonic analysis of neural networks. Applied and Computational Harmonic Analysis, **6** (1999), 197 .
[81] Candès, E. J. and Donoho, D. L. Ridgelets: a key to higher-dimensional intermittency? RSPTA, **357** (1999), 2495.

[82] Candes, E. J. and Donoho, D. L. Curvelets: A surprisingly effective nonadaptive representation for objects with edges. Tech. rep., Stanford Univ Ca Dept of Statistics (2000).

[83] Candès, E. J. and Donoho, D. L. Curvelets, multiresolution representation, and scaling laws. In *Wavelet Applications in Signal and Image Processing VIII*, vol. 4119, pp. 1–12 (2000).

[84] Candès, E. J. and Donoho, D. L. New tight frames of curvelets and optimal representations of objects with piecewise C2 singularities. CPAM, **57** (2004), 219.

[85] Candès, E. J. and Demanet, L. The curvelet representation of wave propagators is optimally sparse. CPAM, **58** (2005), 1472.

[86] Capozziello, S., D'Agostino, R., and Luongo, O. Extended gravity cosmography. IJMPD, **28** (2019), 1930016.

[87] Cardoso, J.-F. High-order contrasts for independent component analysis. Neural computation, **11** (1999), 157.

[88] Cardoso, J.-F. et al. Component Separation With Flexible Models—Application to Multichannel Astrophysical Observations. IEEE Journal of Selected Topics in Signal Processing, **2** (2008), 735.

[89] Carlberg, R. G. et al. The Average Mass Profile of Galaxy Clusters. ApJ, **485** (1997), L13.

[90] Carlstrom, J. et al. CMB-S4. In BAAS, vol. 51, p. 209 (2019).

[91] Carlstrom, J. E., Holder, G. P., and Reese, E. D. Cosmology with the Sunyaev-Zel'dovich Effect. ARA&A, **40** (2002), 643.

[92] Carlstrom, J. E. et al. Imaging the Sunyaev-Zel'dovich Effect. PhST, **85** (2000), 148.

[93] Carlstrom, J. E. et al. The 10 Meter South Pole Telescope. PASP, **123** (2011), 568.

[94] Carroll, S. M. The Cosmological Constant. LRR, **4** (2001), 1.

[95] Carvalho, P., Rocha, G., and Hobson, M. P. A fast Bayesian approach to discrete object detection in astronomical data sets - PowellSnakes I. MNRAS, **393** (2009), 681.

[96] Carvalho, P. et al. PowellSnakes II: a fast Bayesian approach to discrete object detection in multi-frequency astronomical data sets. MNRAS, **427** (2012), 1384.

[97] Catelan, P. and Theuns, T. Evolution of the angular momentum of protogalaxies from tidal torques: Zel'dovich approximation. MNRAS, **282** (1996), 436.

[98] Cavaliere, A. and Fusco-Femiano, R. The Distribution of Hot Gas in Clusters of Galaxies. A&A, **70** (1978), 677.

[99] Chabanier, S., Millea, M., and Palanque-Delabrouille, N. Updated matter power spectrum constraints from the Lyα forest and other probes. MNRAS, **489** (2019), 2247.

[100] Chluba, J. and Dai, L. Multiple scattering Sunyaev-Zeldovich signal - II. Relativistic effects. MNRAS, **438** (2014), 1324.

[101] Chluba, J. and Mannheim, K. Kinetic Sunyaev-Zel'dovich effect from galaxy cluster rotation. A&A, **396** (2002), 419.

[102] Chluba, J. et al. A fast and accurate method for computing the Sunyaev-Zel'dovich signal of hot galaxy clusters. MNRAS, **426** (2012), 510.

[103] Chluba, J. et al. Sunyaev-Zeldovich signal processing and temperature-velocity moment method for individual clusters. MNRAS, **430** (2013), 3054.

[104] Cialone, G. and others (including A. S. Baldi). Morphological estimators on Sunyaev–Zel'dovich maps of MUSIC clusters of galaxies. MNRAS, **477** (2018), 139.

[105] Clarke, T. E., Blanton, E. L., and Sarazin, C. L. The Complex Cooling Core of A2029: Radio and X-Ray Interactions. ApJ, **616** (2004), 178.

[106] Clavico, S. et al. Growth and disruption in the Lyra complex. Preprint (arXiv:1908.02276), (2019).

[107] Cohen, R. Signal denoising using wavelets (2012). https://pdfs.semanticscholar.org/3dfd/6b2bd3d6ad3c6eca50747e686d5ad88b4fc1.pdf.

[108] Coifman, R. R. and Donoho, D. L. Translation-invariant de-noising. In *Wavelets and statistics*, p. 125. Springer (1995).

[109] Coles, P. and Lucchin, F. *Cosmology: The origin and evolution of cosmic structure*. John Wiley & Sons (2003).

[110] Cooley, J. W. and Tukey, J. W. An algorithm for the machine calculation of complex fourier series. MaCom, **19** (1965), 297.

[111] Cooper, L. N. Bound Electron Pairs in a Degenerate Fermi Gas. Physical Review, **104** (1956), 1189.

[112] Cooray, A. and Chen, X. Kinetic Sunyaev-Zel'dovich effect from halo rotation. ApJ, **573** (2002), 43.

[113] Cooray, A. and Sheth, R. Halo models of large scale structure. Phys. Rep., **372** (2002), 1.

[114] Couchman, H. M. P. Mesh-refined P 3M: A Fast Adaptive N-Body Algorithm. ApJ, **368** (1991), L23.

[115] Croton, D. J. Damn You, Little h! (Or, Real-World Applications of the Hubble Constant Using Observed and Simulated Data). PASA, **30** (2013), e052.

[116] Cui, W. and others (including A. S. Baldi). The Three Hundred project: a large catalogue of theoretically modelled galaxy clusters for cosmological and astrophysical applications. MNRAS, **480** (2018), 2898.

[117] Davé, R., Katz, N., and Weinberg, D. H. X-Ray Scaling Relations of Galaxy Groups in a Hydrodynamic Cosmological Simulation. ApJ, **579** (2002), 23.

[118] Davé, R., Oppenheimer, B. D., and Sivanand am, S. Enrichment and pre-heating in intragroup gas from galactic outflows. MNRAS, **391** (2008), 110.

[119] Davis, M. and Peebles, P. J. E. A survey of galaxy redshifts. V. The two-point position and velocity correlations. ApJ, **267** (1983), 465.

[120] Day, P. K. et al. A broadband superconducting detector suitable for use in large arrays. Nature, **425** (2003), 817.

[121] De Bernardis, F. et al. Detection of the pairwise kinematic Sunyaev-Zel'dovich effect with BOSS DR11 and the Atacama Cosmology Telescope. J. Cosmology Astropart. Phys., **2017** (2017), 008.

[122] de Bernardis, P. et al. A flat Universe from high-resolution maps of the cosmic microwave background radiation. Nature, **404** (2000), 955.

[123] De Petris, M. et al. MITO: the 2.6 M millimetre telescope at Testa Grigia. New A, **1** (1996), 121.

[124] Dean, S. *The Radon Transform and Some of Its Applications*. John Wiley & sons (1983).

[125] Delabrouille, J., Cardoso, J. F., and Patanchon, G. Multidetector multicomponent spectral matching and applications for cosmic microwave background data analysis. MNRAS, **346** (2003), 1089.
[126] Delabrouille, J. et al. A full sky, low foreground, high resolution CMB map from WMAP. A&A, **493** (2009), 835.
[127] Deledalle, C. A., Denis, L., and Tupin, F. Iterative Weighted Maximum Likelihood Denoising With Probabilistic Patch-Based Weights. ITIP, **18** (2009), 2661.
[128] DES Collaboration. Dark Energy Survey year 1 results: Cosmological constraints from galaxy clustering and weak lensing. Phys. Rev. D, **98** (2018), 043526.
[129] DES Collaboration, LIGO Scientific Collaboration, and Virgo Collaboration. First Measurement of the Hubble Constant from a Dark Standard Siren using the Dark Energy Survey Galaxies and the LIGO/Virgo Binary-Black-hole Merger GW170814. ApJ, **876** (2019), L7.
[130] DES Collaboration and SPT Collaboration. Detection of the kinematic Sunyaev-Zel'dovich effect with DES Year 1 and SPT. MNRAS, **461** (2016), 3172.
[131] Désert, F.-X. et al. Observations of the Sunyaev-Zel'dovich effect at high angular resolution towards the galaxy clusters A665, A2163 and CL0016+16. New A, **3** (1998), 655.
[132] Di Mascolo, L., Churazov, E., and Mroczkowski, T. A joint ALMA-Bolocam-Planck SZ study of the pressure distribution in RX J1347.5-1145. MNRAS, (2018), 4037.
[133] Dicke, R. H., Peebles, P. J. E., Roll, P. G., and Wilkinson, D. T. Cosmic Black-Body Radiation. ApJ, **142** (1965), 414.
[134] Dicker, S. R. et al. MUSTANG: 90 GHz science with the Green Bank Telescope. In *Millimeter and Submillimeter Detectors and Instrumentation for Astronomy IV*, vol. 7020 of Proc. SPIE, p. 702005 (2008).
[135] Diego, J. M. et al. A Bayesian non-parametric method to detect clusters in Planck data. MNRAS, **336** (2002), 1351.
[136] Diemand, J., Kuhlen, M., and Madau, P. Formation and Evolution of Galaxy Dark Matter Halos and Their Substructure. ApJ, **667** (2007), 859.
[137] Dobbs, M. et al. APEX-SZ first light and instrument status. New A Rev., **50** (2006), 960.
[138] Dodelson, S. *Modern Cosmology*. Academic Press (2003).
[139] D'Onghia, E. and Navarro, J. F. Do mergers spin-up dark matter haloes? MNRAS, **380** (2007), L58.
[140] Dupke, R. A. and Bregman, J. N. Velocity Gradients in the Intracluster Gas of the Perseus Cluster. ApJ, **547** (2001), 705.
[141] Ebeling, H., Mullis, C. R., and Tully, R. B. A Systematic X-Ray Search for Clusters of Galaxies behind the Milky Way. ApJ, **580** (2002), 774.
[142] Eckert, D., et al. The gas distribution in the outer regions of galaxy clusters. A&A, **541** (2012), A57.
[143] Eckert, D. et al. The X-ray/SZ view of the virial region. II. Gas mass fraction. A&A, **551** (2013), A23.
[144] Eckert, D. et al. The XMM cluster outskirts project (X-COP). AN, **338** (2017), 293.
[145] Eckert, D. et al. Non-thermal pressure support in X-COP galaxy clusters. A&A, **621** (2019), A40.
[146] Einasto, J. et al. Structure of superclusters and supercluster formation - III. Quantitative study of the Local Supercluster. MNRAS, **206** (1984), 529.
[147] Einasto, M. et al. Optical and X-Ray Clusters as Tracers of the Supercluster-Void Network. I. Superclusters of Abell and X-Ray Clusters. AJ, **122** (2001), 2222.
[148] Einstein, A. Die Grundlage der allgemeinen Relativitätstheorie. AnP, **354** (1916), 769.

[149] Eke, V. R., Cole, S., and Frenk, C. S. Cluster evolution as a diagnostic for Omega. MNRAS, **282** (1996), 263.
[150] Ensslin, T. A. and Kaiser, C. R. Comptonization of the cosmic microwave background by relativistic plasma. A&A, **360** (2000), 417.
[151] Eriksen, H. K. et al. On Foreground Removal from the Wilkinson Microwave Anisotropy Probe Data by an Internal Linear Combination Method: Limitations and Implications. ApJ, **612** (2004), 633.
[152] Erler, J. et al. Planck's view on the spectrum of the Sunyaev-Zeldovich effect. MNRAS, **476** (2018), 3360.
[153] Etherington, I. M. H. On the Definition of Distance in General Relativity. PMag, **15** (1933), 761.
[154] Ettori, S. et al. Hydrostatic mass profiles in X-COP galaxy clusters. A&A, **621** (2019), A39.
[155] Evrard, A. E. Formation and Evolution of X-Ray Clusters: A Hydrodynamic Simulation of the Intracluster Medium. ApJ, **363** (1990), 349.
[156] Evrard, A. E. and Henry, J. P. Expectations for X-Ray Cluster Observations by the ROSAT Satellite. ApJ, **383** (1991), 95.
[157] Evrard, A. E. et al. Virial Scaling of Massive Dark Matter Halos: Why Clusters Prefer a High Normalization Cosmology. ApJ, **672** (2008), 122.
[158] Fabian, A. C. Cooling Flows in Clusters of Galaxies. ARA&A, **32** (1994), 277.
[159] Fabjan, D. et al. Simulating the effect of active galactic nuclei feedback on the metal enrichment of galaxy clusters. MNRAS, **401** (2010), 1670.
[160] Fadili, J. and Starck, J.-L. *Curvelets and Ridgelets*, pp. 754–773. Springer New York (2012).
[161] Faltenbacher, A. et al. Supersonic motions of galaxies in clusters. MNRAS, **358** (2005), 139.
[162] Fang, T., Humphrey, P., and Buote, D. Rotation and turbulence of the hot intracluster medium in galaxy clusters. ApJ, **691** (2009), 1648.
[163] Feroz, F. et al. Bayesian modelling of clusters of galaxies from multifrequency-pointed Sunyaev–Zel'dovich observations. MNRAS, **398** (2009), 2049.
[164] Finkbeiner, D. P., Davis, M., and Schlegel, D. J. Extrapolation of Galactic Dust Emission at 100 Microns to Cosmic Microwave Background Radiation Frequencies Using FIRAS. ApJ, **524** (1999), 867.
[165] Fixsen, D. J. The Temperature of the Cosmic Microwave Background. ApJ, **707** (2009), 916.
[166] Fixsen, D. J. et al. The Cosmic Microwave Background Spectrum from the Full COBE FIRAS Data Set. ApJ, **473** (1996), 576.
[167] Forni, O. and Aghanim, N. Separating the kinetic Sunyaev-Zel'dovich effect from primary cosmic microwave background fluctuations. A&A, **420** (2004).
[168] Friedmann, A. Über die Möglichkeit einer Welt mit konstanter negativer Krümmung des Raumes. ZPhy, **21** (1924), 326.
[169] Gabor, D. Theory of communication. Part 1: The analysis of information. JIEE, **93** (1946), 429.
[170] Gamow, G. The Evolution of the Universe. Nature, **162** (1948), 680.
[171] Gaspari, M. et al. The dance of heating and cooling in galaxy clusters: three-dimensional simulations of self-regulated active galactic nuclei outflows. MNRAS, **411** (2011), 349.
[172] Ghirardini, V. et al. The XMM Cluster Outskirts Project (X-COP): Thermodynamic properties of the intracluster medium out to R_{200} in Abell 2319. A&A, **614** (2018), A7.
[173] Ghirardini, V. et al. Universal thermodynamic properties of the intracluster medium over two decades in radius in the X-COP sample. A&A, **621** (2019), A41.
[174] Giannone, P. *Elementi di astronomia*. Pitagora editrice (2004).

[175] Gingold, R. A. and Monaghan, J. J. Smoothed particle hydrodynamics: theory and application to non-spherical stars. MNRAS, **181** (1977), 375.
[176] Giodini, S. et al. Scaling Relations for Galaxy Clusters: Properties and Evolution. Space Sci. Rev., **177** (2013), 247.
[177] Girardi, M. et al. The velocity field of the Lyra complex. Preprint (arXiv:1908.02277), (2019).
[178] Glenn, J. et al. Bolocam: a millimeter-wave bolometric camera. In *Advanced Technology MMW, Radio, and Terahertz Telescopes*, vol. 3357 of Proc. SPIE, p. 326 (1998).
[179] Gonzalez, E. J. et al. Analysis of candidates for interacting galaxy clusters. I. A1204 and A2029/A2033. A&A, **611** (2018), A78.
[180] Gottlöber, S. and Yepes, G. Shape, spin and baryon fraction of clusters in the marenostrum universe. ApJ, **664** (2007), 117.
[181] Goz, D. et al. Cosmological Simulations in Exascale Era. Preprint (arXiv:1712.00252), (2017).
[182] Grossmann, A. and Morlet, J. Decomposition of hardy functions into square integrable wavelets of constant shape. SJMA, **15** (1984), 723.
[183] Guilloux, F., Faÿ, G., and Cardoso, J.-F. Practical wavelet design on the sphere. Appl. Comput. Harmon. Anal., **26** (2009), 143.
[184] Gunn, J. E. and Gott, J. R. On the Infall of Matter Into Clusters of Galaxies and Some Effects on Their Evolution. ApJ, **176** (1972), 1.
[185] Gupta, N. et al. SZE observables, pressure profiles and centre offsets in Magneticum simulation galaxy clusters. MNRAS, **469** (2017), 3069.
[186] Guth, A. H. Inflationary universe: A possible solution to the horizon and flatness problems. Phys. Rev. D, **23** (1981), 347.
[187] Guth, A. H. Inflation. Preprint (arXiv:0404546), (2004).
[188] Guth, A. H. and Pi, S. Y. Fluctuations in the New Inflationary Universe. Phys. Rev. Lett., **49** (1982), 1110.
[189] Hamden, E. T. et al. Measuring Transverse Motions for Nearby Galaxy Clusters. ApJ, **716** (2010), L205.
[190] Hand, N. et al. Evidence of galaxy cluster motions with the kinematic Sunyaev-Zel'dovich effect. PhRvL, **109** (2012), 041101.
[191] Harrison, E. R. Fluctuations at the Threshold of Classical Cosmology. Phys. Rev. D, **1** (1970), 2726.
[192] Hasselfield, M. et al. The Atacama Cosmology Telescope: Sunyaev-Zel'dovich selected galaxy clusters at 148 GHz from three seasons of data. J. Cosmology Astropart. Phys., **7** (2013), 008.
[193] Heeschen, D. S. The Very Large Array. S&T, **49** (1975), 344.
[194] Heisenberg, W. Über den anschaulichen Inhalt der quantentheoretischen Kinematik und Mechanik. ZPhy, **43** (1927), 172.
[195] Herbig, T. et al. A Measurement of the Sunyaev-Zel'dovich Effect in the Coma Cluster of Galaxies. ApJ, **449** (1995), L5.
[196] Herbonnet, R. et al. Ellipticity of Brightest Cluster Galaxies as tracer of halo orientation and weak-lensing mass bias. MNRAS, **490** (2019), 4889.
[197] Herranz, D. et al. Filtering techniques for the detection of Sunyaev-Zel'dovich clusters in multifrequency maps. MNRAS, **336** (2002), 1057.
[198] Herranz, D. et al. Scale-adaptive Filters for the Detection/Separation of Compact Sources. ApJ, **580** (2002), 610.
[199] Hitomi Collaboration. The quiescent intracluster medium in the core of the Perseus cluster. Nature, **535** (2016), 117.
[200] Hitomi Collaboration. Solar abundance ratios of the iron-peak elements in the Perseus cluster. Nature, **551** (2017), 478.

[201] Ho, P. T. P. et al. The Yuan-Tseh Lee Array for Microwave Background Anisotropy. ApJ, **694** (2009), 1610.

[202] Hobson, M. P. et al. Foreground separation methods for satellite observations of the cosmic microwave background. MNRAS, **300** (1998), 1.

[203] Hogg, D. W. Distance measures in cosmology. Preprint (arXiv:9905116), (1999).

[204] Holder, G. P. et al. Expectations for an Interferometric Sunyaev-Zeldovich Effect Survey for Galaxy Clusters. ApJ, **544** (2000), 629.

[205] Holland, W. S. et al. SCUBA: a submillimeter camera operating on the James Clerk Maxwell Telescope. In *Advanced Technology MMW, Radio, and Terahertz Telescopes*, vol. 3357 of Proc. SPIE, p. 305 (1998).

[206] Holland, W. S. et al. SCUBA-2: The next generation wide-field imager for the James Clerk Maxwell Telescope. In *American Astronomical Society Meeting Abstracts*, vol. 32 of *Bulletin of the American Astronomical Society*, p. 1491 (2000).

[207] Holzapfel, W. L. et al. Limits on the Peculiar Velocities of Two Distant Clusters Using the Kinematic Sunyaev-Zeldovich Effect. ApJ, **481** (1997), 35.

[208] Holzapfel, W. L. et al. The Sunyaev-Zeldovich Infrared Experiment: A Millimeter-Wave Receiver for Cluster Cosmology. ApJ, **479** (1997), 17.

[209] Hu, W. and Dodelson, S. Cosmic Microwave Background Anisotropies. ARA&A, **40** (2002), 171.

[210] Hubble, E. A Relation between Distance and Radial Velocity among Extra-Galactic Nebulae. PNAS, **15** (1929), 168.

[211] Hudson, D. S. et al. What is a cool-core cluster? a detailed analysis of the cores of the X-ray flux-limited HIFLUGCS cluster sample. A&A, **513** (2010), A37.

[212] Hurier, G. High significance detection of the tSZ effect relativistic corrections. A&A, **596** (2016), A61.

[213] Hurier, G., Adam, R., and Keshet, U. First detection of a virial shock with SZ data: implication for the mass accretion rate of Abell 2319. A&A, **622** (2019), A136.

[214] Hurier, G., Aghanim, N., and Douspis, M. MILCANN : A neural network assessed tSZ map for galaxy cluster detection. Preprint (arXiv:1702.00075), (2017).

[215] Hurier, G., Macías-Pérez, J., and Hildebrandt, S. MILCA, a modified internal linear combination algorithm to extract astrophysical emissions from multifrequency sky maps. A&A, **558** (2013), A118.

[216] Hwang, H. S. and Lee, M. G. Searching for Rotating Galaxy Clusters in SDSS and 2dFGRS. ApJ, **662** (2007), 236.

[217] Inogamov, N. A. and Sunyaev, R. A. Turbulence in Clusters of Galaxies and X-ray Line Profiles. AstL, **29** (2003), 791.

[218] Isobe, T. et al. Linear regression in astronomy. ApJ, **364** (1990), 104.

[219] Itoh, N. and Nozawa, S. Relativistic corrections to the Sunyaev-Zeldovich effect for extremely hot clusters of + galaxies. A&A, **417** (2004), 827.

[220] Jeans, J. H. The stability of a spherical nebula. RSPTA, **199** (1902), 1.

[221] Jeltema, T. E. et al. Cluster Structure in Cosmological Simulations. I. Correlation to Observables, Mass Estimates, and Evolution. ApJ, **681** (2008), 167.

[222] Jenkins, A. et al. The mass function of dark matter haloes. MNRAS, **321** (2001), 372.

[223] Johnston-Hollitt, M. et al. Using SKA Rotation Measures to Reveal the Mysteries of the Magnetised Universe. In *Advancing Astrophysics with the Square Kilometre Array (AASKA14)*, p. 92 (2015).

[224] Jones, M. et al. An image of the Sunyaev-Zel'dovich effect. Nature, **365** (1993), 320.

[225] Kaiser, N. Evolution and clustering of rich clusters. MNRAS, **222** (1986), 323.

[226] Kaiser, N. Evolution of Clusters of Galaxies. ApJ, **383** (1991), 104.

[227] Kalberla, P. M. W. et al. The Leiden/Argentine/Bonn (LAB) Survey of Galactic HI. Final data release of the combined LDS and IAR surveys with improved stray-radiation corrections. A&A, **440** (2005), 775.

[228] Kamdar, H. M., Turk, M. J., and Brunner, R. J. Machine learning and cosmological simulations - I. Semi-analytical models. MNRAS, **455** (2016), 642.

[229] Kashlinsky, A. et al. A Measurement of Large-Scale Peculiar Velocities of Clusters of Galaxies: Technical Details. ApJ, **691** (2009), 1479.

[230] Katz, N. and White, S. D. M. Hierarchical Galaxy Formation: Overmerging and the Formation of an X-Ray Cluster. ApJ, **412** (1993), 455.

[231] Kay, S. T. et al. Cosmological simulations of the intracluster medium. MNRAS, **355** (2004), 1091.

[232] Kay, S. T. et al. The evolution of clusters in the CLEF cosmological simulation: X-ray structural and scaling properties. MNRAS, **377** (2007), 317.

[233] Kay, S. T. et al. Sunyaev-Zel'dovich clusters in Millennium gas simulations. MNRAS, **422** (2012), 1999.

[234] Khatri, R. Linearized iterative least-squares (LIL): a parameter-fitting algorithm for component separation in multifrequency cosmic microwave background experiments such as Planck. MNRAS, **451** (2015), 3321.

[235] Killedar, M. et al. How baryonic processes affect strong lensing properties of simulated galaxy clusters. MNRAS, **427** (2012), 533.

[236] King, I. The structure of star clusters. I. an empirical density law. AJ, **67** (1962), 471.

[237] Kippenhahn, R., Weigert, A., and Weiss, A. *Stellar Structure and Evolution*. Springer Berlin Heidelberg (2012).

[238] Kitayama, T. et al. The Sunyaev-Zel'dovich effect at 5": RX J1347.5-1145 imaged by ALMA. PASJ, **68** (2016), 88.

[239] Klypin, A. et al. Resolving the structure of cold dark matter halos. ApJ, **554** (2001), 903.

[240] Klypin, A. et al. MultiDark simulations: the story of dark matter halo concentrations and density profiles. MNRAS, **457** (2016), 4340.

[241] Knebe, A. et al. Haloes gone mad: The halo-finder comparison project. Mon. Not. R. Astron. Soc., **415** (2011), 2293.

[242] Knollmann, S. R. and Knebe, A. AHF: Amiga's Halo Finder. Astrophys. J. S., **182** (2009), 608.

[243] Komatsu, E. and Seljak, U. Universal gas density and temperature profile. MNRAS, **327** (2001), 1353.

[244] Komatsu, E. and Seljak, U. The Sunyaev-Zel'dovich angular power spectrum as a probe of cosmological parameters. MNRAS, **336** (2002), 1256.

[245] Komatsu, E. et al. Seven-year Wilkinson microwave anisotropy probe (WMAP) observations: cosmological interpretation. ApJS, **192** (2011), 18.

[246] Kompaneets, A. S. The establishment of thermal equilibrium between quanta and electrons. JETP, **4** (1957), 730.

[247] Kozmanyan, A. et al. Deriving the Hubble constant using Planck and XMM-Newton observations of galaxy clusters. A&A, **621** (2019), A34.

[248] Kravtsov, A. V. and Borgani, S. Formation of Galaxy Clusters. ARA&A, **50** (2012), 353.

[249] Kunieda, H. et al. Mission overview of Suzaku and topics of observations. In *American Astronomical Society Meeting Abstracts*, vol. 37 of *Bulletin of the American Astronomical Society*, p. 1413 (2005).

[250] Kutz, J. *Data-Driven Modeling & Scientific Computation: Methods for Complex Systems & Big Data*. Data-driven Modeling & Scientific Computation: Methods for Complex Systems & Big Data. OUP Oxford (2013).

[251] Lacey, C. and Cole, S. Merger rates in hierarchical models of galaxy formation. MNRAS, **262** (1993), 627.
[252] Lagache, G. Exploring the dusty star-formation in the early Universe using intensity mapping. In *Peering towards Cosmic Dawn*, vol. 333 of *IAU Symposium*, pp. 228–233 (2018).
[253] LaRoque, S. J. et al. The Sunyaev-Zel'dovich Effect Spectrum of Abell 2163. Preprint (arXiv:astro-ph/0204134), (2002).
[254] Lau, E. T., Kravtsov, A. V., and Nagai, D. Residual gas motions in the intracluster medium and bias in hydrostatic measurements of mass profiles of clusters. ApJ, **705** (2009), 1129.
[255] Lau, E. T., Nagai, D., and Nelson, K. Weighing Galaxy Clusters with Gas. I. On the Methods of Computing Hydrostatic Mass Bias. ApJ, **777** (2013), 151.
[256] Lau, E. T. et al. Mass Accretion and its Effects on the Self-similarity of Gas Profiles in the Outskirts of Galaxy Clusters. ApJ, **806** (2015), 68.
[257] Leach, S. M. Component separation methods for the PLANCK mission. A&A, **491** (2008), 597.
[258] Lemaître, G. Expansion of the universe, A homogeneous universe of constant mass and increasing radius accounting for the radial velocity of extra-galactic nebulae. MNRAS, **91** (1931), 483.
[259] Lenz, D., Doré, O., and Lagache, G. Large-scale Maps of the Cosmic Infrared Background from Planck. ApJ, **883** (2019), 75.
[260] Lewis, A. D., Stocke, J. T., and Buote, D. A. Chandra Observations of Abell 2029: No Cooling Flow and a Steep Abundance Gradient. ApJ, **573** (2002), L13.
[261] L'Huillier, B. et al. Probing features in the primordial perturbation spectrum with large-scale structure data. MNRAS, **477** (2018), 2503.
[262] Li, Y.-C. et al. Measurement of the pairwise kinematic Sunyaev-Zeldovich effect with Planck and BOSS data. Phys. Rev. D, **97** (2018), 23514.
[263] Liddle, A. *An Introduction to Modern Cosmology.* Wiley (2003).
[264] Linde, A. D. A new inflationary universe scenario: A possible solution of the horizon, flatness, homogeneity, isotropy and primordial monopole problems. Physics Letters B, **108** (1982), 389.
[265] Liu, A. and Tozzi, P. Testing the rotation versus merger scenario in the galaxy cluster Abell 2107. MNRAS, **485** (2019), 3909.
[266] Liu, A. et al. A Method to Search for Bulk Motions in the ICM with Chandra CCD Spectra: Application to the Bullet Cluster. ApJ, **809** (2015), 27.
[267] Luzzi, G. et al. Constraining the evolution of the CMB temperature with SZ measurements from Planck data. J. Cosmology Astropart. Phys., **9** (2015), 011.
[268] Macciò, A. V., Dutton, A. A., and Van den Bosch, F. C. Concentration, spin and shape of dark matter haloes as a function of the cosmological model: WMAP1, WMAP3 and WMAP5 results. MNRAS, **391** (2008), 1940.
[269] Mallat, S. *A Wavelet Tour of Signal Processing: The Sparse Way.* Academic Press (2008).
[270] Mallat, S. G. Multiresolution approximations and wavelet orthonormal bases of $L^2(R)$. TAMS, **315** (1989), 69.
[271] Manolopoulou, M. and Plionis, M. Galaxy cluster's rotation. MNRAS, **465** (2017), 2616.
[272] Mantz, A. B. et al. Cosmology and astrophysics from relaxed galaxy clusters - II. Cosmological constraints. MNRAS, **440** (2014), 2077.
[273] Marshall, P. J., Hobson, M. P., and Slosar, A. Bayesian joint analysis of cluster weak lensing and Sunyaev-Zel'dovich effect data. MNRAS, **346** (2003), 489.
[274] Martin, D. H. and Puplett, E. Polarised interferometric spectrometry for the millimetre and submillimetre spectrum. InfPh, **10** (1970), 105.
[275] Martínez, V. et al. *Data Analysis in Cosmology.* Springer (2009).

[276] Masi, S. et al. OLIMPO: a balloon–borne, arcminute-resolution survey of the sky at mm and sub-mm wavelengths. In *European Rocket and Balloon Programmes and Related Research*, vol. 530 of *ESA Special Publication*, p. 557 (2003).

[277] Materne, J. and Hopp, U. The cluster of galaxies SC 0316-44 Does it rotate? A&A, **124** (1983), L13.

[278] Mather, J. C. The Cosmic Background Explorer (COBE). OptEn, **21** (1982), 769.

[279] Medezinski, E. et al. Frontier Fields: Subaru Weak-Lensing Analysis of the Merging Galaxy Cluster A2744. ApJ, **817** (2016), 24.

[280] Meisner, A. M. and Finkbeiner, D. P. Modeling thermal dust emission with two components: application to the planck high frequency instrument maps. ApJ, **798** (2015), 88.

[281] Melin, J.-B., Bartlett, J. G., and Delabrouille, J. Catalog extraction in SZ cluster surveys: a matched filter approach. A&A, **459** (2006), 341.

[282] Melin, J. B. et al. A comparison of algorithms for the construction of SZ cluster catalogues. A&A, **548** (2012), A51.

[283] Meneghetti, M. et al. Weighing simulated galaxy clusters using lensing and X-ray. A&A, **514** (2010), A93.

[284] Meneghetti, M. et al. The MUSIC of CLASH: Predictions on the Concentration-Mass Relation. ApJ, **797** (2014), 34.

[285] Mernier, F. et al. Radial metal abundance profiles in the intra-cluster medium of cool-core galaxy clusters, groups, and ellipticals. A&A, **603** (2017), A80.

[286] Mernier, F. et al. Solar chemical composition in the hot gas of cool-core ellipticals, groups, and clusters of galaxies. MNRAS, **480** (2018), L95.

[287] Merten, J. et al. Creation of cosmic structure in the complex galaxy cluster merger Abell 2744. MNRAS, **417** (2011), 333.

[288] Meszaros, P. The behaviour of point masses in an expanding cosmological substratum. A&A, **37** (1974), 225.

[289] Metzler, C. A. and Evrard, A. E. A Simulation of the Intracluster Medium with Feedback from Cluster Galaxies. ApJ, **437** (1994), 564.

[290] Meyer, Y. *Wavelets and operators*. Cambridge university press (1992).

[291] Molnar, S. M. and Birkinshaw, M. Contributions to the Power Spectrum of Cosmic Microwave Background from Fluctuations Caused by Clusters of Galaxies. ApJ, **537** (2000), 542.

[292] Molnar, S. M. et al. Accretion Shocks in Clusters of Galaxies and Their SZ Signature from Cosmological Simulations. ApJ, **696** (2009), 1640.

[293] Monaghan, J. J. and Lattanzio, J. C. A refined particle method for astrophysical problems. A&A, **149** (1985), 135.

[294] Monfardini, A. et al. NIKA: A millimeter-wave kinetic inductance camera. A&A, **521** (2010), A29.

[295] Moore, B. et al. Resolving the Structure of Cold Dark Matter Halos. ApJ, **499** (1998), L5.

[296] Moré, J. J. The levenberg-marquardt algorithm: Implementation and theory. In *Numerical Analysis*, vol. 630 of *Lecture Notes in Mathematics*, pp. 105–116. Springer Berlin Heidelberg (1978).

[297] Mroczkowski, T. et al. Application of a Self-Similar Pressure Profile to Sunyaev-Zel'dovich Effect Data from Galaxy Clusters. ApJ, **694** (2009), 1034.

[298] Mroczkowski, T. et al. A Multi-wavelength Study of the Sunyaev-Zel'dovich Effect in the Triple-merger Cluster MACS J0717.5+3745 with MUSTANG and Bolocam. ApJ, **761** (2012), 47.

[299] Mroczkowski, T. et al. Astrophysics with the Spatially and Spectrally Resolved Sunyaev-Zeldovich Effects. A Millimetre/Submillimetre Probe of the Warm and Hot Universe. Space Sci. Rev., **215** (2019), 17.

[300] Muanwong, O., Kay, S. T., and Thomas, P. A. Evolution of X-Ray Cluster Scaling Relations in Simulations with Radiative Cooling and Nongravitational Heating. ApJ, **649** (2006), 640.
[301] Mukhanov, V. F., Feldman, H. A., and Brandenberger, R. H. Theory of cosmological perturbations. Phys. Rep., **215** (1992), 203.
[302] Murtagh, F., Starck, J. L., and Bijaoui, A. Image restoration with noise suppression using a multiresolution support. A&AS, **112** (1995), 179.
[303] Nagai, D., Kravtsov, A. V., and Vikhlinin, A. Effects of galaxy formation on thermodynamics of the intracluster medium. ApJ, **668** (2007), 1.
[304] Nagai, D., Vikhlinin, A., and Kravtsov, A. V. Testing X-Ray Measurements of Galaxy Clusters with Cosmological Simulations. ApJ, **655** (2007), 98.
[305] Navarro, J. F., Frenk, C. S., and White, S. D. M. Simulations of X-ray clusters. MNRAS, **275** (1995), 720.
[306] Navarro, J. F., Frenk, C. S., and White, S. D. M. The Structure of Cold Dark Matter Halos. ApJ, **462** (1996), 563.
[307] Navarro, J. F., Frenk, C. S., and White, S. D. M. A universal density profile from hierarchical clustering. ApJ, **490** (1997), 493.
[308] Nelson, K. et al. Evolution of the Merger-induced Hydrostatic Mass Bias in Galaxy Clusters. ApJ, **751** (2012), 121.
[309] Nelson, K. et al. Weighing Galaxy Clusters with Gas. II. On the Origin of Hydrostatic Mass Bias in ΛCDM Galaxy Clusters. ApJ, **782** (2014), 107.
[310] Neto, A. F. et al. The statistics of ΛCDM halo concentrations. MNRAS, **381** (2007), 1450.
[311] Neugebauer, G. et al. The Infrared Astronomical Satellite (IRAS) mission. ApJ, **278** (1984), L1.
[312] Niemack, M. D. et al. ACTPol: a polarization-sensitive receiver for the Atacama Cosmology Telescope. In *Millimeter, Submillimeter, and Far-Infrared Detectors and Instrumentation for Astronomy V*, vol. 7741 of Proc. SPIE, p. 77411S (2010).
[313] Nipoti, C. et al. Magnetorotational instability in cool cores of galaxy clusters. JPlPh, **81** (2015), 495810508.
[314] Nozawa, S., Kohyama, Y., and Itoh, N. Study on the solutions of the Sunyaev-Zeldovich effect for clusters of galaxies. Phys. Rev. D, **79** (2009), 123007.
[315] Nozawa, S. et al. Relativistic Corrections to the Sunyaev-Zeldovich Effect for Clusters of Galaxies. IV. Analytic Fitting Formula for the Numerical Results. ApJ, **536** (2000), 31.
[316] Nozawa, S. et al. An improved formula for the relativistic corrections to the kinematical Sunyaev-Zeldovich effect for clusters of galaxies. NCimB, **121** (2006), 487.
[317] Oegerle, W. R. and Hill, J. M. Structure, Rotation, and Peculiar Velocity cD Galaxy in ABELL 2107. AJ, **104** (1992), 2078.
[318] Okabe, N. et al. Universal profiles of the intracluster medium from Suzaku X-ray and Subaru weak-lensing observations*. PASJ, **66** (2014), 99.
[319] Padmanabhan, T. *Theoretical astrophysics vol.1 (structure formation in the universe)*. Cambridge university press (1993).
[320] Particle Data Group Collaboration. Review of particle physics. PhRvD, **98** (2018), 030001.
[321] Pearce, F. R. et al. The effect of radiative cooling on the X-ray properties of galaxy clusters. MNRAS, **317** (2000), 1029.
[322] Peebles, P. J. E. Origin of the angular momentum of galaxies. ApJ, **155** (1969), 393.
[323] Peebles, P. J. E. Structure of the Coma Cluster of Galaxies. AJ, **75** (1970), 13.
[324] Peebles, P. J. E. and Yu, J. T. Primeval Adiabatic Perturbation in an Expanding Universe. ApJ, **162** (1970), 815.

[325] Penzias, A. A. and Wilson, R. W. A Measurement of Excess Antenna Temperature at 4080 Mc/s. ApJ, **142** (1965), 419.
[326] Perlmutter, S. et al. Measurements of Ω and Λ from 42 High-Redshift Supernovae. ApJ, **517** (1999), 565.
[327] Peterson, J. R. and Fabian, A. C. X-ray spectroscopy of cooling clusters. Phys. Rep., **427** (2006), 1.
[328] Pierpaoli, E., Anthoine, S., Huffenberger, K., and Daubechies, I. Reconstructing Sunyaev-Zel'dovich clusters in future cosmic microwave background experiments. MNRAS, **359** (2005), 261.
[329] Pierpaoli, E., Scott, D., and White, M. Power-spectrum normalization from the local abundance of rich clusters of galaxies. MNRAS, **325** (2001), 77.
[330] Piffaretti, R. and Valdarnini, R. Total mass biases in X-ray galaxy clusters. A&A, **491** (2008), 71.
[331] Pires, S. et al. Sunyaev-Zel'dovich cluster reconstruction in multiband bolometer camera surveys. A&A, **455** (2006), 741.
[332] Plagge, T. et al. Sunyaev-Zel'dovich Cluster Profiles Measured with the South Pole Telescope. ApJ, **716** (2010), 1118.
[333] Planck Collaboration. Planck early results. I. The Planck mission. A&A, **536** (2011), A1.
[334] Planck Collaboration. Planck intermediate results. V. Pressure profiles of galaxy clusters from the Sunyaev-Zeldovich effect. A&A, **550** (2013), A131.
[335] Planck Collaboration. Planck intermediate results. VIII. Filaments between interacting clusters. A&A, **550** (2013), A134.
[336] Planck Collaboration. Planck 2013 results. IX. HFI spectral response. A&A, **571** (2014), A9.
[337] Planck Collaboration. Planck 2013 results. XI. All-sky model of thermal dust emission. A&A, **571** (2014), A11.
[338] Planck Collaboration. Planck 2013 results. XXIX. The Planck catalogue of Sunyaev–Zeldovich sources. A&A, **571** (2014), A29.
[339] Planck Collaboration. Planck 2013 results. XXVIII. The Planck Catalogue of Compact Sources. A&A, **571** (2014), A28.
[340] Planck Collaboration. Planck 2013 results. XXXII. The updated Planck catalogue of Sunyaev-Zeldovich sources. A&A, **581** (2015), A14.
[341] Planck Collaboration. Planck 2015 results. VII. High Frequency Instrument data processing: Time-ordered information and beams. A&A, **594** (2016), A7.
[342] Planck Collaboration. Planck 2015 results. VIII. High Frequency Instrument data processing: Calibration and maps. A&A, **594** (2016), A8.
[343] Planck Collaboration. Planck 2015 results X. Diffuse component separation: Foreground maps. A&A, **594** (2016), A10.
[344] Planck Collaboration. Planck 2015 results. XIII. Cosmological parameters. A&A, **594** (2016), A13.
[345] Planck Collaboration. Planck 2015 results. XXVI. The Second Planck Catalogue of Compact Sources. A&A, **594** (2016), A26.
[346] Planck Collaboration. Planck 2015 results. XXVII. The second Planck catalogue of Sunyaev-Zeldovich sources. A&A, **594** (2016), A27.
[347] Planck Collaboration. Planck intermediate results. XXXVII. Evidence of unbound gas from the kinetic Sunyaev-Zeldovich effect. A&A, **586** (2016), A140.
[348] Planck Collaboration. Planck 2018 results. VI. Cosmological parameters. Preprint (arXiv:1807.06209), (2018).
[349] Planck Collaboration. Planck 2018 results. I. Overview and the cosmological legacy of Planck. Preprint (arXiv:1807.06205), (2018).
[350] Planelles, S. et al. On the role of AGN feedback on the thermal and chemodynamical properties of the hot intracluster medium. MNRAS, **438** (2014), 195.

[351] Planelles, S. et al. Pressure of the hot gas in simulations of galaxy clusters. MNRAS, **467** (2017), 3827.
[352] Polikar, R. The story of wavelets. Phys. Mod. Top. Mech. Elec. Eng., (1999), 192.
[353] Power, C., Knebe, A., and Knollmann, S. R. The dynamical state of dark matter haloes in cosmological simulations – I. Correlations with mass assembly history. MNRAS, **419** (2012), 1576.
[354] Prada, F. et al. Halo concentrations in the standard ΛCDM cosmology. MNRAS, **423** (2012), 3018.
[355] Pratt, G. W. et al. The Galaxy Cluster Mass Scale and Its Impact on Cosmological Constraints from the Cluster Population. Space Sci. Rev., **215** (2019), 25.
[356] Press, W. H. and Schechter, P. Formation of galaxies and clusters of galaxies by self-similar gravitational condensation. ApJ, **187** (1974), 425.
[357] Prokhorov, D. A. and Colafrancesco, S. The first measurement of temperature standard deviation along the line of sight in galaxy clusters. MNRAS, **424** (2012), L49.
[358] Prunet, S. et al. Initial Conditions For Large Cosmological Simulations. ApJS, **178** (2008), 179.
[359] Puget, J.-L. et al. Tentative detection of a cosmic far-infrared background with COBE. A&A, **308** (1996), L5.
[360] Raghunathan, S. et al. An Inpainting Approach to Tackle the Kinematic and Thermal SZ Induced Biases in CMB-Cluster Lensing Estimators. J. Cosmology Astropart. Phys., **2019** (2019), 037.
[361] Ragone-Figueroa, C. et al. Brightest cluster galaxies in cosmological simulations: achievements and limitations of active galactic nuclei feedback models. MNRAS, **436** (2013), 1750.
[362] Rasia, E., Tormen, G., and Moscardini, L. A dynamical model for the distribution of dark matter and gas in galaxy clusters. MNRAS, **351** (2004), 237.
[363] Rasia, E. et al. Systematics in the X-ray cluster mass estimators. MNRAS, **369** (2006), 2013.
[364] Rasia, E. et al. Temperature Structure of the Intracluster Medium from Smoothed-particle Hydrodynamics and Adaptive-mesh Refinement Simulations. ApJ, **791** (2014), 96.
[365] Rasia, E. et al. Cool Core Clusters from Cosmological Simulations. ApJ, **813** (2015), L17.
[366] Rees, M. J. and Sciama, D. W. Large-scale Density Inhomogeneities in the Universe. Nature, **217** (1968), 511.
[367] Reiprich, T. H. et al. Outskirts of Galaxy Clusters. Space Sci. Rev., **177** (2013), 195.
[368] Remazeilles, M., Aghanim, N., and Douspis, M. Reconstruction of high-resolution Sunyaev–Zeldovich maps from heterogeneous data sets using needlets. MNRAS, **430** (2013), 370.
[369] Remazeilles, M., Delabrouille, J., and Cardoso, J. F. CMB and SZ effect separation with constrained Internal Linear Combinations. MNRAS, **410** (2011), 2481.
[370] Rephaeli, Y. Comptonization of the cosmic microwave background: The Sunyaev-Zel'dovich Effect. ARA&A, **33** (1995), 541.
[371] Rephaeli, Y. Cosmic Microwave Background Comptonization by Hot Intracluster Gas. ApJ, **445** (1995), 33.
[372] Richards, P. L. Bolometers for infrared and millimeter waves. JAP, **76** (1994), 1.
[373] Ricker, P. M. Off-Center Collisions between Clusters of Galaxies. ApJ, **496** (1998), 670.
[374] Ricker, P. M. and Sarazin, C. L. Off-axis cluster mergers: effects of a strongly peaked dark matter profile. ApJ, **561** (2001), 621.

[375] Riess, A. G. et al. Observational Evidence from Supernovae for an Accelerating Universe and a Cosmological Constant. AJ, **116** (1998), 1009.
[376] Riess, A. G. et al. Large Magellanic Cloud Cepheid Standards Provide a 1% Foundation for the Determination of the Hubble Constant and Stronger Evidence for Physics beyond ΛCDM. ApJ, **876** (2019), 85.
[377] Robertson, H. P. Kinematics and World-Structure. ApJ, **82** (1935), 284.
[378] Roettiger, K. and Flores, R. A prediction of observable rotation in the intracluster medium of abell 3266. ApJ, **538** (2000), 92.
[379] Romero, C. E. et al. Galaxy Cluster Pressure Profiles, as Determined by Sunyaev-Zeldovich Effect Observations with MUSTANG and Bolocam. I. Joint Analysis Technique. ApJ, **807** (2015), 121.
[380] Romero, C. E. et al. Galaxy Cluster Pressure Profiles as Determined by Sunyaev Zel'dovich Effect Observations with MUSTANG and Bolocam. II. Joint Analysis of 14 Clusters. ApJ, **838** (2017), 86.
[381] Roncarelli, M. et al. Large-scale inhomogeneities of the intracluster medium: improving mass estimates using the observed azimuthal scatter. MNRAS, **432** (2013), 3030.
[382] Roncarelli, M. et al. Measuring turbulence and gas motions in galaxy clusters via synthetic Athena X-IFU observations. A&A, **618** (2018), A39.
[383] Rossetti, M. et al. Measuring the dynamical state of Planck SZ-selected clusters: X-ray peak-BCG offset. MNRAS, **457** (2016), 4515.
[384] RubiñoMartín, J. A. CMB experiments at European sites. In *Towards the European Coordination of the CMB programme* (2017).
[385] Ruppin, F. et al. First Sunyaev-Zel'dovich mapping with the NIKA2 camera: Implication of cluster substructures for the pressure profile and mass estimate. A&A, **615** (2018), A112.
[386] Ruppin, F. et al. Impact of the mean pressure profile of galaxy clusters on the cosmological constraints from the *Planck* tSZ power spectrum. MNRAS, **490** (2019), 784.
[387] Rybicki, G. and Lightman, A. *Radiative processes in Astrophysics*. Wiley (2004).
[388] Sachs, R. K. and Wolfe, A. M. Perturbations of a Cosmological Model and Angular Variations of the Microwave Background. ApJ, **147** (1967), 73.
[389] Salvati, L., Douspis, M., and Aghanim, N. Constraints from thermal Sunyaev-Zel'dovich cluster counts and power spectrum combined with CMB. A&A, **614** (2018), A13.
[390] Salvati, L. et al. Mass bias evolution in tSZ cluster cosmology. A&A, **626** (2019), A27.
[391] Sayers, J. et al. Optics for MUSIC: a new (sub) millimeter camera for the Caltech Submillimeter Observatory. In *Astronomical Telescopes and Instrumentation*, p. 77410W (2010).
[392] Sayers, J. et al. A Measurement of the Kinetic Sunyaev-Zel'dovich Signal Toward MACS J0717.5+3745. ApJ, **778** (2013), 52.
[393] Sayers, J. et al. Sunyaev-Zel'dovich-measured Pressure Profiles from the Bolocam X-Ray/SZ Galaxy Cluster Sample. ApJ, **768** (2013), 177.
[394] Sayers, J. et al. A Comparison and Joint Analysis of Sunyaev-Zel'dovich Effect Measurements from Planck and Bolocam for a Set of 47 Massive Galaxy Clusters. ApJ, **832** (2016), 26.
[395] Sayers, J. et al. Peculiar Velocity Constraints from Five-Band SZ Effect Measurements Towards RX J1347. 5-1145 with MUSIC and Bolocam from the CSO. ApJ, **820** (2016), 101.
[396] Sayers, J. et al. Imaging the Thermal and Kinematic Sunyaev-Zel'dovich Effect Signals in a Sample of 10 Massive Galaxy Clusters: Constraints on Internal Velocity Structures and Bulk Velocities. ApJ, **880** (2019), 45.

[397] Schillaci, A. et al. Efficient differential Fourier-transform spectrometer for precision Sunyaev-Zel'dovich effect measurements. A&A, **565** (2014), A125.

[398] Schindler, S. and Diaferio, A. Metal Enrichment Processes. Space Sci. Rev., **134** (2008), 363.

[399] Schramm, D. N. and Steigman, G. Relic Neutrinos and the Density of the Universe. ApJ, **243** (1981), 1.

[400] Schroeder, D. J. *Astronomical optics*. Academic press (1999).

[401] Schuecker, P. et al. Observational constraints on general relativistic energy conditions, cosmic matter density and dark energy from X-ray clusters of galaxies and type-Ia supernovae. A&A, **402** (2003), 53.

[402] Seljak, U. and Zaldarriaga, M. Lensing-induced Cluster Signatures in the Cosmic Microwave Background. ApJ, **538** (2000), 57.

[403] Sembolini, F. et al. The MUSIC of Galaxy Clusters - I. Baryon properties and Scaling Relations of the thermal Sunyaev-Zel'dovich Effect. MNRAS, **429** (2013), 323.

[404] Sembolini, F. et al. The MUSIC of Galaxy Clusters - III. Properties, evolution and $Y - M$ scaling relation of protoclusters of galaxies. MNRAS, **440** (2014), 3520.

[405] Sembolini, F. et al. nIFTy galaxy cluster simulations - I. Dark matter and non-radiative models. MNRAS, **457** (2016), 4063.

[406] Shannon, C. E. A mathematical theory of communication. BSTJ, **27** (1948), 379.

[407] Sharma, S. and Steinmetz, M. The angular momentum distribution for gas and dark matter in galactic halos. ApJ, **628** (2005), 21.

[408] Sheth, R. K., Mo, H. J., and Tormen, G. Ellipsoidal collapse and an improved model for the number and spatial distribution of dark matter haloes. MNRAS, **323** (2001), 1.

[409] Sheth, R. K. and Tormen, G. Large-scale bias and the peak background split. MNRAS, **308** (1999), 119.

[410] Shi, X. et al. Analytical model for non-thermal pressure in galaxy clusters - II. Comparison with cosmological hydrodynamics simulation. MNRAS, **448** (2015), 1020.

[411] Sijacki, D. et al. A unified model for AGN feedback in cosmological simulations of structure formation. MNRAS, **380** (2007), 877.

[412] Silk, J. Cosmic Black-Body Radiation and Galaxy Formation. ApJ, **151** (1968), 459.

[413] Simionescu, A. et al. Constraining Gas Motions in the Intra-Cluster Medium. Space Sci. Rev., **215** (2019), 24.

[414] Smirnov, A. V. et al. Space mission Millimetron for terahertz astronomy. In *Space Telescopes and Instrumentation 2012: Optical, Infrared, and Millimeter Wave*, vol. 8442 of Proc. SPIE, p. 84424C (2012).

[415] Springel, V. The cosmological simulation code GADGET-2. MNRAS, **364** (2005), 1105.

[416] Springel, V., Di Matteo, T., and Hernquist, L. Modeling feedback from stars and black holes in galaxy mergers. MNRAS, **361** (2005), 776.

[417] Springel, V. and Hernquist, L. Cosmological smoothed particle hydrodynamics simulations: a hybrid multiphase model for star formation. MNRAS, **339** (2003), 289.

[418] Starck, J.-L., Candes, E. J., and Donoho, D. L. The curvelet transform for image denoising. IEEE Transactions on Image Processing, **11** (2002), 670.

[419] Starck, J. L., Donoho, D. L., and Candès, E. J. Astronomical image representation by the curvelet transform. A&A, **398** (2003), 785.

[420] Starck, J.-L., Murtagh, F. D., and Bijaoui, A. *Image processing and data analysis: the multiscale approach*. Cambridge University Press (1998).

[421] Stolyarov, V. et al. All-sky component separation in the presence of anisotropic noise and dust temperature variations. MNRAS, **357** (2005), 145.

[422] Strüder, L. et al. The European Photon Imaging Camera on XMM-Newton: The pn-CCD camera. A&A, **365** (2001), L18.
[423] Sunyaev, R. A., Norman, M. L., and Bryan, G. L. On the detectability of turbulence and bulk flows in x-ray clusters. AstL, **29** (2003), 783.
[424] Sunyaev, R. A. and Zeldovich, Y. B. Small-Scale Fluctuations of Relic Radiation. Ap&SS, **7** (1970), 3.
[425] Sunyaev, R. A. and Zel'dovich, Y. B. The interaction of matter and radiation in the hot model of the Universe, II. Ap&SS, **7** (1970), 20.
[426] Sunyaev, R. A. and Zeldovich, Y. B. The Observations of Relic Radiation as a Test of the Nature of X-Ray Radiation from the Clusters of Galaxies. CoASP, **4** (1972), 173.
[427] Sunyaev, R. A. and Zel'dovich, Y. B. Microwave background radiation as a probe of the contemporary structure and history of the universe. ARA&A, **18** (1980), 537.
[428] Swetz, D. S. et al. Overview of the Atacama Cosmology Telescope: Receiver, Instrumentation, and Telescope Systems. ApJS, **194** (2011), 41.
[429] Takahashi, T. et al. The ASTRO-H (Hitomi) x-ray astronomy satellite. In Proc. SPIE, vol. 9905 of *Society of Photo-Optical Instrumentation Engineers (SPIE) Conference Series*, p. 99050U (2016).
[430] Tarrío, P., Melin, J. B., and Arnaud, M. ComPRASS: a Combined Planck-RASS catalogue of X-ray-SZ clusters. A&A, **626** (2019), A7.
[431] Tarrío, P. et al. Joint signal extraction from galaxy clusters in X-ray and SZ surveys: A matched-filter approach. A&A, **591** (2016), A39.
[432] Tashiro, M. et al. Concept of the X-ray Astronomy Recovery Mission. In Proc. SPIE, vol. 10699 of *Society of Photo-Optical Instrumentation Engineers (SPIE) Conference Series*, p. 1069922 (2018).
[433] Thomas, P. A. and Couchman, H. M. P. Simulating the formation of a cluster of galaxies. MNRAS, **257** (1992), 11.
[434] Tinker, J. et al. Toward a Halo Mass Function for Precision Cosmology: The Limits of Universality. ApJ, **688** (2008), 709.
[435] Tinker, J. L. et al. The Large-scale Bias of Dark Matter Halos: Numerical Calibration and Model Tests. ApJ, **724** (2010), 878.
[436] Tovmassian, H. M. The Rotation of Galaxy Clusters. Ap, **58** (2015), 328.
[437] Tozzi, P. and Norman, C. The Evolution of X-Ray Clusters and the Entropy of the Intracluster Medium. ApJ, **546** (2001), 63.
[438] Trotta, R. Bayes in the sky: Bayesian inference and model selection in cosmology. ConPh, **49** (2008), 71.
[439] Trümper, J. The ROSAT mission. AdSpR, **2** (1982), 241.
[440] Turner, M. J. L. et al. The European Photon Imaging Camera on XMM-Newton: The MOS cameras : The MOS cameras. A&A, **365** (2001), L27.
[441] Tutukov, A. V., Dryomov, V. V., and Dryomova, G. N. Dynamical Evolution of Galaxy Clusters in the Framework of the N -Body Problem. The Formation of Supermassive cD Galaxies. ARep, **51** (2007), 435.
[442] Umetsu, K. et al. The Projected Dark and Baryonic Ellipsoidal Structure of 20 CLASH Galaxy Clusters. ApJ, **860** (2018), 104.
[443] Valdarnini, R. Iron abundances and heating of the intracluster medium in hydrodynamical simulations of galaxy clusters. MNRAS, **339** (2003), 1117.
[444] Vale, C. and White, M. Finding clusters in SZ surveys. New A, **11** (2006), 207.
[445] Van Cittert, P. H. Zum Einfluß der Spaltbreite auf die Intensitätsverteilung in Spektrallinien. II. ZPhy, **69** (1931), 298.
[446] Van den Bosch, F. C. et al. The Angular Momentum of Gas in Protogalaxies. I. Implications for the Formation of Disk Galaxies. ApJ, **576** (2002), 21.

[447] van Weeren, R. J. et al. Diffuse Radio Emission from Galaxy Clusters. Space Sci. Rev., **215** (2019), 16.
[448] Vazza, F. et al. Turbulent motions and shocks waves in galaxy clusters simulated with adaptive mesh refinement. A&A, **504** (2009), 33.
[449] Vazza, F. et al. Properties of gas clumps and gas clumping factor in the intra-cluster medium. MNRAS, **429** (2013), 799.
[450] Vega, J., Yepes, G., and Gottlöber, S. On the shape of dark matter halos from MultiDark Planck simulations. MNRAS, **467** (2017), 3226.
[451] Vikhlinin, A., Forman, W., and Jones, C. Outer Regions of the Cluster Gaseous Atmospheres. ApJ, **525** (1999), 47.
[452] Vikhlinin, A. et al. Chandra Sample of Nearby Relaxed Galaxy Clusters: Mass, Gas Fraction, and Mass-Temperature Relation. ApJ, **640** (2006), 691.
[453] Voit, G. M. Tracing cosmic evolution with clusters of galaxies. RvMP, **77** (2005), 207.
[454] Voit, G. M. and Bryan, G. L. Regulation of the X-ray luminosity of clusters of galaxies by cooling and supernova feedback. Nature, **414** (2001), 425.
[455] Voit, G. M., Kay, S. T., and Bryan, G. L. The baseline intracluster entropy profile from gravitational structure formation. MNRAS, **364** (2005), 909.
[456] von der Linden, A. et al. Weighing the Giants - I. Weak-lensing masses for 51 massive galaxy clusters: project overview, data analysis methods and cluster images. MNRAS, **439** (2014), 2.
[457] Walker, A. G. On Milne's Theory of World-Structure. P.Lond.Math.Soc., **42** (1937), 90.
[458] Walker, S. et al. The Physics of Galaxy Cluster Outskirts. Space Sci. Rev., **215** (2019), 7.
[459] Walker, S. A. et al. X-ray observations of the galaxy cluster Abell 2029 to the virial radius. MNRAS, **422** (2012), 3503.
[460] Weinberg, S. *Gravitation and Cosmology: Principles and Applications of the General Theory of Relativity*. Wiley (1972).
[461] Weinberg, S. The cosmological constant problem. RvMP, **61** (1989), 1.
[462] Weisskopf, M. C. et al. Chandra X-ray Observatory (CXO): overview. In Proc. SPIE, vol. 4012, pp. 2–16 (2000).
[463] Wen, Z. L., Han, J. L., and Liu, F. S. Mass function of rich galaxy clusters and its constraint on σ_8. MNRAS, **407** (2010), 533.
[464] White, S. D. M. The dynamics of rich clusters of galaxies. MNRAS, **177** (1976), 717.
[465] Wiener, N. Extrapolation, interpolation, and smoothing of stationary time series (1949).
[466] Wong, K. C. et al. H0LiCOW XIII. A 2.4% measurement of H_0 from lensed quasars: 5.3σ tension between early and late-Universe probes. Preprint (arXiv:1907.04869), (2019).
[467] Wu, H.-Y. et al. RHAPSODY-G simulations: galaxy clusters as baryonic closed boxes and the covariance between hot gas and galaxies. MNRAS, **452** (2015), 1982.
[468] Young, A. et al. MUSTANG2: High-resolution SZE Imaging Of Galaxy Clusters With The GBT. In *American Astronomical Society Meeting Abstracts*, vol. 219, p. 446.08 (2012).
[469] Young, B.-L. A survey of dark matter and related topics in cosmology. FrPhy, **12** (2016), 121201.
[470] Zel'dovich, Y. B. Gravitational instability: An approximate theory for large density perturbations. A&A, **5** (1970), 84.
[471] Zeldovich, Y. B. A hypothesis, unifying the structure and the entropy of the Universe. MNRAS, **160** (1972), 1P.